Novel manufacturing routes for solid-state batteries

Michael Metzler

Wolfson College

University of Oxford

A thesis submitted for the degree of Doctor of Philosophy

Trinity 2025

Supervised by Prof. P.S. Grant & Dr. E. Liotti

Abstract

Solid-state batteries (SSBs) based on sulphide solid electrolytes (SEs) have the potential to increase safety and energy density compared with lithium-ion batteries (LIBs). However, SSB fabrication is at an immature stage. The thesis describes three novel investigations of materials design and associated manufacturing approaches to SE separators and anode-free SSBs.

A solvent-free processing approach was developed for sulphide separators based on polytetrafluoroethylene binder fibrillation and hot calendering, and the microstructure and performance compared with slurry cast equivalents. Optimized free-standing SE sheets had density $\sim$ 84 %, pore diameter $<$ 1 µm and ionic conductivity $>$ 1 mS/cm at 60 °C. Dry processed 600 μm thick separators had a critical current density for Li dendrite penetration of 1 mA/cm^2 compared with 2 mA/cm^2 for slurry cast separators.

Anode-free SSB cells with $LiNi_{0.8}Mn_{0.1}Co_{0.1}O_2$/sulphide hybrid cathodes were fabricated with different $\sim$ 13 μm spray-printed Ag/C particulate interlayer architectures to promote uniformity of plated metallic Li on charging. Interlayers with increased Ag fraction at the current collector showed improved performance, including an initial discharge capacity of $>$ 190 mAh/g, reduced capacity degradation during cycling and a Coulombic efficiency $>$ 98% after 100 cycles. The greater uniformity of Li plating was revealed by cross-sectional microscopy, and a mechanism proposed.

Building on these findings, two alternative, novel Ag/C interlayer processing techniques for anode-free cells were investigated. Precipitation of Ag nanoparticles onto a carboxymethyl cellulose/C precoating allowed control of Ag diameters (10 - 150 nm), but electrochemical performance was not

improved. However, sputtering of $\sim$ 100 nm thick Ag onto a $\sim$ 1 μm C pre-coated Cu current collector again facilitated greater uniformity of both Li plating and stripping that was revealed by cross-sectional microscopy, leading to a high performing initial discharge capacity of $>$ 200 mAh/g and an initial Coulombic efficiency of 86 %.

Declaration

All of the research presented was carried out by the author in the *Department of Materials* at the *University of Oxford* under the supervision of Prof P. S. Grant & Dr E. Liotti. The project was partially funded by the Faraday Institution project award SOLBAT and the Henry Royce Institute through the UK Engineering and Physical Science Research Council (EPSRC). The work is original and where work from others has been included it has been clearly referenced and acknowledged. No part of this thesis has been submitted or accepted for any other degree at this university or elsewhere.

Michael Metzler

Trinity 2025

Acknowledgements

I am grateful to my supervisors Professor Patrick Grant and Dr Enzo Liotti for their guidance throughout my time as a DPhil student and for providing the opportunity to work on this highly relevant topic. I am grateful to my assessors, Professor David Armstrong, Dr Jicheng Gong, and Professor Robert House for their helpful feedback during my transfer and confirmation of status.

I would like to thank Dr Guillaume Matthews for his SEM/EDX, TEM, and XRD measurements reported in Chapters 5 and 6. Thanks is also given to Dr Yige Sun for her support with P-FIB/SIMS measurements shown in Chapters 5 and 6. I am grateful to Dr Enzo Liotti for his help with image analysis shown in Chapters 4 and 5. A special thanks to Dr Christopher Doerrer for the extensive training and continuous support he provided and his assistance with spray printing, experimental design, and data interpretation.

I am grateful to the David Cockayne Centre for Electron Microscopy, especially Dr Phani Kharamched, Dr Gareth Hughes, and Graham Wyatt. I would like to thank the Oxford Materials Characterisation Service, especially Dr Kerstin Jurkschat, Dr Colin Johnston, Dr Wai Man Chan, Chris Salter and Dr Andrew Lui for XCT, XPS laser diffraction, and Raman measurements shown in Chapters 4 to 6. I would like to thank Gideon Ring, Greg Cook, Richard Turner, Anthony Wheeler, Benjamin Morley, Andrew Green and Mark Richey for their technical support of my experimental work. I would also like to thank Dr Samuel Wheeler, Dr Marveh Forghani, and Dr Julia Ramirez-Gonzalez for their advice and support.

My thanks go to Samantha Pearce and Leigh Mapledoram for their help with administrative and

organizational activities.

I am grateful to the EPSRC, the Faraday Institution, and the Henry Royce Institute for funding training and travel opportunities and providing essential equipment for this work.

I would like to thank my family and friends and my partner Gayoung for all their support during my DPhil program.

Publications and conference presentations

1. "Impact of dry processing and slurry casting on the properties of separators for solid-state batteries", Faraday Institution Early Career Researcher Conference and Training Event 2024, Warwick, United Kingdom, 26th and 27th March 2024 [In-person oral presentation].

2. "Novel manufacturing routes for solid-state batteries", Materials Research Exchange 2024, London, United Kingdom, 23rd and 24th April 2024 [Poster competition - **expected impact for user industry winner**].

3. "Novel manufacturing routes for solid-state batteries", All-Energy & Dcarbonise 2024, Glasgow, United Kingdom, 15th and 16th May 2024 [Poster exhibition].

4. **M. Metzler**, C. Doerrer, Y. Sun, G. Matthews, E. Liotti, and P.S. Grant, "The Effect of Silver Particle Distribution in a Carbon Nanocomposite Interlayer on Lithium Plating in Anode-Free All-Solid-State Batteries," *ACS Appl. Mater. & Interfaces*, vol. 17 (27), pp. 39089–39096, 2025.

5. C. Doerrer, **M. Metzler**, G. Matthews, J. Bu, D. Spencer-Jolly, P.G. Bruce, M. Pasta, and P.S. Grant, "Spraying Li_6PS_5Cl and silver-carbon multilayers to facilitate large-scale fabrication of all-solid-state batteries," *Device*, vol. 2 (8), no. 100468, 2024.

6. S.P. Zankowki, S. Wheeler, T. Barthelay, W.M. Chan, **M. Metzler**, and P.S. Grant, "Chemical

staining - a toolbox for fundamental studies and practical optimization of binders in negative Li-ion electrodes" (submitted to *Nat. Commun.*).

Contents

Abbreviations

AC	alternating current
AM	active material
ASSB	all-solid-state battery
BSE	backscattered electron
C	capacitor
CA	citric acid
CB	carbon black
CBD	carbon binder domain
CC	current collector
CCD	critical current density
CCE	carbon conductivity enhancer
CE	Coulombic efficiency
CMC	carboxymethyl cellulose
CT	charge transfer
3DP	dry 3D printing
DC	direct current
DEC	diethyl carbonate
DIB	dual-ion battery
DMC	dimethyl carbonate

DME	dimethoxyethane
DOL	dioxolane
EC	ethylene carbonate
EDS, EDX	energy-dispersive X-ray spectroscopy
EIS	electrochemical impedance spectroscopy
EMC	ethyl methyl carbonate
EsB	energy-selective backscattered
FAST	field assisted sintering
FDM	fused deposition modelling
FE-SEM	field emission scanning electron microscopy
FTIR	Fourier transform infrared spectroscopy
GB	grain boundary
HRTEM	high-resolution transmission electron microscopy
IPA	isopropyl alcohol
IR	infrared
LAGP	lithium aluminium germanium phosphate
LATP	lithium aluminum titanium phosphate
LCO	lithium cobalt oxide
LIB	lithium-ion battery
LiPON	lithium phosphorus oxynitride
LISICON	lithium superionic conductors
LiTFSI	lithium bis(trifluoromethanesulfonyl)imide
LGPS	lithium germanium phosphorus sulfide
LLTO	lithium lanthanum titanate
LLZO	lithium lanthanum zirconium oxide
LLZTO	lithium lanthanum zirconium tantalum oxide

LPS	lithium phosphorus sulfur chloride
LRLO	lithium-rich layered oxide
LSB	lithium-sulfur battery
MSB	magnesium-sulfur battery
NASICON	sodium superionic conductors
NBR	nitrile butadiene rubber
NCA	lithium nickel cobalt aluminum Oxide
NHE	normal hydrogen electrode
NMC	lithium nickel manganese cobalt oxide
NMP	N-Methyl-2-pyrrolidone
NP	nanoparticle
PAN	polyacrylonitrile
PC	polycrystalline
PEEK	polyether ether ketone
PEO	polyethylene oxide
P-FIB	plasma focused ion beam
PTFE	polytetrafluoroethylene
PVD	physical vapour deposition
PVDF	polyvinylidene fluoride
Q	constant phase element
QSSB-LSB	quasi-solid-state lithium/sulfur battery
R	resistor
RF	radio frequency
RT	room temperature
$\mathbf{S_a}$	arithmetical mean height
SBR	styrene butadiene rubber

SC	single crystalline
SE	solid electrolyte
SEI	solid electrolyte interface
SEM	scanning electron microscopy
SIMS	secondary-ion mass spectrometry
SPS	spark plasma sintering
SSB	solid-state battery
$\mathbf{S_q}$	root mean square height
TEM	transmission electron microscopy
TPA	thermoplastic polyamide
W	Warburg
XCT	X-ray computed tomography
XPS	X-ray photoelectron spectroscopy
XRD	X-ray diffraction

Chapter 1

Introduction

The continued electrification of a significant share of global transport systems, industry, and private homes (e.g. heating) will require the development of new generations of energy storage systems [1]. When electric vehicles are combined with energy generated by renewable sources, significantly decreased carbon emissions will follow. However, the generation of renewable energy does not always correlate with demand peaks [2]. This mismatch in demand and supply requires the transformation of conventional power grids into decentralized grids with intermediate timescale ($\sim$ 4-10 h) energy storage of renewable power that otherwise will limit peak power generation and consumption, and reduce renewable system expansion [3, 4]. Using vehicle-to-grid technologies, electric vehicle batteries could become an important component of local/national storage grids when parked [2, 3]. Consequently, batteries are not only essential components of mobile applications, but can be an integral part of the planned energy transition to decentralized renewable energy and energy efficiency [3]. Technically effective and economically efficient electricity storage is still a missing link to a CO_2-neutral society. As an example, improving battery performance could enable electric aviation, that would further reduce global carbon emissions [5].

Lithium-ion batteries (LIBs) based on liquid organic electrolytes are the dominant technology for electrochemical energy storage systems [1]. However, the technology is tending towards a maximum

energy density of approximately 300 Wh kg^{-1}, based on the intrinsic properties of the materials used [6, 7]. Although LIB improvements and dramatic reductions in cost over the last 30 years will preserve LIB applications for many years, there are disadvantages, alongside the plateau in performance. In particular, the organic electrolytes used in conventional LIBs are toxic and flammable [1]. In contrast, because solid-state batteries (SSBs) use a more chemically inert solid-state electrolyte (SSE), they can make use of a thin (< 50 μm) Li metal anode that has a very high theoretical energy density (3860 mAh/g), greater even than kerosene [8, 9, 10]. SSEs can also operate at relatively large negative potential (3.06 vs. normal hydrogen electrode (NHE)) that can increase battery energy density > 400 Wh kg^{-1}, if the high capacity metal anode can be coupled with high capacity and high voltage cathode materials [8, 11, 12]. SSBs might offer other potential advantages, such as safety, wider operating temperature range, increased volumetric energy density that efficiently utilizes limited space, and faster charging [13]. These attributes may enable electric vehicle performance comparable with the internal combustion engine, and open up an enormous consumer market [13]. The energy densities of different cell chemistries from theory (label 1) to more technologically applicable formats (label 6) are shown in Figure 1.1 [9]. Although theoretical performance is reduced in practical applications (realistic cell and pack formats), SSBs can still outperform the gravimetric and volumetric energy density of LIBs. However, several significant issues need to be addressed for the implementation of practical SSBs [14]:

- High interfacial resistance at practical, low stack pressure (< 1 MPa). Stack pressure is the external pressure that is typically applied to lab-scale SSB cells to avoid contact losses between the electrodes and the electrolyte during cycling
- Limited ionic and electronic mobility in the cathode
- Materials that can better withstand the stresses of cycling
- The tendency for the Li metal anode to transform from a smooth as-plated layer to complex dendritic filaments that penetrate the separator and cause short circuits, even at moderate current

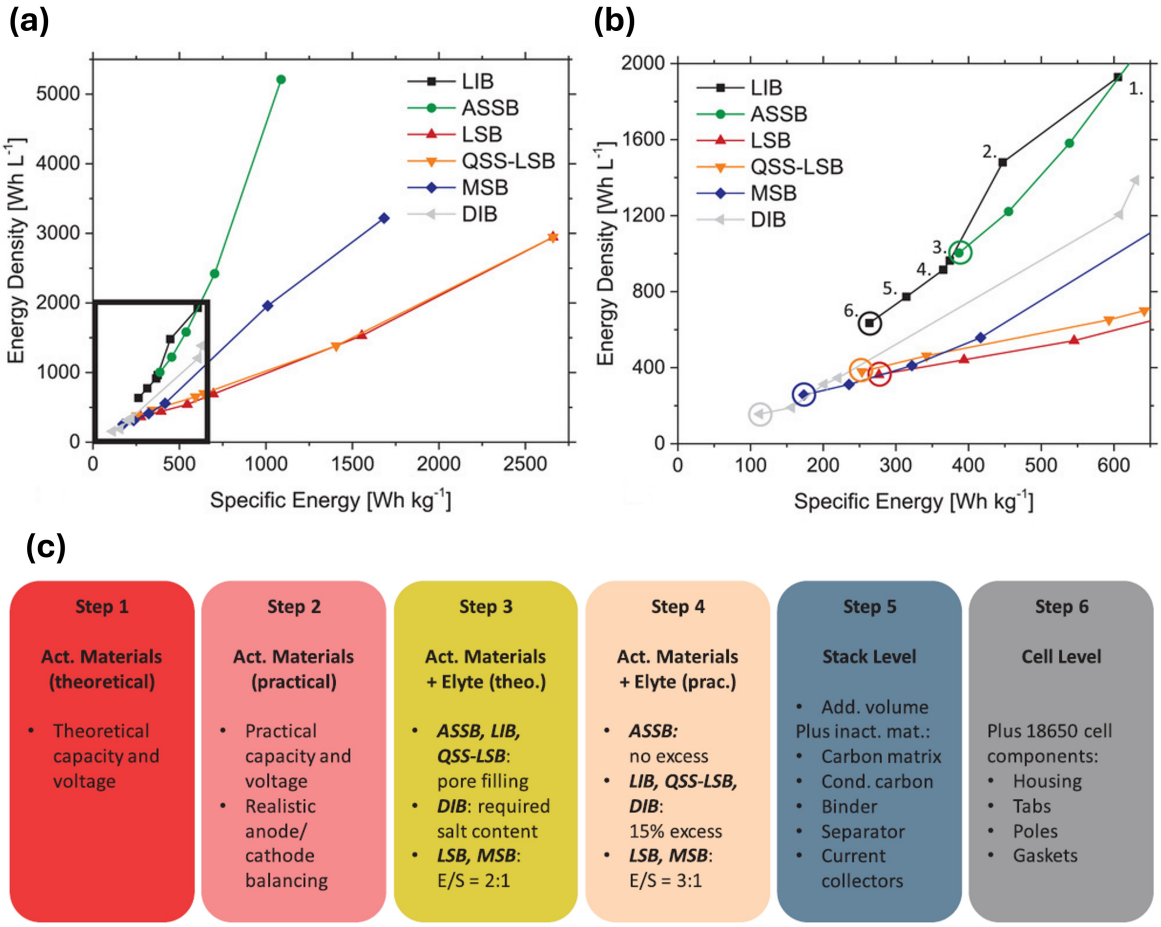

Figure 1.1: (a) Energy density versus specific energy for various battery technologies from theoretical (Step 1) to cell level (Step 6). (b) A magnified inset. (c) Depiction of the six calculation steps used to display the influence of different cell components on the energy content. The abbreviations are: all-solid-state battery (ASSB), lithium/sulfur battery (LSB), quasi-solid-state lithium/sulfur battery (QSS-LSB), magnesium/sulfur battery (MSB), dual-ion battery (DIB), electrolyte/sulfur ratio (E/S). Reproduced from [9].

densities ($\sim$ 1 mA/cm^2)

- The need to demonstrate superior performance compared with advanced LIBs in practice

- The development of scalable processing routes and acceptable cost

In the slurry casting process that is widely used for LIB electrode processing, the different battery materials (active material, electrolyte, carbon, and binder) are mixed in a fugitive solvent to form a slurry that is then cast and dried on a foil current collector substrate [15]. Commercial LIB electrodes have a porosity of ca. 30 %, so the liquid electrolyte can infiltrate the electrodes and transfer the Li ions to the active material via the electrolyte-filled tortuous, interconnected pores [16]. However, since SSBs use an SSE, SSB composite cathodes and separators should be fully dense to maximize ion mobility, which affects the required manufacturing approach [17]. Although slurry casting is the only electrode fabrication process operated at true commercial scale, its suitability for SSB processing is uncertain, and alternatives are being pursued at the laboratory scale. For example, dry processing techniques use "powder to film" manufacturing routes that avoid the need for solvents or a drying step [18]. These approaches may also offer the potential to require less process energy and be more environmentally friendly compared with slurry casting. Dry processing may also produce a fundamentally different and potentially more controllable structure than slurry casting. Alternatively, spray printing may offer improved control over the arrangement of electrode materials during formation and drying and has demonstrated significant performance improvement and extra functionality for a variety of LIB systems [19, 20, 21]. Sputtering represents an attractive alternative to conventional wet techniques for thin film preparation due to its high potential for scalability and process controllability [22, 23].

The thesis aims to investigate challenges related to developing commercial SSBs through two interrelated activities:

1. Novel processing to give better and more precise control of the anode and separator microstructure and interfaces; and

2. Systematic analysis of the structure-property performance of the arising novel SSB electrodes by the application of state-of-the-art tools and analyses, such as X-ray computed tomography (XCT) or plasma focused ion beam (PFIB) microscopy.

A better fundamental understanding of the processes taking place during manufacture, how the microstructure evolves, and subsequent cell cycling performance can help to identify not only improved

cell designs but also optimised manufacturing processes.

Chapter 2 describes the main components and functions of an SSB and outlines different manufacturing approaches with examples from the literature. Chapter 3 describes the experimental techniques used in subsequent chapters 4 to 6. Chapter 4 demonstrates that slurry casting and dry processing can be applied to process free-standing SE membranes for SSBs with ionic conductivity > 1 mS/cm via hot calendering to a density of approximately 83 %, but also highlights limitations. Chapter 5 shows an Ag/C interlayer in an "anode-free" SSB arrangement with an increased Ag concentration towards the current collector fabricated using spray printing. The structured Ag bilayer arrangement achieved superior cycling performance and delivered an initial discharge capacity of > 190 mAh/g and slowed capacity degradation during cycling, at a high coulombic efficiency of $> 98\%$ after 100 cycles. Chapter 6 explores silverising techniques for Ag/C interlayers for anode-free SSBs via precipitation of Ag nanoparticles and sputtering. The precipitation of Ag nanoparticles by exposure of carboxymethyl cellulose binder to $AgNO_3$ solution demonstrates the potential applicability to various catalytic processes, such as organic synthesis. Finally, a < 1 μm thick Ag/C interlayer fabricated by sputtering delivered an initial discharge capacity > 200 mAh/g and an initial Coulombic efficiency of 86 % at a current density of 1 mA/cm^2. Lastly, chapter 7 summarizes the work and suggests possible avenues for future investigations.

Chapter 2

Literature review

Starting with an overview of various solid electrolyte, cathode, and anode materials for SSBs, aspects of their properties and performance are discussed with a progressive focus on sulphide-based solid electrolytes (SEs), lithium nickel manganese cobalt oxide (NMC) as the active cathode material, and Ag/C interlayers as the SSB anode, which are the main materials used in this thesis. Their use and properties in SSBs are described, and consideration is given to the associated processing requirements. Processing alternatives to conventional slurry casting of electrodes and separators are discussed, including solvent-free processing, spray printing, and sputtering, all of which are explored in subsequent experiments. Efforts to improve processing techniques are discussed, and finally a brief summary of the relevant SSB scientific challenges is given.

2.1 Solid-state battery components

A schematic diagram of a typical LIB is shown in the centre of Figure 2.1. Figure 2.1 also shows two other battery formats that might offer improvements over LIBs: an SSB with a lithium-metal anode (left) and a SSB with a conventional graphite-based anode (right). The porous, particulate based electrodes in a LIB are generally 50-100 μm thick and the whole cell is flooded with a Li^+ ion

containing liquid, organic electrolyte [24]. SEs for SSBs should be both solid ion (e.g. Li^+, Na^+, etc) conductors and electron-insulators [25, 26]. The SE must facilitate ionic mobility to/from the active particulate material in the cathode, and between the cathode and anode, forming an electrically insulating separator layer between anode and cathode to prevent a short circuit [27].

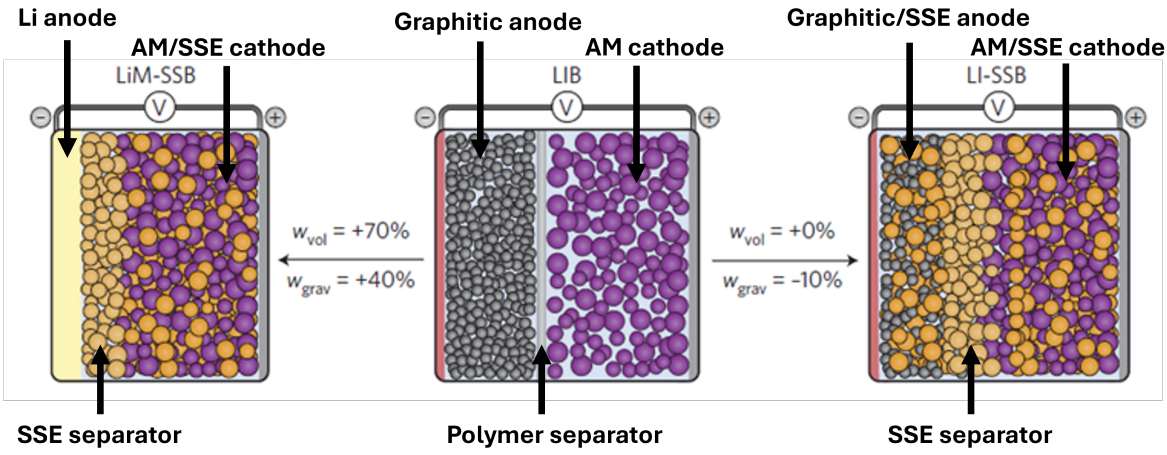

Figure 2.1: Schematic diagrams of typical battery architectures for conventional lithium-ion and SSBs. w_{vol} is the volumetric energy density and w_{grav} is the gravimetric energy density. The illustration in the centre shows a conventional porous, liquid filled LIB. The illustration to the right shows a lithium-ion SSB with a conventional anode. The illustration to the left shows a lithium-ion SSB with a dense lithium-metal anode. The grey circles represent graphite, the violet circles represent the active material (AM), the dark orange circles represent the solid electrolyte, and the orange circles represent another or the same solid electrolyte. The grey band represents a thin, porous but electrically insulating separator, the dark grey band represents the aluminium foil, the dark-orange band the copper foil. The light-yellow band represents the lithium-metal anode. Reproduced from [8].

The most investigated active cathode materials for SSBs are generally the same as those used in conventional LIBs, such as $LiCoO_2$ (LCO), $LiNi_{1-x-y}Co_xAl_yO_2$ (NCA) and $LiNi_xMn_yCo_zO_2$ (NMC) [28]. (De)lithiation takes place at the surface of these particulate active materials during cycling. Usually, a minority of polymer binders such as nitrile butadiene rubber (NBR), polytetrafluoroethylene

(PTFE), or polyvinylidene difluoride (PVDF) are mixed into the separator and hybrid cathode to confer mechanical stability, maintain a coherent electrode despite the mechanical stress generated during cycling, and adhere the electrode to the current collector [29]. Fine-scale carbon is also usually added to the cathode, e.g., carbon nanoparticles or carbon nanotubes, to enhance the electrical conductivity [30]. Typical weight percentages of the materials used in LIBs and SSBs are shown in Figure 2.2.

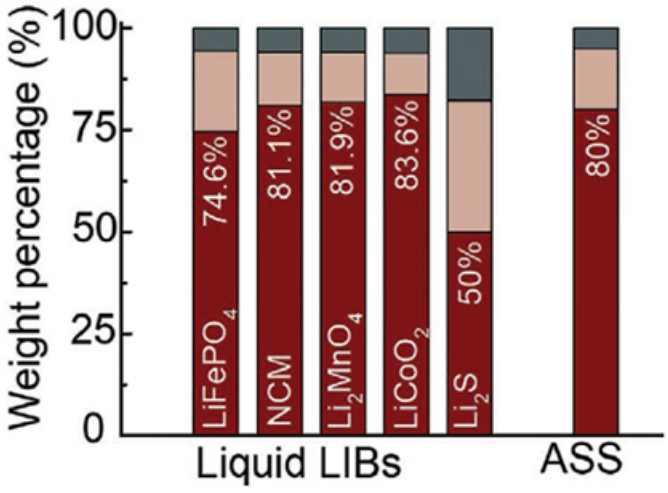

Figure 2.2: Typical weight percentage of electrode materials for different battery types. Red represents the active material, brown the electrolyte, and grey the carbon/binder. Reproduced from [31].

2.1.1 Electrolytes for SSBs

SSEs both provide ionic mobility and act as an electronically insulating separator between SSB electrodes. Therefore, SSEs must meet four main requirements [25, 32, 33, 34]:

- High ionic conductivity ($> 10^{-4}$ S cm^{-1})
- Low activation energy for lithium-ion diffusion
- Mechanical attributes sufficient to resist lithium dendrite penetration
- Low-cost raw resources and facile preparation processes

The most commonly investigated SSE material types that have the potential to meet these requirements are polymer, oxide, and sulphide electrolytes.

Polymer electrolytes

Many SSEs have been explored for SSBs as shown in Figure 2.3. In general, solid polymer electrolytes consist of ionically-conducting solutions of a Li salt in a polymer host matrix [35, 36, 37, 38]. They are attractive because of the possibility to use scalable polymer processing techniques, such as co-extrusion, film blowing, and 3D-printing [39, 40, 41, 42].

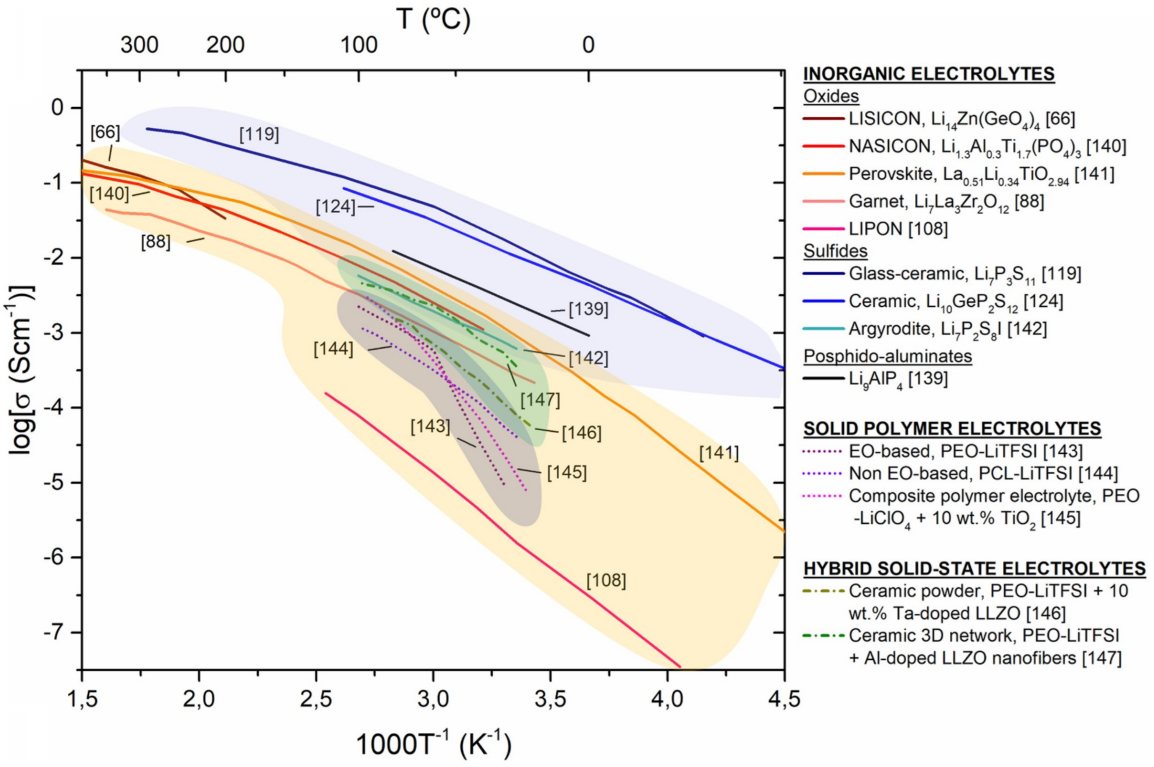

Figure 2.3: Arrhenius plot of the ionic conductivity for various types of SSEs. Reproduced from [1].

Also, polymers have a low density, e.g. 1.1 g/mL for PEO [43]. A host matrix based on PEO represents the most common type of solid polymer electrolyte [44]. Since PEO complexes are normally semi-crystalline at room temperature and show relatively low conductivity ($< 10^{-5}$ S cm^{-1}), they are best operated at temperatures higher than 60 °C [45, 46, 47]. Various approaches have been inves-

tigated to increase the Li-ion conductivity at room temperature, for example by preventing polymer crystallization by increasing the disorder of the polymer matrix [48, 49, 50]. This can be achieved by the use of co-polymers, cross-linkers, comb-type polymer matrices, or by increasing the salt concentration [51, 52, 53, 54, 55]. Alternatively, the glass transition temperature can be decreased by increasing the polymer chain mobility and by decreasing the matrix viscosity, typically by the use of plasticizers [55, 56, 57]. Another approach utilizes the addition of inorganic particles, such as SiO_2, Al_2O_3, TiO_2, ZrO_2, to hinder polymer crystallization and lower the glass transition temperature [46]. However, the high interface resistance between the two phases can limit the mobility achieved in practice. Polymer electrolytes generally suffer from poor electrochemical stability and low/poor rate performance [58].

Oxide electrolytes

Various oxide electrolytes have been developed: Lithium Superionic Conductors (LISICONs), Sodium Superionic Conductors (NASICONs), perovskite-type, garnet-type, and lithium phosphorus oxynitride (LiPON)-type [59, 60]. Some oxide electrolytes have reasonable or even good ionic conductivity (up to 1×10^{-3} S cm^{-1}), relatively wide electrochemical stability windows against Li, e.g. 0-6 V for garnet-type SEs, and can be used in high-voltage cathodes that can be paired with Li metal anodes, delivering (at least for a few cycles) encouraging power density and energy density [58, 61, 62, 63, 64]. On the other hand, oxides have several significant drawbacks.

First, they have poor mechanical properties because they are generally hard with a high Young's modulus e.g. 186–200 GPa for $Li_{0.33}La_{0.57}TiO_3$ and a low fracture toughness of around 1 MPa $\cdot$ m$^{1/2}$ [58, 65, 59]. The high hardness makes it difficult to obtain an intimate contact between the SE and the active material within the cathode, which increases overall interfacial ionic resistance. The low toughness is particularly problematic when aiming for thin (< 100 μm) and large area electrolyte separator layers in pouch cell formats [58]. Consequently, oxide processing may use mechanical buffer layers (to protect the oxide) or a mixture of electrolytes and additives (to try to increase toughness).

Second, oxides generally require a high-temperature sintering step (> 700 °C) during manufacture

to achieve sufficient separator density (> 90 %), which is not compatible with most cathode materials [66]. While advancements in sintering techniques have been made to reduce sintering temperature and time, such as spark plasma sintering (SPS) and high-pressure field assisted sintering (FAST), further progress is needed to ensure process compatibility with the other SSB materials [52].

Last, oxides undermine overall gravimetric energy density due to their relatively high density, e.g. 5.1 g/cm^3 for $Li_7La_3Zr_2O_{12}$ (LLZO) [67].

Sulphide electrolytes

Sulphide electrolytes can be classified into glassy sulphides, glass-ceramic sulphides, and ceramic sulphides [68]. Glassy sulphides are generally binary systems such as Li_2S–SiS_2, Li_2S–P_2S_5 and Li_2S-GeS_2, often also combined in ternary systems with other compounds such as Li_3N or LiI [69, 70]. If the materials are processed at temperatures above their crystallization temperature, there is a stabilisation of crystalline phases precipitated from precursor glass phases. These materials are referred to as glass-ceramic sulphides, and generally have a conductivity of approximately 10^{-4} S cm^{-1} to 10^{-3} S cm^{-1} at room temperature [71]. They have elastic moduli between 10-30 GPa and good formability, and can even be pressed at room temperature (at pressures > 50 MPa) into both separator layers and hybrid cathodes [72, 73].

Crystalline thio-LISICON-like materials have an orthorhombic structure and are characterised by the formula $Li_{3+x}(P_{1-x}M_x)S_4$ (M = Si, Ge, Sn) [74, 75]. Materials such as $Li_{4-x}Ge_{1-x}P_xS_4$ or $Li_{4-x}Sn_{1-x}As_xS_4$ achieve conductivities of up to 2.2×10^{-3} S cm^{-1} [76, 77]. A different group of this material type is described by the formula $Li_{10}MP_2S_{12}$ (being M = Si, Ge, Sn) and are primarily represented by $Li_{10}GeP_2S_{12}$ (LGPS) with a tetragonal unit cell where Li-ions are distributed in four different crystallographic sites [78]. The overall ionic conductivity of LGPS at room temperature may reach 1.2×10^{-2} S cm^{-1}, and it has a relatively low elastic modulus of approximately 20 GPa [79, 80].

Argyrodite-type sulphide electrolytes are characterised by the formula Li_6PS_5X (X = Cl, Br). The crystal structure of this type is illustrated in Figure 2.4 and is based on a tetrahedral close packing of

S^{2-}/X^{-} anions, in which the P^{5+} cations are distributed in ordered PS_4^{3-} tetrahedra [81]. The remaining unoccupied tetrahedral holes are filled with Li-ions, causing a random distribution of univalent cations. This contributes to relatively high Li ion conductivities of up to 2.4×10^{-2} S cm^{-1} at room temperature [81, 82].

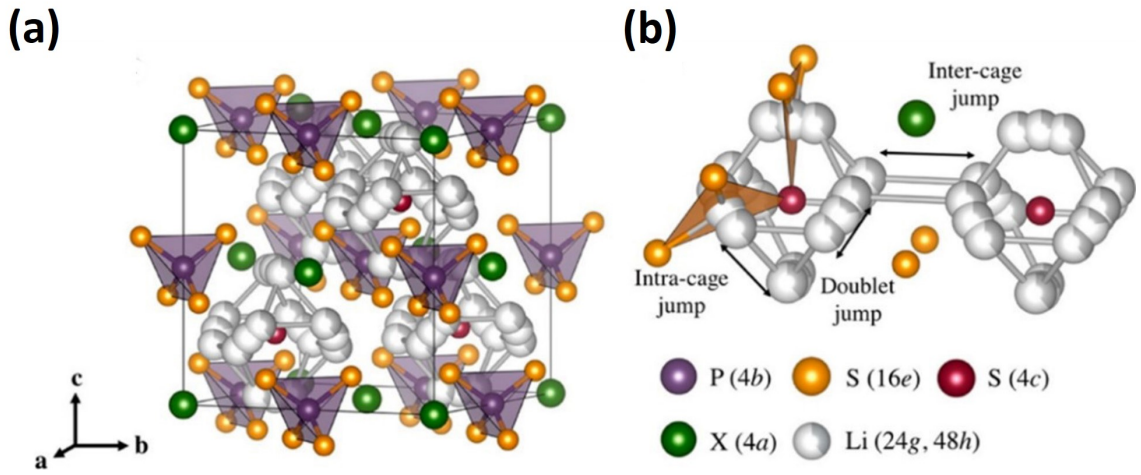

Figure 2.4: : (a) Illustration of the crystal structure of argyrodite-type Li_6PS_5X which crystallizes with cubic symmetry in the space group F43m. For X = Cl, the Li^+ ions occupy the 24g positions of the split site 48h-24g-48h'. For X = Br, I, the Li^+ ions are distributed both over the 24g positions and the 48h positions. 16e is occupied by S^{2-} forming PS_4^{3-} tetrahedra, P is located on the 4b positions. For X = I, the halide anions occupy the 4a positions. For X = Br, the occupation factors amount to 78 % for 4a and 22% for 4d according to neutron diffraction. For X = Cl, the occupation factors are 39% for 4a and 61% for 4d. Most Cl^- anions occupy the inner centres of the Li cages. (b) Illustration of the intracage and intercage Li^+ diffusion pathways. Jumps between the lithium positions (48h–24g–48h', doublet jump), intracage jumps (48h–48h'), and intercage jumps can occur. Reproduced from [83].

Figure 2.5 schematically summarises the properties of solid electrolyte materials. Overall, sulphide electrolytes have a relatively high Li-ion conductivity, a high Li transference number, low stiffness, and low flow stress that permits electrode and electrolyte layer pressing without the need for high temperature [84, 85, 86, 87]. This increases options for compatibility with other materials and facilitates

thin layer/coating preparation [84]. However, sulphide electrolytes have significant disadvantages. In contact with moisture (including atmospheric water vapour), they form highly toxic H_2S gas [88, 89, 90, 91, 92]. Therefore, processing must be conducted under inert atmosphere. Their relatively low toughness of around 0.23 MPa $\cdot$ $m^{1/2}$ provides low resistance to the propagation of cracks and Li dendrites [1, 93]. Despite their drawbacks, the ionic conductivity and low-temperature processability has made sulphides increasingly popular. The most promising is argyrodite (Li_6PS_5X (X = Cl, Br, I)) that has relatively slow reactions with Li metal at the anode side compared with other sulphide electrolytes that decompose more rapidly [82, 94, 95].

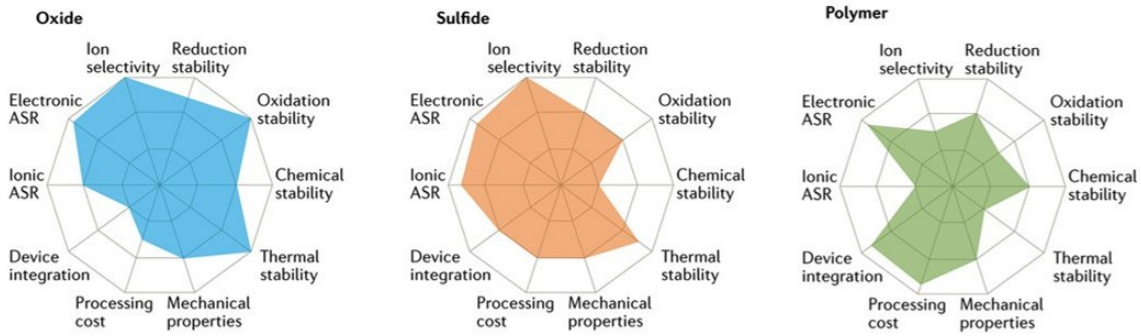

Figure 2.5: Radar plots of oxide, sulphide, and polymer solid electrolyte materials. ASR = area-specific resistance. Reproduced from [96].

2.1.2 Cathode active materials

To achieve a high cell energy density and to balance capacity with a metallic Li anode, the SE must be coupled with cathode materials that possess a high intrinsic specific capacity and/or high average operating potentials. Figure 2.6 schematically presents the properties of active cathode materials in terms of volume change on (de)lithiation, specific capacity, rate capability, working voltage, cost, and cycle performance.

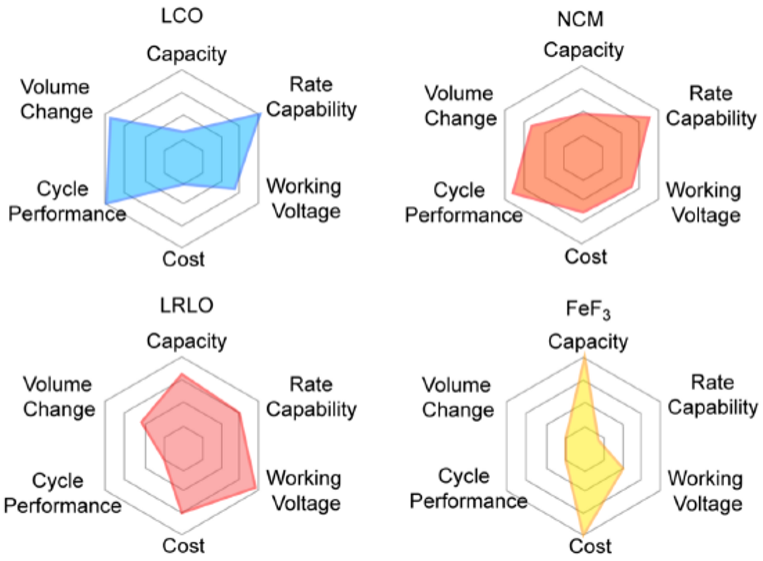

Figure 2.6: Radar plots of four typical cathode active materials in solid-state batteries. $LiCoO_2$ (LCO), $LiNi_xCo_yMn_zO_2$ (NMC), $Li[Li_xTM_{1-x}]O_2$ ($0 \leq x \leq 0.33$) (LRLO), and Li-free cathode materials FeF_3 (in ascending order of specific capacity). Reproduced from [97].

$LiCoO_2$

$LiCoO_2$ (LCO) offers high theoretical capacity ($\sim$ 274 mAh g^{-1}), easy synthesis, high rate capability, and is widely available [98, 99]. However, the practical capacity of $LiCoO_2$ is limited due to its structural instability at high voltages and fast charging [100, 101, 102]. The practical upper cut-off voltage of LCO is 4.2 V vs. Li^+/Li, which yields a specific capacity of only 137 mAh g^{-1}, i.e. due to the irreversible movement of O^{2-} sheets from LCO to CoO_2, the theoretical capacity of LCO is unreachable [97, 103, 104, 97]. Despite strategies to improve LCO stability, such as element doping, degradation stability must be further improved for SSB implementation [105].

LRLO

LRLO with a general formula of $Li[Li_xTM_{1-x}]O_2$ ($0 \leq x \leq 0.33$) offers a high specific capacity (> 250 mAh g^{-1}) and wide potential window (2 - 4.8 V vs. Li/Li^+) [106, 107, 108]. LRLO cathodes

also decrease the use of Co and thereby offer benefits in terms of environmental friendliness and cost [109, 110]. When the voltage is below 4.5 V vs. Li/Li^+, Li^+ is extracted and cations are oxidized to higher valence [97]. When the voltage surpasses 4.5 V vs. Li/Li^+, oxygen ions are involved in the redox process. When irreversible migration of transition metal ions occurs, phase transformation, lattice oxygen release, nanovoids, and transition metal densification occur, resulting in the irreversible oxygen redox reaction and voltage decay [111, 112]. The unstable crystal structure of LRLO and interfacial side reactions that lead to high charge-transfer resistance limit its compatibility with SSBs [113, 103].

Li-free cathodes

Li-free cathodes based on conversion reactions demonstrate high specific capacity and moderate redox potential, which can result in high energy densities [98, 99]. Among various types of conversion cathodes, metal fluorides are a promising but immature Li-free cathode candidate due to their high capacity (450 mAh g^{-1} for FeF_2) and suitable theoretical potential (2.8 V vs. Li/Li^+) [114, 115, 116, 117]. However, substantial volume change (up to 30 %) causes electrode materials to fragment and pulverize, leading to fast capacity degradation [97, 118].

NMC

Ni-rich layered NMCs such as $LiNi_{0.8}Mn_{0.1}Co_{0.1}O_2$ (NMC811) offer high energy density (up to 350 mAh/g), thermal stability, and low Co concentration, which should reduce costs, toxicity, and ethical mining concerns [119, 120, 121]. For NMC, Li^+ is extracted from the structural lattice accompanied by the oxidation of transition metals during the charging process [97]. The capacity is generated from reversible cations redox such as $Ni^{2+/3+/4+}$ [122]. While NMC can tolerate high voltages, it typically suffers from capacity fading during long-term cycling because of NMC cracking and pulverisation, and increasing debonding of the NMC/SE interface [123]. Single crystal (SC) NMC particles showed greater robustness during mixing and densification compared with polycrystalline (PC) NMC, which

suffers from intergranular cracks first during processing and then during cycling due to anisotropic volume expansion [124]. SC-NMC composite cathodes displayed an active material utilization of 71 % after fast charging at 15 mA/cm^2 at room temperature [125]. Overall, due to benefits such as high theoretical capacity, wide voltage windows (2 - 4.8 V vs. Li/Li$^+$), low toxicity, and relatively low cost, NMC-based cathodes currently represent the most promising candidate for high-energy-density SSBs, and SC-NMC811 was selected as the cathode material for this work. Future research on modification strategies such as surface coating aim to address remaining issues of NMC, such as capacity degradation [126].

2.1.3 Anode materials

SSB anodes require high capacity, ionic conductivity, safety, and compatibility with the SSE. Various anode materials have been considered, including metallic Li, Li-In alloys, Si, and Ag/C, including for interlayers in so-called "anode-free" arrangements.

Li metal anodes

While Li metal anodes used in SSBs offer very high gravimetric and volumetric capacity, their application in SSBs also raises significant manufacturing challenges. Li foils are the obvious and widely used approach, fabricated by extrusion and rolling in inert atmosphere facilities (given the very high reactivity of Li to O_2 and H_2O). Ideally, the thickness of a Li anode should be 50 μm or considerably lower to achieve balanced volumetric energy density on the cell level [10]. However, Li foils often stick on tools or rolling cylinders during application to the SSB separator [127]. Lubricants can be used but cause unwanted side-reactions that increase cell resistance.

An alternative approach is physical vapour deposition (PVD) of a thin (1-10 μm) Li anode layer from the vapour phase. PVD allows good thickness control, but also requires highly specialised equipment, high cost, and challenging maintenance [10]. Alternatively, the electrochemical deposition of Li films in galvanic baths has been investigated, but this is a slow process with high costs for electrolyte

regeneration and disposal [10]. Both PVD and plating also lead to cell short circuits if the Li fills any through-separator "pin holes" [128].

Lithium metal anodes face various operational problems as shown in Figure 2.7, e.g. side reactions leading to the generation of a solid electrolyte interphase (SEI) through continuous electrolyte consumption, Li dendrite formation, and development of isolated Li "islands", which cause safety hazards and reduce Coulombic efficiency [129, 130].

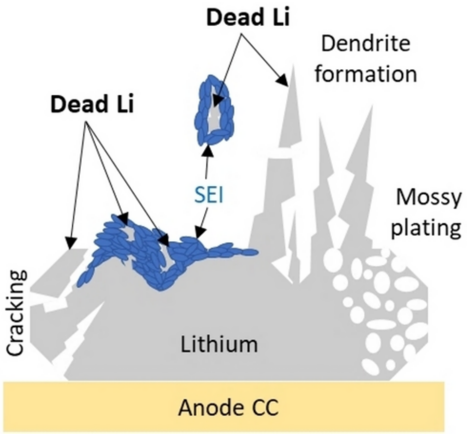

Figure 2.7: Schematic illustration of islands of "dead" Li formation. CC = current collector; SEI = solid electrolyte interface. Reproduced from [131].

The initiation of Li dendrites arises from inhomogeneous Li deposition at the anodic current collector during cell charging. Li may deposit into the subsurface pores of the SE or at pores/voids at the current collector interface, or at any feature that concentrates the electrical field. Once metallic Li is nucleated, further charging may induce a local strain, which is accompanied by a build-up of pressure and slow extrusion of Li (viscoplastic flow) that leads to SE penetration by "dendrites" or "filaments" of Li [132]. Dendrite propagation occurs by wedge opening, and Li drives the dry crack from the rear, not the tip. Factors influencing dendrite propagation are considered to be the intrinsic fracture toughness of the SE, the length of the Li dendrite that partially occupies the dry crack, the applied current density, stack pressure that may help the Li to flow to fill interfacial voids but also promote crack opening, and charge capacity. The penetration of dendrites through the SE results in

mechanical failure and catastrophic short circuits [133].

The subsequent uneven stripping of non-uniform Li deposition morphologies during discharge of the anode can result in the formation of electrically isolated Li "islands", commonly known as "dead" Li [130, 134]. The detached Li is isolated from the electrical conduction path and therefore unable to contribute any capacity in subsequent cycles [135, 136]. Dendrite growth and dead Li formation can then accumulate in subsequent cycles due to progressively increasing surface roughness and non-uniform Li morphologies at the anode [137]. At the coarsest scale, the physical removal of the Li during stripping, will by definition lead to micro-voiding at the anode. The stack pressure aims to close these voids as they form because they may act as a barrier to the returning Li on the next charge cycle, and its uniform plating.

Li-In alloy anodes

Potential alternatives to Li metal anodes are Li-rich alloys that can improve Li^+ mobility and promote uniform Li^+ deposition since only the Li is stripped and the "other" metallic element remains at the anode to help maintain interfacial electrical contact. Metals that have been studied in combination with Li are Sr, Al, Sn, In, Zn and Mg [138, 139, 140, 141]. For the design of Li alloy anodes, various conditions must be met [142]:

- The non-Li element must have high electrical conductivity and be relatively soft to maintain interfacial contact to homogenise local current density, and hence uniformity of Li re-plating.
- The non-Li element should have good chemically compatibility, termed lithiophilic (e.g. forms a solid solution), to promote a uniform alloy dispersion.
- The non-Li element should have sufficient structural stability to mechanically stabilise the Li-X/current collector interface at all stages of cycling and under applied stack pressure.

Indium meets these conditions, can be alloyed with Li under pressure at room temperature, and has a stable reference potential of 0.62 V vs Li^+/Li with a broad Li-In solid-solution region [143, 144, 145].

During plating/stripping, the presence of lithiophilic alloy phases promotes a more uniform deposition of Li, that helps to suppress the formation of Li dendrites. The greater tendency of Li-In dendrites to grow laterally along SE pores and grain boundaries instead of through the SE reduces damage to the SE [146].

Silicon anodes

Silicon anodes in SSBs are attractive due to their high theoretical specific capacity (3590 mAh g^{-1}), relatively low cost, as shown in Figure 2.8, earth abundance, and ready availability from other industries [147, 148]. Compared to Li, Si does not flow visco-elastically and so can withstand very high stacking pressures that improve interfacial contact. Si anodes are also generally less susceptible to dendrite formation since the Li generally intercalates into the Si rather than plating as metallic Li (can easily occur also) [149, 150, 151]. Moreover, Si has good thermodynamic stability with most SEs, including SEs based on sulphides [152, 153].

However, Si anodes face significant challenges such as a low Li^+ diffusion rate ($\approx 10^{-13}$ cm^2 s^{-1}), low electronic conductivity ($\approx 10^{-3}$ S cm^{-1}), and severe volume change (300 %) during (de)lithiation [155, 156, 157]. Volume changes cause exposure of the fresh Si surface to the electrolyte and continuous formation of new SEI, leading to steady electrolyte consumption and capacity loss [147]. Moreover, the very large volume changes lead to large stresses on Si particles, resulting in anode pulverization and delamination [158]. To relieve volume expansion during lithiation, nano-porous Si mixed with SE and conductive carbon in a composite anode has been suggested [159].

Anode-free cells

To address the difficulties of handling large Li foils, coatings, etc., SSBs with an Ag/C composite interlayer between separator and current collector with no excess Li as shown in Figure 2.9 have been suggested [84]. In this cell design, there is no metallic Li anode initially, but one is plated in situ on the first discharge of the pre-lithiated cathode.

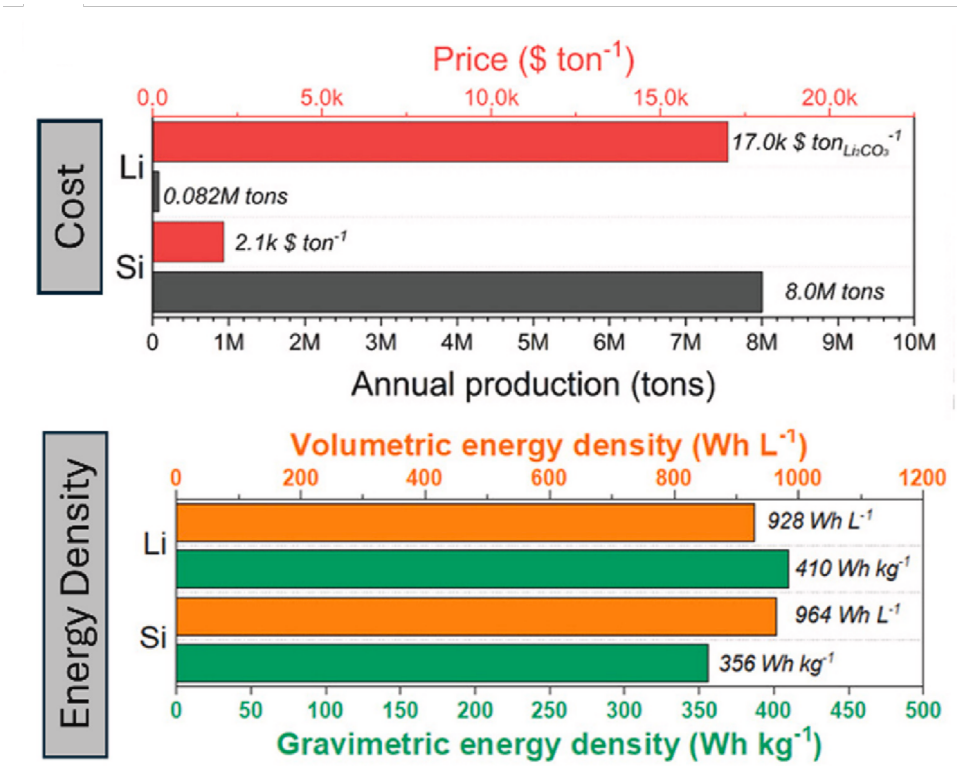

Figure 2.8: A comparison of cost and energy density for Li and Si anodes for SSBs (NMC811 as a cathode, sulphide as SE). Reproduced from [154].

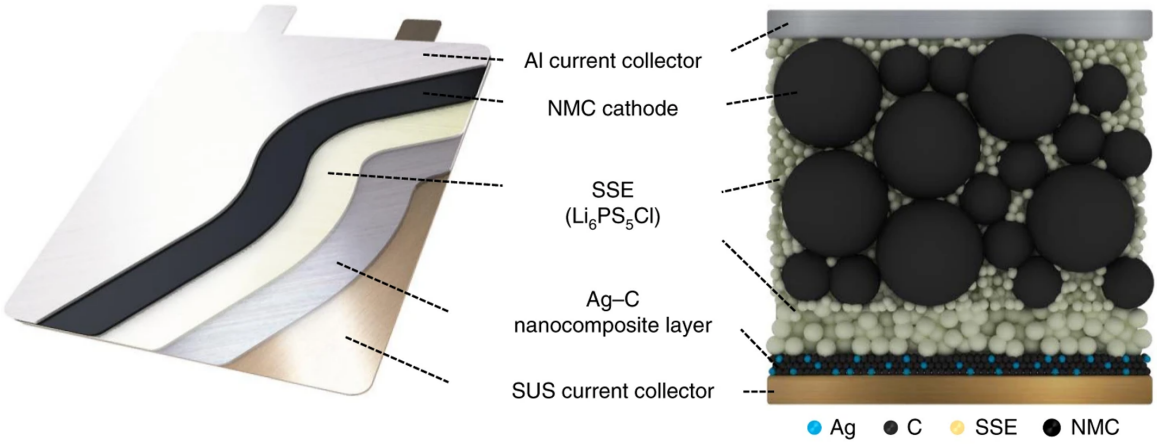

Figure 2.9: Schematic of an SSB composed of a NMC cathode, SSE and an Ag/C nanocomposite anode interlayer that does not involve excess Li. Reproduced from [84].

For heterogeneous nucleation of the Li, the energy barrier for forming a nucleus of a stable, critical size requires the application of an overpotential, as shown in Figure 2.10 [160]. Li nucleation is followed by Li growth because the addition of a Li atom to an existing Li deposit has a lower energy barrier than forming a new Li nucleus of critical size. Undesirable Li dendrite morphologies are favoured when there is a high nucleation barrier and a lack of growth sites. Therefore, anode-free designs usually use an interlayer to lower the Li nucleation free energy barrier, i.e. to catalyse nucleation, at as many locations at the current collector as possible: an infinite number of growth sites would produce an even plating of Li on charging, promoting subsequent uniform stripping, and thereafter during repeated cycling.

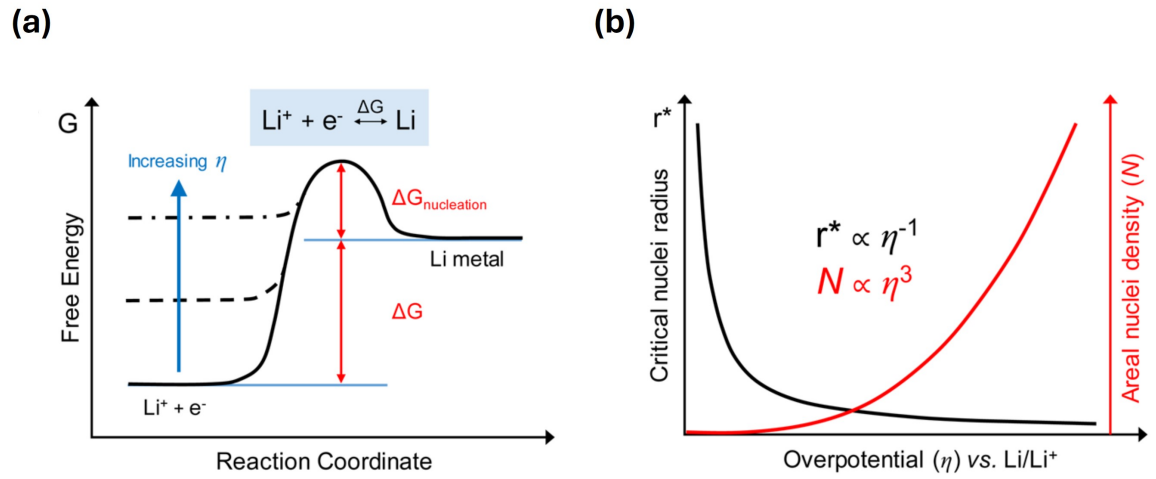

Figure 2.10: Fundamentals of lithium nucleation and growth. (a) Free energy schematic showing the effects of increasing overpotential on the nucleation energy barrier; (b) Schematic plot of the dependence of critical Li nuclei radius and areal nuclei density on the overpotential of Li deposition. Reproduced from [160].

If Li deposition is not controlled, preferential Li deposition particularly at relatively low energy defect sites, surface asperities, etc leads to inhomogeneous Li deposition and dendrite growth [161]. Non-uniform Li growth can also cause uneven volumetric expansion, breaking the protective SEI that covers the electrode surface and leading to electrolyte consumption [162]. Voids formed due to

inhomogeneous plating reduce the SE/Li contact area and increase local current densities, further encouraging Li dendrite growth [163, 164, 165].

Carbon particulate based interlayers that are 10-20 μm thick have been shown to improve the uniformity and reversibility of Li plating by homogenizing the local current density distribution [166, 167]. Carbon reduced the overpotential for Li plating, improved the nucleation and early growth kinetics of Li, and increased the current density before harmful Li dendrite propagation [168]. The amorphous structure of low graphitized carbon has been suggested to perform better than graphitized carbon due to enhanced Li transport and a resulting lower interfacial resistance [169]. Alternatively, hard carbon consisting of a highly irregular and disordered structure has also been suggested to provide 3D pathways for Li transport, increasing critical current density [170]. Overall, almost all types of fine C particulate provide some benefit in lowering the Li plating overpotential.

The addition of metal particles into the C-based interlayer drastically improves SSB performance by extending the cycle life [171]. Ag/C interlayers consisting of a mixture of fine Ag ($\sim$ 60 nm) and C black (CB, $\sim$ 35 nm) particulate, were particularly effective in regulating Li deposition [84, 172, 173, 174, 175, 176]. An additional role of C in these interlayers is to separate physically the SE layer from Li metal after plating, improving the durability of the SE [84, 177, 178, 179, 180, 181]. The C layer reduces the probability of Li nucleation at discrete separator surface flaws or surface breaking cracks that will readily go on to form dendrites [169, 182, 183, 184, 185, 186, 187].

The mechanism by which an Ag/C interlayer facilitates Li plating and stripping is still not fully understood. In the case of an Ag/graphite interlayer in a laboratory cell, Li first electrochemically intercalates into carbon on charge. The lithiated carbon subsequently reacts chemically with Ag to form a series of increasingly Li-rich Li-Ag alloys as shown in Figure 2.11, which deposit between the interlayer and the current collector [188, 189]. The lower interfacial resistance at the Ag/C interlayer and current collector interface compared to the interlayer/SSE interface results in predominant and beneficial Li deposition/plating on the current collector.

Ag does not increase the critical current density at which dendrite penetration occurs, but leads to

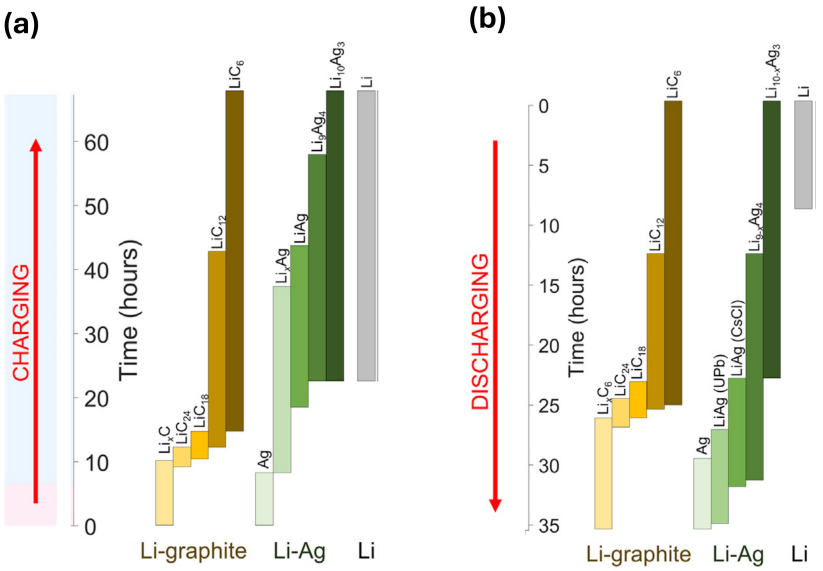

Figure 2.11: The phase behaviour of Li-graphite (gold), Li-Ag (green), and Li metal (gray) during (a) charge and (b) discharge of an Ag-graphite composite layer cell at a current density of 30 μA cm^{-2}. Reproduced from [188].

a more homogeneous layer formation at the current collector. At higher charging rates ($>$ 2 mA/cm^2), Li intercalation into carbon outpaces chemical reactions with Ag, delaying the formation of the Li-Ag phases and resulting in more Li metal deposition at the current collector [188]. On discharge, Li is electrochemically extracted from the plated Li layer and C, through increasingly Li-deficient Li-Ag phases until only C and Ag remain, as illustrated in Figure 2.12.

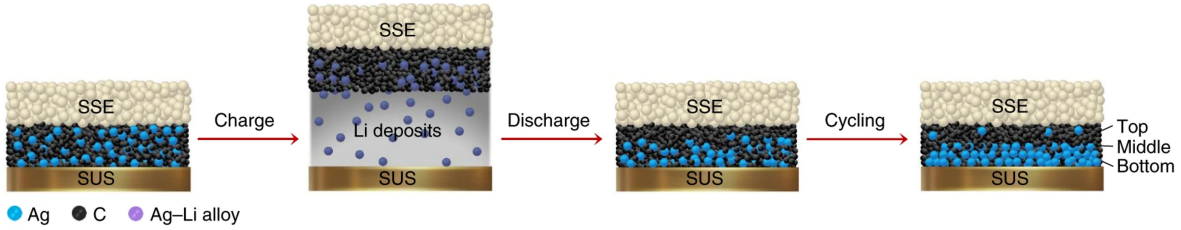

Figure 2.12: Schematic of Li plating/stripping on the current collector with a Ag/C nanocomposite layer during charging and discharging processes. Reproduced from [84].

In other words, during cycling of Ag/C interlayers, Ag continuously alloys with and dissolves into Li, forming a solid-solution that presents a positive attraction potential to Li [190, 191, 192, 193]. Carbon layers with other potentially more economic metals (Zn, Sn, Al, and Ni) have not performed as well as Ag/C [171]. Ag forms a wide composition range Ag/Li (see Figure 2.13) solid-solution, as well as a number of ordered compounds at higher Li concentrations [190]. A final aspect of Ag/C interlayers is that both Ag and C will undergo volume changes on reaction with Li, which in some cases can be significant [190, 194]. The particulate porous nature of the Ag/C interlayer may allow for some physical "buffering" of the associated strains. Residual strains might affect how the soft Li plates and possibly flows, although definitive insight on the likely complexity of such behaviour has not yet been realised [195].

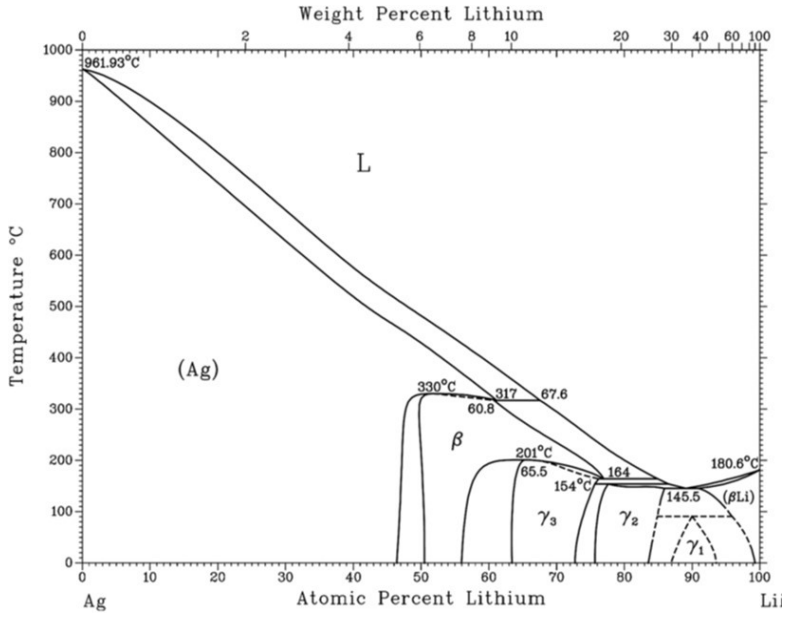

Figure 2.13: Phase diagram of the Li-Ag system. Reproduced from [196].

Overall, avoiding excess Li in the anode by forming the anode in situ by Li plating on the first charge has the potential to reduce cost, increase simplicity, and maximize gravimetric and volumetric performance. However, the practical implementation of sulphide-based anode-free SSBs is limited by operational issues: non-uniform Li nucleation leading to dendrite formation, unstable interfaces

between the plated Li and SE that cause resistance build-up, and interfacial void formation resulting in capacity decay [167]. Refining further the design of Ag/C interlayers may deliver the required improvements in SSB cell performance, and improve their potential for scalability.

2.2 Fabrication of SSB components

Although slurry casting is the dominant LIB fabrication process, other techniques may offer greater microstructural control or potential for scalability for SSB manufacturing. The processing alternatives investigated in this work are dry processing via binder fibrillation, spray printing, and sputtering.

2.2.1 Solvent-free processing

As previously described, in the conventional slurry casting process, the different battery materials (active material, electrolyte, C, and polymer binder) are mixed in a solvent to form a slurry that is then cast on a foil current collector substrate [197]. The electrode is then dried carefully in a sequence of steps, and calendered to the final desired thickness as shown in Figure 2.14. Because of the large installed base of slurry casting equipment and associated knowledge, it has been the starting point for SSB manufacturing research. There are many reports of versions of slurry casting process adapted, at least at the laboratory scale, to the production of both separators and hybrid cathodes for SSBs. However, this approach suffers from significant drawbacks, such as limited stability of sulphide electrolytes against organic solvents and increases in ionic resistance due to the use of insulating polymer binder such as nitrile butadiene rubber [29, 198, 199, 200, 201].

Moreover, the polymeric binder required for mechanical stability of both separators and hybrid cathodes, especially in the absence of a stack pressure, tends to impede interparticle contacts and thereby limit the Li^+ ion transport between SSE particles in the separator, and to and from the active particles in the hybrid cathodes. Also, time-consuming and energy-intensive heating processes are needed for solvent evaporation, which has to take place under a protective atmosphere when sulphides are used [203]. Due to the cost and potential pollution of certain solvents, complex recovery systems

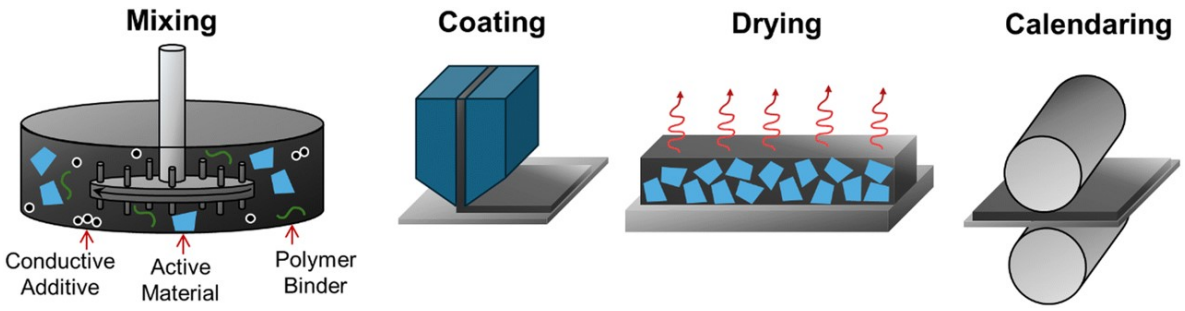

Figure 2.14: Illustration of the slurry casting process. Reproduced from [202].

are needed at industrial scale, which require a large capital investment and operating expense [204]. Solvent-free, or dry processing, can avoid some of these issues and provide different microstructures to slurry casting, e.g. a more homogeneous binder distribution through the thickness by suppressing binder migration during drying [204, 205, 206, 207, 208, 209, 210]. Field emission scanning electron microscopy (FE-SEM) images of the top view and energy-dispersive X-ray spectroscopy (EDXS) elemental maps for S of both dry- and slurry-mixed cathodes for ASSBs are shown in Figure 2.15. The elemental maps give the impression of a more heterogeneous arrangement of the S-rich SSE for the electrodes with higher weight fractions of active materials (D85 and W85) and for the slurry-mixed electrodes (W70 and W85). The more heterogenous arrangements may lead to poorer ionic percolation [211]. This could explain the lower capacity of the slurry-mixed electrodes (90 mA h $g_{electrode}^{-1}$ for W70) than dry-mixed (107 mA h $g_{electrode}^{-1}$ for D70) [211].

Dry processing techniques have been studied principally for LIB electrodes rather than SSBs, although there are some recent reports of the later [29, 18]. SSBs have specific design requirements, such as thin SE separators (ideally < 50 μm), high packing density of the cathodes (minimisation of porosity), and conformal interfacial contacts between the solid phases and between layers [18, 212].

In the case of dry spraying, materials are dry mixed with a sticky polymeric binder before the mixture is granulated as flowing particles [18]. The blended particles are subsequently sprayed on the current collector, gradually forming a composite film, which is calendered [213, 214, 207]. Then, hot rolling is used to melt the binder and consolidate the film and promote adherence to the current

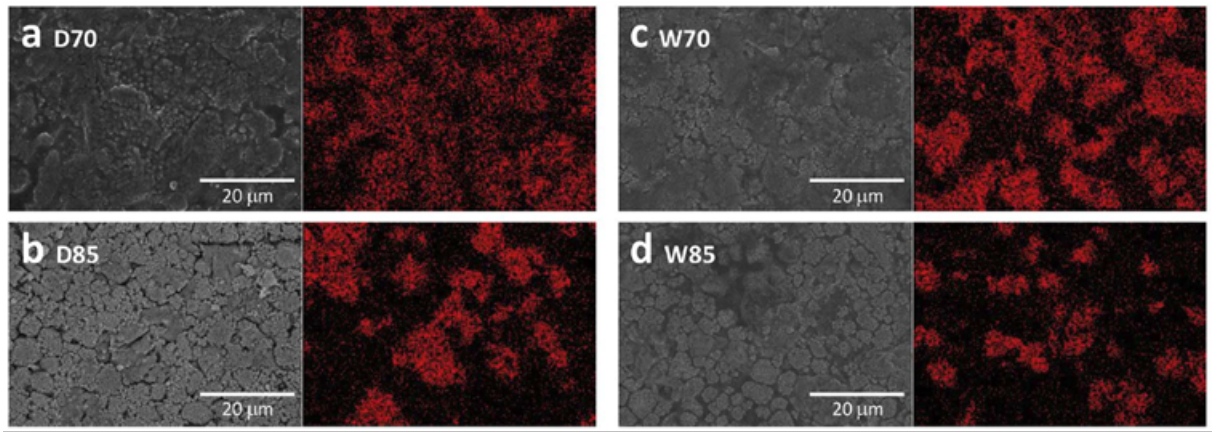

Figure 2.15: FE-SEM surface images and EDX elemental maps for S from NMC/LPS-based electrodes fabricated by dry-mixing process without polymeric binders with a) ca. 70 wt% (D70) and b) ca. 85 wt% (D85), and wet-slurry process using an NBR-binder with c) ca. 70 wt% (W70) and d) ca. 85 wt% of NCM622. Reproduced from [211].

collector [204, 215]. This technique can be applied to most particles and has been demonstrated for a wide range of binders [216]. It is also possible to use organic precursors as binders which are then polymerized by ultraviolet radiation [216]. One approach additionally applies an electrostatic field to improve the adhesion and efficiency of the spraying deposition [217, 218]. But so far, this approach suffers from a lack of control over electrode mass loading, thickness, and homogeneity [18].

Another approach uses hot pressing and melt extrusion, where a Li salt and polymers are dry mixed at room temperature, before the polymer/Li salt mixture is fused together by extrusion or hot pressing due to the thermoplasticity of solid-polymer electrolytes when above their crystallization temperature [18]. Hot pressing and melt extrusion are well-established techniques with good scalability, but they require high polymer contents (up to 30 wt.%) which can undermine ion mobility [18, 219, 220, 221]. These techniques are most applicable to solid-state polymer electrolytes [222]. Also, the extrusion process is sensitive to particle size and time-consuming optimisation of many process parameters such as shear rate, temperature and extrusion time is usually necessary [216].

Dry 3D printing (3DP) employs fused deposition modelling (FDM, a type of 3DP of a hot polymer

filament) [18]. Materials are deposited in a molten polymer, layer by layer [223]. The use of a thermoplastic binder allows the fabrication of self-standing electrodes. The technique can be applied directly to thermoplastic polymer SSE-based electrodes [224]. However, the composite filament required for 3DP is usually prepared with a solvent step [225]. The benefits of 3DP are that the shape, morphology, and thickness of the electrodes can be reasonably well-controlled and adapted to certain specifications [18]. However, electrode thicknesses below 100 μm are difficult to achieve. 3DP may be attractive for applications such as microelectronics or flexible, wearable devices, but suffers from restricted build size, low productivity, and the need for post-processing steps [226, 227].

A different approach simply mixes the SSE with a deformable binder which is then subject to the application of shear forces through ball milling or mortaring [18, 228, 229, 230]. The binder undergoes extensive deformation into a range of morphologies, while the active particulates and any added C should remain pristine. Under optimum conditions, the powder mass becomes an integral pre-cursor pellet for further processing, such as warm/hot calendering into free-standing layers or electrodes on a metallic current collector or polymeric transfer film [231]. The most commonly used binder is polytetrafluoroethylene (PTFE) [29, 232]. All the process steps of this technique (blending, fibrillization, feeding, compacting, and bonding to the current collectors) are compatible with continuous large-scale processing. Critically, fibrillization of the binder takes place during blending under the application of a continuous shear force [233, 234, 235]. An SEM image of PTFE fibrils around NMC particulates is displayed in Figure 2.16.

Calendering can be used to control the separator layer or electrode thickness and to reduce porosity [18, 236]. The fibrillation technique can be applied to inorganic SSEs and requires remarkably low binder contents ($<$ 1 wt%) and large-sheet films (ca. 8 $\times$ 6 cm^2) are achievable [18, 203, 237, 238]. It is not yet clear if any other polymers are able to undergo the critical fibrillization step, and if so, under what conditions. This is an increasing area of research, since the continued use of PTFE is subject to growing environmental scrutiny.

In a seminal work, a freestanding separator membrane composed of an interconnected PTFE poly-

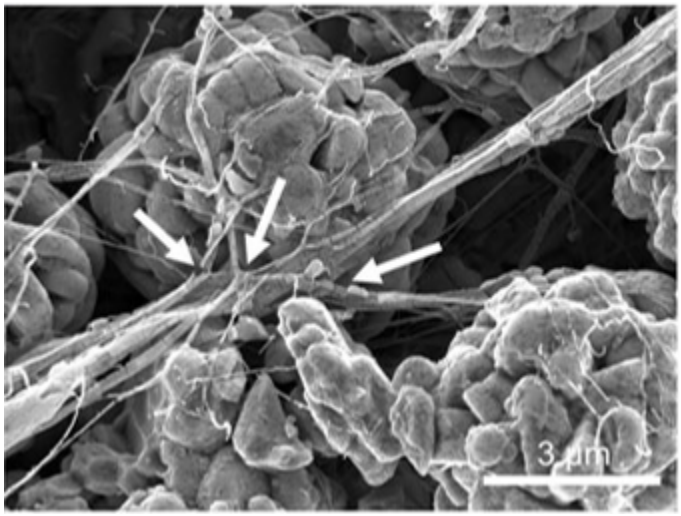

Figure 2.16: SEM image showing the formation of PTFE fibrils. Two NMC particles have drawn out smaller bundles of PTFE strands to form fibrils (indicated by the arrows). Reproduced from [233].

mer fibril network and a $Li_{5.4}PS_{4.4}Cl_{1.6}$ sulphide electrolyte was synthesized by ball-milling, followed by hot calendaring at 80 °C and cells showed best-in-class performance [237]. The process is illustrated in Fig. 2.17.

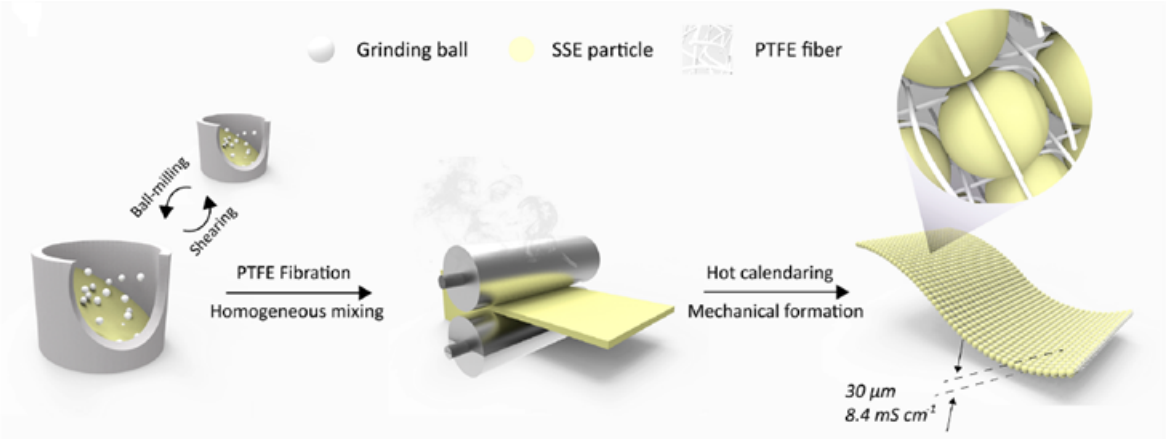

Figure 2.17: Schematic illustration of dry processing of a battery component based on the premixing of the materials and the subsequent film formation caused by shearing forces. Reproduced from [237].

PTFE has a glass transition temperature of approximately 30 °C, above which the fibrillization

occurs as the packed PTFE molecules in the crystalline form are unwound by shear forces that overcome the relatively low PTFE crystallite cohesive force [239]. Because of fibrillization, PTFE has emerged as the preferred binder material, and also has low coefficient of friction, high melting point, and good chemical resistance to solvents/electrolytes [240]. A higher degree of PTFE fibrillation increases the separator tensile strength while maintaining ionic conductivity. However, increasing the degree of fibrillation can negatively affect cycling stability because of the chemical reduction of PTFE to conductive carbon species in contact with Li, which can propagate through the PTFE, resulting in early cell failure due to current leakage and ion blockage [241].

Using PTFE fibrillation, an NMC811 and a Li_3InCl_6-$LiCoO_2$ cathode film and an anode film composed of graphite, carbon nanofibers and LPS were successfully produced [203, 242]. These sheet-type membranes were free-standing, thin (< 100 μm), required only remarkably small amounts of binder (< 0.7 wt%), and showed good cell performance. SSB cathodes prepared via PTFE fibrillation had a higher percentage (67.2 %) of electrolyte-covered surface area of the active materials than slurry cast equivalents (33.3 %) [243]. Greater contact translates to reduced internal resistance and improved capacity and rate capability [244, 245]. The post-calendering processing of an SSE via coating with a polymer precursor and subsequent heating used cross-linking polymerisation, resulting in a flexible high ceramic content SSE with improved stability of the electrode/SSE interface [246].

To avoid issues associated with PTFE deterioration during cycling, alternative binders have been investigated. For instance, a percolation network of thermoplastic polyamide (TPA) binder prepared by thermocompression facilitates the formation of an LPS film with beneficial mechanical properties and a high Li^+ conductivity of 2.1 mS cm^{-1} [247]. However, TPA requires complex synthetic methods, which increase production costs [248].

In summary, solvent-free processing of SSB components via PTFE fibrillization is at an early stage, but preliminary reports suggest a high potential for technological impact. Critical is understanding the fibrilization, or other binder dispersion, step and how electrodes perform in real solid-state cells. Regardless of fibrillation or other binder dispersion steps, final densities approaching 100 % are es-

sential. Encouraging laboratory processes are not often scalable to practical applications [249]. For instance, laboratory cells usually operate under an applied, or stack, pressure and hybrid cathodes can be pressed directly to high density in coin or mold cells, avoiding the need for a binder and current collector which are required for a practical battery. High stack pressures ($>$ 10 MPa) are assumed unworkable for practical cells with larger area dimensions.

2.2.2 Spray printing

Spray printing of LIB and other energy storage electrodes offers additional options for microstructural control not available by slurry casting. Spray printing has been successfully applied to produce different electrode microstructures that enhanced the performance of LIBs and lithium-ion capacitors. The process is shown schematically in Figure 2.18. The electrode materials are dissolved/suspended in a dilute suspension and pumped into a spray nozzle attached to a stiff x-y-z manipulator gantry [20]. The position and speed of the nozzle and the flow rate are computer-controlled. The suspension is continuously atomised by compressed air and the resulting spray of suspension droplets is deposited onto a metallic current collector on a vacuum chuck typically heated at up to 140 ° C [20]. The sprayed solvent evaporates almost instantaneously. A layer is already dried by the time the subsequent layer is applied during the next cycle.

Spray printing can enable a low fraction of inactive components that otherwise hinder ion mobility and increase the resistance to electron transport [251]. Further microstructural flexibility arises because different layers can have different proportions of materials – allowing graded or layered electrodes with a more controlled arrangement of active material (AM) and carbon conductivity enhancer (CCE) to be fabricated [20]. For example, LIB electrodes were produced with designed spatial variations in local microstructure and fraction through the electrode thickness, from the current collector towards the separators, i.e. AM-CCE, CCE-AM-CCE, and CCE-AM. For $LiFePO_4$ (LFP)-based cathodes, the AM-CCE arrangement had a reduced charge transfer resistance, and in the case of AM-CCE and CCE-AM-CCE the internal overpotential distribution was made more uniform. These effects reduced

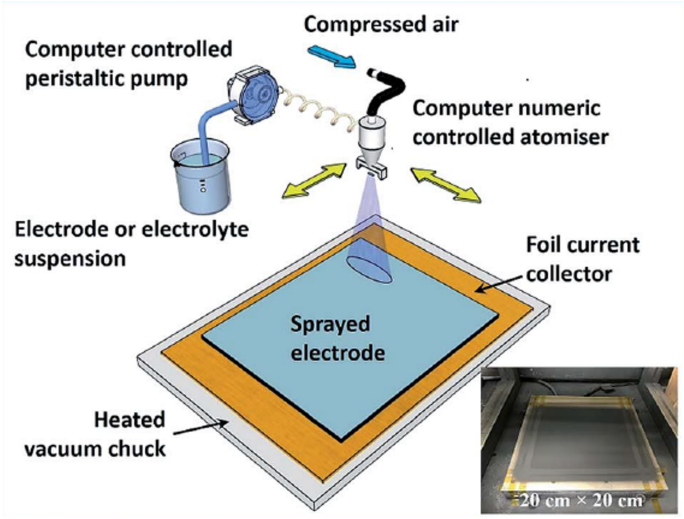

Figure 2.18: Schematic illustration of the possible setup of a spray printing experiment. Reproduced from [250].

SEI interface reactions, which improved the electrochemical performance, such as slowing capacity degradation during cycling [20, 251].

By "structuring" the electrodes more carefully, different power and energy density balances are possible [252]. Discrete layers can also be introduced within electrodes by spray printing, such as interleaving a low resistance graphene layer between the current collector and the electrode simply by switching between the feedstock suspensions during deposition [251, 253].

As described earlier, Si is an intrinsically high energy density Li insertion material, but suffers from large volume changes during charge/discharge, causing physical pulverisation and poor cyclability [254]. Spray printing a Si/SiO_x nanocomposite layer between two mechanically compliant C interlayer accommodated the volume expansion of Si and improved electrical contact with the current collector [254]. Spray printing of LIBs and capacitors demonstrates a large variety of microstructural design possibilities. However, the process is yet to be demonstrated reliably at a scale that can approach that of slurry casting.

While SSBs have different requirements than conventional batteries (dense electrodes rather than porous), spray printing may be useful. For example, promising preliminary studies include a symmetric

all-organic SSB based on organic porous electrodes spray printed in a single step [255]. The active material was based on disperse blue 134 anthraquinone was used for both negative and positive electrode reactions. An inter-connected honeycomb electrode consisting of the active material and carbon black was formed by using differential evaporation of two fugitive miscible liquids [255]. An SSE based on a polymeric ionic liquid was subsequently sprayed as the second layer, which infiltrated the electrode. While it was demonstrated that the same molecule could be used in positive and negative electrode reactions, the discharge capacity faded from approximately 80 mA h g^{-1} to approximately 50 mA h g^{-1} at 0.5 C after 50 cycles [255]. Similar effects were realised for $LiFePO_4$ and PEO-$Li_{1.5}Al_{0.5}Ge_{1.5}(PO_4)_3$ hybrid cathodes with a honeycomb morphology which was coupled with a Li anode [250]. In this case, a layered honeycomb structure was achieved by optimising the substrate temperature, bi-solvent ratio, and electrode material concentration and is schematically illustrated in Figure 2.19. This configuration improved rate performance and long-term cycle stability over a conventional arrangement of the identical materials, providing 150 mA h g^{-1} at 0.1 C and 97.2 % retention after 100 continuous cycles at 60 °C [250].

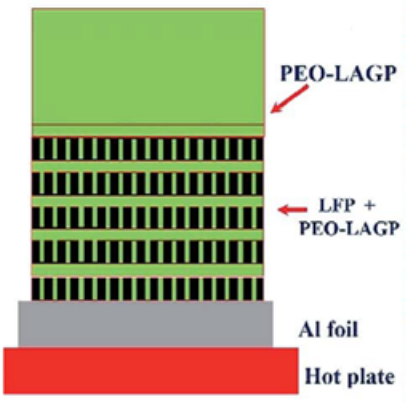

Figure 2.19: Illustration of the layered honeycomb structure of an LFP-based electrode. LFP = $LiFePO_4$, PEO = polyethylene oxide, LAGP = $Li_{1.5}Al_{0.5}Ge_{1.5}(PO_4)_3$, PEO-LAGP = hybrid electrolyte. Reproduced from [250].

The general applicability of spray printing under inert atmosphere to sulphide-based sheet-type SSB

components, such as sulphide separator, composite cathode, and Ag/C interlayer has recently been demonstrated [256]. Spray-printed separators had an ionic conductivity of 1 mS/cm and were made from an ethyl acetate Li_6PS_5Cl dispersion. A sprayed composite cathode cycled for 800 cycles showed a capacity retention of 63%. Generally, using spray printing to interleave the electrolyte improved the critical interfacial contact between electrode and SSE, and cells showed comparatively high capacity and good cycle stability.

In summary, spray printing offers increased microstructural design that has shown to be beneficial to LIBs. The application of spray printing to sulphide SSBs, which present additional challenges (high density, reactivity, etc), has been realized as a manufacturing proof of concept.

2.2.3 Sputtering

Sputtering is a PVD technique in which energetic particles of plasma or gas bombard the surface of a solid and detach atoms/particles as shown in Figure 2.20. The detached particles enter the gas phase as atoms and then condense on a nearby substrate surface, adhere to it, and form a thin film coating [257]. Sputtering can lead to good adhesion (critical load of metal coatings on a silicon–carbon substrate of 4.86-6.51 N), a smooth surface finish, and large area steady-state coverage (up to 10^{16} cm^{-2} of foreign atoms simultaneously) [258, 259, 260, 261]. In direct current (DC) sputtering, a cathodic electrode is the sputtering target and the substrate is placed on the anode [262, 263]. A DC voltage between the two electrodes is applied, and at low pressure the discharge current is transported to the cathode mainly by positive ions and to the anode by electrons from the plasma generated by the incoming ion beam. The ions formed in the plasma are accelerated by the electric field and bombard the target surface ejecting surface atoms and secondary electrons of the material. The sputtering target must be electrically conducting, since an insulating surface will develop a surface charge that will prevent ion bombardment of the surface.

In radio frequency (RF) sputtering, the electrical potential of the current in the vacuum environment is alternated to avoid charge build-up, which allows the sputtering of electrically insulative

targets [264, 257]. First, electrons gather at the target surface as the voltage sweeps positive, creating a negative bias. The processing gas ions are then accelerated toward these electrons. As the voltage sweeps negative, the ions cannot compensate for the electron saturation at the target surface due to their slower movement, resulting in a net negative bias.

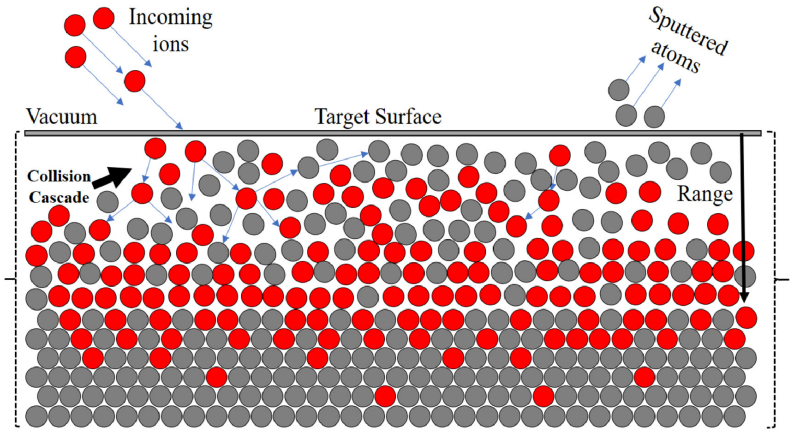

Figure 2.20: Schematic illustration of the ion-solid interaction process in sputtering. Reproduced from [265].

Various sputter types are: ion beam, reactive, and magnetron. Ion beam sputtering is based on bombarding the target material with an intense ion beam under high vacuum to create uniform thin layers [266]. Reactive sputtering applies both an inert working gas and an additional reactive gas that reacts with the elemental target to a sputter formation compound [267, 268]. Because compounds may form on the deposited film as well as on the surface of the sputtering target, the reaction can cause processing stability issues with respect to the control of the deposition rate. Magnetron sputtering employs a magnetic field configured parallel to the target surface to constrain the motion of secondary electrons [269]. This increases the probability of an ionising electron–atom collision occurring, which increases the efficiency of the sputtering process and the deposition rate. Most sputtering applications use a low pressure Ar atmosphere because of its atomic mass, inert reactivity, and low cost (around 43 GBP per m^3) [270].

The application of sputtering to the preparation of low-loading catalysts e.g. Ag/C interlayers in

SSBs might represent an attractive alternative to conventional wet techniques for interlayer production and sputtering for layer preparation is used already in many industries [22, 271]. As a chemical-, solvent-, and waste-free catalysis preparation method, sputtering also offers benefits in terms of sustainability [272]. Although yet hardly explored, these processing benefits have emerged in a few publications that advocate sputtering as an attractive choice for the preparation of thin films in SSBs [273]. In the case of Ag, for example, the deposition of interconnected layers resulted in higher lateral electrical conductivity than provided by nanoparticles of the same loading [274].

2.3 Summary of challenges

SSBs offer the prospect of higher energy densities, improved safety, and a wider operating temperature range compared with conventional liquid batteries, such as the ubiquitous Li-ion battery [1]. However, significant scientific challenges remain, including improving ionic conductivity (which affects capacity and power), mechanical stability (which affects lifetime), and chemical stability (which affects safety and lifetime). The higher reactivity of materials used and the demand for near-full density require the development of economic, safe, and sustainable manufacturing techniques for SSBs to enable successful mass production.

Because of the benefits of relatively high ionic conductivity and low-temperature processability, sulphide-based LPS has emerged as the SE of choice, and is used as electrolyte in this thesis. It is coupled with an SC-NMC-based cathode because of the advantages provided in terms of electrochemical stability and capacity. Taking these cathodes as standard, the research focus of the thesis is on processing opportunities for improved SSBs, concentrating on dry processing of separators, and then Ag/C interlayers as an alternative to conventional metallic Li anodes. Conventional battery processing via slurry casting is resource intensive and offers limited microstructural control. PTFE has been revealed as a critical deformable binder whose fibres can mechanically stabilise particulates. This project aims to combine dry processing based on PTFE fibrillation with calendering of free-standing SE sheets, which offers high potential for industrial applications. This project will explore the effect of

different processing parameters in comparison with a slurry cast SE reference to better understand the underlying mechanical and chemical processes that take place during cell production and operation. Although Ag/C interlayers represent an attractive anode design because of their potential to maximise gravimetric and volumetric SSB performance, inhomogeneous Li plating can lead to the formation of regions of isolated Li and the corresponding loss of CE. Spray printing allows microstructural control through layer-by-layer deposition, including graded and layered electrodes. While this process has been investigated for LIBs, only few applications to SSBs have been reported. This project uses the high controllability of spray printing for the design optimization of Ag/C interlayers. Concentrating Ag towards the current collector aims to facilitate Li plating and improve SSB cycling performance. The use of Ag nanoparticles (NPs) restricts the potential of Ag/C interlayers for scalability and tends to result in Ag agglomeration, limiting the Ag active surface area. The project aims to investigate the precipitation of Ag NPs on carboxymethyl cellulose (CMC) binder by exposure to $AgNO_3$-solution as a potential scalable silverising technique. Also, sputtering represents a processing technique with a high level of controllability widely used for catalyst preparation. This project will demonstrate a facile approach to Ag/C interlayer fabrication by sputtering of a $\sim$ 100 nm thick Ag layer on a precoated current collector foil. Each of the results and discussion chapters 4-6 describes the specific scientific objectives of the chapter, and provides a short reminder of the key relevant challenges. Each chapter concludes with a short summary and chapter 7 consolidates the findings and gives suggestions for further work.

Chapter 3

Experimental techniques

This Chapter describes the general experimental techniques used for the electrochemical and physical characterisation in the subsequent Chapters. Fabrication techniques and characterization techniques specific to materials that appear only in one Chapter are described in that Chapter. All sample preparation and characterization that involved sulphides or other air-sensitive materials was carried out in an Ar-filled glovebox (O_2 and H_2O levels < 1 ppm). Some secondary techniques were used only occasionally and with help from others, and appropriate acknowledgements are given in these instances.

3.1 Electrochemical characterization

3.1.1 Anode-free full cells

All electrochemical full cells used a sulphide solid electrolyte separator of approximately 900 μm thickness and 5 mm diameter. SE separator pellets were pressed from 30 mg powder, uniaxially in a PEEK mold (⌀5 mm) at 250 MPa at room temperature. The argyrodite SE was Li_6PS_5Cl (LPS) (MSE Supplies, USA), with a D50 particle diameter of ~ 1 μm. The cathode mixture was made by mixing SE, single crystal $LiNi_{0.83}Mn_{0.06}Co_{0.11}O_2$ (NMC, 1-2 μm) (MSE Supplies, USA), and carbon

nanofibers (MSE Supplies, USA) in a 40 mL ZrO_2 grinding bowl containing 55 g of 5 mm diameter ZrO_2 balls in a planetary mill (Fritsch Pulverisette 7) at 140 rpm for 30 min. 4 mg of cathode powder mixture and then the Ag/CB coated current collector were inserted sequentially into the PEEK mold, and the whole arrangement uniaxially again pressed, against the LPS pellet at 500 MPa. Finally, a 15 μm thick Al foil was added as current collector for the cathode. The resulting pellet-like SSB shown in Figure 3.1 therefore comprised: the Ag/C interlayer, an LPS SSE separator, and finally a composite cathode consisting of a mixture of NMC, LPS, and carbon nanofibers, at an overall mass fraction ratio of 75:22:3.

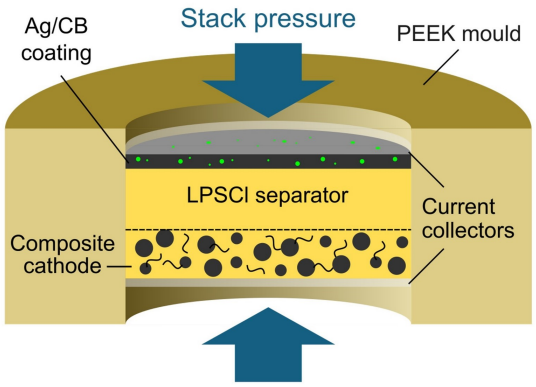

Figure 3.1: Illustration by Dr Christopher Doerrer of the SSB full-cell arrangement.

Full cells were cycled at 60 °C under a uniaxial stack pressure of 2 to 20 MPa in a cell holder shown schematically in Fig. 3.2 that connected the cell to a potentiostat with two conductive plungers made of stainless steel. A torque wrench (Bahco 1/4 in Square Drive, 0–9 Nm) was used to adjust the uniaxial stack pressure by tightening the screw on top.

Cycling experiments were carried out in an oven at a constant temperature (30, 60, 90, and 120 °C) in an Ar-filled glovebox as shown in Figure 3.3. The cells in the oven were connected to a potentiostat (BioLogic) over an airtight feedthrough. This arrangement allowed the assembly, cycling, and exchange of cells in the same glovebox.

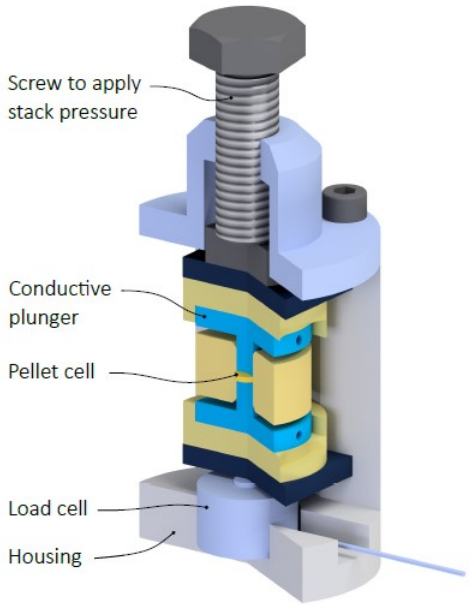

Figure 3.2: Illustration of the set-up and full cell holder design which allows to adjustment of the uniaxial stack pressure. Reproduced from [124].

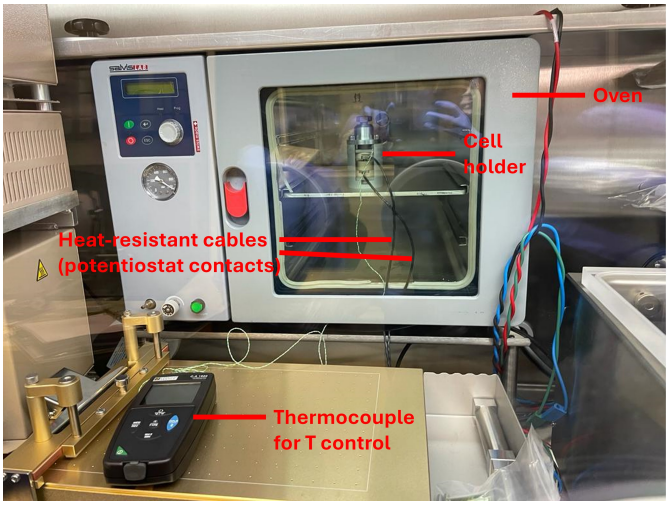

Figure 3.3: Photograph of the set-up used for SSB cycling in a temperature-controlled oven in an Ar-filled glovebox

3.1.2 Three-electrode cells

Three-electrode half-cells with Li as counter and reference electrodes were assembled as shown in Figure 3.4 to allow the separate contributions of working and counter electrodes to the Li nucleation

overpotential in anode-free SSBs to be resolved [275]. An LPS SE pellet from typically 30 mg powder was pressed uniaxially in a stainless steel mold (∅5 mm) at 250 MPa at room temperature and subsequently retrieved. Li electrodes for half-cells were prepared by rolling Li foil (Sigma-Aldrich, UK) in a pouch to a thickness of approximately 150 μm. Circular electrodes of ∅3 mm and ∅1 mm were punched out with a hand-held stainless steel cutting tool (EMS, Germany). A 30 μm thick Cu foil was used as current collector for the Li electrodes. For the Ag/C interlayers, ∅2 mm circular discs were laser cut and assembled as anodic current collectors.

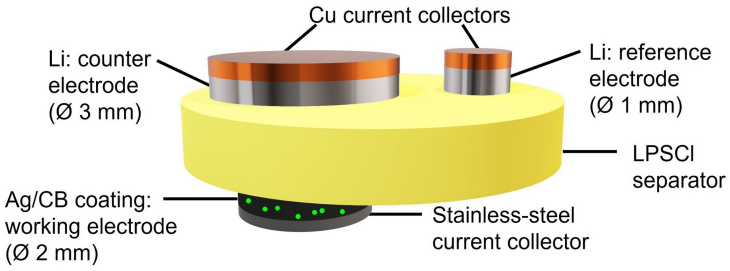

Figure 3.4: Illustration of the three-electrode cell arrangement.

The three-electrode cell was placed in a heat-sealable pouch composed of sheets of laminated Al foil. Hot melt adhesive tape was placed between the Cu current collectors and the pouch for heat sealing. The sides of the pouch were subsequently sealed using a vacuum heat sealer inside a glovebox. The Cu current collectors were connected to a potentiostat and the sealed pouch cell clamped between two acrylic sheets to apply a uniaxial stack pressure of 4 MPa prior to cycling at 60 °C. Figure 3.5 shows photographs of the pouch cell arrangement.

3.1.3 Symmetric cells

SE separators were calendered to a thickness of 600 µm and ∅5 mm discs punched from the calendered sheets with a hand-held stainless steel cutting tool (EMS, Germany). Li electrodes for symmetrical cells were prepared by rolling Li foil (Sigma-Aldrich, UK) in a pouch to approximately 150 μm thickness

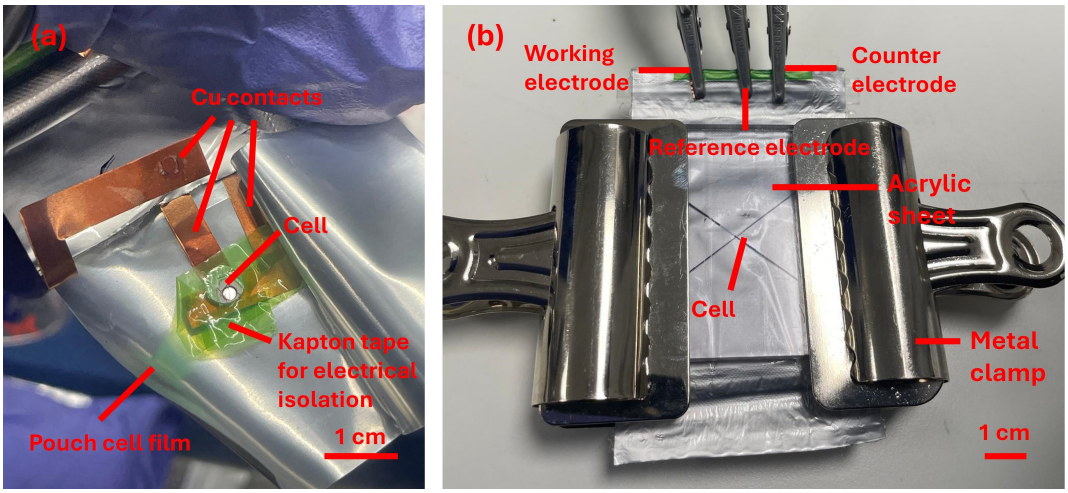

Figure 3.5: Photographs of the (a) inside and (b) outside of the pouch cell arrangement of three-electrode cells

and then ∅3 mm electrodes were punched out. 30 μm thick Cu foil was used as current collector foil for the Li electrodes. Symmetrical two-electrode cells (Li-separator-Li) as illustrated in Figure 3.6 were assembled and then sealed in a pouch in the same way as three-electrode cells and cycled at 60 °C and a uniaxial stack pressure of 4 MPa.

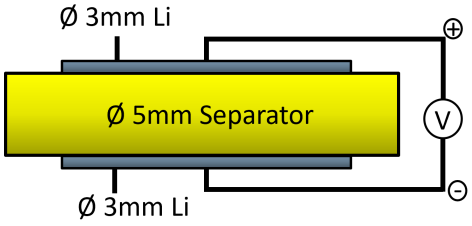

Figure 3.6: Illustration of the symmetric cell setup used for critical current density measurement and impedance studies.

Electrochemical data were collected and evaluated with the help of "Data Analysis" software (Batalyse, Germany).

3.1.4 Electrochemical impedance spectroscopy (EIS)

Impedance studies were used to determine the ionic conductivity and interfacial resistances of calendered separator pellets or an anode-free SSB. The ionic conductivity was calculated according to:

$$\sigma = \frac{t}{AR_t} \tag{3.1}$$

where σ = ionic conductivity; t = separator thickness; A = area of the electrode; R_t = total Ohmic resistance.

An electrochemical system is often modelled using a combination of series and parallel configurations of AC circuit components, which should closely mirror the physical arrangement, known as an equivalent circuit. Since several equivalent circuit best-fit solutions to an EIS spectrum are often possible, guidelines should be followed, e.g. use the simplest model with the fewest elements possible and ensuring that physical and chemical meaning is maintained [276]. The fitting of equivalent circuit models was conducted using "EC-Lab" software (BioLogic, France). Figure 3.7 shows the equivalent elements applied to fit impedance data. Resistors can represent bulk ionic and grain boundary resistance of the SE and charge-transfer resistance between the SE and electrodes [276]. Capacitors can represent charge accumulation/depletion occurring across phase boundaries and at the SE/electrode interface. Constant phase elements represent non-ideal capacitances, which are attributed to inhomogeneity and porosity of electrochemical materials and interfaces [277]. Warburg impedance is caused by resistances that occur due to limitations on Li^+ mobility.

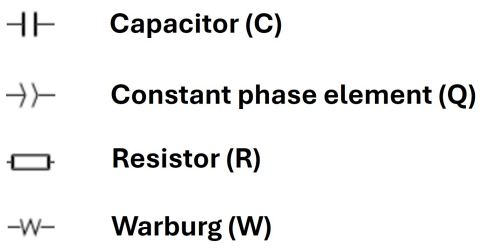

Figure 3.7: Electrical equivalent elements used to fit impedance data.

3.2 Physical characterization

3.2.1 Cross-sectioning

Consolidated separator pellets (⌀5 mm) and Ag/C interlayers for cross-sectional imaging were mounted on a Ti blade using Ag paste and cross-sectioned by broad beam Ar ion milling using a Gatan PECS II at a voltage of 8 kV and an etching time of typically 4 h.

3.2.2 Scanning electron microscope (SEM) and energy-dispersive X-ray spectroscopy (EDX)

Samples for top-down view SEM imaging were mounted on an adhesive C coating placed on a stub. Air-sensitive separator pellets were transferred under Ar atmosphere using an airtight transfer device. SEM analysis of Ag/C interlayers was performed with a Zeiss Merlin FEG-SEM equipped with an Oxford Instruments X-max EDX detector at an accelerating voltage of 10 kV. SEM analysis of consolidated separator pellets was performed in a Tescan Mira3 FEG-SEM equipped with an Everhart-Thornley Type SE detector at an accelerating voltage of 2, 5, and 10 kV. EDS acquisition was performed at a variety of times and magnifications and analysis using an Oxford Instruments X-maxN 80 EDS system.

3.2.3 X-ray diffraction (XRD)

XRD measurements of LPS and consolidated separator pellets (⌀5 mm) were carried out in order to explore the effect of processing on the crystal structure and were performed in a Rigaku MiniFlex with $K_{\alpha 1}$ radiation inside an N_2-filled glovebox. Patterns were collected from 5° to 90° in $\theta/2\theta$ using a step size of 0.01° at room temperature. Characteristic XRD peaks were identified by comparison with the Inorganic Crystal Structure Database: LPS (259205-ISCD). LPS powder was placed on a Si low background holder and fixed with vacuum grease to avoid powder spillage during the measurement. Separator pellets were mounted on a lowered Al holder using a pressure-sensitive adhesive (Blu Tack) and levelled with the holder using a glass plate.

XRD analysis of carbon black used for spray printed Ag/CB interlayers was conducted by Dr Guillaume Matthews with the author present using a PANalytical Empyrean diffractometer equipped with a K_α-Cu source. The spectrum was recorded at 40 kV and 40 mA.

3.2.4 X-ray photoelectron spectroscopy (XPS)

To characterize the composition of the deposited anode layer of anode-free SSBs after charging via XPS, cold-pressed three-electrode cells were charged and disassembled, and the current collector upon which the anode was plated was removed for XPS-analysis. The deposited layer was etched to a depth of 25 nm to avoid potential surface impurities. XPS was conducted with a Thermo Scientific K-Alpha XPS instrument using monochromated Al K_α line X-rays at 1486.6 eV. For a survey scan, a pass energy of 200 eV and a step size of 1 eV were applied. For individual scans, a step size of 0.1 eV was applied. Measurements were made by Dr Wai Man Chan.

3.2.5 Plasma focused ion beam (PFIB) with secondary-ion mass spectrometry (SIMS)

Three-electrode cells for P-FIB microscopy were assembled disassembled in a glovebox after cycling and cross-sections of the anodic current collector region were imaged. A Thermo-Fisher Scientific Helios G4 PFIB CXe DualBeam, equipped with a Xe^+ plasma focused-ion beam, was employed for cross-sectioning and polishing. To characterize the morphology of the electrode cross-section, electron-induced secondary electron (SE) images were acquired at 5 and 10 kV with a beam current of 1.6 nA. Additionally, utilizing the Xe^+ primary beam, ion-induced secondary electrons (iSEs) were observed at 30 kV with a current of 0.1 nA. For elemental mapping excluding Li, the spatial distributions of Ag, C, Fe, Cu, and S across the sectioned surface were acquired through EDS analysis using an Oxford EDS system with an Ultim Max 170 SDD detector. The data were captured and stored using Aztec software (version 4.1 SP1, Oxford Instruments), with a field of view (FoV) measuring 52.1 x 35.8 μm^2, comprised of 1024 x 704 pixels. To obtain the spatial distribution of $^7Li^+$ isotope at a spatial resolution

of 113 nm, SIMS was employed, utilizing a Hiden EQS SIMS detector. Imaging was conducted in the P-FIB with a field of view sized at 45.2 x 45.2 μm^2, containing 400 x 400 pixels. A Xe^+ beam operating at 30 keV and 1 nA was utilized to generate secondary ions. Hiden SIMS MAPPER software (version 2.0.0.5) was employed to map and record all SIMS data. SIMS acquisition was lead by Dr Yige Sun with the author present.

Chapter 4

Dry processing and slurry casting of solid-state separators

4.1 Introduction

In conventional LIB processing, active material (AM), binder, and a conductive agent are mixed together in specific mass ratios during the preparation of the composite electrode slurry [278]. Positive electrodes generally consist of a lithium metal oxide as the active material mixed with carbon black (CB) conductive agent and polyvinylidene fluoride (PVDF) binder. PVDF is dissolved in organic N-Methyl-2-pyrrolidone (NMP). Negative electrodes consist of graphite as the active material and a carboxymethyl cellulose-based (CMC) binder in combination with styrene butadiene rubber (SBR) using water as a solvent. Additional CB may also be added. The viscous slurries are spread onto a current collector using a doctor blade or slot die with a specific cast wet thickness in the range 100 to 400 μm, and then carefully dried to remove the solvent while avoiding cracking and unwanted binder migration to the electrode top surface. During subsequent calendering, the electrodes are compressed between two rotating cylindrical rolls for densification, smoothing, contact resistance reduction, and thickness control, in the range of 40 to 160 μm [279]. Unlike SSB electrodes (e.g. in the composite

cathode), residual porosity of 20-40 vol.% is required after the calendering step [280]. The calendered electrodes are subsequently cut, assembled into multilayer cells (cylindrical, prismatic, or pouch) and infiltrated with a liquid electrolyte, most commonly $LiPF_6$ salt dissolved in a binary or ternary solvent mixture of ethylene carbonate (EC) and linear carbonates such as dimethyl carbonate (DMC), diethyl carbonate (DEC), and ethyl methyl carbonate (EMC) [281].

However, when sulphide SEs are considered for slurry casting, they will decompose when in contact with binder solvents with a polarity index > 4.0, ruling out conventional solvents and limiting the selection of suitable solvents [282, 283]. Moreover, a new suitable binder that is soluble in a sulphide compatible solvent must be identified. The binder should also be chemically stable in contact with the sulphide SE. Nitrile butadiene rubber (NBR) is widely employed as an SSB binder and may cause only a small reduction of the ionic conductivity of the SE if dispersed and processed optimally [282]. In general, xylene is preferred as the NBR solvent as it also has low reactivity with sulphide SEs [284]. Slurry casting generally requires large volumes of solvent e.g. 22 - 36 wt.% of the slurry, and is an energy intensive process due to the elevated temperature required for the removal of organic solvents (drying, recovery, and recycling) [210, 228, 285, 286]. Solvent-free or dry processing, on the other hand, potentially requires less energy and is more environmentally friendly, because it does not require a drying and solvent recovery step [18]. The absence of potentially hazardous solvents also improves process safety and waste management.

Potentially, dry processing also enables a different and possibly more controlled microstructural arrangement since solvent evaporation and binder precipitation can be hard to control. Moreover, the CB distribution is intimately related to the binder distribution as CB preferentially segregates to binder as it precipitates to form the "carbon binder domain" (CBD). It has also been reported that there was a more homogeneous SE distribution in a dry processed SSB electrode compared with a slurry-cast equivalent, resulting in increased capacity [211].

The three main techniques for dry processing of battery SEs and electrodes are dry painting, powder extrusion moulding, and PTFE-fibrillation. In dry painting, a mixture of binder-coated dry

active particles is fluidized by a dispensing device such as a Venturi pump before being electrostatically charged and then dispersed as a fine spray. The charged particles in the spray are electrostatically deposited onto the grounded current collector through the electric field, followed by a final, sometimes elevated temperature, consolidation step such as calendering to impart mechanical stability and thermal binder activation [287, 288, 217]. In this step, the powder coating becomes "sticky" and the particles cohere with one another at triple points, and adhere to the current collector. In powder extrusion moulding, AM is first mixed with a large binder fraction (40–50 vol.%) to a blend that is then extruded, before thermal and/or solvent de-binding and sintering at high temperature (500–900 °C) [289, 290, 291].

The most popular approach to solvent-free processing is based on PTFE binder fibrillation. First, the AM is dry-mixed with PTFE particles. The mixture PTFE is then subject to the application of shear forces at temperatures typically in the range of 30 °C to 100 °C [18, 292, 235]. Under optimum shearing conditions, the PTFE undergoes extensive deformation and "unwinding" to form fibrils of micron and sub-micron diameter that are mechanically anchored at various points along their length to the AM. Unlike many other polymers, the inherent chain structure and high crystallinity of PTFE facilitate its transformation into cohesive fibrils under mechanical force [235]. Because there is no binder precipitation, there is no means to secure particulate CB into the structure and therefore there is no conventional CBD [233]. Instead, a different carbon form is added to the mixture, such as carbon nanofibres (CNF), which are co-tangled with the PTFE fibrils to form an electron-percolating network [293]. The network or web of PTFE fibrils provide mechanical stability for the mass of SE and AM particles, and the entire electrode [294, 233]. This integral "pre-form" is then used as the feedstock for further processing, usually by hot calendering to a sheet electrode of the desired thickness. Although developed principally for LIB cathodes and anodes, this form of solvent-free processing has also been explored for SSB composite cathodes and SE separators. However, the requirement for near-full density makes this much more demanding than LIB applications. Figure 4.1 shows schematically the usual laboratory-scale processing approach based either on pestle and mortar warm shearing or conventional

slurry casting involving a solvent. A further approach for SSB SE separators and composite cathodes is simple uniaxial hot pressing of a dry mixture [295]. This is practised in the academic literature and can produce dense material ($\sim$ 99 %) but is limited to small diameters of 10-30 mm and thicknesses of 200 - 1000 μm. The calendering of preforms into free-standing electrolyte sheets has been demonstrated to have high potential for scalability, with porous, dry processed electrodes based on PTFE fibrillation in some commercial LIB cells. The status of SSB implementations of dry processing at commercial scale remains closely guarded.

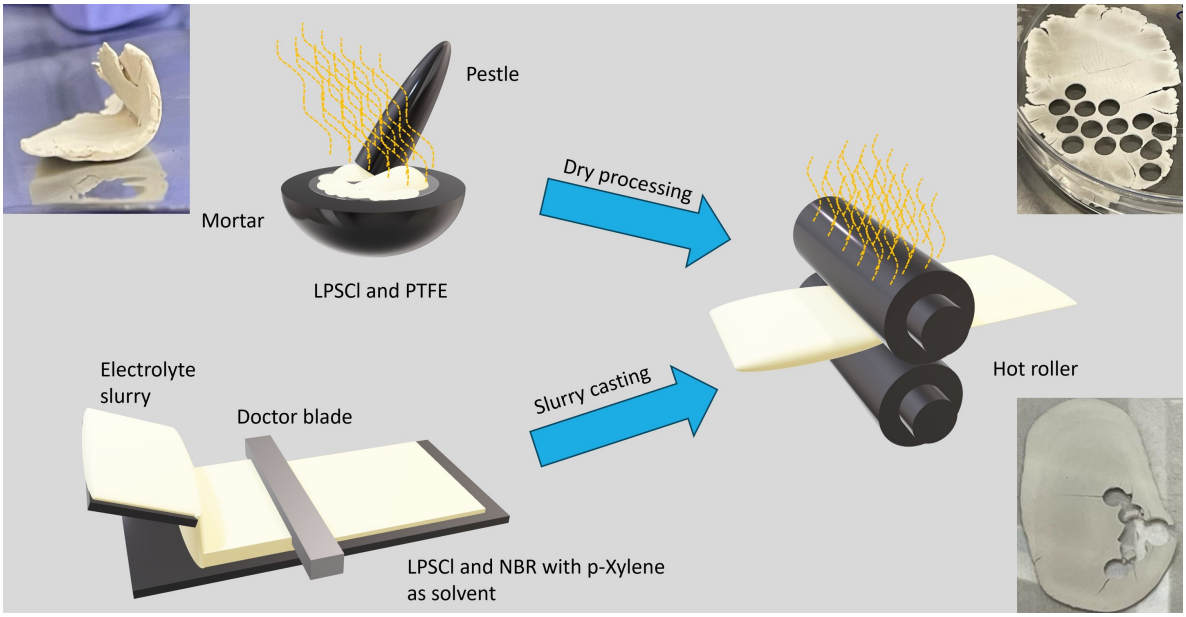

Figure 4.1: Schematic illustration of hot calendering of dry processed and slurry cast solid-state separators.

Although the successful assembly of SSBs through PTFE-fibrillation has already been reported at laboratory scale, there have been only limited systematic studies of the effect of the parameters of the manufacturing process on the resulting microstructure and properties [242, 203, 237, 241]. The objectives of this chapter are:

- To investigate how dry processing influences a sulphide SE-based separator microstructure to enable future scale-up requirements and options.

- To investigate the relationship between separator microstructure and electrochemical properties for both slurry cast and solvent-free processed sulphide separators.

4.2 Experimental methods

4.2.1 Calendering of solid-state separators

For slurry cast SE separators for subsequent calendering to high density, 1.0 g of Li_6PS_5Cl (LPS) (325 mesh, D50 $\sim$ 1 μm, MSE Supplies, USA) was dispersed with 1 wt.% NBR in 2.3 g of p-xylene and mixed with a Thinky planetary mixer at 2000 rpm for 5 min. The resulting slurry was cast by Dr Junfu Bu onto a 10 μm thick stainless-steel foil using a doctor blade in an Ar-filled glovebox to a wet thickness of $\sim$ 1 mm and dried at room temperature overnight. For dry processed SE separators, 2 wt.% PTFE (3M Dyneon, Germany) was warm pestle and mortared with the same LPS at 80 ° C by hand for 5 min to fibrillate the PTFE and to form a single coherent preform.

Due to the high reactivity of the LPS electrolyte with atmospheric moisture, a Kapton (Sigma-Aldrich, USA) pouch was designed as illustrated in Figure 4.2(a) to facilitate safe calendering in the ambient laboratory. Within the pouch, the free-standing composite preforms from the pestle and mortar were additionally placed between two (10 μm thick) stainless steel sheets to prevent the LPS from sticking to the Kapton. The pouch assembly was placed between two (100 μm thick) stainless steel shims to prevent contamination of the calender in the event of pouch breakage. In addition to their protective function, the protective layers also helped spread the rolling load applied to the separator preform to avoid cracking rather than compression. The pouch temperature was monitored during calendering using a small infrared camera as shown in Figure 4.2(b). To avoid the reflection of thermal infrared (IR) by the steel sheet surface, black paint was applied to the pouch surface. The calibration of the infrared camera was confirmed by measuring a heated metallic cylinder with a known temperature. The entire operation took place beneath a close fitting, high volumetric throughput external extraction system and with a hydrogen sulphide sensor.

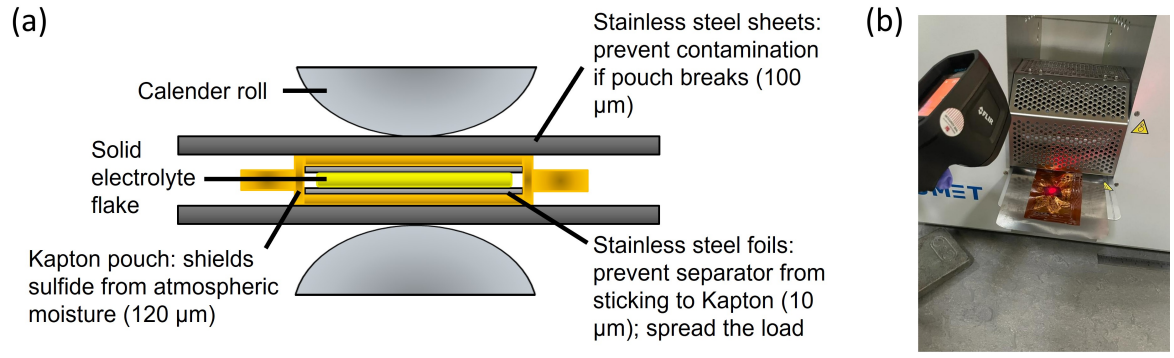

Figure 4.2: (a) Schematic illustration and (b) photograph of the pouch design used for hot calendering of LPS separators.

The sealed preforms were compressed using a pressure-controlled (i.e., dynamic roll-gap control) SUMET CA3 hot calender at a constant forward rolling speed of 0.2 m/min. The calender rolls had a width of 15 cm and a diameter of 9 cm. SE sheets had a typical width of $\sim$ 2 cm and the target thickness for electrochemical characterization was 600 µm. The applied press force per calender width, indicating how hard the rollers press along their edge (in N/m), can be converted into calendering pressure via [296]:

$$p = \frac{P}{bL_P} \tag{4.1}$$

where p = specific roll pressure; P = rolling load = press force per roller width $\times$ roller width; b = material width.

$$L_P = [R(h_0 - h_f) - \frac{(h_0 - h_f)^2}{4}]^{1/2} \tag{4.2}$$

where R = radius of calender rolls; h_0 = membrane thickness before rolling; h_f = membrane thickness after rolling; L_P = length of the arc of contact.

The typical reduction in the thickness of the SE sheet during calendering and the corresponding pressure for a press force per calender width of 50 N/mm, which varied between approximately 115 MPa

and 400 MPa, are shown in Figure 4.3. The SE sheet thickness was measured with a Mitutoyo 293-340-30 Digimatic micrometre. Initial calendering passes smoothed the SE surface prior to consolidating the bulk material. Gradual incremental compression through various passes was required to avoid tearing the pouch and the SE sheet. The SE target thickness was fine-tuned in the final calendering passes.

To maintain an SE sheet temperature of approximately 80 ° C, the pouch was heated in an oven next to the calender for 40 min before calendering and for 5 min between each calendering pass.

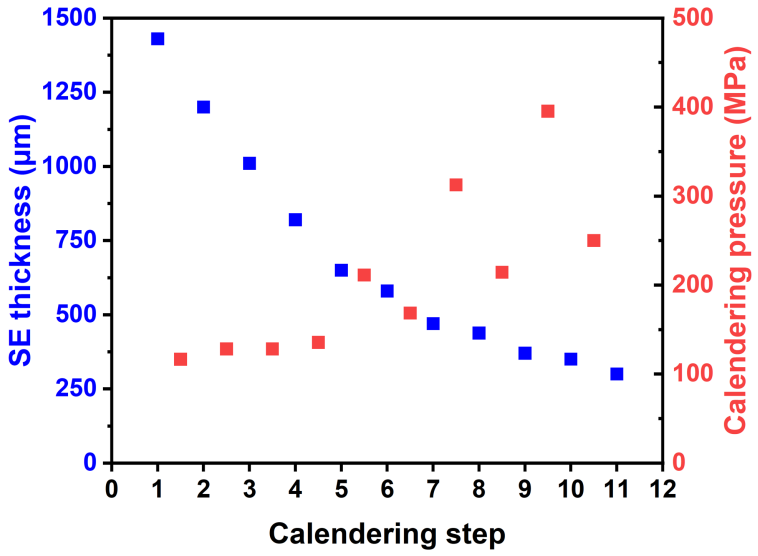

Figure 4.3: Typical compression profile of SE membrane thickness and corresponding calendering pressure.

Figure 4.4 shows the plot of the averaged temperature profile of the pouch surface for 3 calendering passes. The pouch surface temperature drops by approximately 20 ° C during transfer from the oven to the calender. Due to the higher thermal conductivity of stainless steel (14 W m^{-1} K^{-1}) than LPS (0.6 W m^{-1} K^{-1}), the loss of temperature on the pouch surface was assumed to be more marked than in the centred SE sheet [297, 298]. To account approximately for the loss of heat during pouch transfer, the oven was heated to 10 ° C above the target temperature.

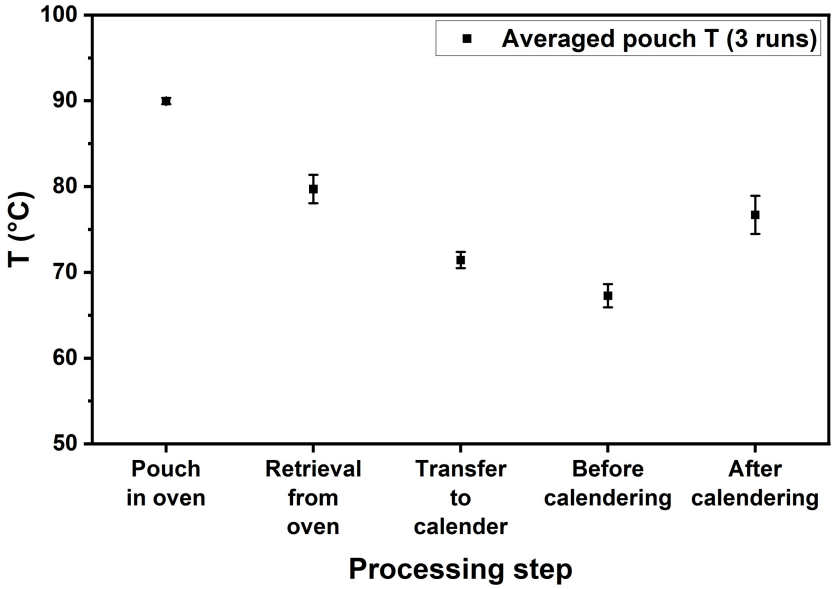

Figure 4.4: Averaged pouch temperature profile (3 runs) during a calendering pass for a target T of 80 °C.

4.2.2 X-ray computed tomography (XCT)

SE separators for XCT were again calendered to a thickness of 600 µm and then ∅5 mm separator discs were punched out with a hand-held stainless steel cutting tool (EMS, Germany) and sealed in Kapton foil (Sigma-Aldrich, USA) to allow handling under ambient atmosphere. Cone beam XCT was performed by Dr Andrew Lui using a North Star ImagiX CT system under the following scanning conditions: 90 kV tube voltage, 100 μA tube current and a frame rate of 1.5 Hz. The tomograph was constructed from the projected data and visualised using North Star Imaging efX-CT software with an isotropic voxel size of 7.5 μm. With this resolution, the XCT studies were focused on identifying only large-scale voids and macro-cracking. For finer-scale features and Li dendrite formation during cycling, much higher resolution, higher flux arrangements would be required, and would normally require synchrotron X-rays.

4.2.3 Fourier transform infrared spectroscopy (FTIR)

In order to assess the composition of the feedstock PTFE, infrared spectroscopy was performed by Dr Colin Johnston using an Agilent Digilab Excalibur Fourier Transform Infrared Spectrometer. A permanently aligned attenuated total internal reflection sampling attachment (Golden Gate ATR with diamond window) was used to measure the IR spectrum of as-received PTFE over the wavenumber range 500 to 4000 cm^{-1}. The material was placed directly on the diamond window, and the obtained spectra were compared with the diamond spectrum.

4.3 Results and discussion

Figure 4.5 shows the FTIR spectrum of the feedstock PTFE. The spectrum showed two characteristic peaks at 1200 cm^{-1} and 1144 cm^{-1} that were attributed to asymmetrical and symmetrical stretching of the CF_2 group, respectively [299]. A third weaker peak at 638 cm^{-1} was attributed to CF_2 wagging [300, 301]. The FTIR spectrum conformed to high-purity PTFE without any resolvable additives or contamination and within the sensitivity of the equipment the spectrum was entirely consistent with previous reports [302].

4.3.1 Hot calendering of LPS separators

Two calendering temperatures (80 °C and 200 °C) and press forces (50 N/mm and 250 N/mm) were explored for their effect on separator density. Table 4.1 shows the LPS relative density as a function of calender settings, where each value is an average of 8 measurements from the same SE sheet. The applied press force was converted into applied pressure as previously described assuming a rolling gap of 100 μm. As expected, an increase in calendering temperature and rolling line pressure reduced SE density. Excess load and temperature can weaken the SE and introduce defects during rolling. However, the range of attainable densities was narrow at 76-84 %, despite the widely separated variables. It is likely that at around a density of 75-80 %, internal friction dominates and restricts further consol-

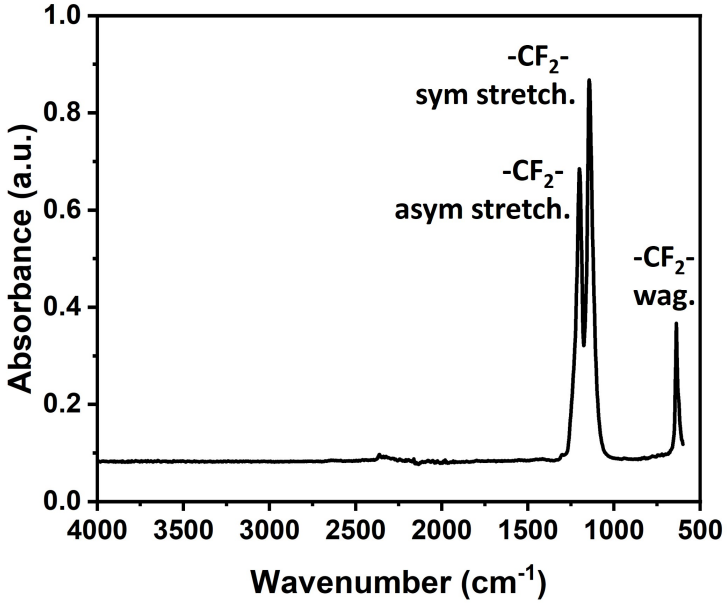

Figure 4.5: FTIR spectrum of the feedstock PTFE.

idation. Therefore, a moderate press force of 50 N/mm at 80 °C was selected for further experiments to promote densification while avoiding needlessly demanding conditions on the equipment. To investigate batch-to-batch reproducibility under the same conditions (80 °C and 50 N/mm), 3 measurements of the relative density were taken from 2 other dry processed SE sheets made under nominally the same conditions and were highly similar at: 84.6 % (std dev = 1.4) and 85.7 % (std dev = 3.0).

T (°C)	**Press force (N/mm)**	**Pressure (MPa)**	**Rel. density (%)**	**Std dev**
80	50	177	83.8	3.5
80	250	884	82.1	2.9
200	50	177	78.0	3.2
200	250	884	76.3	3.9

Table 4.1: Comparison of relative density of dry processed LPS separators at different calendering settings.

While high calendering pressure does not improve consolidation, it may nonetheless damage the preform AM or SE, or the protective pouch. Excess load during rolling contact can result in accumulation of local defects in the SE, which induces the propagation of cracks after a sufficient number of cycles [303]. Consistent with the results here, a moderate temperature of 80 °C was previously reported to initiate softening of an LPS/PTFE membrane during hand shearing and calendering so that the material could undergo plastic deformation without excessive cracking [237]. Thermal softening describes the reduction of the yield stress as the temperature increased [304]. The resulting reduction in yield stress reduced the internal resistance to deformation and increased relative sliding between adjacent particles that may cause shearing that results in particle rupture, resulting in higher packing densities [305, 306, 303, 307, 308]. However, in this work and over the range studied, these effects were hard to resolve. It is noticeable from the literature, e.g. described by Singh et al.[309], that consolidation pressures of above several 100 MPa are usually maintained for times up to 1 h to achieve densites > 90 %, whereas calendering - although highly scalable - applies pressure each pass for only ≤ 1 s.

4.3.2 Impact of SE processing on ionic conductivity

The distribution of residual porosity and binders in slurry cast and dry processed LPS separators after hot calendering to a thickness of 600 μm and a density of $\sim$ 83 % were investigated by microscopy. Figures 4.6(a) to (c) show cross-sectional SE images after calendering. In Figure 4.6(a), NBR binder appeared extruded from the microstructure onto the free surface, possibly indicative of internal residual stresses. NBR was also most easily resolved where it filled larger pores and cracks. The overall microstructure was relatively free from large-scale inter-connected pores but there were regions of low relative density between some LPS particles. In the dry processed SE sheet in Figure 4.6(b), there were no obvious PTFE agglomerations at low magnification and no regions of macroporosity. At higher magnification in Figure 4.6(c), PTFE could be resolved with a distinct branch-like morphology of PTFE strands (ϕ 0.5 - 1 μm) with protruding fibres (ϕ 0.04 - 0.09 μm) forming a 3D fibril net that

connected the LPS particles. This observation was consistent with previous reports of PTFE strands ($\sim \phi$ 1 μm) unwinding into fibrils ($\sim \phi$ 0.05 μm) upon the application of shear forces and elevated temperature (80 °C) [233]. At the macroscale, the PTFE fibril web provided a flexible separator that was easy to handle, whereas the slurry cast equivalent was brittle and more prone to obvious cracking during handling.

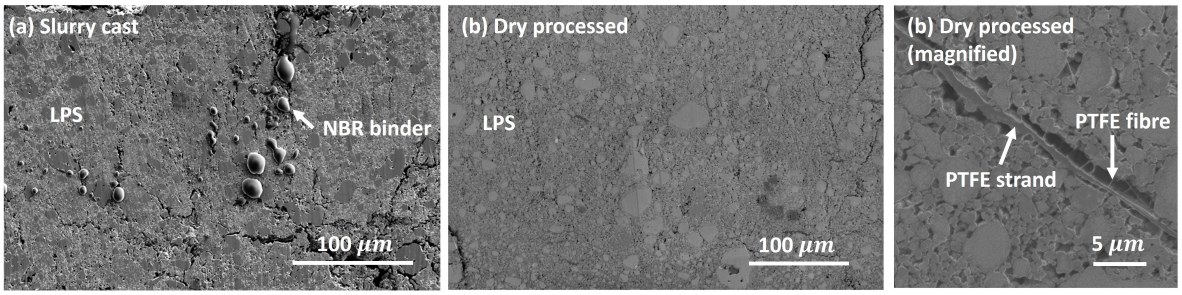

Figure 4.6: Cross-sectional SE micrographs of (a) slurry cast and (b) dry processed separators after hot calendering. (c) Higher resolution region of a dry processed separator.

The various separators were assembled into cells as described in chapter 3, and the temporal evolution of cell impedance was tracked as shown by the Nyquist plots in Figure 4.7. Impedance measurements were performed before the start of a bidirectional critical current density (CCD) test and after any change in the applied current density, in the frequency range of 100 mHz – 1 MHz with a nominal AC voltage of 10 mV. Alternating charge/discharge currents of 0.1 (2 cycles), 0.2, 0.5, 1, 2, and 5 (5 cycles each) mA/cm^2 were applied to symmetric cells to a capacity of 1 mAh/cm^2 at 60 °C and under a uniaxial stack pressure of 4 MPa until SE failure occurred. Ionic conductivities of 1.19 mS/cm (std dev = 0.03) and 1.45 mS/cm (std dev = 0.07) were estimated by averaging 3 slurry cast and 3 dry processed separator cells, respectively. These conductivities were comparable to SSB separators of similar composition in the literature [310, 311].

Figure 4.7(a) shows an increase in impedance of 9.7 % of the dry processed separator and Figure 4.7(b) by 2.5 % of the slurry cast separator, each after initial cycling at 0.1 mA/cm^2. There was no resolvable trend in the impedance response of either separator as the subsequent current densities

were applied. One factor that may affect impedance evolution is that LPS is known to have a limited electrochemical stability window, but is able to form a relatively stable solid electrolyte interface (SEI) in contact with metallic Li [312, 313, 314]. SEI formation is based on LPS decomposition via a multi-step mechanism through partially reduced phosphide species that are typically formed under Li deficient conditions [315, 316, 317]:

$$Li_6PS_5Cl \rightarrow Li_2S + P + LiCl \rightarrow Li_3P \tag{4.3}$$

The resulting decomposition products Li_2S, LiCl, and Li_3P are poor Li^+ ion conductors [318]. Although a stable SEI can prevent continuous SE decomposition, the initial SEI formation increases interfacial impedance [94, 319, 79, 320].

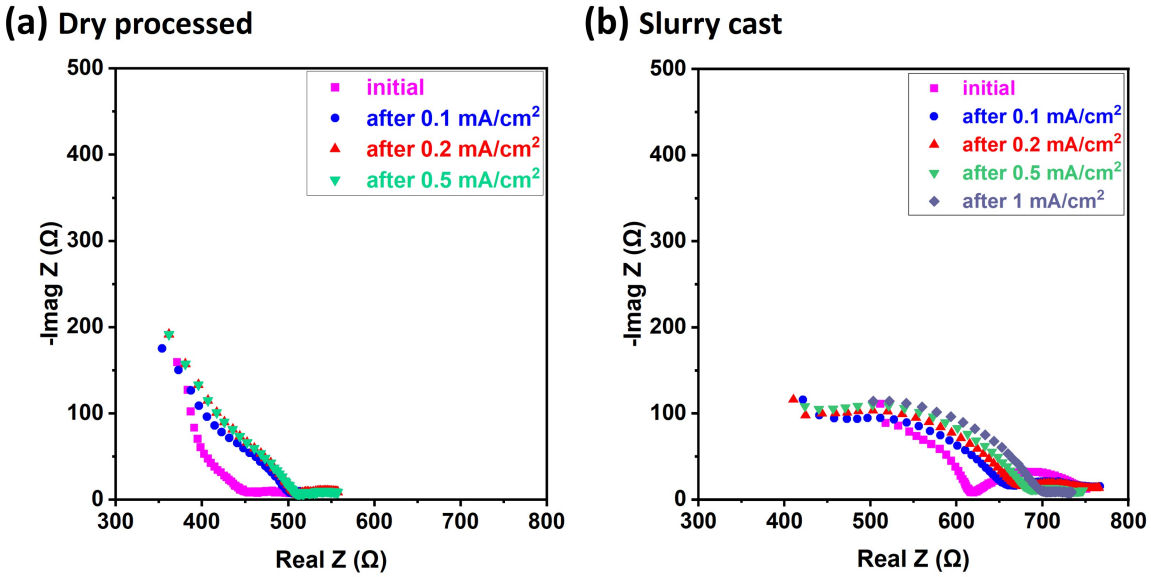

Figure 4.7: Nyquist plots of (a) dry processed and (b) slurry cast LPS separators. Impedance measurements were performed on symmetric Li-LPS-Li cells under 4 MPa stack pressure at 60 °C before the start of a bidirectional critical current density (CCD) test and after any change in the applied current density, in the frequency range of 100 mHz – 1 MHz with a nominal AC voltage of 10 mV. Alternating charge/discharge currents were 0.1 (2 cycles), 0.2, 0.5, 1, and 2 (5 cycles each) mA/cm^2.

Figures 4.8(a) and (b) show the Nyquist plots of dry processed and slurry cast LPS separators after 2 cycles at 0.1 mA/cm^2 and an equivalent circuit best-fit, respectively. The data were best-fit to the equivalent circuit model shown in Figure 4.8(c), based on models previously used for similar cell arrangements [321, 322, 316, 276]. Going from high to low frequencies, impedance contributions to the data can be attributed to both bulk and grain boundary (GB) resistance, any SEI formed at the interface between SE and metallic Li, and charge-transfer (CT) processes [323, 324]. The best-fit to the dry processed separator impedance data suggested a lower bulk/GB contribution to overall resistance (R1 = 400 Ω) than the slurry cast separator (R1 = 465 Ω). In slurry-based SEs, the precipitated non-

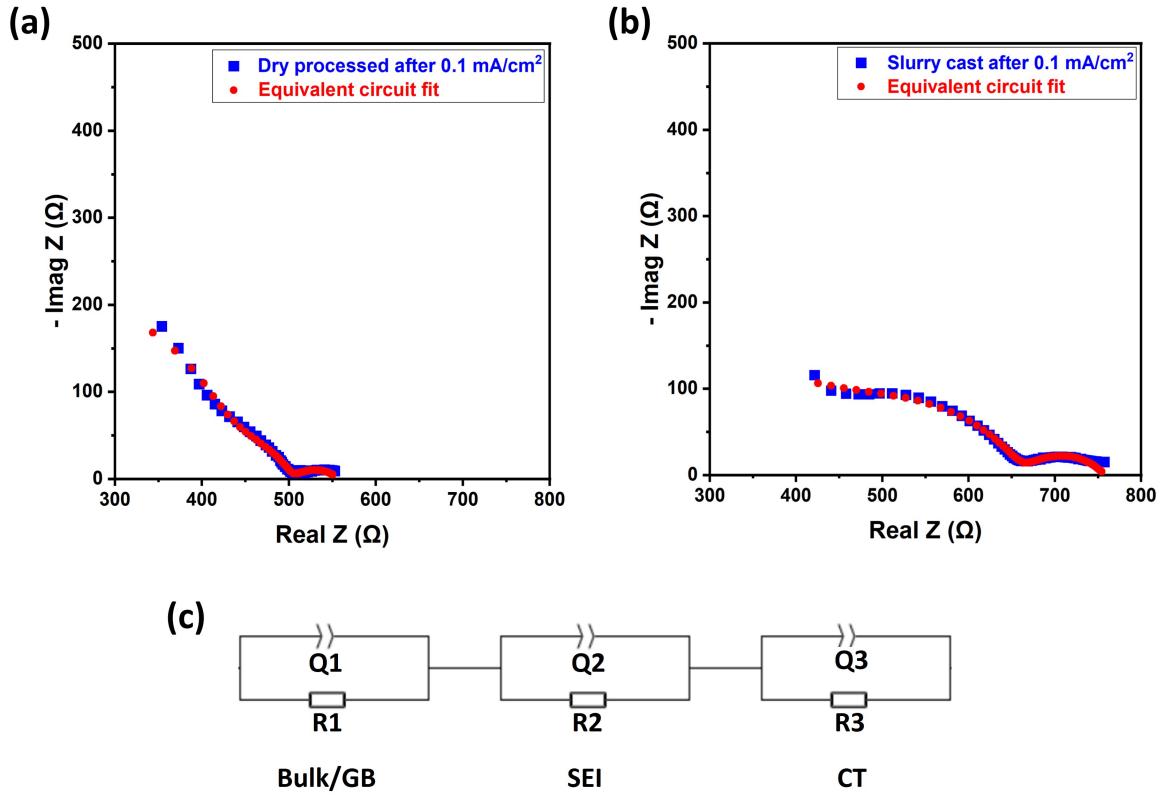

Figure 4.8: Initial Nyquist plots and equivalent circuit best-fits for the (a) dry processed and (b) slurry cast separator; (c) equivalent circuit model used for fitting.

conductive binder covers SE particles and thus likely increases "bulk" impedance, while the fibre-like binder network of dry-processed SEs may result in an overall smaller polymer contact area with SE

particles [325, 326]. Interfacial impedance comprises the SEI and CT components that are represented by the low-frequency segment of the spectra [316]. The dry processed separator exhibited a lower interfacial impedance contribution (R2 + R3 = 158 Ω) than the slurry cast equivalent (R2 + R3 = 293 Ω). This might arise because the greater mechanical flexibility displayed by dry processed LPS during manual handling was more likely to support Li-LPS interface contact during cell assembly and subsequent cycling. Overall, the data suggested a relatively high impedance arrangement in all the separators, but it should be noted that, compared to the literature, a low/very low but more practical stack pressure of 4 MPa was used. The best-fit values for the dry processed and slurry cast separators are given in Table 4.2.

Equivalent circuit element	**Dry processed**	**Slurry cast**
R1 (Ω)	400.0	465.0
Q1 ($F.s^{(\alpha-1)}$)	0.2×10^{-9}, $\alpha = 1$	36.3×10^{-9}, $\alpha = 0.6$
R2 (Ω)	103.0	196.0
Q2 ($F.s^{(\alpha-1)}$)	0.9×10^{-6}, $\alpha = 0.7$	0.4×10^{-6}, $\alpha = 0.7$
R3 (Ω)	55.0	97.0
Q3 ($F.s^{(\alpha-1)}$)	4.2×10^{-3}, $\alpha = 0.4$	0.8×10^{-3}, $\alpha = 0.5$

Table 4.2: Equivalent circuit best-fits for the dry processed and slurry cast separators.

To determine the activation energies of Li^+ mobility in the dry processed and slurry cast separators, impedance measurements were performed at 30, 60, 90, and 120 °C. The resulting ionic conductivities were plotted in the Arrhenius plots shown in Figure 4.9 and the activation energy E_a was calculated from the slope of the best-fit linear regression by manipulating [327]:

$$\sigma = Ae^{\frac{-E_a}{k_b T}} \tag{4.4}$$

to:

$$ln(\sigma) = \frac{-E_a}{k_b T} + ln(A) \tag{4.5}$$

where σ = ionic conductivity; A = pre-exponential factor; k_b = Boltzmann constant; T = absolute temperature.

In the context of ionic conductivity, E_a refers to the minimum energy needed for Li^+ ions to be mobile within the SE and contribute to conduction [328]. Activation energies of 0.297 (0.015) and 0.426 (0.019) eV were determined for the dry processed and the slurry cast separators, respectively, and are comparable to previous reports of 0.27-0.34 eV for separators of similar composition [310, 329, 330, 331]. The increased ionic conductivity of LPS at higher temperatures was attributed to temperature-dependent transitions of the Li diffusion process [332]. Although Li^+ jumps rarely occur at low temperatures, the activation of additional Li^+ diffusion pathways at higher temperatures is necessary for long-range percolation. However, as previously mentioned, the polymeric binders commonly used in SSBs are ionic insulators and can interfere with charge carrier transport [244]. Although both dry-processed and slurry-cast separators exhibited good interparticle contact, the finer distribution of non-conductive PTFE binder in the dry-processed separator may have facilitated a lower activation energy.

To examine whether there was any decomposition of LPS during processing, Figure 4.10 compares the XRD spectra of dry processed and slurry cast separators with the feedstock LPS. The as-received LPS crystal structure was largely maintained after processing by either route, and the sharp reflection peaks indicated strong crystallinity. The argyrodite crystal structure of sulphidic SEs provides low-resistance cage-like 3D conduction pathways for Li^+ ions, which is critical to achieve high conductivities [333]. There was an unidentified low-intensity peak at 26.92° in the feedstock LPS that disappeared after slurry casting and might indicate a feedstock trace additive that dissolved in p-xylene during slurry formulation.

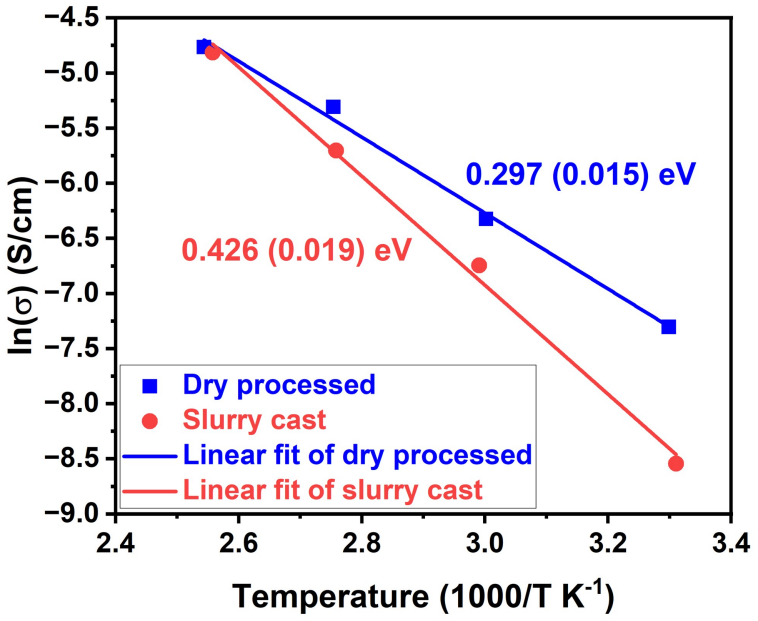

Figure 4.9: Arrhenius plots of the natural logarithm of the ionic conductivity σ as a function of inverse temperature for dry processed and slurry cast separators.

4.3.3 Impact of SE processing on critical current density

Figure 4.11 shows a series of 2D reconstructions taken from 3D XCT measurements of dry processed and slurry-cast SE pellets with an isotropic voxel size of 7.5 μm at an interval of 16 slices after hot calendering at 80 °C and 50 N/mm to a thickness of 600 μm. XCT image analysis was performed by Dr Enzo Liotti. The XCT map uses a colour scale where high voxel intensity is shown in orange, and low intensity is shown in blue. In general, both pellets were free of macropores at this resolution. However, both pellets showed long-range ($\sim$ 500 μm) variations in intensity suggestive of underlying microporosity variations, and microcracks (2 for the slurry cast pellet and 12 for the dry processed pellet). Circular cracks at the edge as arrowed in Figure 4.11(a) were attributed to mechanical punching for pellet retrieval. Microcracks might possibly be induced during punching of the pellets or manipulating the pellet onto the stub for XCT measurements, as well as enduring from the calendering step. In general, over the examination of many pellets, the qualitative impression was that dry processed

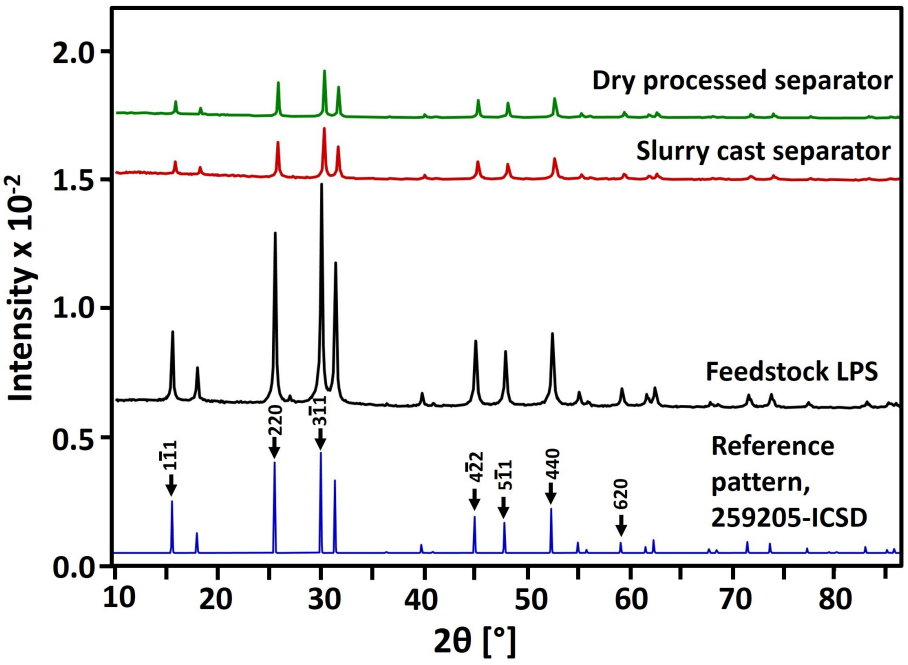

Figure 4.10: XRD spectra of as-supplied LPS, dry processed and slurry cast SSBs, and the relevant ICSD standard.

pellets showed more microcracks, even though they were more robust to handling, i.e. they may crack more easily, but the cracks did not lead to macrofailures because of the stabilising effect of the PTFE fibril web.

Using these types of pellet, gradual increases in current density in alternating directions in symmetric Li cells are commonly used to determine the CCD for cell short circuiting by Li dendrite formation [334]. Figure 4.12 shows the bidirectional CCD measurements of dry processed and slurry cast separators that were calendered to a thickness of 600 μm and a relative density of $\sim$ 83 % for reversible current densities of 0.1, 0.2, 0.5, 1, 2, and 5 mA/cm^2, applied up to a capacity of 1 mAh/cm^2. Both dry processed and slurry cast separators showed ongoing polarization effects as voltage fluctuations during periods of constant current density, as arrowed in Figures 4.12(a) and (c). The voltage fluctuations were attributed to the degradation of the Li/SE interface interface due to the formation of voids and SE spallations [334, 132]. The dry processed separator showed a sudden and sharp drop in cell voltage

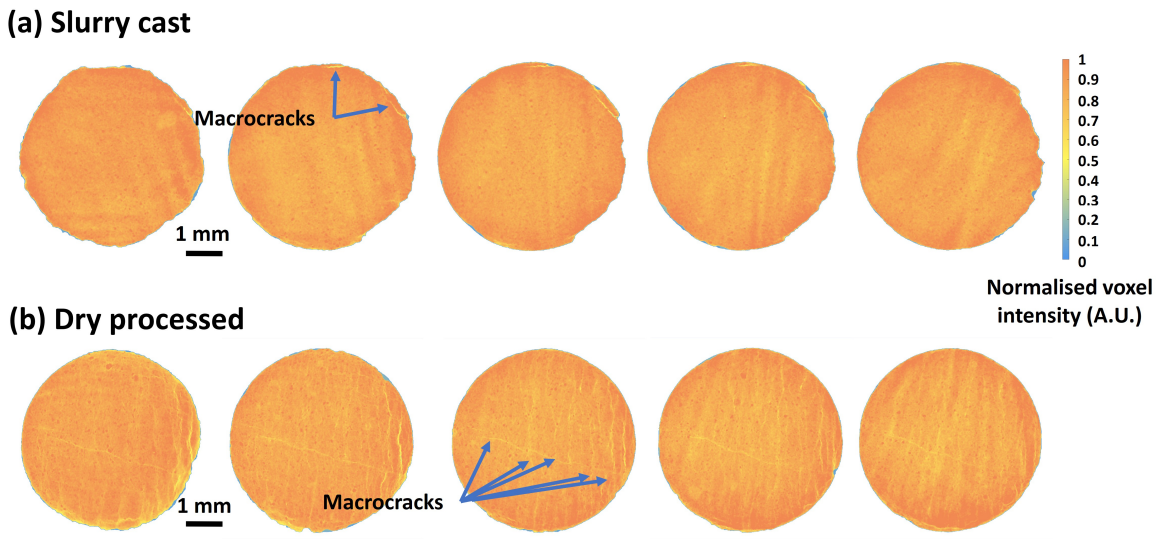

Figure 4.11: 2D slices of 3D XCT scans at different layers of (a) slurry cast and (b) dry processed separators after hot calendering.

at 1 mA/cm^2 and the slurry cast separator at 2 mA/cm^2, as arrowed in Figures 4.12(b) and (d), respectively. This drop likely indicated and was typical of SE failure by crack formation coupled with Li dendrite growth, electrically connecting the electrodes [334]. Subsequent voltage increases occurred as a result of temporary dendrite disconnection.

Figure 4.13 illustrates the types of failures exhibited in the CCD tests. Voids form above a certain stripping current because lattice vacancies are formed in Li at the Li/SE interface at a faster rate than are replenished [335, 322]. The resulting vacancy accumulation leads to void formation and increasing resistance to Li transfer. Voids in turn serve as a precursor for dendrite formation because the current focusses on the remaining contact points [336, 337, 338]. Li fills pre-existing separator cracks and macropores as charge is applied and gradually wedges open cracks until it reaches the other electrode [132]. Consequently, the greater tendency of dry processed separators to exhibit microcracks facilitated the propagation of Li dendrites, resulting in a lower CCD.

To assess the average diameter of the separator pores, cross-sectional SEM images were analysed using ImageJ software. The images were calibrated by converting pixels to micrometers using their

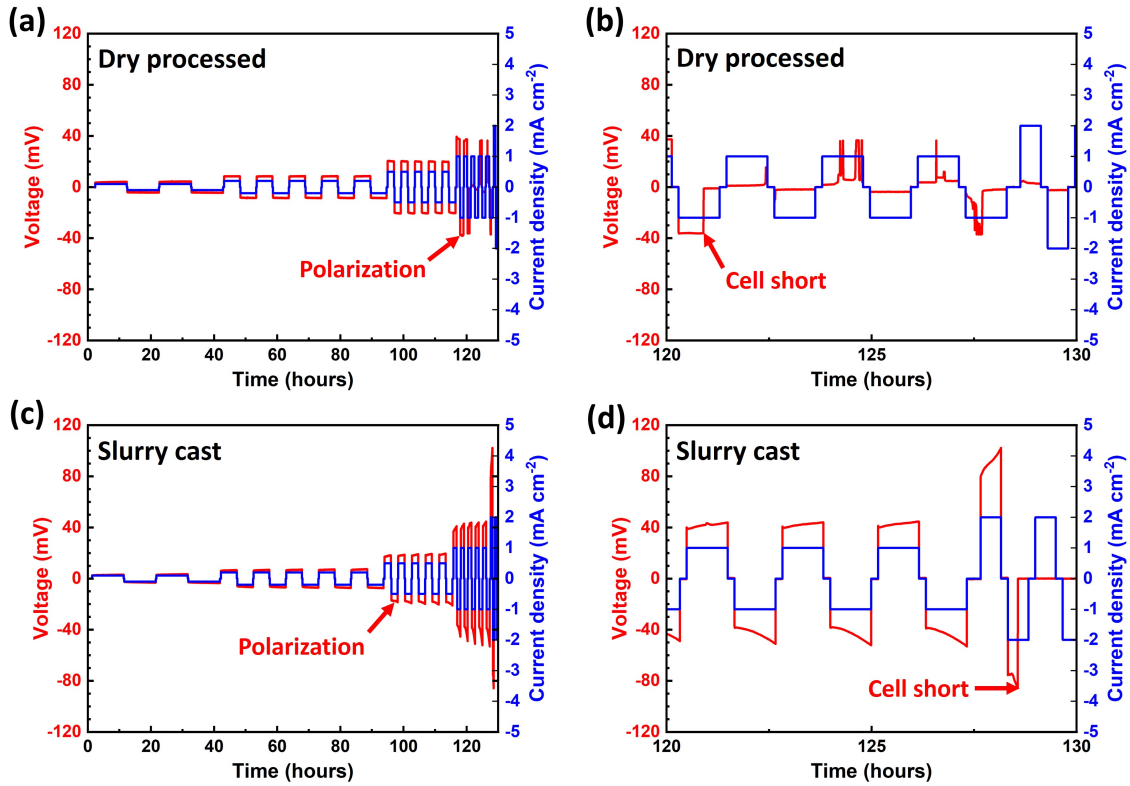

Figure 4.12: Critical current density tests symmetric cells at 60 °C and 4 MPa stack pressure at a fixed capacity of 1 mAh cm^{-2}. (a) critical current density test of dry processed separator; (b) zoomed in cycling shows a cell short of a dry processed separator; (c) critical current density test of slurry cast separator; (d) zoomed in cycling shows a cell short of a slurry cast separator.

scale bars (Analyze > Set Scale). A manual grey-level threshold was applied to segment LPS and pores based on pixel intensity values as shown in Figure 4.14 (Image > Adjust > Threshold). ImageJ calculates the pore diameter by fitting ellipses to segmented pores, measuring their major/minor axes, area, and perimeter (Analyze > Analyze Particles). Area fraction porosity measurements were taken for three separate sections of dry processed and slurry cast separators each. The average pore diameters were 0.57 μm (std dev 0.09 μm) and 0.50 μm (std dev 0.13 μm) of dry processed and slurry cast separators, respectively. Consequently, the higher CCD of slurry cast separators was attributed to the lower amount of microcracks as shown by XCT in Figure 4.11 rather than differences in pore

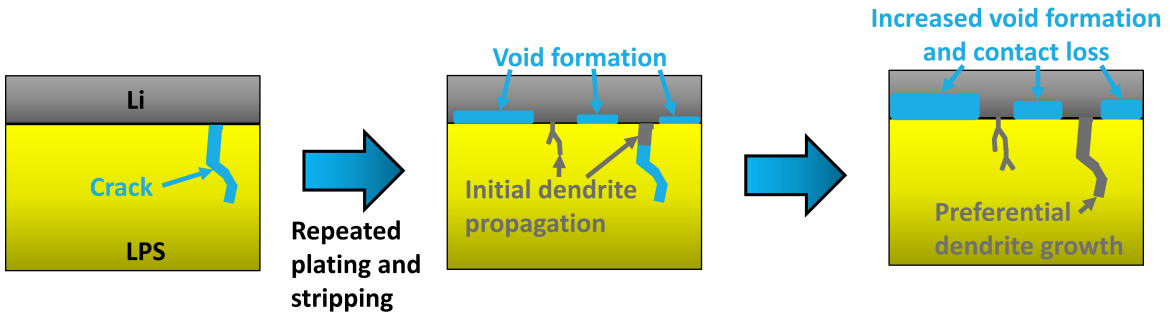

Figure 4.13: Schematic illustration of void formation at the Li/LPS interface and Li dendrite growth and propagation during cycling.

sizes. For a constant porosity fraction, small pore diameters are generally considered less detrimental to a uniform Li^+ flux than fewer large pores, and resulting in more uniform Li electrodeposition at the electrodes, and therefore a lower tendency to promote Li dendrite growth [339, 340]. Dendrites are more likely to detach within separator channels due to localised electro-(re)dissolution during cycling if the dendrite width falls below the critical thermodynamic radius of the electrodeposit (1.25 μm) [341, 342].

To improve separator resistance to Li dendrite induced crack propagation, SE toughening approaches have been suggested, and increasing the SE fracture toughness in at least some cases, has been reported to increase the CCD [343, 344]. That said, intrinsic SE property effects are likely only significant or relevant when SE extrinsic macrodefects such as pores or cracks have been minimised or eliminated. In composite systems, cracks generally have a higher tendency for deflection than penetration when the composite is comprised of dissimilar elastic materials [345]. Consequently, toughening additives in the SE might achieve crack deflection at the LPS/toughening additive interface especially if the SE were near theoretical density. This would make crack propagation more three-dimensional and convoluted, rather than planar and straight through the separator.

Although not developed significantly in this thesis, some preliminary thought is given to this idea here. Zirconia (ZrO_2) powders have been used as ceramic toughening additives to improve strength,

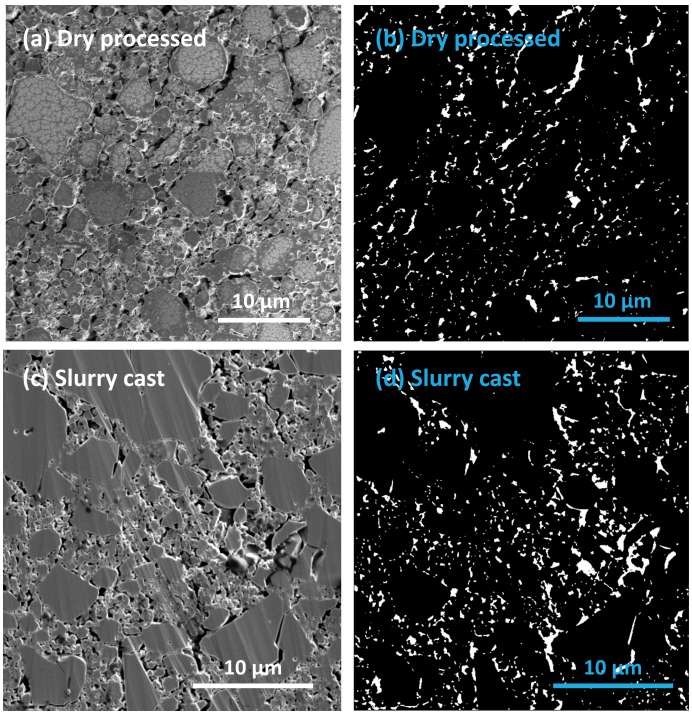

Figure 4.14: Cross-sectional SE micrographs and corresponding porosity thresholded maps of (a)/(b) dry processed and (c)/(d) slurry cast separators.

fracture toughness, or wear resistance [346, 347, 348, 349]. ZrO_2 may not be an obvious choice for adding to an SE, but has the advantage of chemical inertness and commercial availability in different morphologies of potentially useful dimensions. As an aside to the main thrust of work, to demonstrate the compatibility of SE dry processing with ZrO_2 fibres as toughening additives, LPS was mixed with 2 wt.% PTFE and 28 wt.% ZYBF-5 (10 vol.%) (Zircar Zirconia, USA) in a 40 mL ZrO_2 grinding bowl containing 55 g of 5 mm diameter ZrO_2 balls in a planetary mill (Fritsch Pulverisette 7) at 140 rpm for 30 min. The resulting mixture was then calendered at 80 °C and 50 N/mm to a thickness of 600 μm. Figure 4.15(a) shows the adhesion of ZrO_2 fibres to LPS and PTFE, illustrating the bulk cohesion of the pellet. Surprisingly, feedstock ZrO_2 fibres shown in Figure 4.15(b) did not break or crack excessively during the dry processing. Figure 4.15(c) shows a 2D slice of a 3D XCT scan of the separator pellet, demonstrating a reasonable distribution of ZrO_2 fibres within the separator. A side benefit of ZrO_2 is the density difference between ZrO_2 (5.68 g/cm^3) and LPS (1.64 g/cm^3) that allows

clear differentiation by X-ray absorption contrast in the XCT data [350, 150]. This might also suggest the potential to facilitate the traceability of crack-fibre interactions during cycling during operando-XCT studies. EDS maps shown in Figure 4.15(d) and (e) further confirmed a reasonable distribution of ZrO_2 fibres within the separator. Improving strength and fracture toughness should also improve handleability during processing and cell assembly as relevant factors for scaling up. It was hoped that micro-cantilever bend testing to assess the toughness of these composites might be undertaken but the challenging experimental conditions, such as handling under an inert atmosphere, reproducibility of measurements, or the sticking of sulphides to the micro-cantilever tip, suggested this would be far from trivial, and better pursued separately in further work.

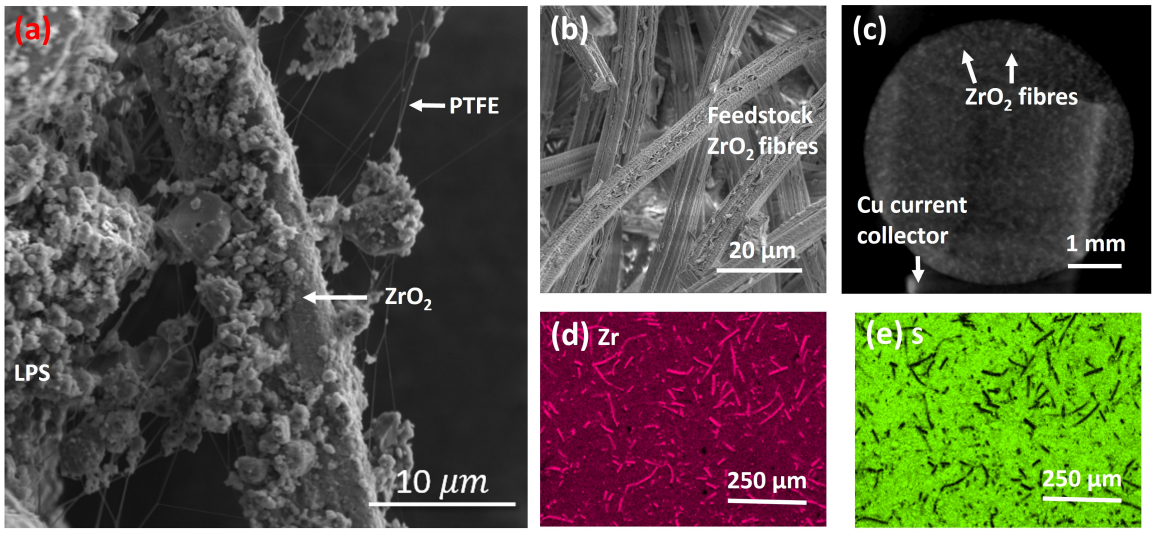

Figure 4.15: Microstructure of dry processed separator with ZrO_2 fibres as a potential toughening additive. (a) SE image of dry processed separator with ZrO_2 fibres; (b) SE image of feedstock ZrO_2 fibres; (c) 2D slice of a 3D XCT scan of dry processed LPS-based separator pellet with ZrO_2 fibres; (d) and (e) EDS map of Zr and S of a dry processed separator with ZrO_2 fibres.

4.3.4 Optimization strategies

A relative density of $> 98\%$ is generally recommended for effective SE separators and was beyond those achieved here using scalable, but transient pressurisation by calendering. It further illustrates why many academic publications use uniaxially pressed, ultra-high pressure (up to 500 MPa) pellets [351]. Although hot calendering alone may not achieve similar consolidation, it represents a highly scalable technique that allows for the regulation of SE thickness and geometry for industrial processing, but should be combined with an additional consolidation step. Additional densification can also provide healing of calendering induced defects, such as cracks, and the reduction of surface roughness, which is critical to allow defect-free cycling at low SE thicknesses. The SE also adds parasitic mass to a cell and consequently, to achieve a high energy density, the ideal thickness of the SE should be < 20 μm [352, 353].

Possible additional densification techniques for SEs are sintering or warm isostatic pressing (WIP). Sintering is known to decrease grain boundary resistance, reduce the number of voids, and thereby improve Li^+ conductivity and dendrite suppression capability. In one case, LPS was first sintered at 550 °C for 6 h and reached a conductivity of 9.58 $\times 10^{-4}$ S/cm at room temperature [354]. The sintered electrolyte was subsequently ground into powder and again sintered at 550 °C with an annealing time of 6 h, reaching an ionic conductivity of 3.19 $\times$ 10^{-3} S/cm at room temperature. Two-step sintering at 260 °C was reported to reduce LPS porosity and cause grain boundaries to disappear, which allowed a conductivity of 8.04 mS/cm at room temperature [355]. An ionic conductivity of 3.15 $\times$ 10^{-3} S/cm at room temperature was reported for LPS after sintering at 550 °C for 10 min [330]. The higher temperature resistance of PTFE ($\sim$ 260 ° C) compared with NBR ($\sim$ 120 ° C) indicates better compatibility of dry processed SEs with any subsequent relatively high temperature consolidation [356, 357].

Alternatively, WIP at 490 MPa and 80 °C achieved high densification (> 98 %) with high uniformity, and improved mechanical strength [84, 171]. WIP was applied not only to an electrode, but to an SSB *assembly* to additionally ensure good interfacial contact between the stacked cell components.

In terms of SEI formation, interlayers at the SE-electrode interface, such as Al_2O_3, can reduce SEI formation while allowing Li^+ ion transfer at the anode/separator interface [358]. Alternatively, a fine-scale graphite layer was reported to facilitate Li plating and accommodate volume changes, leading to reduced resistance and improved cycling performance [359]. Moreover, PTFE is reactive with Li metal, potentially causing unwanted side reactions that might be mitigated by protective interlayers [237]. Alternatively, Si-based anodes could be applied that have reduced side reactions with LPS during cycling or LiIn-alloy anodes that exhibit more convoluted dendrite growth compared to their Li counterparts [360, 146].

Finally, so-called "anode-free" cells - investigated in the next chapter - that make use of Ag/C interlayers in which the anode forms in situ upon charging can facilitate more stable cycling at high Coulombic efficiency [84].

4.4 Summary

Slurry casting and dry processing were applied to the fabrication of free-standing LPS-based SE sheets for SSBs using NBR and PTFE binders, respectively. Dry processing via PTFE fibrillation can offer significant environmental, safety, cost, and operational advantages. However, PTFE itself is increasingly recognised as environmentally problematic. NBR is a suitable, more environmentally sustainable binder for SE separators, but its dispersion and effect on ionic conductivity and handleability can be problematic. Upon application of shear forces, PTFE strands (ϕ 0.5 - 1 μm) branched into fibres (ϕ 0.04 - 0.09 μm), resulting in a finely distributed binder network providing mechanical stability. Impedance measurements at 60 °C showed a higher ionic conductivity of 1.45 mS/cm (std dev 0.07) of the dry processed separator compared with 1.19 mS/cm (std dev 0.03) of the slurry cast equivalent, which was attributed to a finer-scale binder distribution than NBR, and a likely easier-to-achieve Li/LPS interface contact. Both separators had average pore diameters < 1 μm and an average pore fraction of 76-84 %. Dry processed separators had a lower CCD of 1 mA/cm^2 compared with 2 mA/cm^2 for slurry cast separators under otherwise approximately similar conditions. XCT measurements showed a

higher tendency for dry processed separators to exhibit microcracks, which increased their susceptibility to Li dendrite propagation, causing earlier cell shorting during cycling. Hot calendering facilitated SE densification up to approximately 84 %, and provided for good thickness control. However, an additional, prolonged consolidation step, such as WIP, will be required to improve density and SE resistance to Li dendrite propagation for implementation in commercial SSBs.

Chapter 5

Spray printing of structured silver-carbon multilayers for anode-free all-solid-state batteries

5.1 Introduction

Li metal anodes in SSBs pose significant manufacturing challenges. Li foils (3-50 μm) fabricated by rolling are widely used in laboratory research, but are problematic due to high reactivity with air and softness that leads to sticking to fabrication tools [361, 127]. Li (1-10 μm) can be deposited by PVD, however, this process is slow and cost-intensive [10]. Electrochemical deposition using a galvanic bath can be used, but is also slow with high costs for electrolyte regeneration and disposal [362]. An SSB should also have only a small Li excess at the negative electrode (anode), and capacity balanced with the positive electrode (cathode). Therefore, the concept of plating the Li anode in situ from a Li-rich cathode on the first charge cycle could simplify battery assembly significantly, reduce material and production energy consumption, and avoid handling large-area Li foils/coatings [363, 364, 256].

Critical to the success of this "anode-free" approach is ensuring that the Li plates homogeneously at the anodic current collector on the first and subsequent charge cycles. This requires constant Li thickness over the current-collector area, with low roughness and minimum porosity. The Li layer should also form only between the current collector and the SSE separator, and nowhere else.

To promote Li layer homogeneity, a thin layer (10's of μm) of a mixture of fine Ag ($\sim$ 60 nm) and carbon black (CB, $\sim$ 35 nm) particulate has been shown to be effective by forming a lithiophilic interface that lowers Li nucleation energy, improves Li^+ ion diffusion, interfacial contact and current distribution, and protects the SE interface from degrading side-reactions with Li [84, 172, 173, 174, 175, 176]. In contrast, if Li plating/deposition is not controlled, for example, using an Ag/C layer, preferential Li deposition at defect sites and surface asperities encourages the formation of uneven Li deposition/plating, and of Li dendrites [161]. Inhomogeneous plating also leads to voids that reduce the SSE/Li contact area and so increase local current densities, further encouraging Li dendrites and premature cell failure [163, 164]. The detail of the Ag/C mechanism was described earlier in chapter 2.

Ag/C layers are generally prepared by slurry casting and require binders usually used in cathodes such as PVDF to hold the Ag/C particles together and adhere to the current collector. Although slurry casting is highly scalable, it struggles to produce uniform layers $<$ 30-40 μm. Alternatively, in previous work in the group, layer-by-layer large-area deposition of Ag/C interlayers was successfully realised by spray printing as a proof of concept [256]. Spray printing allows layer thicknesses from 5 to 100's μm. As shown in Figure 5.1, the spray printed Ag/C layer successfully reduced the Li nucleation overpotential for plating of Li on the first charge compared with an uncoated current collector. However, subsequent attempts to full-cell cycling with an NMC-based cathode led to failure on the second cycle, which was typical of inhomogeneous Li plating and stripping leading to Li dendrite growth and rapid cell failure.

The aim of the work in this chapter was to optimise a spray printed Ag/CB interlayer for improved full-cell cycling of anode-free SSBs. Amorphous rather than crystalline carbon has been reported to

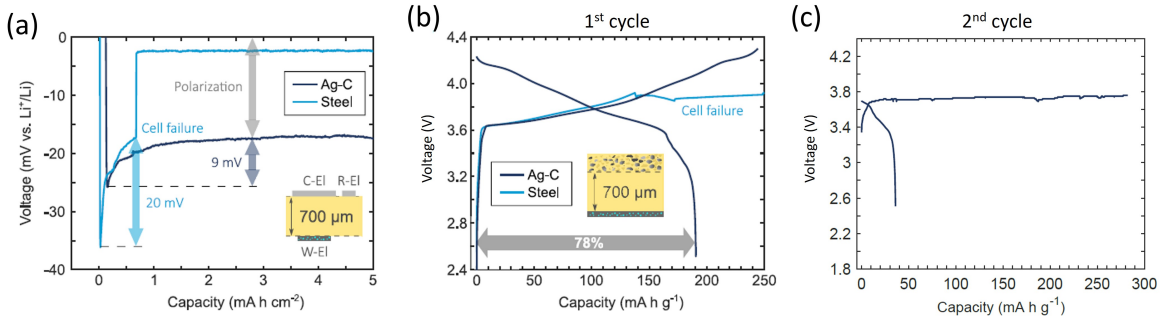

Figure 5.1: Cycling of SSB cells with spray printed Ag/graphite interlayers. (a) Voltage profiles of uncoated and coated current collector vs. a Li^+/Li counter electrode showing the Li nucleation overpotential at 60 °C; (b) First and (c) second charge/discharge cycle of a Li metal anode-free SSB using an Ag-C interlayer with an NMC-based cathode at 30 °C. Reproduced from [256].

be beneficial to promoting uniform Li plating and was used here as a potential improvement [168]. In subsequent descriptions of the experiments, Ag/C interlayers composed of Ag and CB are termed "Ag/CB interlayers". Spray printing was used to deposit composite Ag/CB interlayers on an SSB anodic current collector, without and with a concentration of the Ag particles within the layer at the anodic current collector. The hypothesis under investigation was that improved Li plating and stripping performance might be realized by more careful positioning of the Ag within the Ag/CB layer itself, and has not previously been considered. In particular, the Ag/CB interlayer was enriched with Ag particles locally, close to the current collector, to improve the homogeneity of Li plating and subsequent cell cycling. The application of laser cutting was also developed to obtain discs for cycling tests from the sprayed foils, and was critical in preserving well-adhered Ag/CB interlayers.

5.2 Experimental methods

5.2.1 Spray printing of Ag/CB interlayers

The spray printing of Ag/CB interlayers is illustrated in Figure 5.2. A solution of PVDF in a mixture of 95% isopropyl alcohol (IPA) and 5% N-methyl-2-pyrrolidone (NMP) by volume was prepared. Ag

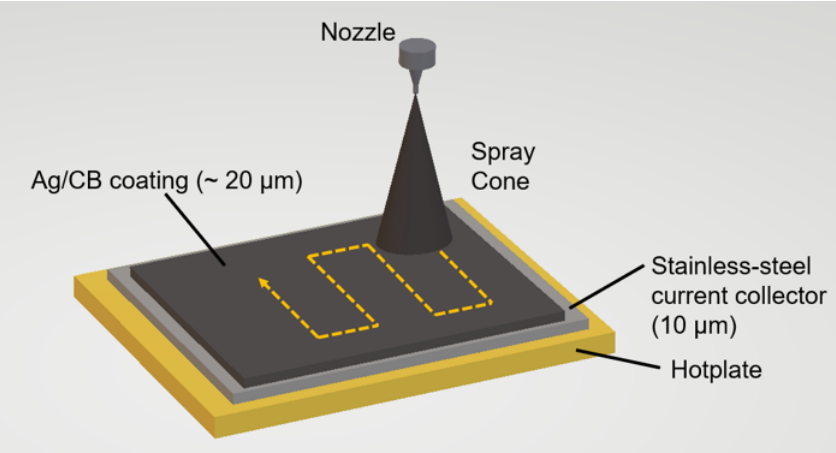

Figure 5.2: Illustration of spray printing.

nanoparticles (US Research Nanomaterials, Inc.; Ag nanopowder, 50-80 nm) and carbon black (CB Asahi Carbon Co., Ltd.; F-200GS) were suspended in this solution at a CB: Ag ratio of 3:1 by weight. The feedstock solution (277.9 mg particulate in 100 mL solvent) was stirred for at least 30 min and all suspensions were sonicated for 5 min (3 s on and 7 s off, 50% amplitude) using an ultrasonic horn sonicator (Qsonica 500) prior to spray printing. A reagent bottle containing the feedstock solution was connected to the spray printing system and the mixture continually stirred to avoid particle sedimentation. The feedstock solution was then spray printed onto a 10 μm thick stainless-steel foil that formed the anodic current collector in the subsequent solid-state cell. Spray printing was conducted inside a custom-made spray tool in an Ar-filled glovebox (M-Solv, MSV-700G). The spray process was supplemented by an integrated vision system and a non-contact laser displacement height sensor that allowed for nozzle control and dimensional monitoring.

The feedstock solution was Ar atomized in an industrial spray nozzle to create a myriad of suspension droplets that were deposited onto the heated stainless-steel foil where the solvent evaporated almost instantly and the PVDF binder thus rapidly reprecipitated to adhere the particulates to the substrate and to previously deposited layers. The metal foil was fixed by a vacuum chuck onto an Al hotplate which was kept at a constant temperature of 110 °C. One layer was formed through a zigzag motion of the spray nozzle in the x and y direction (10 mm pitch) in relation to the substrate at a

constant distance in the z direction (190 mm). The total spray area was approximately 10 × 10 cm^2 and the 20 μm thick Ag/CB interlayers were typically formed from 18 layers. The composite interlayer composed of 22.5 wt% Ag nanoparticles, 67.5 wt% CB and 10 wt% PVDF binder.

To achieve a localized Ag concentration towards the current collector for the structured variant of the Ag/CB interlayer, 87.5 wt% of the total Ag was concentrated in the lower half of the interlayer, and the remaining 12.5 wt% content deposited in the upper half in two successive spray printing configurations.

5.2.2 Laser cutting

The spray-printed Ag/CB interlayers were fixed to an Al holder plate and cut with a Needham NLase Desktop Pro laser cutter as shown in Figure 5.3(a). The device applied a Q-switched, solid state, MOPA laser that operates at a wavelength of 1064±4nm and a peak laser power > 10kW. The beam diameter was approximately 7 mm and had a beam divergence of < 2 mrad. Laser cutting enabled cleaner cutting, as shown in Figures 5.3(b) and (c) that compare discs obtained by laser cutting with the rougher edges and delamination produced by conventional mechanical punching.

5.2.3 High-resolution transmission electron microscopy (HRTEM)

CB particles were dispersed in IPA and drop cast directly onto C-coated Cu grids. HRTEM analysis was performed using a Jeol 2100 TEM (LaB6 source) at an accelerating voltage of 200 kV to characterize the crystallinity of the CB particles. Imaging was undertaken by Dr Guillaume Matthews with the author present.

5.2.4 Laser diffractometry

To measure nanoparticle size distribution, feedstock Ag and CB were dispersed in IPA. Measurements were conducted at 15 °C by Dr Kerstin Jurkschat with the author present using a NanoSight Nano Tracking Analysis laser diffraction analyzer with a Blue405 laser and an sCMOS camera capturing at

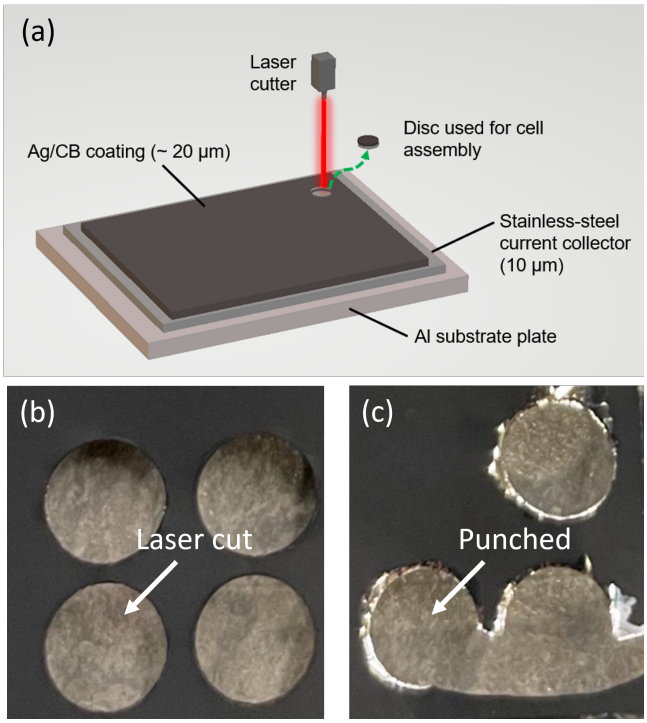

Figure 5.3: (a) Illustration of laser cutting. Comparison of Ag/CB interlayers on stainless steel foil obtained by (b) laser cutting that allowed cutting without tearing and delamination, and (c) mechanical punching.

25 frames per second. NTA 3.4 Build 3.4.4 software was used to obtain particle size distribution data.

5.3 Results and discussion

5.3.1 Interlayer characterization

The feedstock Ag and CB particle size distributions in suspension obtained by laser diffraction are shown in Figures 5.4(a) and (b) with approximately log-normal distributions and mean diameters of $\sim$ 60 nm and $\sim$ 80 nm respectively. Figure 5.4(c) shows that feedstock Ag particles readily formed $>$ 1 μm agglomerates in the dried condition. These agglomerates proved difficult to break up and were retained into the Ag/CB interlayers shown in Figure 5.6.

HRTEM and XRD of the CB particulates in Figure 5.5 suggested a predominantly amorphous

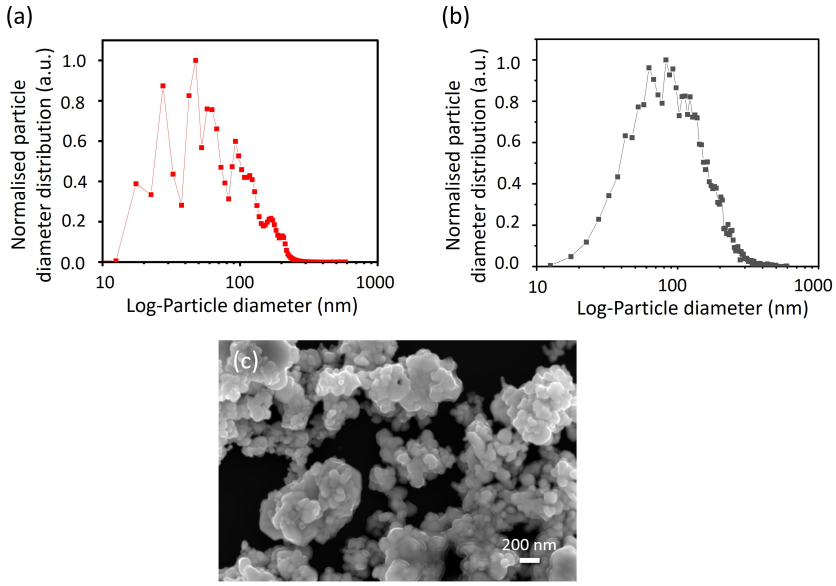

Figure 5.4: Analysis of the Ag and CB feedstock powders. Normalized particle size distribution obtained by laser diffraction in suspension of (a) Ag and (b) CB; and (c) SEM image of the as-supplied Ag powder.

structure with crystalline sub-domains. Figure 5.5(a) shows a high magnification SEM image of the pristine CB powder also with a strong tendency to agglomerate. Figure 5.5(b) shows an HRTEM image of the CB agglomerates and Figure 5.5(c) shows a corresponding diffraction pattern comprising blurred rings suggesting the CB was largely amorphous, and consistent with previous reports [365, 366]. Figure 5.5(d) shows the XRD spectrum from the CB particulates with a broad underlying peak again suggesting a predominantly amorphous structure, but also with superimposed broad peaks at approximately 24.0° and 43.3°, which were ascribed to (002) and (101) planes of disordered carbon (JCPDS card No. 34-0567, DOI: 10.1002/adfm.201604356). This may indicate a turbostratic carbon structure comprising a largely amorphous "matrix" with fine-scale regions of crystalline carbon [367].

Figure 5.6 shows backscattered electron (BSE) images of the cross-section of as-manufactured (a) unstructured and (b) structured Ag/CB interlayers after uniaxial compression at 500 MPa. BSE and EDS measurements were performed by Dr Guillaume Matthews with the author directing the investigation. Interlayer thickness after compression was ~ 13 μm. Interlayers were free of large pores

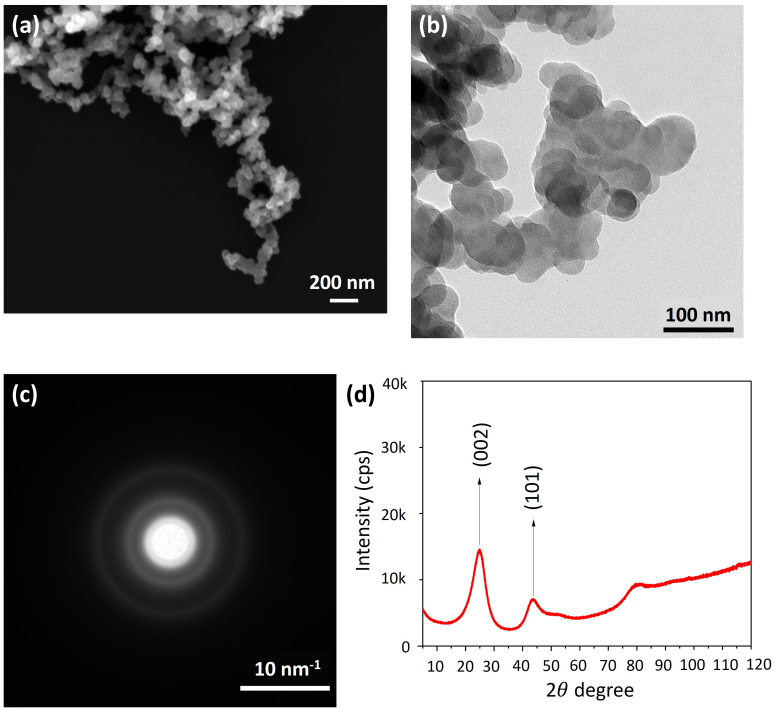

Figure 5.5: The microstructure of pristine CB. (a) SEM, and (b) HRTEM images; (c) corresponding HRTEM diffraction pattern: (d) XRD spectrum of CB.

or delamination, and as intended, there was a marked difference in Ag distribution. Figure 5.6 (c) and (d) show corresponding Ag (green) and C (blue) EDS maps, indicating an approximately uniform distribution of 2-4 μm Ag agglomerates and smaller particles in the unstructured interlayer, and a $\sim$ 5 μm thick Ag-rich sub-layer against the current collector.

To quantify differences in the Ag distribution in the Ag/CB interlayers, the cumulative Ag area fraction of the BSE backscattered electron images shown in Figure 5.7 was measured along the vertical, through-thickness direction. The local Ag fraction was obtained by Dr Enzo Liotti by segmenting the Ag particles within the BSE images by global intensity thresholding (Otsu's method) and cumulatively summing the segmented area, line by line of pixels through the interlayer, followed by normalisation by the total Ag area. The spatial distribution of Ag in the structured interlayer shown in Figure 5.7(a) illustrates the successful Ag concentration towards the current collector compared with the unstructured interlayer shown in Figure 5.7(b).

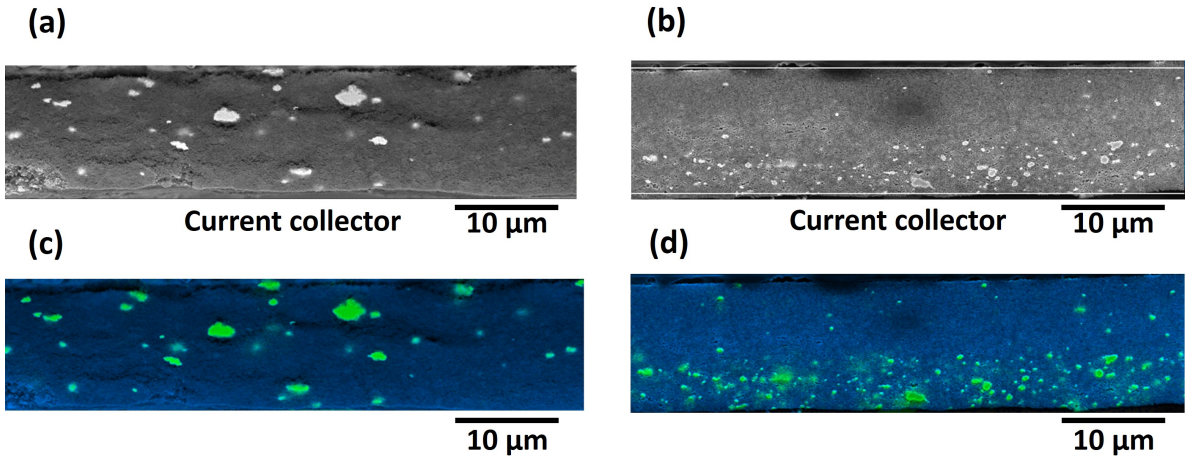

Figure 5.6: BSE cross-section images of the spray printed (a) unstructured and (b) structured Ag/CB interlayers after uni-axial compression at 500 MPa; corresponding superimposed Ag and C EDS maps of the (c) unstructured and (d) structured interlayers. Green: Ag, Blue: C.

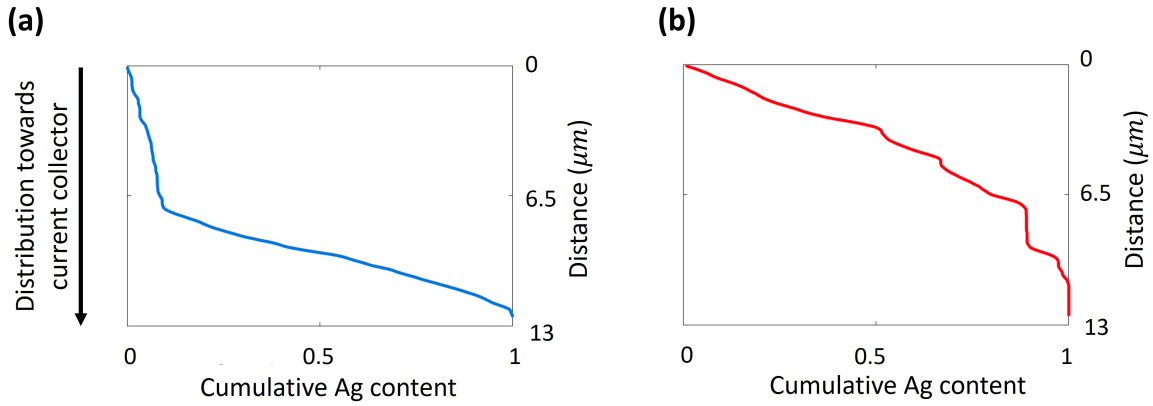

Figure 5.7: Spatial distribution analysis of Ag particles in (a) structured and (b) unstructured Ag/CB interlayers after uniaxial cold pressing at 500 MPa.

5.3.2 Electrochemical characterization

To explore the effect of Ag/CB interlayers on Li nucleation overpotential, three-electrode cells with different anodic current collector arrangements were charged at 1 mA/cm^2 up to a capacity of 1 mAh/cm^2: stainless steel only, and three cells each with unstructured and structured Ag/CB interlay-

ers. Figure 5.8(a) shows a comparison of the voltage versus Li^+/Li counter electrode as a function of time for the first charge cycle. The sharp minima were the instant of the first deposition of metallic Li [368]. Bare stainless steel required the highest overpotential magnitude to initiate plating, with both unstructured and structured Ag/CB arrangements requiring approximately 13 mV less overpotential, consistent with catalysed Li nucleation [369, 370, 160].

Figure 5.8(b) shows the first cell charge/discharge cycle between 2.5 and 4.3 V at a charge/discharge current of 1 mA/cm^2, using unstructured and structured Ag/CB interlayers. Full cells comprised the Ag/CB interlayer, an LPS SSE separator, and a composite cathode consisting of a mixture of NMC811, LPS, and carbon nanofibers, at an overall mass fraction ratio of 75:22:3, and were cycled at 60 ° C under a uniaxial stack pressure of 4 MPa. For the unstructured interlayer, the initial cathode discharge capacity was 172 mAh/g, which was comparable with 166 mAh/g for similar arrangements [171]. For the structured interlayer, the capacity increased to 198 mAh/g, and the initial coulombic efficiency (CE) increased from 72% to 83%. Figures 5.8(c) and (d) show the subsequent cycling stability at 1 mA/cm^2 for the two cell types. Both arrangements showed a typical reduction in cathode capacity, but no catastrophic failure. Both arrangements had a CE >99% after 100 cycles. Unlike the first charge cycling data, the long-term cycling behaviour revealed differences between the interlayers, with the structured arrangement having improved charge and discharge capacity retention at 100 cycles, up from 27% to 39% and from 37% to 47% respectively. Figure 5.8(e) shows the reproducibility of Ag/CB structuring on charge capacity for the first three cycles, and showing capacity differences between the arrangements were more significant than inevitable cell-to-cell variations. Figure 5.8(f) shows similar plots for discharge capacity with a more distinct improvement conferred by the structured interlayers.

To explore resolvable nucleation potential differences between unstructured and structured interlayers, Figures 5.9(a) and (b) compare the voltage versus Li^+/Li at the counter electrode as a function of time for the first charge cycle of three-electrode cells at charge currents of 1 mA/cm^2 and 0.5 mA/cm^2 respectively, up to a capacity of 1 mAh/cm^2. While structured and unstructured interlayers significantly lowered the overpotential magnitude to initiate plating, there was no reproducible overpotential

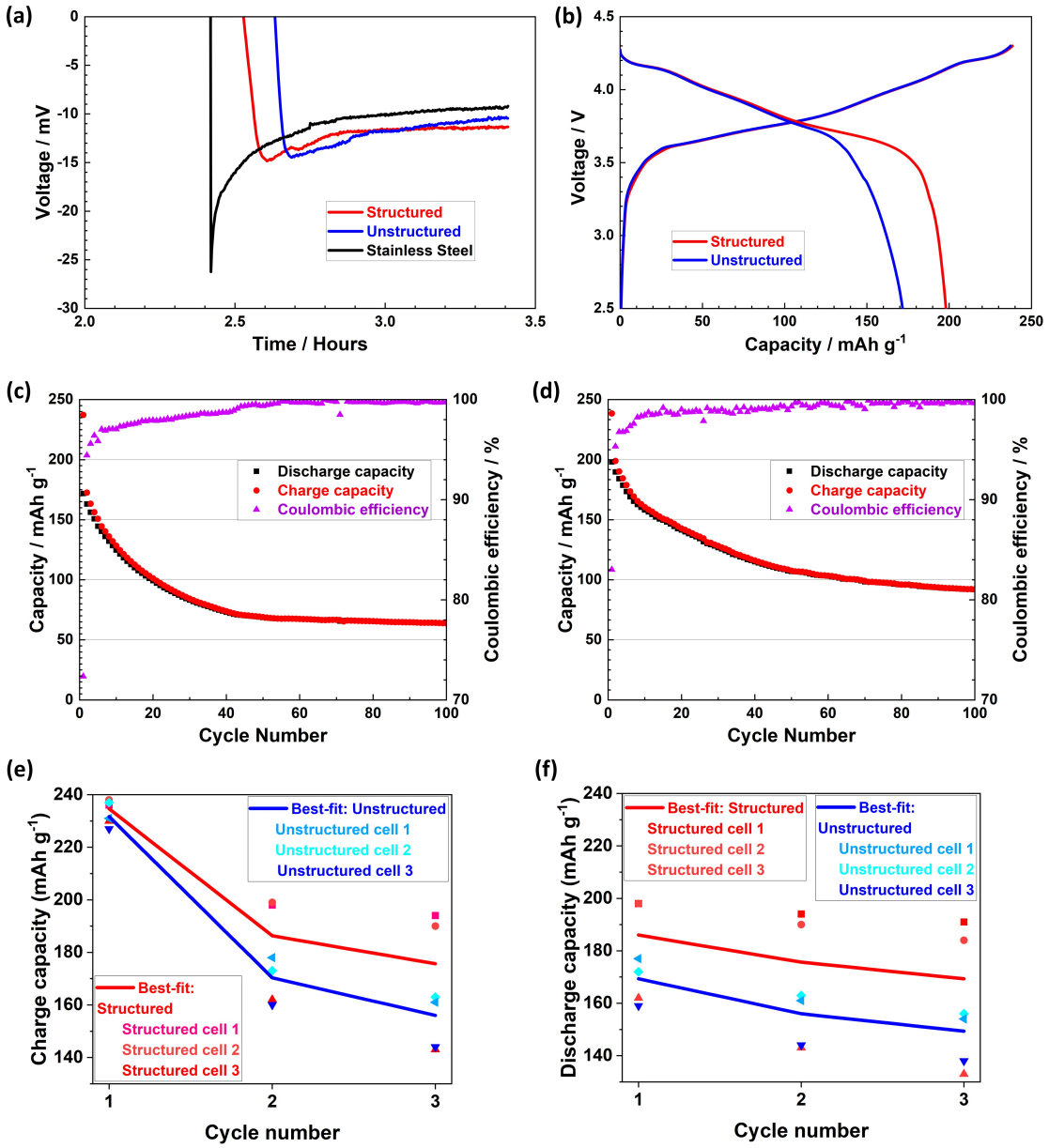

Figure 5.8: Cycling of SSB cells with Ag/CB interlayers at 60 °C and 4 MPa stack pressure. (a) Voltage/time during single-charge tests of three-electrode cells with and without Ag/CB interlayers at 1 mA/cm^2; (b) Voltage/capacity during the first charge/discharge cycle of full-cells with unstructured and structured Ag/CB interlayers at 1 mA/cm^2 charge/discharge current; Long-term full-cell cycling stability with an (c) unstructured and (d) structured Ag/CB interlayer at 1 mA/cm^2 charge/discharge current; averaged (e) charge and (f) discharge capacities for three full-cells with structured and unstructured Ag/CB interlayers each.

difference.

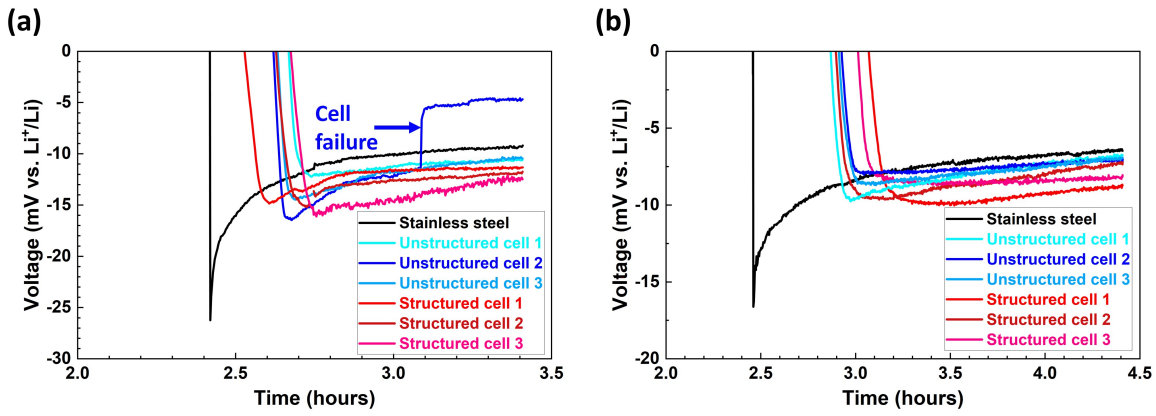

Figure 5.9: Single-charging of three-electrode cells using a stainless-steel current collector and structured and unstructured Ag/CB interlayers at (a) 1 mA/cm^2 and (b) 0.5 mA/cm^2, to a capacity of 1 mAh/cm^2.

Figure 5.10 shows the Ag/CB interlayer effect at a lower discharge current density of 0.2 mA/cm^2 and a stack pressure of 20 MPa. Again, the structured interlayer provided an improvement in retained charge capacity from 40% to 45%, although the effect was less marked.

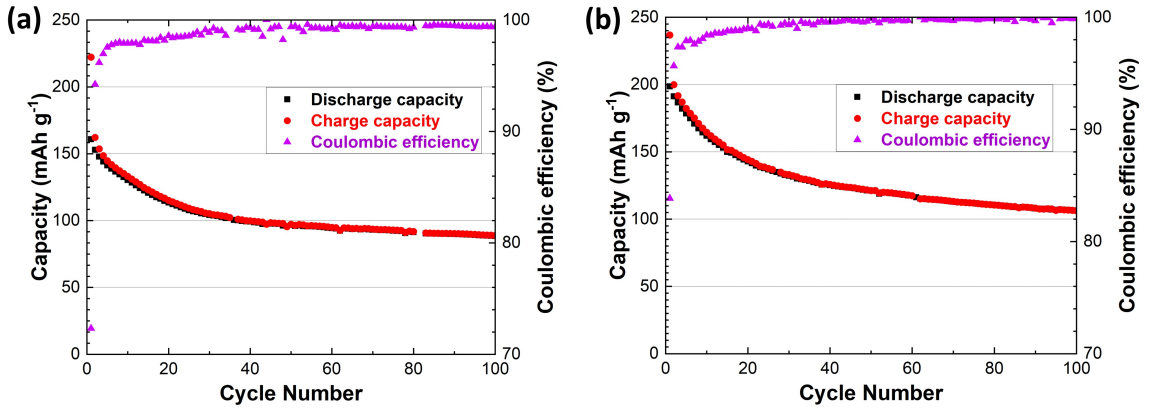

Figure 5.10: Cycling of full-cell setup at 1 mA/cm^2 charge rate 0.2 mA/cm^2 discharge rate at a stack pressure of 20 MPa of (a) unstructured and (b) structured Ag/CB interlayer.

To compare the impedance evolution of structured and unstructured interlayers, impedance analysis of full cells after charge/discharge cycling at 1/0.5 mA/cm^2 and 4 MPa and after 1, 5, and 10 cycles is shown in the Nyquist plots in Figure 5.11(a). A frequency range of 10 mHz – 10 kHz with a nominal AC voltage of 10 mV was applied. The best-fit to the structured interlayer first cycle data using a typical equivalent circuit model, shown in the plot as an inset, is shown in Figure 5.11(b). The data revealed an ionic conductivity of $\sim$ 5 mS/cm for both cells and no resolvable difference between the Ag/CB arrangements or in their impedance evolution up to 10 cycles.

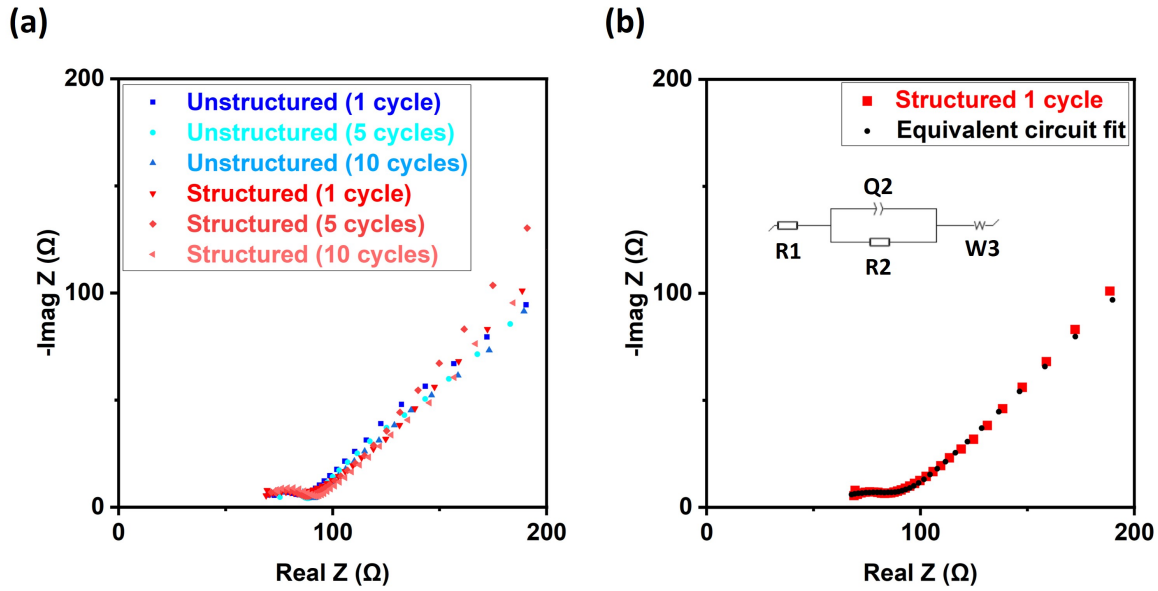

Figure 5.11: (a) Nyquist plots of structured and unstructured interlayers after 1, 5, and 10 cycles; (b) equivalent circuit fit to the structured interlayer after 1 cycle. R1 = 53.5 Ω, R2 = 40.5 Ω, Q2 = 0.7 × 10^{-3} F.s$^{(\alpha-1)}$.

To analyse the effect of the structured arrangement on rate capability, full cells were cycled at current densities of 1 mA/cm^2 and 2 mA/cm^2 for 5 cycles, respectively, at a stack pressure of 2 MPa as shown in Figure 5.12(a). Increased current density resulted in faster capacity degradation and cell failure occurred when the current density was increased further to a demanding 3 mA/cm^2 for both structured and unstructured interlayers. Figures 5.12(b) and (c) compare the voltage versus Li$^+$/Li

at the counter electrode as a function of time for the first charge cycle of hot-pressed three-electrode cells at charge currents of 2.5, 3, and 3.5 mA/cm^2 respectively, up to a capacity of 5 mAh/cm^2. Stable charging of structured and unstructured interlayers took place at 2.5 mA/cm^2. The unstructured interlayer displayed a more unstable charging curve at 3 mA/cm^2 and cell failure occurred for both interlayer arrangements at 3.5 mA/cm^2.

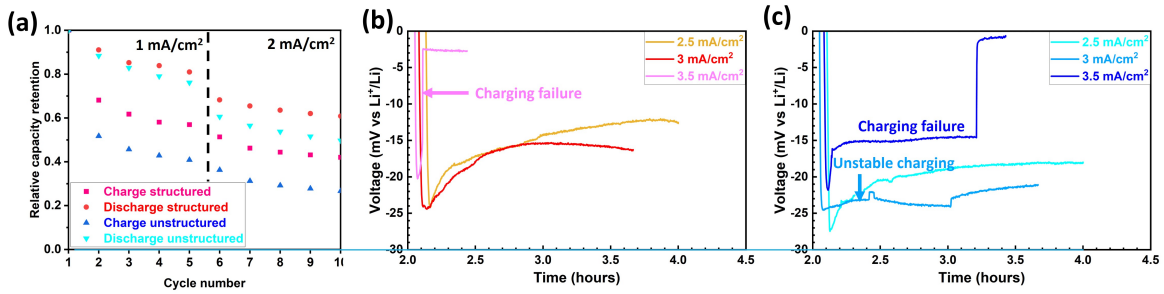

Figure 5.12: Rate capability tests of (a) full-cell setup at 1 and 2 mA/cm^2 charge and discharge rate at a stack pressure of 2 MPa of unstructured and structured Ag/CB interlayers; (b) rate capability test of structured three-electrode cells; (c) rate capability test of unstructured three-electrode cells.

For completeness, Figure 5.13 shows the inability of the uncoated stainless-steel current collector to provide any recognisable cycling response.

5.3.3 Characterisation of the plated anode

To understand the physical role of the Ag/CB interlayer, three-electrode cells for P-FIB microscopy were assembled via uniaxial hot pressing at 500 MPa and 200 °C and charged to a capacity of 5 mAh/cm^2 at 60 °C at a uniaxial stack pressure of 4 MPa. The P-FIB SIMS measurements were carried out by Dr Yige Sun with the author directing the investigation. Figure 5.14(a) shows a secondary electron (SE) image of a FIB cross-section of a disassembled cell, taken from the region of the structured Ag/CB interlayer on the stainless steel current collector after a single plating cycle at a very high current density of 2.5 mA/cm^2. There was an approximately 20 μm thick layer between the current collector (top of image), and the Ag/CB and the LPS separator (bottom of image). EDS

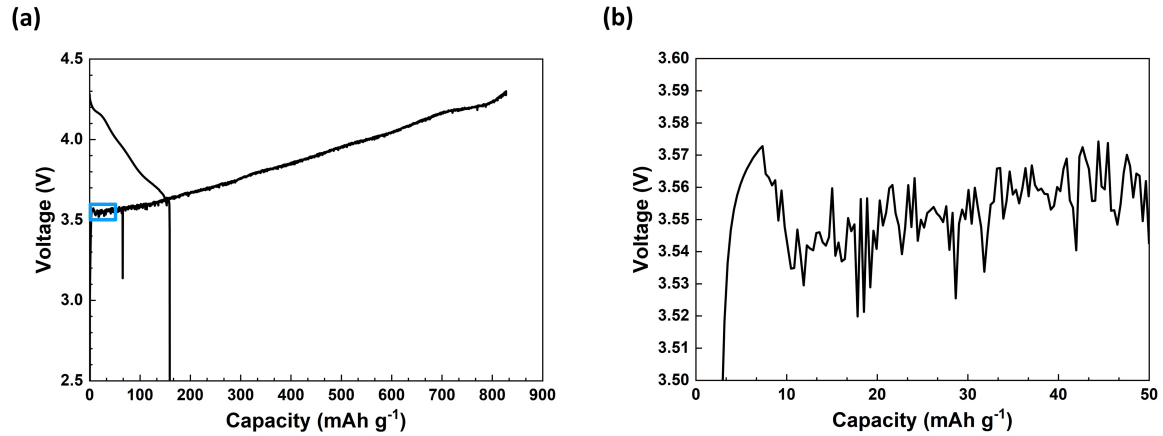

Figure 5.13: (a) Full-cell cycling test using an uncoated stainless-steel current collector at a charge rate of 1 mA/cm^2, discharge rate of 0.5 mA/cm^2, and stack pressure of 20 MPa; and (b) zoomed in region of the blue box in (a), showing signs of significant instability.

maps for S, C, Ag, and Fe in Figures 5.14(b) to (e) unambiguously identify the stainless steel current collector (Fe-rich), LPS separator (S-rich), and the Ag/CB layer (C, Ag-rich). Figures 5.14(g) to (i) show a similar sequence of inter-linked SEM image, C-EDS map, and Fe-EDS map from the anode region using an unstructured Ag/CB interlayer. Now, the new layer formed predominantly between the Ag/CB interlayer and the LPS separator, which can be expected to increase contact loss and impair cycling behavior as previously shown in Figure 5.8 [177, 178, 179, 180, 181].

EDS mapping cannot unambiguously identify the new layer in Figure 5.14 as Li because of the low X-ray energy of Li, the resulting low probability of X-ray emission and the high likelihood of Li X-ray absorption [371, 372]. This makes Li generally unresolvable by EDS. Therefore, SIMS was applied to the same region of interest in the same instrument. In SIMS, a charged and focused primary ion beam bombards the sample surface, sputtering secondary ions from the top few atomic layers that are analyzed on the basis of their mass-to-charge ratio in a mass spectrometer. SIMS can resolve light elements such as Li, but the signal intensity for a particular ionic species is not solely influenced by its local concentration but also by other factors such as material crystallography (known as the matrix

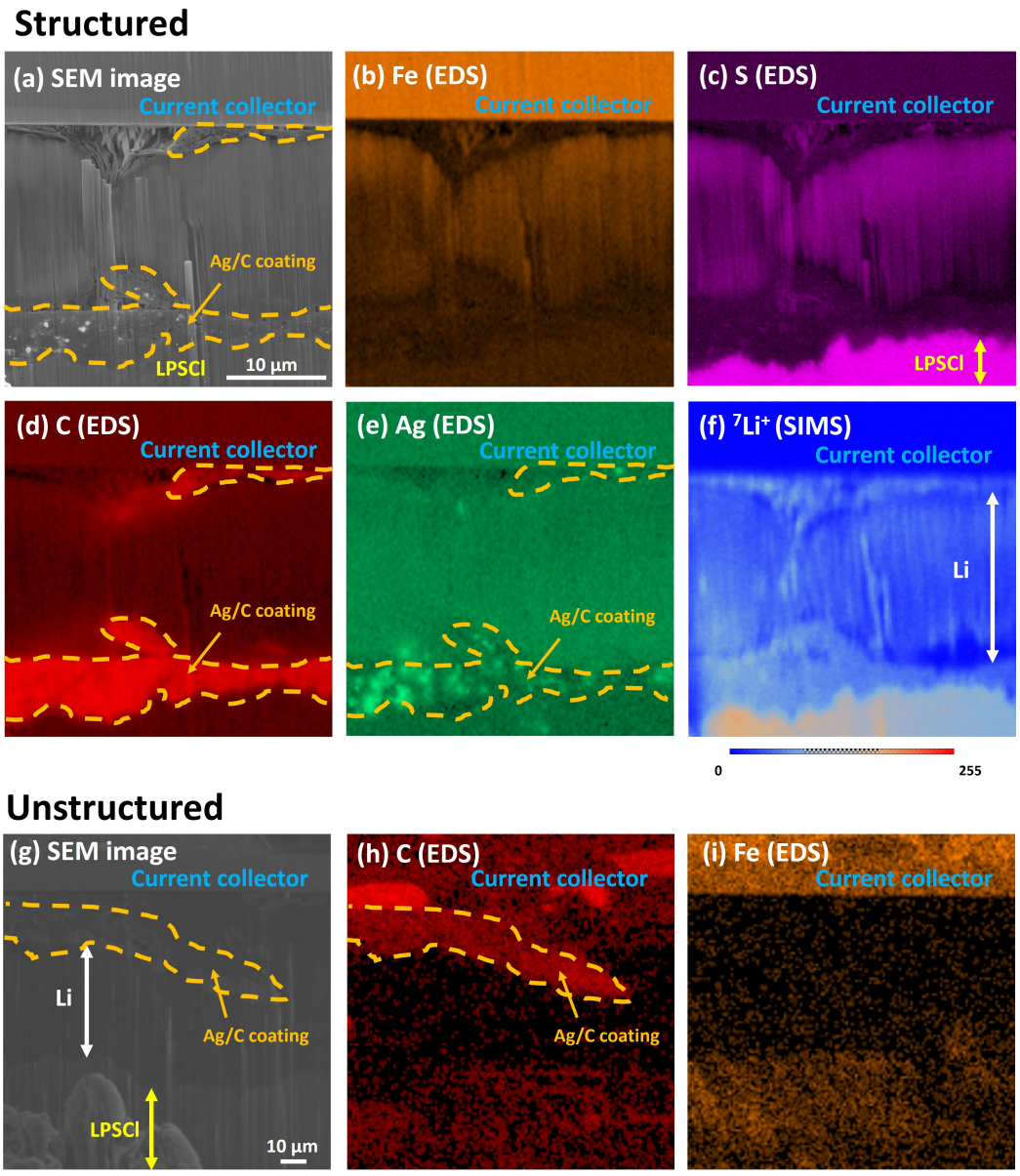

Figure 5.14: A cross-section of the stainless steel current collector, deposited layer, Ag/CB interlayer and LPS separator region for a single charge at 2.5 mA/cm^2. (a) SE image of the structured Ag/CB; (b) to (e) EDS maps of S, C, Ag, and Fe respectively; (f) $^{7}Li^{+}$ SIMS map; (g) SEM image of the unstructured Ag/CB interlayer; (h) and (i) EDS maps of C and Fe respectively.

effect), surface topography, etc [373, 374, 375]. Notably, this effect can lead to Li intensity appearing higher for Li-containing compounds (such as LPS) than for metallic Li [376, 377]. Figure 5.14(f) shows the Li^+ map obtained by SIMS from the same region in Figure 5.14(a), with the new layer adjacent to the current collector showing a strong Li signal with intensity sensitive to surface topography induced by the Xe^+ milling. There was also a strong Li^+ signal from the LPS separator. The Li^+ map uses a colour scale where a high pixel intensity is shown in red, and low intensity is shown in blue.

To assess if the Li signal from the layer could be consistent with metallic Li only, and not another Li containing material, the relative intensities of the Li^+ signal under the same SIMS imaging conditions were compared with a specially constructed Li foil/LPS couple reference, as shown in Figure 5.15. A piece of high-purity Li was pressed uniaxially onto a dense LPS pellet at 500 MPa at room temperature to form a Li/LPS bilayer reference for SIMS analysis. The Li:LPS intensity ratio for the couple was 38:100 and similar to 36:100 for the nominally Li layer and LPS separator in the sectioned cell, confirming the presence of plated Li. The significant drop in Li/LPS signal intensity ratio for the Ag/CB region in the plated cell relative to the adjacent Li-containing sections indicated a low concentration of Li in CB-rich parts of the interlayer. This suggested that the Ag/CB interlayer functioned principally as a catalyst for Li plating rather than storing (by intercalation) significant Li concentrations itself.

To further validate Li deposition, the deposited layer at the anode from a single-charged cell at 1 mA/cm^2 with a structured Ag/CB interlayer was investigated by XPS. Figure 5.16 shows the XPS spectrum and peak position summary. Noting the difficulty in physically uncovering the layer while avoiding oxidation, the strongest intensity peak was due to oxidized Li metal. The strong oxidised Li signal and no other significant candidate peaks were again highly suggestive of Li metal plating. Overall, combining electrochemical, EDS, SIMS, and XPS investigations, the 20 μm layer in Figure 12 can confidently be ascribed to metallic Li plated on the first cell charge. However, a trace amount of Ag may have been distributed into the Li-plated layer.

The expected plated Li thickness after charging was estimated as follows:

Transferred material per area = (applied charge of 2.5 mA/cm^2 for 2 hours)/(theoretical capacity

of Li: 3482 mAh/g) = 0.001436 g/cm^2

The diameter of Ag/CB working electrode of 2 mm had an area of 0.03141 cm^2.

Therefore, the transferred mass of Li = 0.001436 g/cm^2 × 0.03141 cm^2 = 4.51 × 10^{-5} g

Volume = transferred mass (4.51 × 10^{-5} g)/density of Li (0.534 g/cm^3) = 8.44792 × 10^{-5} cm^3

Theoretical thickness of the Li layer = volume/area ≈ 27 μm

Figures 5.17(a) and (e) show SE images of the Li deposition via structured/unstructured interlayers, respectively, after a single plating cycle at a current density of 2.5 mA/cm^2 for 2h at a wider field of view than listed in Figure 5.14. In all P-FIB investigations of the anodic current collector, it was difficult to maintain compression of the interlayer, and some delamination during milling was likely. This is a typical challenge for all ion battery electrode cross-sections. Figures 5.17(b) to (d) show EDS maps of Fe, Ag, and C, respectively, for the unstructured interlayer, indicating a tendency for Ag/CB interlayer retention on the current collector, rather than displacement of the interlayer and

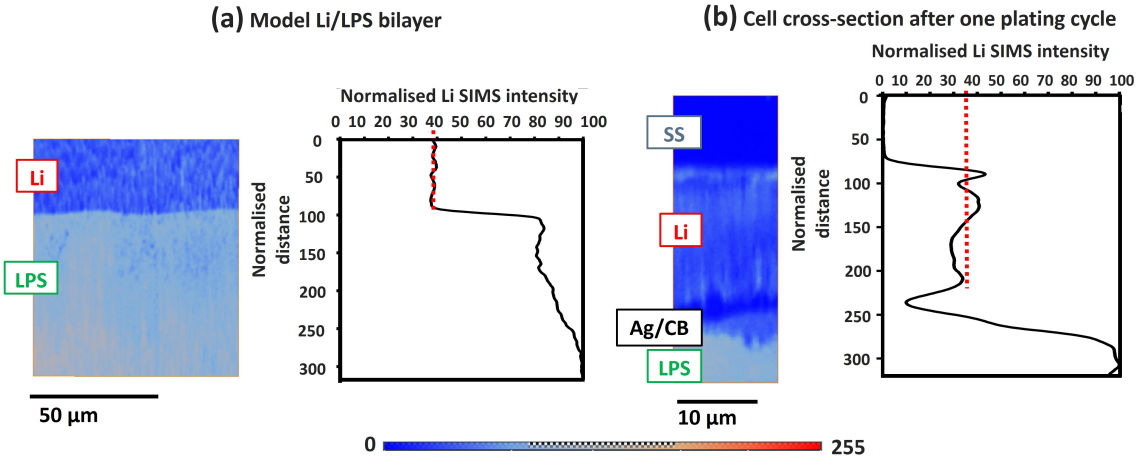

Figure 5.15: Cross-section Li SIMS maps of (a) the model Li/LPS reference bilayer, and (b) the anodic current collector region of a cell with a structured Ag/CB interlayer after one plating cycle at 2.5 mA/cm^2. In each case the Li SIMS intensity from the LPS region was set to 100 and the Li SIMS intensity from other regions scaled accordingly. The green dotted line indicates the intensity in (a) Li foil and (b) the nominal Li plated layer.

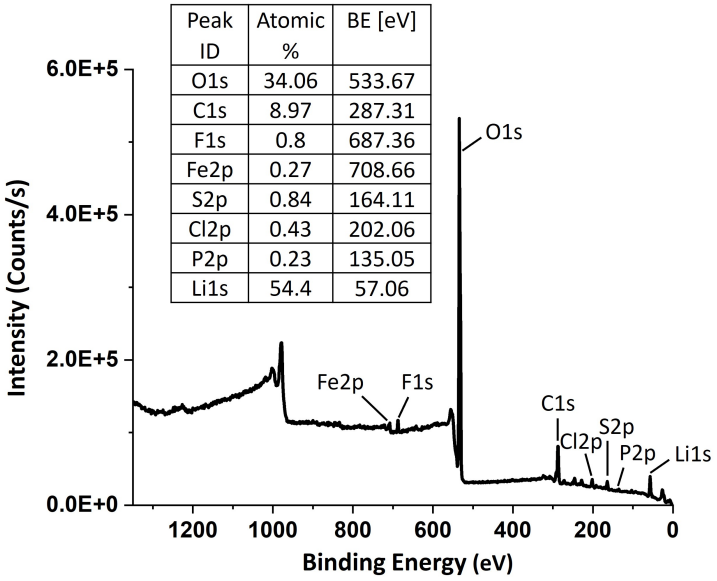

Figure 5.16: XPS spectrum and peak table of the layer deposited at the anode after one cycle at 1 mA/cm^2. The detected signals were attributed as follows: O – oxidized Li; C – interlayer, oxidized Li; P, S, and Cl - solid electrolyte; Li – solid electrolyte and oxidised Li at the anode; F - PVDF binder in interlayer, and Fe - current collector.

consistent Li plating predominantly on the current collector. Figures 5.17(f) to (h) show EDS maps of Fe, Ag, and C, respectively, for Li plated via a structured interlayer compared with an unstructured interlayer. Compared with an unstructured interlayer, there was an increased tendency of the Ag/CB interlayer to displace towards the separator and more consistent plating of the Li directly onto the current collector. While there were local variations in the plated Li thickness (20-25 μm), the plated Li thickness was approximately similar to the estimated thickness of 27 μm.

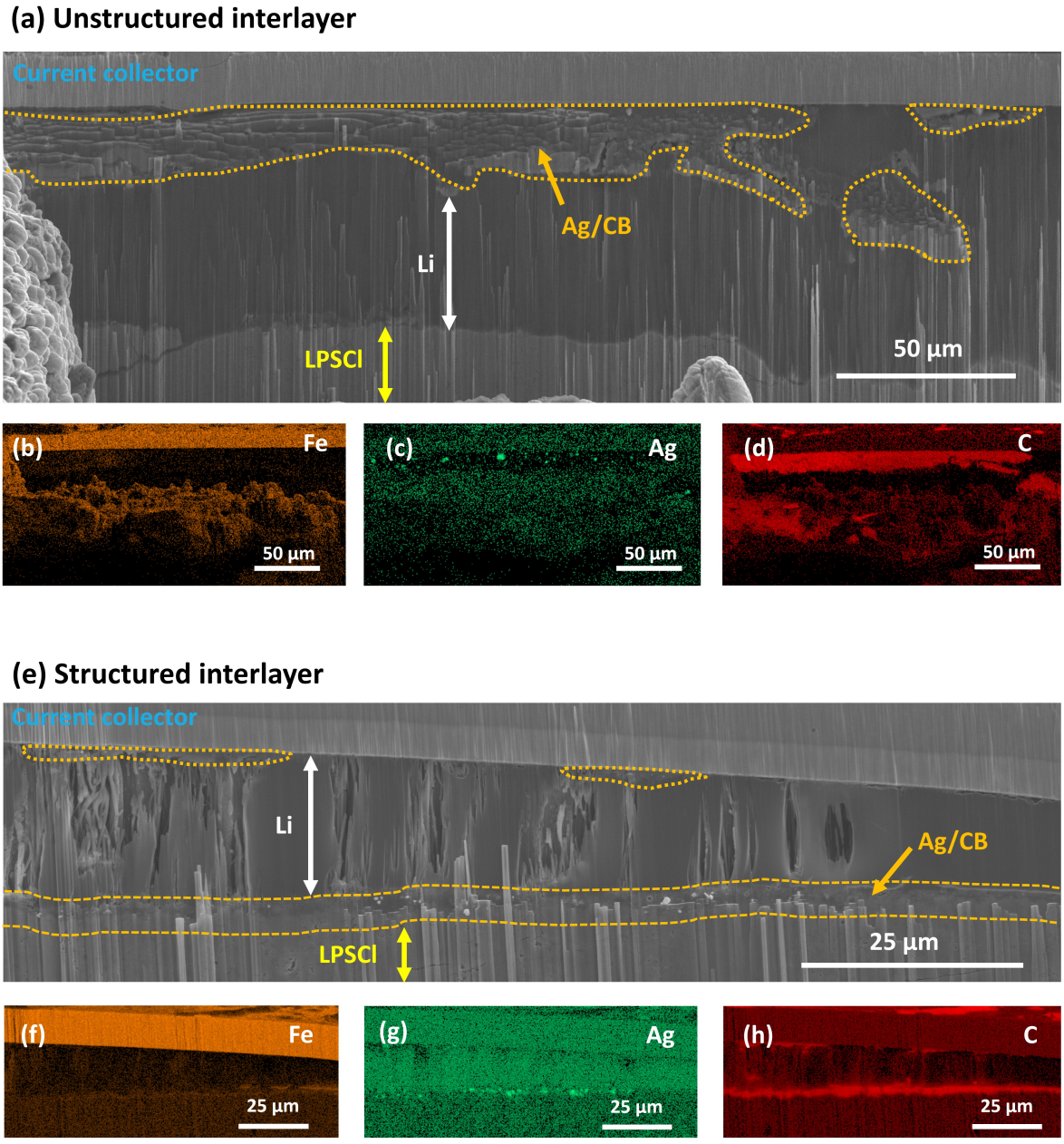

Figure 5.17: A cross-section of the stainless steel current collector, plated Li layer, Ag/CB interlayer and LPS separator region for a single charge at 2.5 mA/cm^2. (a) SE image of the unstructured Ag/CB arrangement; (b) to (d) corresponding EDS maps for Fe, Ag, and C respectively; (e) SEM image of the structured Ag/CB arrangement; (f) to (h) corresponding EDS maps for Fe, Ag, and C respectively.

To account for reproducibility, Figure 5.18 shows an SE image and corresponding Fe, Ag, and C EDS maps of another three-electrode cell with a structured interlayer after a single plating cycle at a slightly lower current density of 2 mA/cm^2 for 2.5 h, again showing an approximately 20 μm Li layer plated onto the current collector.

Figure 5.19(a) summarises schematically the suggested effect of concentrating the Ag particles in the Ag/CB interlayer at the current collector. Initially, regardless of Ag location, Li^+ ions are intercalated into the CB [189]. As the CB becomes saturated, metallic Li is formed on the Ag particles due to their catalyzing effect in reducing the nucleation potential. There will be a tendency to form the Li close to the current collector, providing the required nucleation overpotential is not too high. For the case

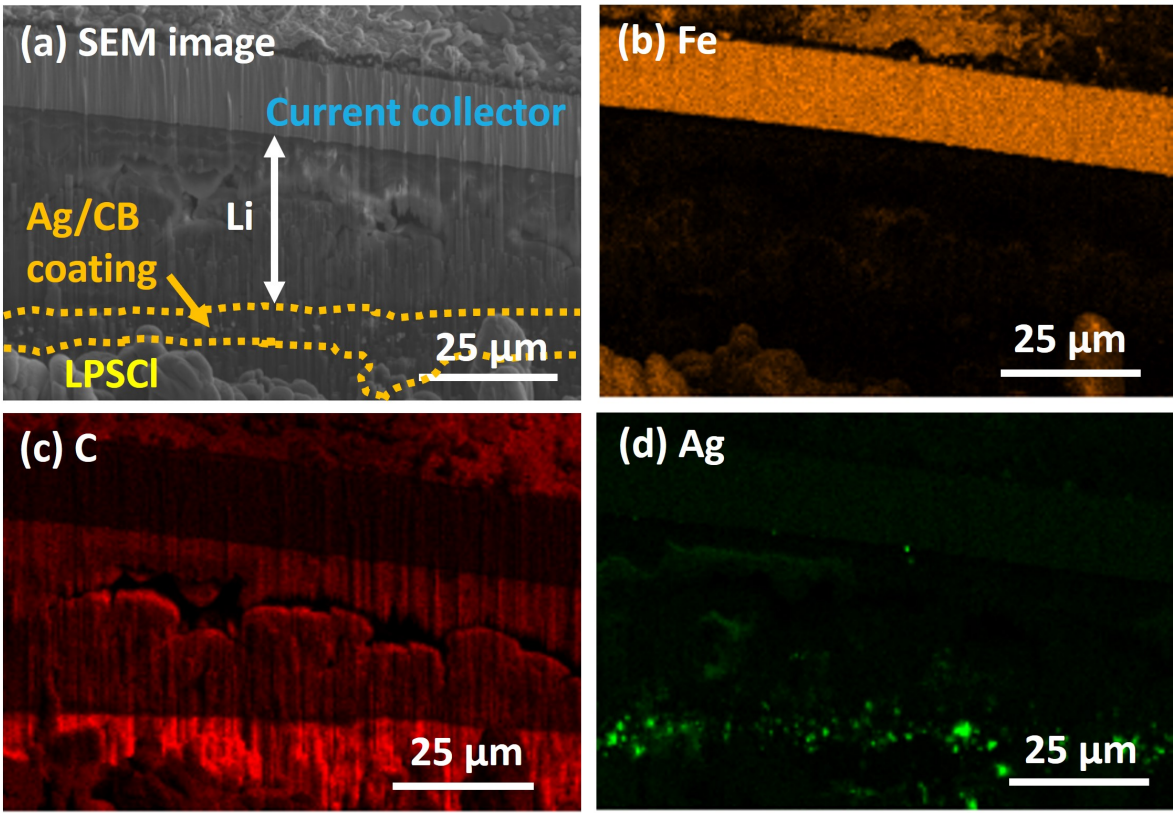

Figure 5.18: A cross-section of the stainless steel current collector, deposited layer, structured Ag/CB interlayer and LPS separator region for a single charge at 2 mA/cm^2. (a) SE image of the structured Ag/CB; (b) to (d) corresponding EDS maps for Fe, C, and Ag respectively.

of Ag enrichment at the current collector, the forming Li metal on the current collector progressively "pushes" the interlayer away from the current collector. For the unstructured interlayer, metallic Li again forms but is more distributed within the interlayer, as well as on the current collector, albeit with less uniformity. On subsequent cycling and as Li is removed, there is an increased tendency for isolated or "dead" regions of Li far and electrically disconnected from the current collector to develop, leading to capacity fade and reduction in round trip efficiency [135]. The cooperative physical rearrangement of the structured Ag/CB interlayer is likely facilitated by the compliant nature of the "spongy" porous CB-rich region [185, 186, 187]. The interlayer also helpfully forms a phyiscal barrier that prevents the forming Li during plating from touching the LPS separator and thus making the nucleation of Li at separator surface flaws or surface breaking cracks to form dendrites shown in Figure 5.19(b) less likely [169, 182, 183, 184].

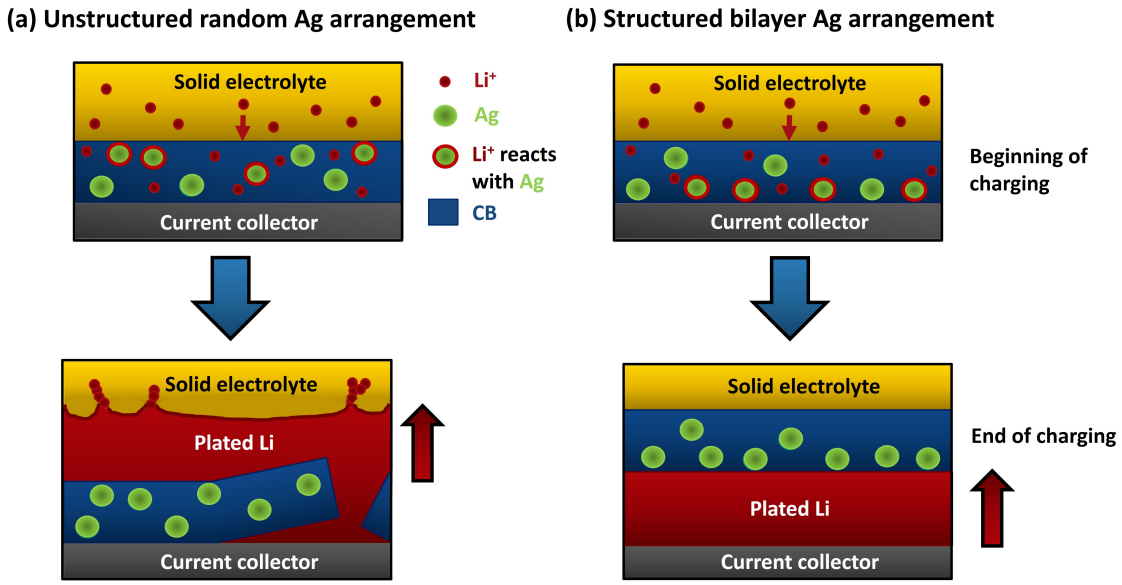

Figure 5.19: Schematic and idealised illustration of the Li plating mechanism upon charging for different Ag/CB interlayer arrangements. Plating mechanism for (a) unstructured and (b) structured Ag/CB interlayers.

5.4 Summary

A thin (< 20 μm) Ag/CB interlayer with an increased Ag concentration towards the current collector was fabricated successfully using spray printing. Although there was some unavoidable Ag agglomeration, both structured and unstructured Ag/CB interlayers facilitated metallic Li formation on the first charge cycle at reduced overpotential. On subsequent cycling, the structured Ag bilayer arrangement was superior and delivered an initial discharge capacity of > 190 mAh/g and slower capacity degradation during cycling, at a high CE of $> 98\%$ after 100 cycles. The formation of a Li plated layer and the displacement of the Ag/CB interlayer itself was identified unambiguously by a combination of SEM, SIMS, EDS and XPS. This work suggests that there remain opportunities for design optimization of interlayers to deliver improvements in SSB cell performance. Spray printing is a flexible platform to explore a wide range of interlayer designs with micro-scale composition control. Laser cutting was established as a scalable and effective technique to process deposited Ag/CB interlayers while avoiding the tearing and delamination associated with mechanical punching.

Chapter 6

Alternative silver-carbon nanocomposite interlayers

6.1 Introduction

The previous chapter showed that although increasing the Ag concentration towards the current collector in an Ag/CB interlayer using spray printing facilitated Li plating and improved SSB cell performance, several processing challenges persist. Ag nanoparticles (NPs) tended to agglomerate into micrometer-sized clusters despite ultra-sonication prior to spray printing, likely lowering their effective surface area and ability to catalyse Li plating. Although nanostructured materials provide high specific catalytic surface area, NPs also represent a safety hazard during processing requiring closed environment procedures [378, 379, 380, 381]. Therefore, two alternative approaches to generating an interlayer with high Ag specific area are explored in this chapter. A further objective was to consider manufacturing processes with the potential, like spray printing, to be scaled to a more commercial-like application. The approaches are: (1) chemical staining of a pre-deposited carboxymethyl cellulose (CMC)/CB composite coating with $AgNO_3$ solution followed by in situ precipitation of Ag NPs, and (2) sputtering a thin layer of Ag onto a commercially supplied pre-coated thin, high surface area C

particulate layer.

Previous work has shown that Ag NPs can be precipitated on polymer coated C particles by exposing the polymer first to an $AgNO_3$ solution, and then by carbonisation at 350 °C and then 600 °C [183]. However, the high temperature step limits the potential of this approach for SSB interlayers. Instead, and to avoid high temperature processing, a novel approach was developed here, based on the staining, using an aqueous $AgNO_3$ solution of a thin pre-coated layer of CMC binder (commonly used in LIB graphite-based anodes) onto CB particulate. This is followed by a chemical reduction step to form metallic Ag. The Ag staining approach was originally developed by the group to stain electrode binders such as CMC so they could be more easily imaged in the electron microscope, and was modified and repurposed here for Ag/CB interlayers.

CMC is readily dispersed in water and offers environmental benefits compared to fluorinated binders such as PVDF, which as previously described in chapter 5, has been commonly used to help cohere/adhere integral Ag/C interlayers, but requires organic solvents such as NMP [84, 382]. As an aqueous slurry with CB and graphite, CMC forms a few nanometer thick, continuous layer on the CB particles. This becomes the binder in the final, dried electrode but also acts as a surfactant for dispersing the CB while the slurry is still wet. The surfactant stabilised slurry can be readily applied by slot die casting or doctor blade as a uniform coating to a current collector and dried. Here, on subsequent exposure to aqueous $AgNO_3$ solution, the Ag^+ ions selectively bind to the CMC. Following washing and drying, the adsorbed ions undergo an autolytic redox reaction with the carboxylate functional groups of CMC, leading to the formation of Ag NPs according to:

$$HCOOH + 2H_2O \rightleftharpoons CO_2(g) + 2e^- + 2H_3O^+ \tag{6.1}$$

$$Ag^+ + e^- \rightleftharpoons Ag^0 \tag{6.2}$$

$$CMC - COO^-(Ag^+) \rightarrow CMC + Ag^0 \downarrow + CO_2 \uparrow (g) \tag{6.3}$$

The autolytic redox reaction relies on the difference in standard reduction potentials U^0 of the metal ions (Ag^+ with U^0 = 0.799 vs. NHE) and the polymer functional groups (COO^- with U^0 = -0.610 vs.

NHE for the CO_2/HCOOH redox pair) [383, 384]. Nonetheless, the reaction to form the Ag NPs can occur slowly, and may be facilitated by adding a secondary reducing agent such as citric acid ($C_6H_8O_7$) (CA) [385].

6.2 Precipitation of Ag NPs on a CB particulate/polymer composite layer

6.2.1 Experimental methods

Given the likely importance of Ag surface area on the ability to facilitate homogeneous Li plating, the dependence of Ag NP size and distribution on CMC:CB and CA:CMC ratio was first studied. Interlayers for microscopy were prepared via doctor blade slurry casting on stainless steel, with the different slurry compositions listed in Table 6.1. Slurry casting was used to prepare the CB/CMC-based interlayers because of its ease of preparation in early experiments. Later, spray printing was used as it allowed for greater microsctructural consistency and reproducibility, and was applied to form the CB/CMC-based interlayers used in electrochemical tests.

First, 3 wt.% aqueous CMC with 10 wt.% aqueous CA monohydrate solution were mixed in a Thinky planetary mixer at 500 rpm for 5 min, followed by mixing with the same CB as used in the previous chapter at 2000 rpm for 10 min, and then dilution of the slurry with 3 g of water at 2000 rpm for 10 min. Then, the slurry was doctor blade cast on a 10 μm thick stainless-steel current collector to a thickness of 60 µm and dried at room temperature. The dried interlayers were submerged in a 0.5 M $AgNO_3$-solution for 3 min and then washed with deionised H_2O. Finally, the interlayers were dried at 50 °C for 15 min and annealed at 120 °C overnight in an attempt to promote and complete reactions to form the Ag NPs.

Interlayers for assembling into cells for electrochemical testing were prepared by first mixing 3 wt.% aqueous CMC with 10 wt.% aqueous CA monohydrate solution, followed by mixing with CB at the same conditions as above, and diluting the slurry with 150 mL of water. All suspensions were stirred

Target interlayer composition	Slurry formulation (+ 3 g H_2O)
C 1 - CA/CMC 0.01; CMC/CB 0.2	CMC (3 %): 3 g; CA (10 %): 0.0981 g; CB: 0.45 g
C 2 - CA/CMC 0.2; CMC/CB 0.2	CMC (3 %): 3 g; CA (10 %): 0.1962 g; CB: 0.45 g
C 3 - CA/CMC 0.01; CMC/CB 1.5	CMC (3 %): 3 g; CA (10 %): 0.0971 g; CB: 0.06 g
C 4 - CA/CMC 0.2; CMC/CB 1.5	CMC (3 %): 3 g; CA (10 %): 0.1962 g; CB: 0.06 g
C 5 - CA/CMC 0.105; CMC/CB 0.85	CMC (3 %): 3 g; CA (10 %): 0.103 g; CB: 0.1059 g

Table 6.1: Summary of the CMC-based interlayers with different CA:CMC:CB composition for microscopy.

with an IKA overhead stirrer at 1500 rpm for at least 60 min prior to spray printing. A reagent bottle containing the feedstock solution was connected to the spray printing system and the mixture was continuously stirred during spray printing to avoid CB sedimentation. The feedstock solution was spray printed onto a 10 μm thick stainless-steel foil that formed the anodic current collector in the subsequent solid-state cell. The total spray area was approximately 10 cm $\times$ 10 cm. Spray printing was performed in an ambient atmosphere fume hood with a custom-made spray tool (LG Motion). The metal foil was fixed by a vacuum chuck on an Al hotplate which was kept at a constant temperature of 110 °C. The process route is illustrated in Figure 6.1.

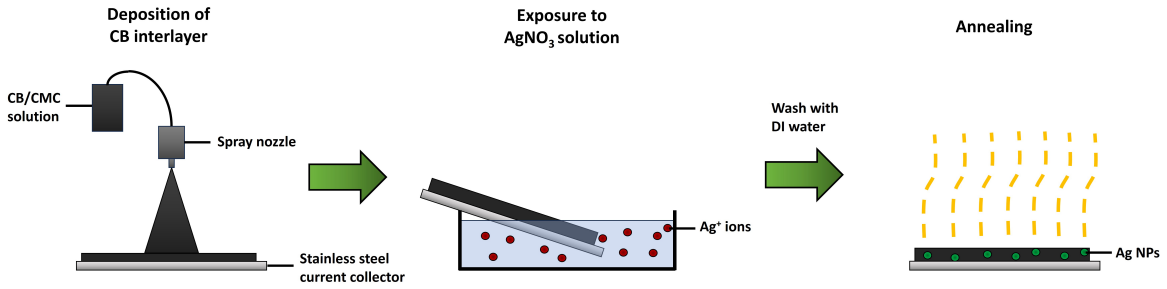

Figure 6.1: Schematic illustration of the process for forming CMC-based Ag/CB interlayers.

Table 6.2 lists the composition of spray printed CMC-based Ag/CB interlayers used for electrochemical investigations, along with a qualitative explanation for the differing fractions.

Approach	Interlayer composition
Relatively high CMC fraction to promote a relatively high final Ag fraction	94 mg CB, 150 wt.% CMC, 313 mg CA. Stained in $AgNO_3$
Reduced CMC fraction to lower insulation induced polarisation	190 mg CB, 20 wt.% CMC, 80 mg CA. Stained in $AgNO_3$
Reduced overall thickness, and relatively low CMC fraction	94 mg CB, 10 wt.% CMC, 20.5 mg CA. Stained in $AgNO_3$
Preformed Ag particles used to isolate effect the of CMC only on the interlayer rather than in-situ precipitation	94 mg CB, 31 mg Ag, 10 wt.% CMC
Minimise CMC fraction	94 mg CB, 31 mg Ag, 3 wt.% CMC

Table 6.2: Summary of the approaches taken to exploring CMC-based interlayers with different compositions for electrochemical performance tests.

6.2.2 Results and discussion

Microstructural characterisation

Figure 6.2 shows secondary electron and energy-selective backscattered (EsB) images of CMC-based interlayers with the CMC:CB and CA:CMC ratios listed in Table 6.1. The images were also analysed on the basis of their contrast via manual thresholding with ImageJ software to estimate the Ag NP diameters, and these are given in Table 6.3. SE and EsB imaging and particle size analysis were performed by Dr Stanislaw Zankowski with the author directing the investigation.

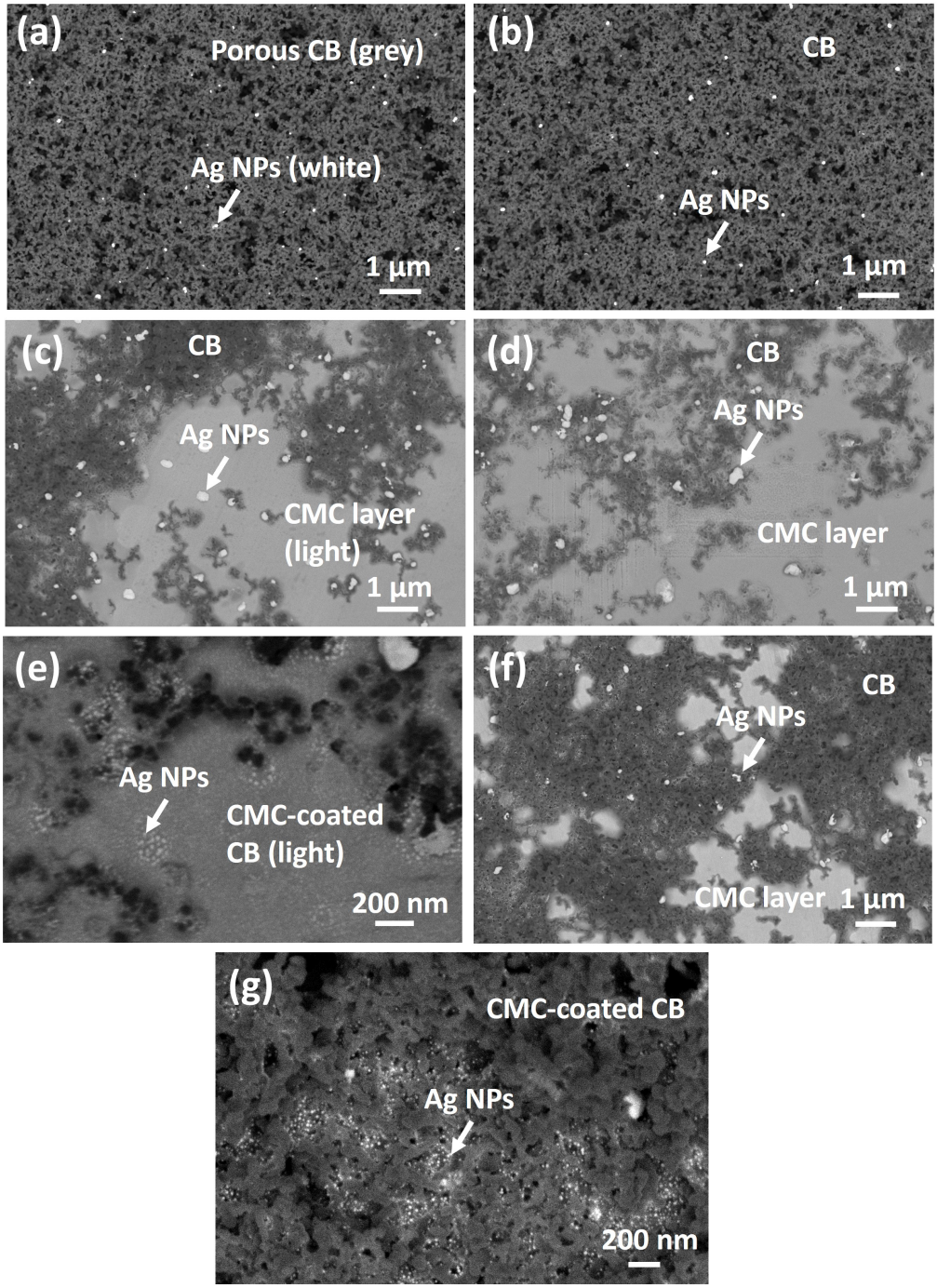

Figure 6.2: Secondary electron and EsB images of CMC-based Ag/CB interlayers. (a) C 1; (b) C 2; (c) C 3; (d) C 4; (e) C 4 at higher magnification; (f) C 5; (g) C 5 at higher magnification.

Sample	Average Ag NP diameter	Std dev	min	max
C 1	56	40	8	171
C 2	57	47	8	168
C 3	144	74	32	338
C 3: in CMC binder	N/A	N/A	N/A	N/A
C 4	143	124	32	570
C 4: in CMC binder	7	7.6	1	80
C 5	152	58	33	281
C 5: in CMC binder	12	11	4	80

Table 6.3: Comparison of the distribution of Ag NP diameters as a function of CA:CMC:CB interlayer composition. All numbers are in nm.

At a relatively low CMC:CB ratio (C 1 and C 2 = 0.2), the interlayer was comprised predominantly of CB and pores, as shown in Figures 6.2(a) and (b). To assess the porosity of C 1 and C 2, SEM images were analysed using ImageJ software by applying a grey-level threshold to segment Ag/CB regions from pores, with examples as shown in Figure 6.3. Area fraction porosity measurements were taken from three separate sections. The average porosities were 13.6 % (std dev 2.1 %) and 13.3 % (std dev 2.7 %) for C 1 and C 2, respectively. At a higher CMC:CB ratio (C 3 and C 4 = 1.5) in Figures 6.2(c) and (d), there was now a near-continuous CMC-based layer. For these cases, earlier results (not shown) established that CA was needed for the formation of Ag NPs from the silverized CMC. An intermediate (0.105) and higher (0.2) CA:CMC ratio promoted the formation of fine (< 10 nm) Ag NPs, as long as the CMC fraction was > 0.85 (C 4 and C 5, Figures 6.2(d) and (e)). If the CMC content was relatively low, < 0.85 (C 1 and C 2), the effect of CA fraction on Ag NP formation was negligible, with NPs having an average diameter of (~ 50 nm and a broad distribution (see Table 6.3). For CMC fractions > 0.85, Ag 'nuggets' (~ 150 nm) formed (C 3, C 4, and C 5), and might be due to merging of Ag NPs during annealing, even at the relatively low temperature of 120 °C on

account of their very high surface area to volume ratio.

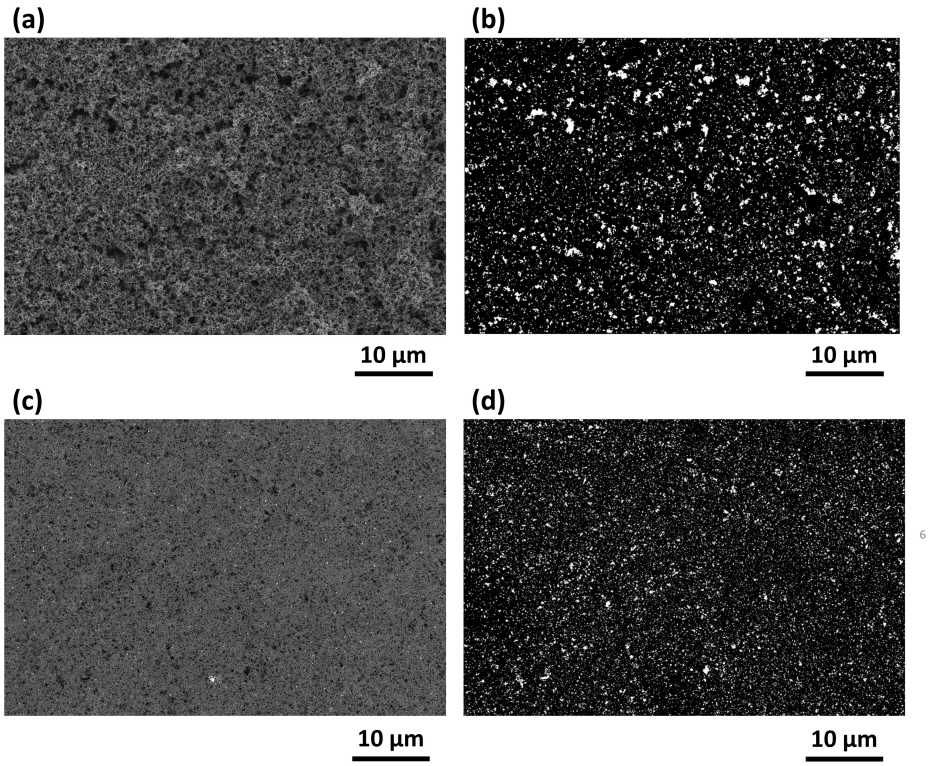

Figure 6.3: SE micrographs and corresponding porosity thresholded maps of CMC-based, Ag-stained interlayers (a)/(b) C 1 and (c)/(d) C 2, with pores shown as bright segmented areas.

Electrochemical characterisation

The same composition CMC-based Ag/CB interlayers listed in Table 6.2 were assembled into pellet-based solid-state full cells, as already described for the cells in the previous chapter. Figures 6.4(a) to (e) show charge/discharge cycles of these cells, composed of the CMC-based Ag/CB interlayers, an LPS+NMC+CNF-based composite cathode and an LPS separator, operating between 2.5 and 4.3 V at a relatively high and demanding charge/discharge current of 1 mA/cm^2. 4 full cells were prepared for each interlayer composition.

Given that the previous chapter established that no cycling of these type of anode-free cells was possible without a functional interlayer, that these cell arrangements in Figure 6.4 successfully facil-

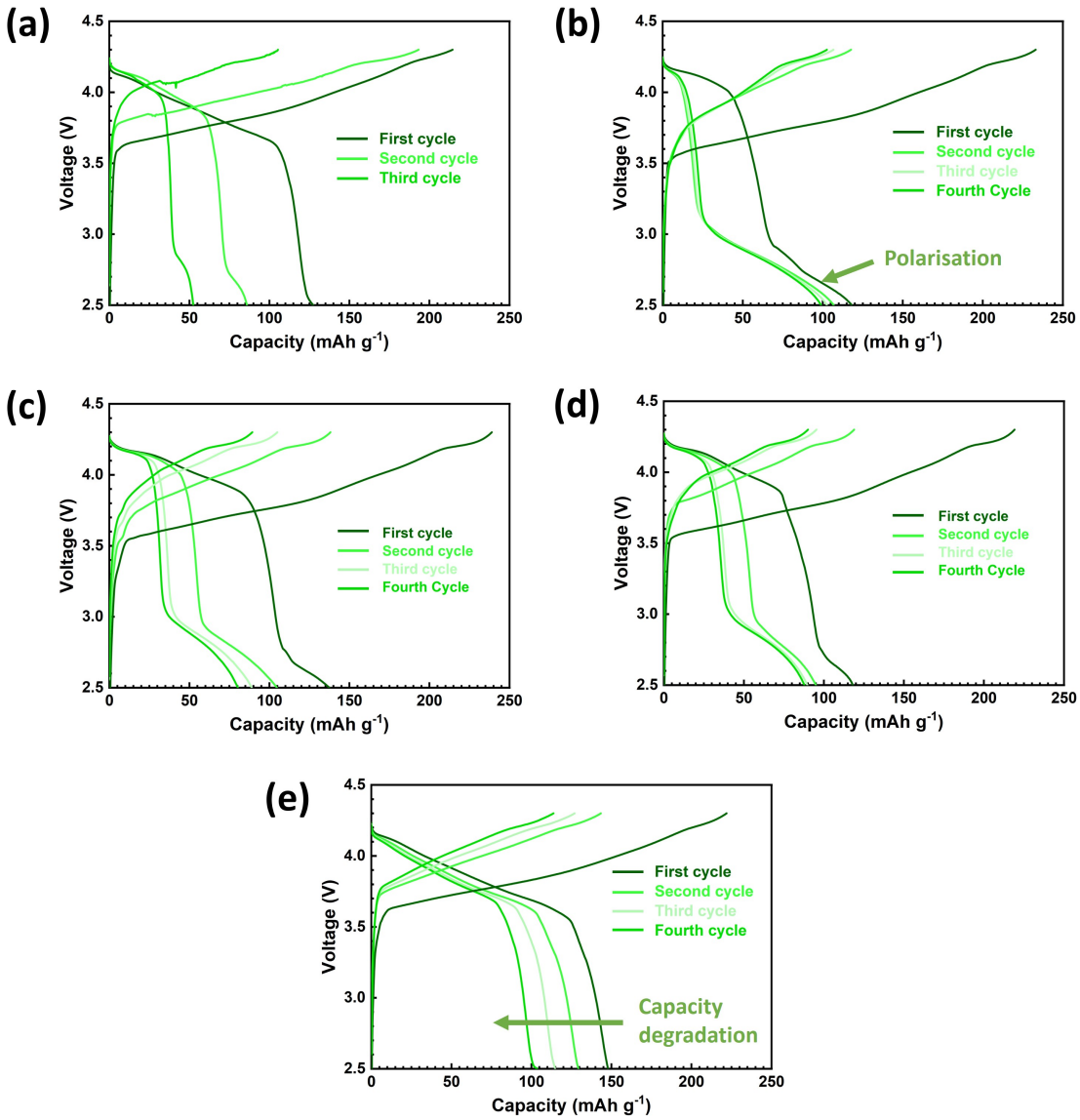

Figure 6.4: Voltage/capacity of full-cells with CMC-based Ag/CB interlayers with varied CMC content at 60 °C and 4 MPa stack pressure at 1 mA/cm^2 charge/discharge current. (a) 150 wt.% CMC and exposure to $AgNO_3$; (b) 20 wt.% CMC and exposure to $AgNO_3$; (c) 10 wt.% CMC and exposure to $AgNO_3$; (d) 10 wt.% CMC with Ag particles; (e) 3 wt.% CMC with Ag particles. (See Table 6.2 for full interlayer composition.)

itated Li plating and stripping was indicative of a broad proof of the Ag stained CMC/C interlayer concept. However, Figure 6.4(a) shows rapid cell failure after just two cycles for the relatively high fraction CMC interlayer (150 wt %) and was the worst performing arrangement. Reducing the CMC fraction to 20 wt % avoided very early cell failure, but in particular, discharge curves showed a marked deviation in the expected shape at $\sim$ 2.7 V in the first discharge plot, as shown in Figure 6.4(b). This deviation became more pronounced and shifted to $\sim$ 3 V on subsequent cycles. This feature was reproduced in other cells, but not always to the same extent or at the exact same voltage. Using half the total interlayer thickness (15 μm) and reducing the insulating CMC fraction to 10 wt.% to reduce overpotential effects were broadly ineffective, as shown in Figure 6.4(c). Therefore, to isolate the insulating effect of the CMC independently of its reaction with $AgNO_3$, CB/CMC interlayers with extrinsically added Ag particles (the same as used in the previous chapter) and 10 wt% CMC were prepared. But again, broadly the same cycling behaviour resulted, as shown in Figure 6.4(d). Minimising the CMC fraction to as low as 3 wt.% removed the unexpected deviations in the qualitative shape of the charge/discharge curve in Figure 6.4(e) and gave the best-performing arrangement, but there was still a steady decrease in charge/discharge capacity during cycling. The origin of the deviation, which relates to an overpotential being applied, was not identified unambiguously but may relate to the electrically insulating nature of CMC, the presence of residual water from the spray processing, or lack of chemical stability of CMC in contact with LPS. Additional post-processing drying under vacuum at 120 °C for 6 h had little effect on subsequent cycling behaviour. A reduction in current density to a less demanding 0.2 mA/cm^2 was also investigated, but again did not achieve a significant improvement in cycling performance or stability. As the tests were conducted in two electrode arrangements, it might be that effects at the hybrid composite cathode may be causing voltage deviations, although other similar cathode arrangements reported elsewhere in the thesis did not show the same features.

6.2.3 Summary

A new approach to introduce Ag NPs into a CB-containing CMC polymer-based interlayer, based on staining with aqueous $AgNO_3$ followed by reduction was developed, and successfully led to fine Ag NP dispersions ($\sim$ 50 nm) that facilitated Li plating and stripping in a laboratory SSB cell arrangement. By varying the CMC and CA reducing agent fractions, it was possible to gain some regulation over Ag NP formation in the CMC. However, all the CMC-based Ag/CB interlayers showed relatively high and somewhat variable polarisation effects in anode-free SSB cells, and capacity fading during cycling. Although this interlayer fabrication approach was ultimately judged insufficiently promising for SSBs, it may potentially have other useful applications - for example, to provide a catalyst interlayer for in-situ formation of metallic negative electrodes in conventional liquid-electrolyte-based batteries. Alternatively, it is potentially applicable to other functional groups beyond carboxylate, e.g. amine or hydroxyl. The general reaction pathway might also be explored for other metals such as Zn, Al, or others.

6.3 Sputtering of Ag nano-interlayers

In the literature, Ag/C interlayers have usually been prepared by slurry casting and occasionally by more specialised processing, such as inkjet printing or spray printing (as used here in the previous chapter) [84, 256]. Less explored is the use of sputtering to create Ag/C interlayers at the anodic current collector. Sputtering may be an attractive choice for the preparation of low-loading catalyst containing layers due to its commercial maturity and potential for scalability [22]. However, previous reports of sputtered anodic Ag nanolayers have mainly focused on assessing cell performance only at low current densities e.g. $\sim$ 0.25 mA/cm^2, 30 μA/cm^2, or even as low as 25 μA/cm^2 [386, 380, 387]. In one case, a higher current density of 1.6 mA/cm^2 and a 200 nm thick sputtered Ag layer on lithium lanthanum zirconium titanium oxide (LLZTO) was explored alongside a composite $\sim$ 7 μm thick Ag/C interlayer and a Li anode [189]. The Ag/C interlayer regulated Li deposition while preventing direct

contact between Li and LLZTO and suppressing dendrite penetration. In this case, the rationalisation was that the sputtered Ag layer enhanced adhesion between LLZTO and the Ag/C interlayer, rather than the Ag catalysing and homogenising Li plating and stripping. Li-Ag/C-Ag-LLZTO-ionic liquid-NCM333 pouch cells achieved a discharge capacity retention of approximately 85% after 800 cycles at room temperature, without application of a stack pressure.

In this section, the sputtering of 100-500 nm thick Ag onto as-supplied commercial C particulate coated Cu current collector foils is explored. The intention is that deposited Ag forms on the thin, pre-existing C layer, to give a comparable interlayer of the same materials (Ag and C) as already explored by spray printing and in-situ precipitation, but now in a more compact arrangement, and based on an industrial feedstock foil and the mature sputtering process. In subsequent descriptions of the experiments, the carbon-coated Cu foil is termed "C-Cu", an uncoated Cu foil after Ag deposition is termed "Ag Cu", and the composite or coated interlayer after Ag deposition is termed "Ag C-Cu".

The use of a carbon particulate coated foil was considered important because previous work on Au interlayers showed that flat and continuous interlayers facilitated only limited Li electrodeposition during in-situ plating compared with those that used a clustered Au morphology [369]. In general, a rough catalyst surface area provides more active sites and, therefore, enhances the overall reaction rate [388, 389]. Zn layers in anode-free cells demonstrated that increasing the Zn thickness from a few hundred nanometers to 1 μm enhanced electrochemical performance due to increased lithiophilic active material alloying with Li [390]. Although Cu has a higher electrical conductivity (5.97×10^7 S/m at 20 °C) than stainless-steel (1.45×10^6 S/m at 20 °C), the greater passivity of the latter is generally preferred for anode-free solid-state cells [391, 392]. For example, Ag interlayers were previously applied by sputtering on Cu current collectors to facilitate Li deposition in combination with electrolytes such as $Li_7La_3Zr_2O_{12}$ (LLZO), lithium bis(trifluoromethanesulfonyl)imide (LiTFSI) in a solution of dioxolane (DOL):dimethoxyethane (DME) with $LiNO_3$, lithium phosphorus oxynitride (LiPON), $LiPF_6$ in a mixed solvent of ethylene carbonate (EC) and dimethyl carbonate (DMC), and $Li_{6.5}La_3Zr_{1.5}Ta_{0.5}O_{12}$ (LLZTO) [393, 394, 395, 396, 397, 398]. But when an LPS SE was then combined

with the Cu current collector in anode-free SSBs, there was Cu corrosion and the formation of Cu-S compounds, which can accelerate Li-consuming electrolyte side reactions [399, 400]. Moreover, the tendency of bare Cu to promote unregulated Li deposition is suggested to be reduced by lithiophilic surface modification techniques e.g. alloying the Cu with metals that have a high affinity for Li, applying conductive coatings, etc [401]. However, as shown later, the C coating on the Cu foil in this study largely mitigated Li-consuming side-reactions with the LPS electrolyte.

6.3.1 Experimental methods

Sputtering

The sputtering process is shown schematically in Figure 6.5 and was undertaken using a Leica EM ACE600 thin-film coater at a current of 35 mA under an Ar atmosphere at an operating pressure of 4.0×10^{-2} mbar. A working distance of 50 mm and a tilt of 0° were applied between target and substrate. The current collector substrate used for sputtering was conductive carbon-coated Cu foil with a 9 μm Cu foil thickness and a 1 μm thick fine particulate C layer (MTI Corporation, USA). It was understood from the supplier that the C-layer was formed from a carbon ink that was coated onto the Cu foil via a form of slot die coating.

Optical profilometry

In order to assess the starting condition and the effect of Ag deposition, the roughness of 3 distinct areas of different current collector surfaces was measured using a whitelight μSurf Nanofocus confocal optical profiler (320-S (50x)) lens with Chris Salter. The applied settings were dR max = +/- 0.5, n = 40, and a cutoff of 800 μm. A Gauss regression filter and a levelling order of 1 were applied to the collected data. All these settings are standard for the instrument.

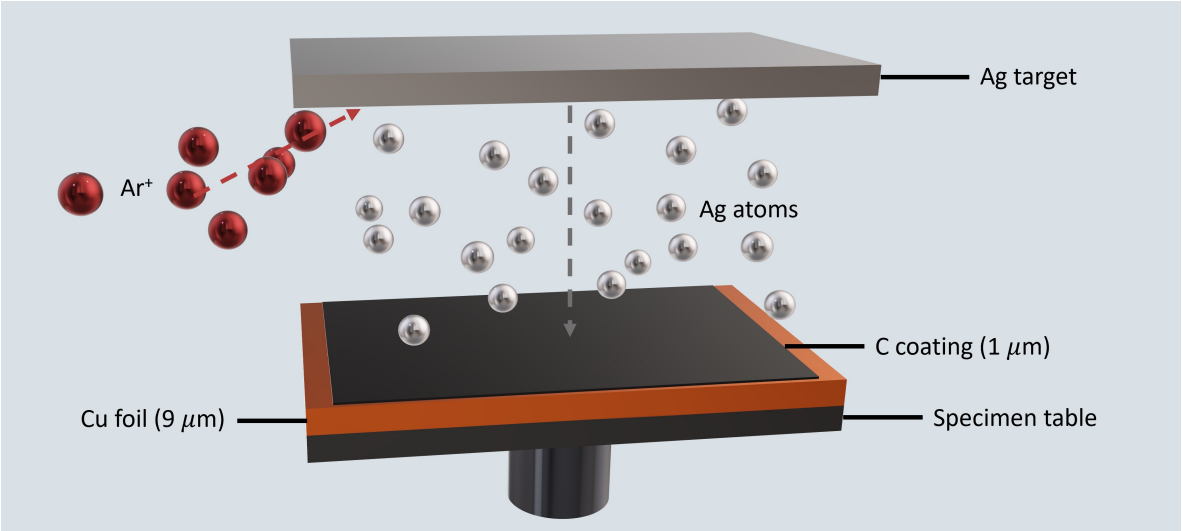

Figure 6.5: Schematic illustration of Ag deposition via sputtering.

Raman spectroscopy

Laser Raman Spectroscopy was performed by Dr Colin Johnston using a Horiba JY LabRam Aramis confocal Raman microscope to assess the crystallinity of the C-coating on the Cu current collector foil, which has been considered a relevant property for the current distribution in carbon-based interlayers, and for any effects of Li intercalation into the C [186]. The Raman spectrum was acquired using 30 s exposure x 16 averages at 1% 532 nm laser over the range of 100 to 3000 cm^{-1} using an x 50 ELWD objective (backscattered geometry).

6.3.2 Results and discussion

Interlayer characterisation

To facilitate homogeneous Li plating/stripping over the full area of the current collector, uniform coverage of the surface of the current collector with an interlayer is likely essential. Figure 6.6 shows SE images and photographs of the surface of (a) the as-supplied C-Cu foil and after sputter deposition of (b) 100 nm and (c) 500 nm Ag. SE and BSE imaging and EDS measurements of sputtered interlayers were performed by Dr Guillaume Matthews with the author directing the investigation. Figure 6.6(a)

suggested there was consistent masking of Cu surface by the C coating, despite its porous, particulate nature, and without significant gaps that exposed the Cu surface to direct Ag deposition. Figure 6.6(b) shows the change in the colour of the surface from dark (C) to silvery (Ag), with no obvious patches of uncovered C at this resolution. When the Ag thickness was increased to 500 nm, there were obvious Ag nodules on the more elevated C particles in Figure 6.6(c). Moreover, the gaps between coated C particles had started to become filled with Ag and the impression was of a somewhat smoother surface.

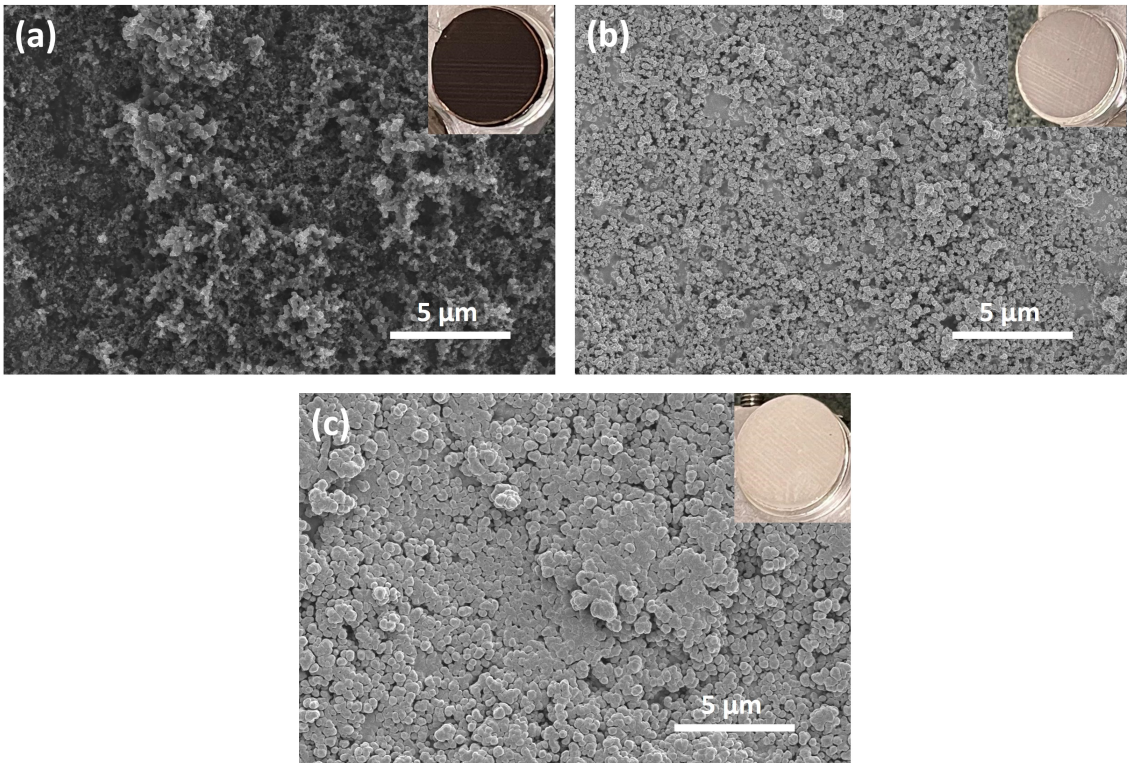

Figure 6.6: SE images and photographs of (a) C-Cu, (b) Ag C-Cu (100 nm), and (c) Ag C-Cu (500 nm).

Table 6.4 summarises the arithmetical mean height (S_a) and the root mean square height (S_q) (obtained by optical profiling) of different current collector arrangements, where each value is an average of 3 measurements from the same foil. The C-Cu surface had a surface roughness (S_a = 0.37 μm) higher than that of either plain stainless steel (S_a = 0.047 μm) or Cu (S_a = 0.167 μm) alone,

even after uniaxial compression at 500 MPa (S_a = 0.245 μm). Ag C-Cu also had a comparable surface roughness after uniaxial compression at 500 MPa (S_a = 0.283 μm). Overall, the feedstock C-Cu foil roughness was largely unaltered by the addition of 100 nm of Ag. However, the surface roughness was reduced by the addition of 500 nm of Ag (S_a = 0.427 μm), consistent with the filling of pores with Ag shown in Figure 6.6(c). After uniaxial compression at 500 MPa, the interlayer was flattened to S_a = 0.075 μm, presumably because of the ready deformation of the thicker Ag layer.

Current collector material	**Average S_a (μm)**	**Std dev**	**Average S_q (μm)**	**Std dev**
Stainless steel	0.047	0.007	0.060	0.009
Cu	0.167	0.019	0.217	0.026
Ag-Cu	0.272	0.110	0.340	0.137
C-Cu	0.370	0.029	0.513	0.046
C-Cu (compressed at 500 MPa)	0.245	0.062	0.332	0.092
Ag C-Cu (100 nm)	0.790	0.143	1.055	0.196
Ag C-Cu (100 nm, compressed at 500 MPa)	0.283	0.167	0.377	0.204
Ag C-Cu (500 nm)	0.427	0.013	0.632	0.071
Ag C-Cu (500 nm, compressed at 500 MPa)	0.075	0.001	0.097	0.001

Table 6.4: S_a and S_q for current collectors stainless steel, Cu, Cu after sputtering of 100 Ag, C-Cu, C-Cu after compression at 500 MPa, Ag C-Cu (100 and 500 nm Ag) and Ag C-Cu (100 and 500 nm Ag) after compression at 500 MPa.

Figure 6.7 shows (a) SEM and (b) BSE images of the cross-section of the C-Cu foil after sputtering of an Ag surface layer thickness of 89 nm, close to a target thickness of 100 nm. Figures 6.7(d) to (f) show corresponding Ag (green), C (red), and Cu (blue) EDS maps and (c) combines them. Despite the high C coating porosity, when Ag was sputtered, deposition was almost exclusively restricted to the upper surface and there was no widespread Ag penetration directly to the Cu foil surface. As the supplier indicated, the C layer was ~ 1 μm thick, and note this is significantly thinner than common previously reported Ag/C interlayer thicknesses in SSBs of 5-10 μm [84, 124, 189].

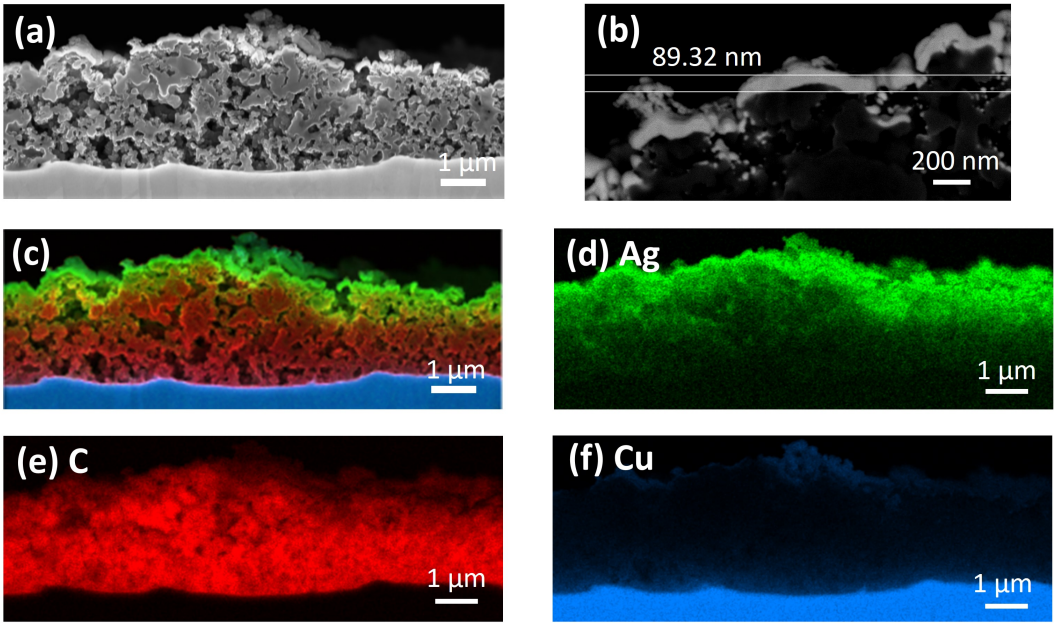

Figure 6.7: (a) Secondary electron and (b) backscattered electrons (BSE) cross-section images of the sputtered C-Cu current collector; (c) corresponding superimposed Ag, C, and Cu EDS maps of the sputtered C-Cu current collector; (d) to (f) corresponding EDS maps for Ag, C, and Cu, respectively.

To assess the impact of compression on the thickness and morphology of the interlayer under cell assembly conditions, Figure 6.8(a) shows a BSE image of the cross section of the sputtered C-Cu foil after uniaxial compression at 500 MPa. The thickness of the interlayer after compression was < 1 μm. Once again, Figures 6.8(b) to (d) show corresponding Cu (blue), C (red), and Ag (green) EDS maps, indicating the presence of a coherent, smoother Ag layer. There was no delamination of the Ag or C.

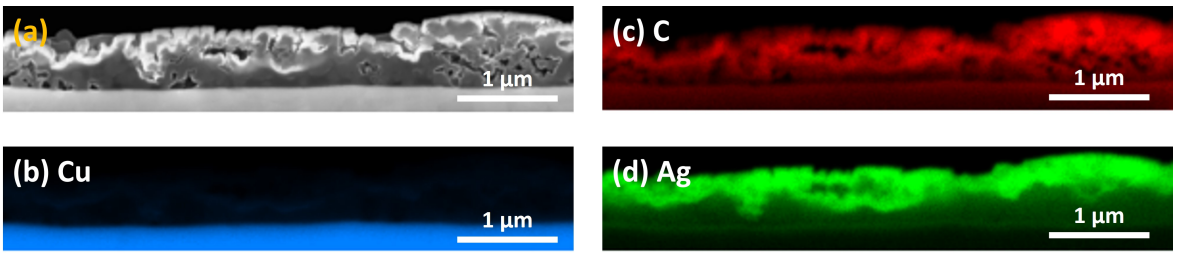

Figure 6.8: (a) BSE cross-section images of the sputtered C-Cu current collector after compression at 500 MPa; (b) to (d) corresponding EDS maps for Cu, C, and Ag, respectively.

To assess the impact of compression on the porosity of the interlayer under cell assembly conditions, cross-sectional SEM images were analysed using ImageJ software by applying a grey-level threshold to segment Ag/C interlayer and pores as shown in Figure 6.9. It was very challenging to reliably quantify such thin coatings and fine-scale porosity. Area fraction porosity measurements were taken for three separate sections of Ag C-Cu interlayers before and after compression. The average porosity was 26.7 % (std dev 1.8 %) and 18.5 % (std dev 1.4 %), respectively. If accurate, this post-compression porosity was below the reported porosity of more common Ag/C interlayers of typically 29% [195]. While compact interparticle contact will promote a more uniform current density, a certain degree of porosity is likely beneficial to accommodate volume changes during plating/stripping (such as Ag-Li alloying, any Li intercalation into C, etc.).

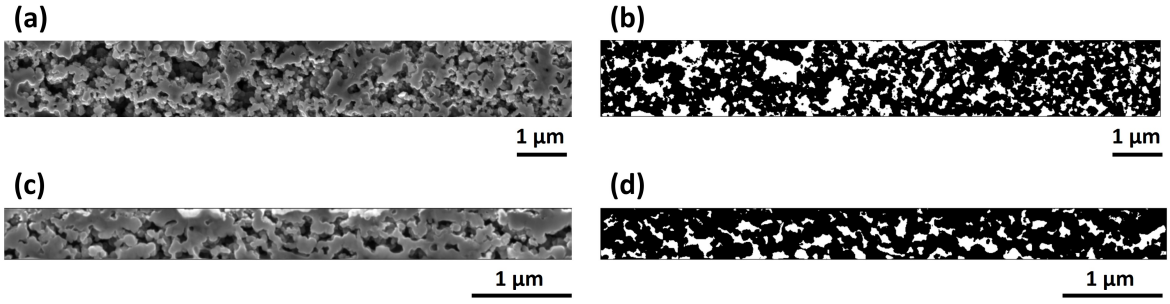

Figure 6.9: Cross-sectional SE micrographs and corresponding porosity thresholded maps of Ag C-Cu (a)/(b) before and (c)/(d) after compression at 500 MPa.

Amorphous rather than crystalline carbon has been suggested as beneficial for promoting uniform Li plating, as it consists of more irregular and disordered structure that provides 3D pathways for Li transport [168, 170]. HRTEM and XRD investigations of the CB used in the spray printed Ag/CB interlayers in chapter 5 suggested a predominantly amorphous structure with crystalline sub-domains. For the sputtered, thin C-coating on the C-Cu current collector, the Raman spectrum in Figure 6.10 showed relatively well-defined D (1359 cm^{-1}) and G (1588 cm^{-1}) bands. The G mode corresponds to tangential atomic vibrations of a graphite mesh, while the D mode shows defect carbon states different from the graphite mesh [402]. A typical Raman spectrum for amorphous carbon is composed usually of only broad peaks in this range [403]. The peaks in Figure 6.10 also indicated graphene-like regions [404, 405]. Another feature is the second order of the D peak, the 2D band (2689 cm^{-1}), whose position and shape are related to the number of graphene layers stacked in graphitic AB ordering [402, 406, 407]. Overall, the Raman spectrum showed that the C-coating on the C-Cu current collector was composed of graphitic carbon, dissimilar to the CB used in spray printing.

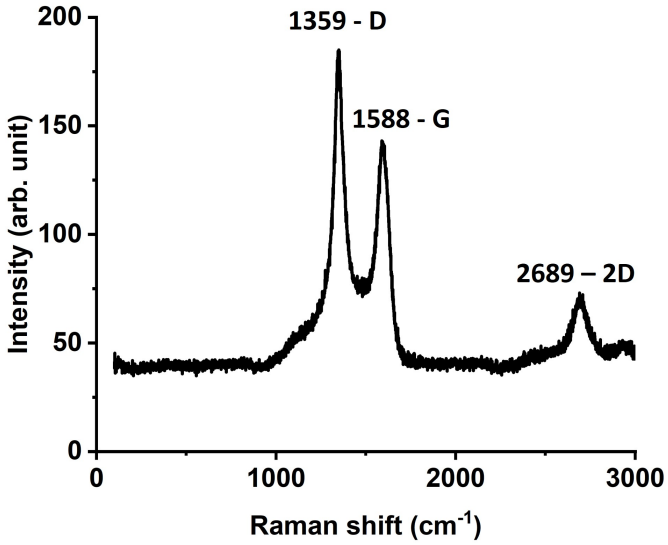

Figure 6.10: Raman spectrum of the C-coating on the C-Cu current collector.

Electrochemical characterisation

Figure 6.11 shows the voltage capacity plots of full cells composed of an LPS + NMC + CNF composite cathode, LPS separator, i.e. identical to those explored elsewhere in this thesis, and C-Cu and Ag Cu interlayers at a current density of 1 mA/cm^2, between 2.5 and 4.3 V, and at a stack pressure of 4 MPa and 60 °C. Encouragingly, both interlayer types allowed first-cycle Li plating/stripping, but

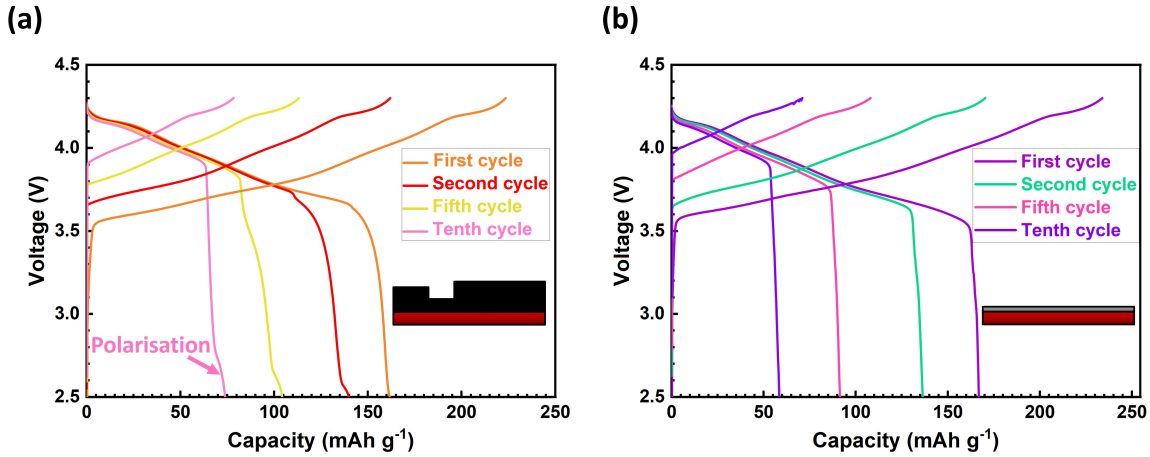

Figure 6.11: Voltage/capacity of full cells with an (a) C-Cu current collector and an (b) Ag Cu current collector at 60 °C and 4 MPa stack pressure at 1 mA/cm^2 charge/discharge current. The insets show the (a) C-Cu and (b) Ag Cu current collectors.

suffered rapid capacity degradation during subsequent cycles. Considering results earlier from spray printed Ag/C, in-situ precipitated Ag/C, and other Ag/C formats from the literature, it is remarkable how flexible and resilient the Ag/C interlayer system is to facilitate Li plating in anode-free SSBs even when the microstructure is significantly different. Nonetheless, when considered in more detail, there was a wide range of cycling responses for the different Ag/C interlayers shown in this thesis, and the optimal Ag/C arrangement is not clear.

Three cells with C-Cu interlayers (i.e. without any sputtered Ag) had an average capacity retention of 37.9 % (std dev 2.4 %) after 10 cycles, which was comparable to the structured spray printed Ag/CB interlayers shown in chapter 5 after 100 cycles. While C alone lowers the Li nucleation energy and

acts as a protective layer that might mitigate Li dendritic growth direct from the current collector, Ag more effectively acts as Li nucleation seeds, lowering the Li nucleation energy barrier and facilitating Li plating at multiple, high areal density sites [178]. Consequently, compared with Ag/C, a C only interlayer is expected to be less effective at promoting uniform Li plating, and C-only interlayers were often accompanied by capacity fade on subsequent cycles. Note there were again slight deviations in the expected shape of the discharge (and charging) curves after one or two cycles, as arrowed in Figure 6.11(a). As previously mentioned, these features occurred in anode-free SSB cells of various compositions and formats, including some cells with spray printed Ag/CB interlayers. A potential explanation could be inhomogeneous plating over time and corresponding resistance build-up during the delithiation process. Time constraints prevented a detailed pursuit of the underlying reason.

Three cells with Ag Cu interlayers (i.e. without any C) had an average capacity retention of 47.6 % (std dev 14.9 %) after 10 cycles. Although better than the C only coating, the relatively fast capacity fade was attributed to the smoother, lower surface area sputtered Ag layer that formed without the C coating (S_a = 0.272 μm). Also, without the protective porous C coating between current collector and separator, Li-consuming side reactions between Cu and LPS were more likely when the Li was stripped away each cycle.

The cycling performance of an interlayer composed of the thicker 500 nm Ag on pre-coated C under the same conditions is shown in Figure 6.12. Three nominally identical cells had an average capacity retention of 34.1 % (std dev 9.6 %) after 10 cycles, i.e. not as good as 100 nm Ag sputtered directly onto the Cu current collector. This may be due to the dense Ag 500 nm layer itself beginning to act as a diffusion barrier and lenghening Li diffusion paths through the Ag layer leading to Li accumulation and unstable plating/stripping [195]. Moreover, the thicker Ag upper layer had a near flat surface after compression (S_a = 0.075 μm), again resulting in limited reaction sites for Li plating.

Finally, Figure 6.13(a) shows the first cell charge/discharge cycle at a charge/discharge current of 1 mA/cm^2 for a non-Ag coated C-Cu foil. The average initial cathode discharge capacity was 163 mAh/g, which was comparable to 166 mAh/g for an Ag-containing Ag/C interlayer [171]. Figure

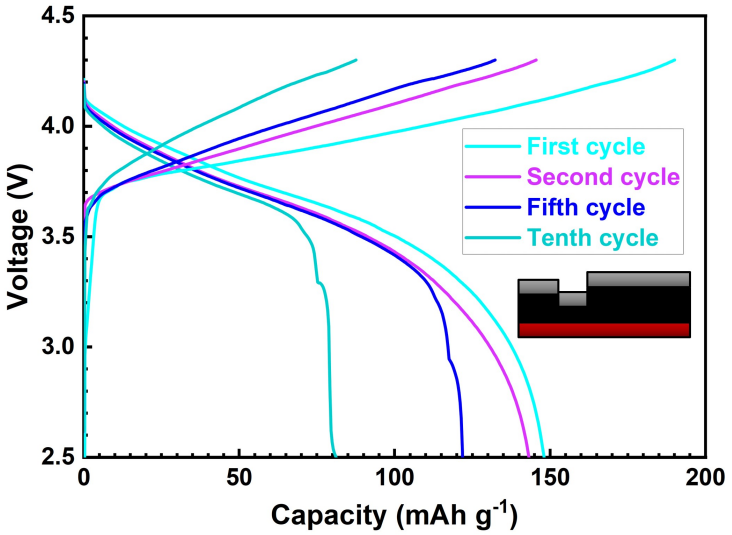

Figure 6.12: Voltage/capacity of full-cell with a sputtered Ag interlayer thickness of 500 nm at 60 °C and 4 MPa stack pressure at 1 mA/cm^2 charge/discharge current. The inset shows the Ag C-Cu (500 nm) current collector.

6.13(a) also shows that when a 100 nm Ag was sputtered on the same C-Cu, the initial discharge capacity then increased to an average of 203 mAh/g, and the initial CE increased from 71 % to 86 %, exceeding the first cycle efficiency achieved with spray printed structured Ag/CB interlayers in chapter 5 (initial discharge capacity of 198 mAh/g and initial CE of 83%). The efficiency was comparable to an initial CE of 89 % reported by Lee et al. under similar cycling conditions in their seminal study on anode-free SSBs [84]. Figure 6.13(b) displays improved capacity retention compared with the C-Cu and Ag-Cu interlayer arrangements previously shown in Figure 6.11. This is suggested to arise because of the combined homogenising effect of Ag when combined with a high areal density of active reaction sites provided by the fine-scale C particulate coating. In contrast to 500 nm sputtered Ag layer, a 100 nm Ag layer apparently did not itself act as a diffusion barrier to Li migration and plating. Three cells of this type had an average capacity retention of 62.4 % (std dev 6.6 %) after 10 cycles. Figures 6.13(c) and (d) show the reduced charge/discharge capacity reduction using the Ag C-Cu interlayer

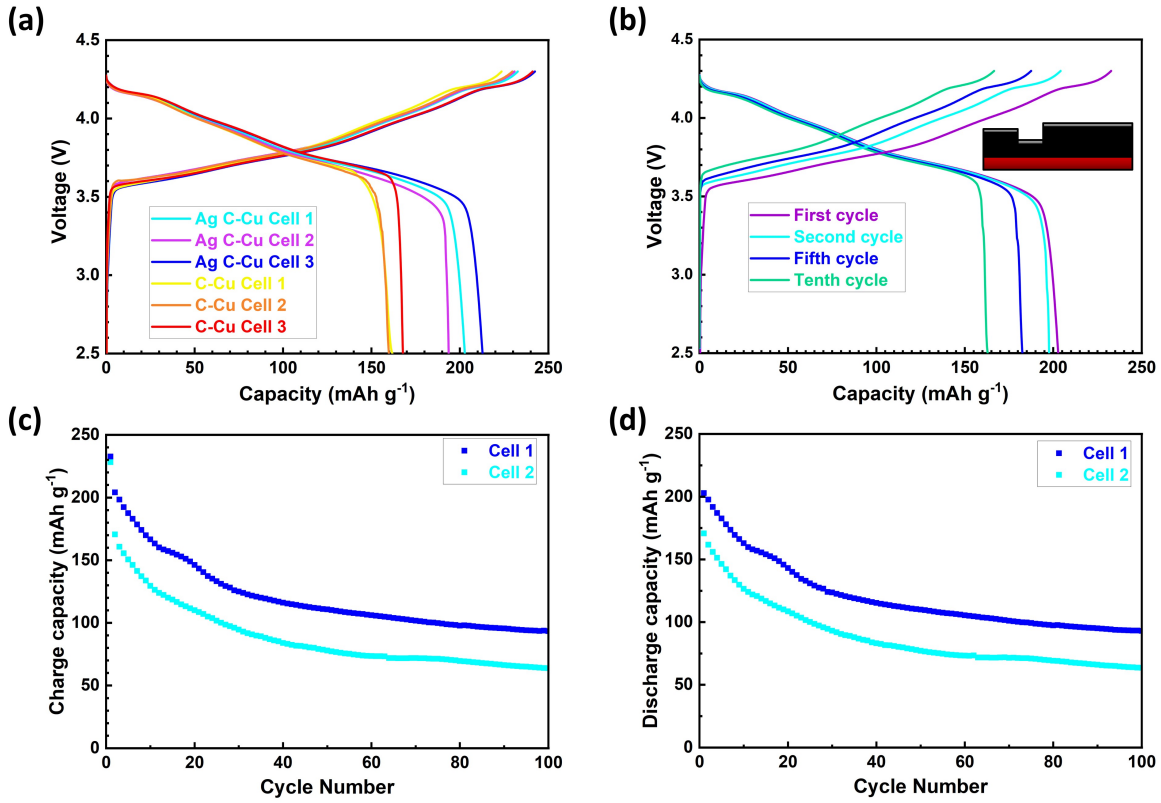

Figure 6.13: Cycling of full cells with C-Cu and Ag C-Cu interlayers at 60 °C, 4 MPa stack pressure, and 1 mA/cm^2 charge/discharge current. (a) Voltage/capacity during the first charge/discharge cycle of C-Cu and Ag C-Cu interlayers; (b) voltage/capacity of Ag C-Cu during first, second, fifth, and tenth cycle; (c) and (d) charge/discharge capacity of Ag C-Cu interlayers over 100 cycles. The inset shows the Ag C-Cu (100 nm) current collector.

over 100 cycles at a current density of 1 mA/cm^2. Cycling without cell failure via short circuiting was achieved even though the sputtered Ag/C interlayer was $\sim$ 20 times thinner than those explored in the literature.

A potential concern of this arrangement was Li diffusion into the Cu and parasitic side-reactions of Cu with LPS, e.g., Cu corrosion by formation of Cu-S compounds, can accelerate Li consumption and contribute to capacity fading in SSBs [399, 408]. Although this could not be ruled out (and recalling

the unexplained deviations previously mentioned), the long-term cycling stability over 100 cycles of Ag C-Cu interlayers was comparable to that of Ag/CB interlayers with inert stainless steel current collectors in chapter 5, indicating at least some protective effect of the Cu foil by the C-coating.

To explore further the effect of current collector interlayer choice on nucleation overpotential, three-electrode cells with Li as counter and reference electrodes and steel, Cu, C-Cu, and Ag C-Cu as working electrodes were prepared. Figure 6.14 compares the voltage versus Li^+/Li at the counter electrode as a function of time for the first charge cycle at charge currents of (a) 1 mA/cm^2 for 1 h and (b) 2 mA/cm^2 for 2.5 h, respectively. Once again, plain stainless-steel and Cu required the highest overpotential magnitude to initiate Li plating, while C-Cu required approximately 6 mV less overpotential compared with Cu. Ag C-Cu exhibited a more stable (flatter, less erratic) subsequent charging profile than C-Cu. For 2 mA/cm^2, five cells with C-Cu interlayers had an average nucleation overpotential of 16.1 mV (std dev 2.4 mV) and five cells with Ag C-Cu interlayers had a much reduced average nucleation overpotential of 3.9 mV (std dev 2.4 mV).

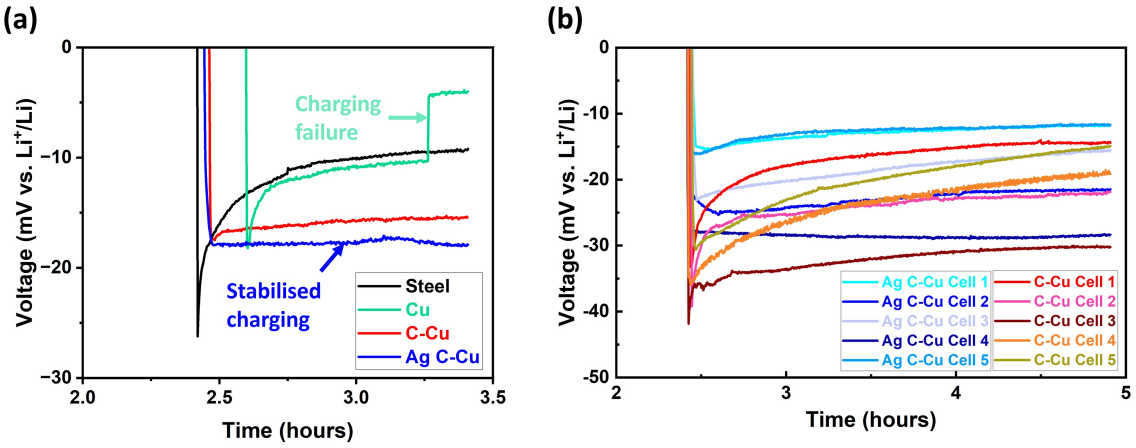

Figure 6.14: Single charge of three-electrode cells using different current collectors; (a) stainless steel, Cu, C-Cu and Ag C-Cu at 1 mA/cm^2 for 1 h, and (b) C-Cu and Ag C-Cu at 2 mA/cm^2 for 2.5 h.

To assess the effect of the sputtered Ag on full cell rate capability, first cycle tests of (a) C-Cu and (b) Ag C-Cu interlayers were carried out at current densities of 1, 2 and 3 mA/cm^2, which are among

the highest currents applied in the field of anode-free cells, as shown in Figure 6.15. An increasing current density led to reduced capacities for Ag C-Cu although the presence of sputtered Ag on the C-Cu extended functionality up to 3 mA/cm^2. In this case, first cycle charging failure was exhibited by significantly (and impossibly) exceeding the theoretical capacity of NMC811 of approximately 230 mAh/g [409].

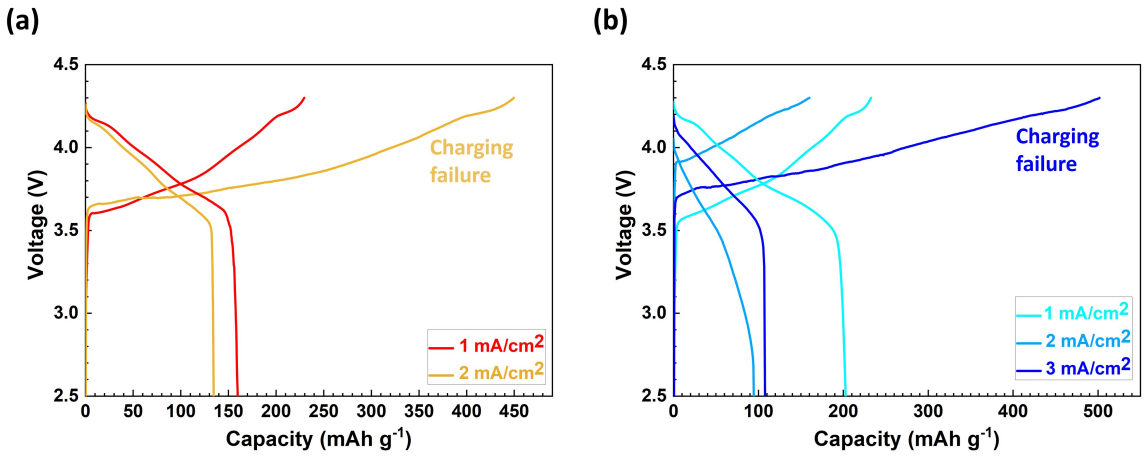

Figure 6.15: Voltage/capacity rate capability tests of full-cells at at 60 °C, 4 MPa stack pressure, and 1, 2 and 3 mA/cm^2 charge/discharge currents of (a) C-Cu and (b) Ag C-Cu.

The effect of the sputtered Ag on the impedance response of C-Cu and Ag C-Cu full cells were investigated after charge/discharge cycling at 1 mA/cm^2 and 4 MPa after 1, 5, and 10 cycles at 60 °C, as shown in the Nyquist plots in Figures 6.16(a) and (b), respectively. A frequency range of 10 mHz – 10 kHz with a nominal AC voltage of 10 mV was applied. The best-fit to the Ag C-Cu interlayer first cycle data using a typical equivalent circuit model (EC-Lab software) is shown in Figure 6.16(c). The data revealed an ionic conductivity of $\sim$ 1.6 mS/cm for both interlayer types and no resolvable difference between them or in their impedance evolution up to 10 cycles. The Ag nanolayer had no resolvable difference in impedance over the first 10 cycles.

Figure 6.17 shows the voltage versus Li^+/Li at the counter electrode as a function of time for the first cycle of Ag C-Cu three-electrode cells at a high charge current density of 2 mA/cm^2, up to a capacity

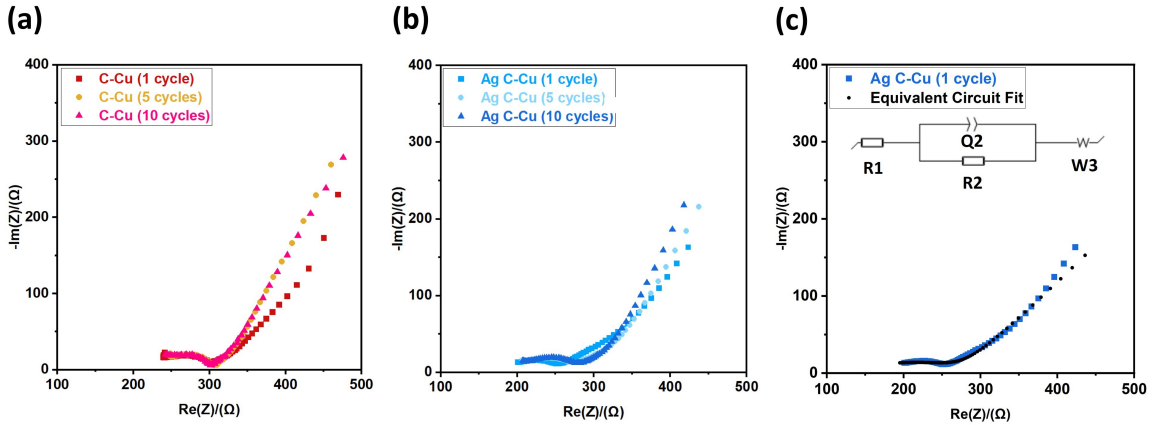

Figure 6.16: Nyquist plots of (a) C-Cu and (b) Ag C-Cu full-cells after 1, 5, and 10 cycles at 60 °C, 4 MPa stack pressure, and 1 mA/cm^2 charge/discharge current; (c) equivalent circuit fit to Ag C-Cu after 1 cycle. R1 = 123.9 Ω, R2 = 175.5 Ω, Q2 = 0.4896 × 10^{-3} F.s$^{(\alpha-1)}$.

of 5 mAh/cm^2, and then a discharge current of 1 mA/cm^2. A peak in voltage after approximately 4h was attributed to the stripping of Li and indicated a round-trip efficiency of approximately 80%, which was comparable to the initial CE of Ag C-Cu full cells.

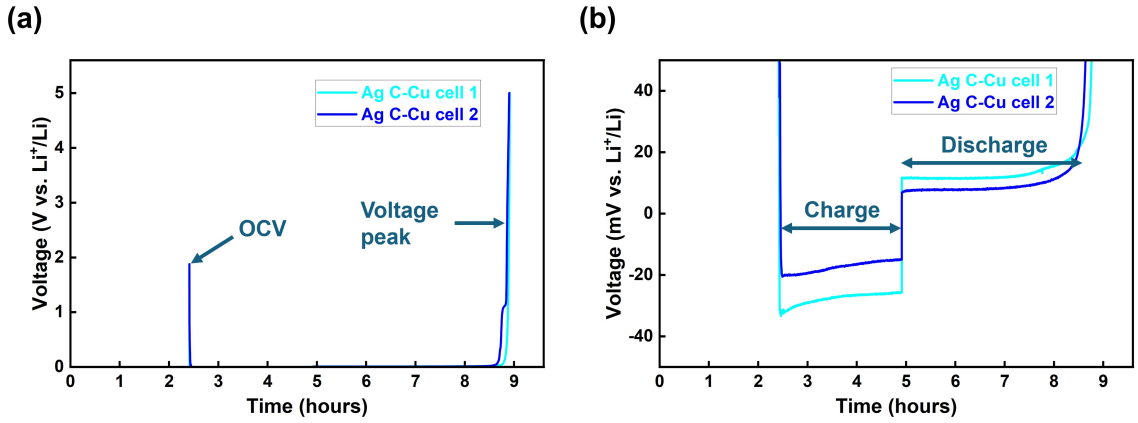

Figure 6.17: Charging response of three-electrode cells with an Ag C-Cu interlayer at 2 mA/cm^2 for 2.5 h and discharge at 1 mA/cm^2; (a) voltage window between 0 and 5 V vs Li$^+$/Li, and (b) magnified voltage window of (a), between -50 and 50 mV vs Li$^+$/Li. OCV = open-circuit voltage.

Characterisation of the plated anode

To understand the physical role of the Ag C-Cu interlayer, a series of plasma FIB cross-sections of plated and stripped cells after the application of various electrochemical regimes were explored. The P-FIB SIMS measurements were carried out with Dr Yige Sun. Figure 6.18(a) shows a cross-section of the current collector region of an Ag C-Cu (100 nm) three-electrode cell after a single plating cycle at 2 mA/cm^2 for 2.5 h. Based on the investigations of spray printed Ag/C interlayers and their influence on plating, using the same techniques and methodology, Figure 6.18(a) shows there was a Li layer formed between the Cu current collector (top of image), and the C coating, which remained adjacent to the LPS separator (bottom of image). However, there were some regions where the C coating remained attached to the Cu (e.g. on the LHS of Figure 6.18(a)), but the Li nonetheless plated towards the current collector, in this case, over the C. Qualitatively, the general Li arrangement was comparable with the Li layer formed using spray printed Ag/CB interlayers in chapter 5 in terms of thickness ($\sim$ 20 μm) and uniformity. EDS maps for Cu, S, C, and Ag in Figures 6.18(b) to (e) indicated the displacement of the C interlayer away from the current collector upon charging, and there was a faint Ag signal distributed throughout the newly plated layer i.e. the initial, distinct $\sim$ 100 nm Ag layer on the C had become distributed into the plated Li, regardless of the behaviour of the C coating. Note again that even though a demanding current density of 2 mA/cm^2 was used, Li plating was reasonably uniform.

Recognising that in small anode-free SSB pellets, 2D cross-sectional microscopy may sample a non-representative area/volume, to investigate reproducibility, Figures 6.19(a) and (b) show additional SEM images of a FIB cross-section of another nominally identical three-electrode cell, again taken from the current collector interface after a single plating cycle at a high current density of 2 mA/cm^2 for 2.5 h. In this case, attempts were made to reduce magnification to capture as large an area as possible while maintaining useful resolution. Figure 6.19(b) then shows a zoomed in area across which an EDS line scan was obtained, shown in Figure 6.19(c). The displacement of the C layer away from the current collector was clearly resolved, along with the re-distribution of Ag into the plated layer.

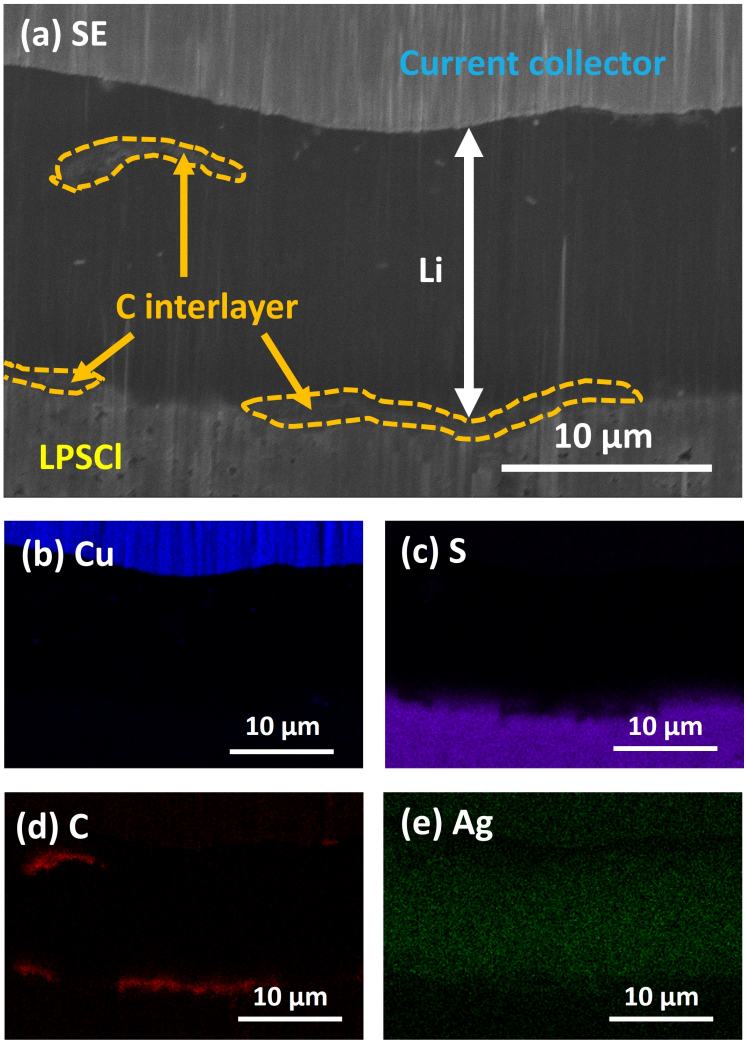

Figure 6.18: A cross-section of an Ag C-Cu (100 nm) current collector, a deposited layer, and LPS separator region after a single charge at 2 mA/cm^2. (a) SEM image of Ag C-Cu; (b) to (e) EDS maps of Cu, S, C, and Ag, respectively.

To check the plated layer was indeed Li, the same idea as previously described for the spray printed Ag/CB interlayer was used to assess whether a Li SIMS signal from the plated layer could be consistent with metallic Li. Figure 6.20 shows the relative intensities of the Li^+ signal obtained by SIMS from the plated layer region of the same three-electrode cell and the custom-made Li/LPS reference previously used in chapter 5. While the Li^+ map obtained by SIMS from the layer adjacent to the current collector

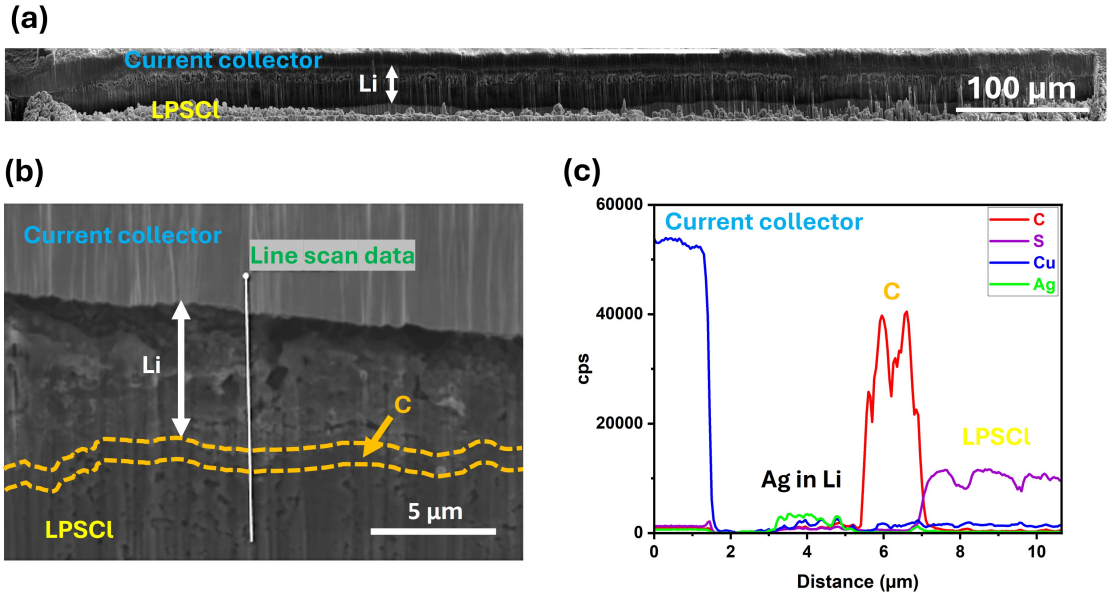

Figure 6.19: A cross-section of an Ag C-Cu (100 nm) current collector, deposited layer, and LPS separator region after a single charge at 2 mA/cm^2. (a) SEM low magnification image of Ag C-Cu; (b) magnified SEM image of Ag C-Cu; (c) EDS line scan spectrum obtained from the line marked in (b).

exhibited a relatively strong Li signal, the LPS SE layer again showed an even stronger Li^+ signal, as in chapter 5. The averaged, relative intensities of the Li^+ signal of the plated layer (42:100) had a slightly greater difference from the reference (38:100) than a Li layer from a spray printed Ag/C interlayer (36:100) shown in Figure 4.15, but was again consistent with plated Li. Differences in the SIMS signal intensity of metallic Li may be attributed to differences in the even-ness of the milled surface.

If the sputtered 100 nm thick Ag layer dissolved in the 20 μm plated Li layer, as suggested by the EDS data, it would correspond to 0.5 vol.% and 8.9 wt.% Ag in Li, which explains the low intensity Ag EDS signal from the plated layer.

To compare the Li plating in the presence of the sputtered Ag with that of a C-Cu only current collector, Figure 6.21 shows an SEM image and corresponding C, Cu, and S EDS maps of a C-Cu three-

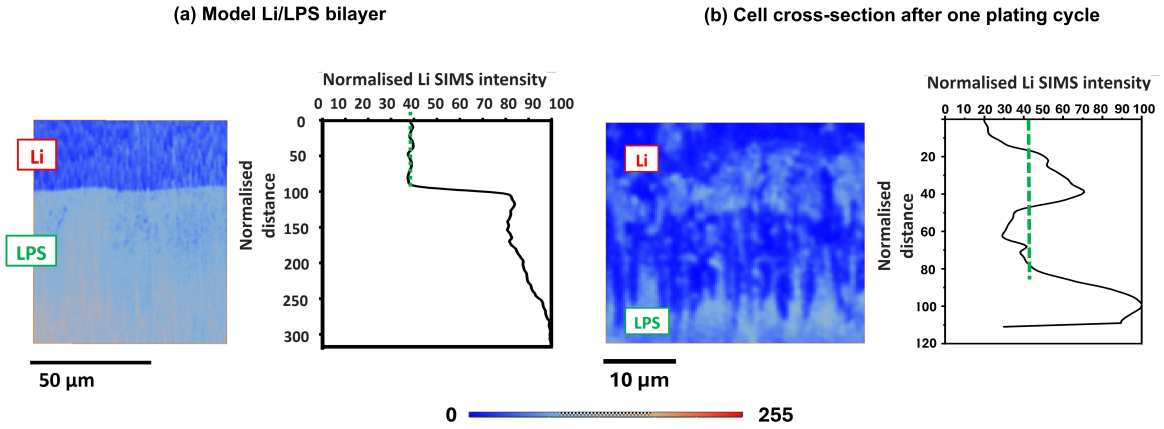

Figure 6.20: Cross-section Li SIMS maps of (a) a model Li/LPS reference bilayer, and (b) the anodic current collector region of a cell with an Ag C-Cu (100 nm) interlayer after one plating cycle at 2 mA/cm^2. In each case the Li SIMS intensity from the LPS region was set to 100 and the Li SIMS intensity from other regions scaled accordingly. The green dotted line indicates the intensity in (a) the Li foil and (b) the nominal Li plated layer.

electrode cell after a single plating cycle of 2 mA/cm^2 for 2.5 h, again showing the displacement of the C interlayer and the plating of an approximately 10-20 μm thick Li layer onto the current collector, i.e. somewhat less uniform. While the C-Cu interlayer arrangement (i.e. no Ag) also facilitated plating of metallic Li on charging, full-cell cycling, rate capability, and single-charge investigations all showed the positive effect of adding the sputtered Ag layer.

To investigate any interlayer morphology changes and damage after Li stripping during subsequent discharge, Figure 6.22 shows a cross-section of the region of a stripped anodic current collector of an Ag C-Cu (100 nm) interlayer, three-electrode cell after a single plating cycle at 2 mA/cm^2 for 2.5 h and subsequent discharge at 1 mA/cm^2. A large void formed between the current collector (top of image) and the C interlayer and the LPS separator (bottom of image). The presence of such voids in all stripped cells presented a significant challenge to sample preparation and the avoidance of preparation induced delamination of the current collector. Such problems are common in trying to preserve the integrity of multiple interfaces in batteries, but were exacerbated here due to the residual

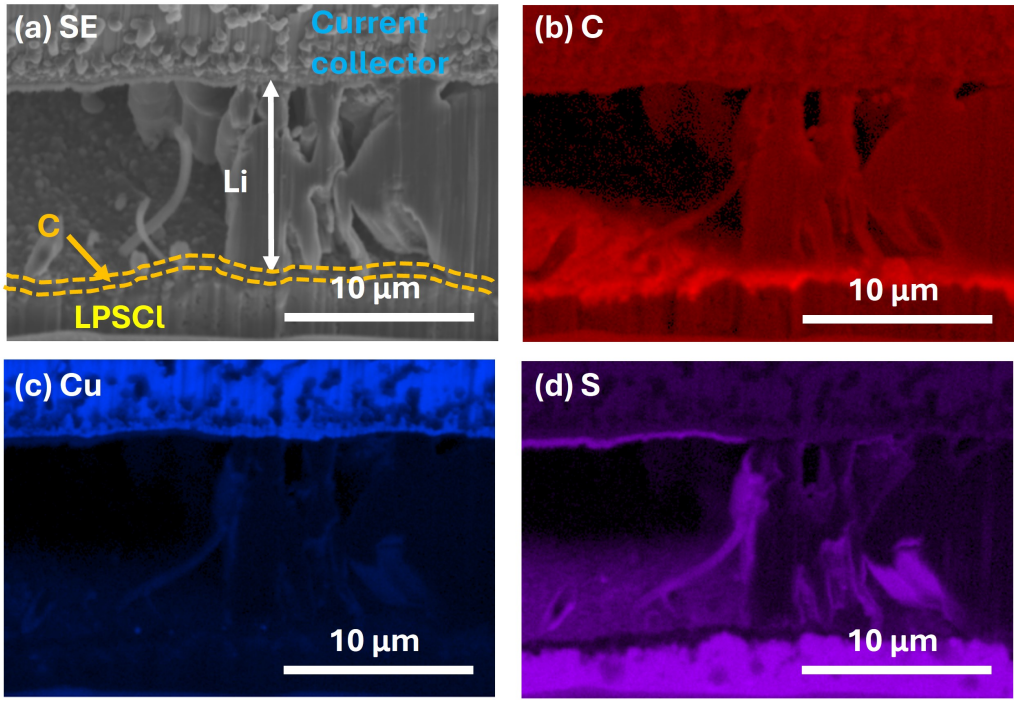

Figure 6.21: A cross-section of the C-Cu current collector, deposited layer, and LPS separator region for a single charge at 2 mA/cm^2. (a) SEM image of C-Cu; (b) to (d) EDS maps of Cu, C, and S, respectively.

voiding produced by Li stripping. Voids also made obtaining a flat cross-section difficult and therefore consistent EDS elemental concentration maps. It is notable that very few publications show, or are able to show, detailed examinations of stripped anode-free cells. Stripping voids were also likely widened after releasing the stack pressure during cell disassembly for microscopy.

EDS maps for Cu, Ag, C, and S in Figures 6.22(b) to (e) show that the C layer, displaced by plating, remained next to the LPS separator. The Ag signal suggested that Ag, left "behind" when the Li was stripped away, re-precipitated onto the C particulate rather than onto the current collector.

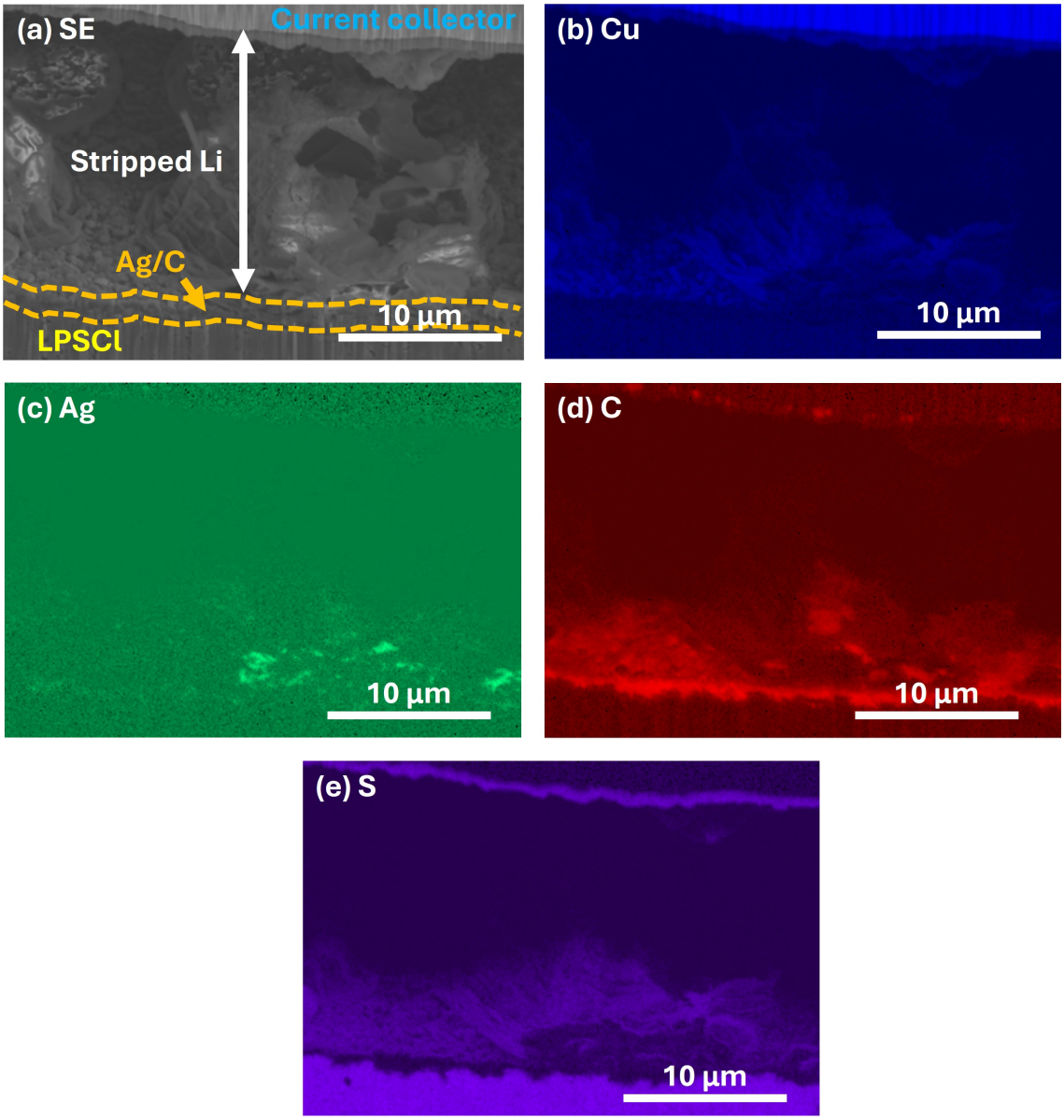

Figure 6.22: A cross-section of the Ag C-Cu (100 nm) current collector, stripped layer, and LPS separator region after charging at 2 mA/cm^2 and discharging at 1 mA/cm^2. (a) SEM image of Ag C-Cu after discharge; (b) to (e) EDS maps of Cu, Ag, C, and S, respectively.

To investigate further the location of different elements, Figure 6.23 shows an SE image and corresponding EDS line scan of a different section of the same cell, again suggestive of precipitated Ag onto the displaced C coating.

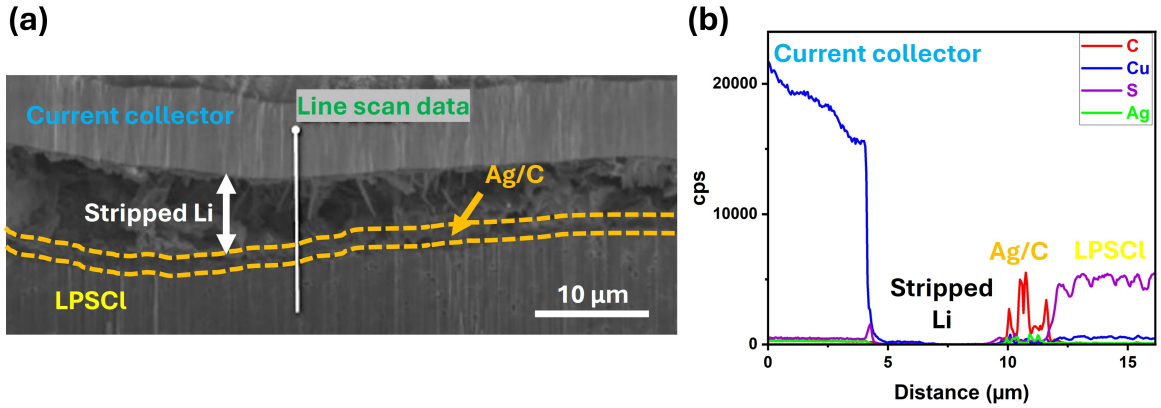

Figure 6.23: A cross-section of an Ag C-Cu (100 nm) current collector, stripped layer, and LPS separator region after charging at 2 mA/cm^2 and discharging at 1 mA/cm^2. (a) SEM image of Ag C-Cu after discharge; (b) EDS line scan spectrum.

To assess reproducibility, Figure 6.24 shows another nominally identical Ag C-Cu (100 nm) three-electrode cell after a single plating cycle at 2 mA/cm^2 for 2.5 h and subsequent discharge at 1 mA/cm^2. A large void again formed between the current collector (top of image) and the C coating and the LPS separator (bottom of image), while in this case some non-stripped Li remained next to the current collector. EDS maps for Cu, C, Ag and S in Figures 6.24(b) to (e) confirmed that the displaced C coating remained next to the separator after discharge while the Ag was again associated with the C coating. To gain more robust insights into the stripped current collector region, and not withstanding sample preparation difficulties, further similar investigations should be conducted using detailed cross-sectional microscopy.

Chapter 5 suggested that concentrating Ag particles close to the current collector surface facilitated Li plating. Similarly, sputtering an Ag nanolayer in close proximity to the current collector promoted Li plating at the current collector (reduced nucleation potential) up to a high current density of 2 mA/cm^2. Although the C-layer on the current collector was itself not uniform but comprised nano-scale carbon particulate, this may be advantageous as it promoted a high surface area to the sputtered Ag, and then for Li plating. Even though the C-particulate layer was porous ($\sim$ 20 %), it was sufficiently

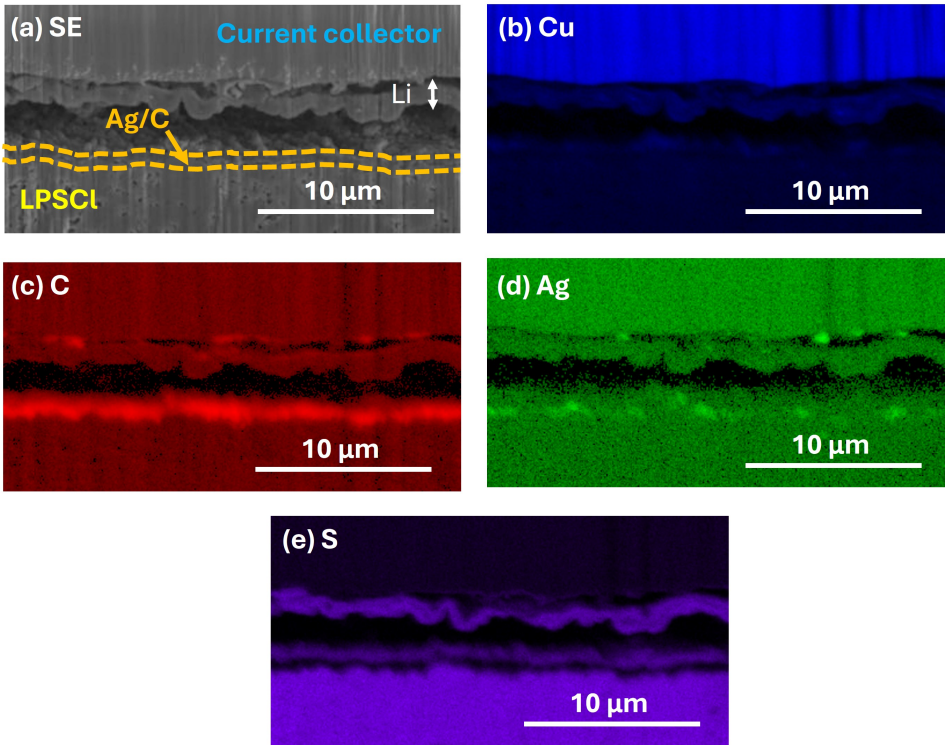

Figure 6.24: A cross-section of the Ag C-Cu (100 nm) current collector, stripped layer, and LPS separator region after charging at 2 mA/cm^2 and discharging at 1 mA/cm^2. (a) SEM image of Ag C-Cu after discharge; (b) to (e) EDS maps of Cu, C, Ag, and S, respectively.

dense to suppress any large-scale Li-consuming side reactions with Cu. The near-continuous sputtered Ag layer likely provided a larger active surface area for alloying with Li^+ ions compared with locally concentrated Ag particles used in chapter 5.

When the Li metal formed at the current collector surface, the C interlayer was displaced from the current collector, but not always uniformly, as illustrated schematically in Figure 6.25. As the Li layer formed, catalysed by the Ag, the pre-sputtered Ag was itself dissolved and distributed into the plated Li. After discharge, the Li was largely stripped away and the C coating remained next to the current collector, while Ag precipitated onto the C coating wherever it was. Voiding was present after stripping, although it was hard to ascribe this to operando behaviour or a result, or exacerbated, by sample preparation. Nonetheless, patches of Li residue were sometimes present after stripping, and

will have undermined Coulombic efficiency. Voids will also act as inactive sites in subsequent cycles, leading to elevated interfacial resistance and preferred dendrite growth [313, 338, 336]. The reasonable cycling stability of Ag C-Cu at a high current density of 1 mA/cm^2, and generally uniform Li plating after charging indicated that the extent of carbon crystallinity was not decisive for Li (de)intercalation processes at these interlayer thicknesses ≤ 1 μm due to short bulk Li diffusion pathways. Overall, while reducing the Ag/C interlayer thickness from 13 μm (applied in chapter 5) to < 1 μm , the ~ 1 μm C $+ \sim 100$ nm Ag interlayer arrangement was generally as good as, or even better than the much thicker layers generally explored in the literature [195, 410]. However, differences in electrolyte type/thickness, cell geometry, stack pressure, areal loadings, other interlayer differences used in literature studies, etc, make definitive comparisons difficult, and suggest the field might benefit from a "standard" test for anode-free cell research.

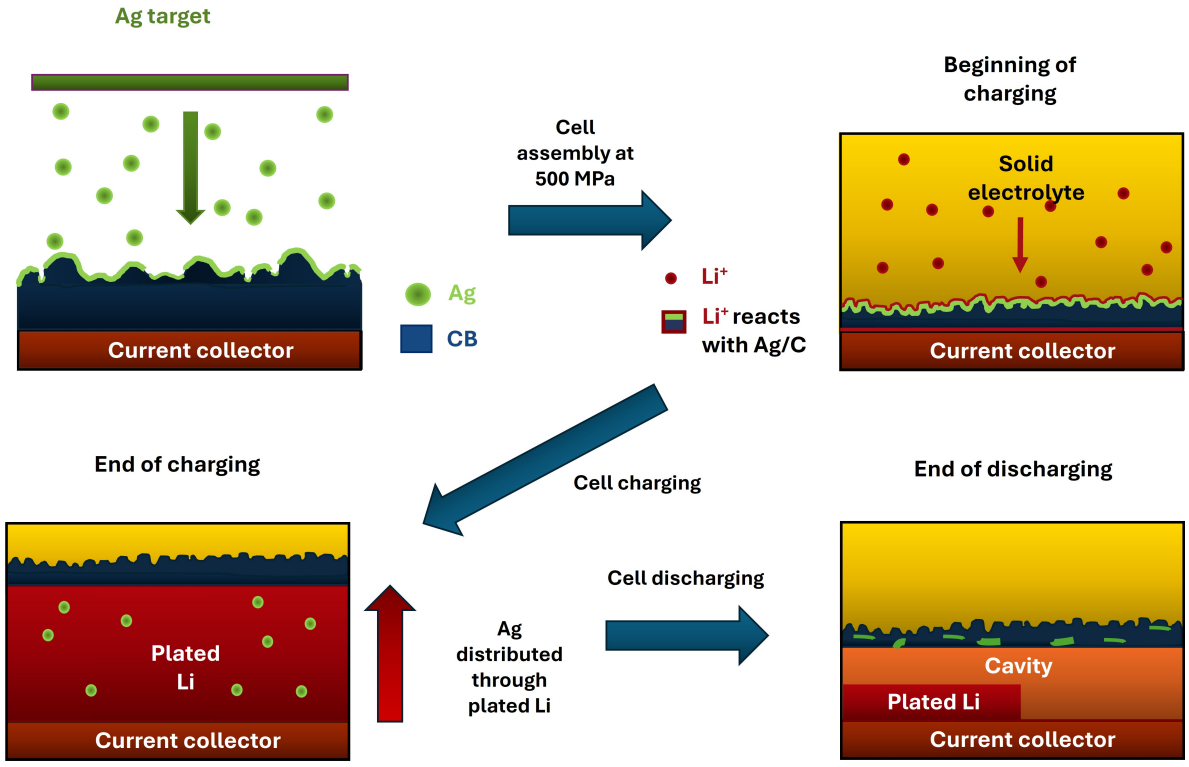

Figure 6.25: Schematic and idealised illustration of the preparation of the Ag C-Cu interlayer and Li plating and stripping upon charging and discharging.

6.3.3 Summary

An Ag/C interlayer was fabricated by sputtering a $\sim$ 100 nm thick Ag layer onto a pre-coated C-Cu current collector foil. The Ag/C interlayer facilitated the formation of metallic Li on the first charge cycle at a reduced overpotential, delivered an initial discharge capacity $>$ 200 mAh/g, and an initial coulombic efficiency of 86 % at a current density of 1 mA/cm^2, which are among the highest reported in the field of anode-free cells, especially using a practical hybrid cathode formulation as was used throughout these investigations, i.e. many studies on plating/stripping use Li or Li-In counter electrodes. The formation of a Li-plated layer and the displacement of the $<$ 1 μm thick C coating were identified by a combination of SEM, P-FIB SIMS, and EDS. Ag was distributed in the Li-plated layer after charge and re-precipitated on the C coating after discharge. The use of a C-precoated Cu foil facilitated processability, increased the active surface area for Ag deposition, and allowed the combination of Cu as a current collector material with LPS, without excessive degrading side reactions at the current collector interface. Nonetheless, voiding and inhomogeneous stripping undermined efficiency and capacity and further improvements are required. Those likely include aspects beyond the interlayer itself such as achieving $\sim$ 100 % density in the separator and especially the cathode, reducing interfacial impedances, improving the cathode electrical conductivity, etc. Regardless, the results here suggest a much wider range of interlayer designs may be feasible, and realised by a greater number of fabrication approaches, than previously assumed. This opens a wider design space for interlayers in terms of thickness, compositions, and placing influential materials more rationally in the design, where they are most effective.

Chapter 7

Conclusions

This thesis has considered some of the challenges associated with SSBs, especially with regard to manufacturing technology and focussing on the requirement for near-full density of cathodes and separators, the high reactivity of sulphide based SEs, and the difficulties of scalable Li metal anode solutions. In some cases, this has involved the development of novel processing alternatives to conventional LIB manufacturing.

The preparation of free-standing Li_6PS_5Cl SE sheets for SSBs through slurry casting and dry processing via PTFE fibrillation was explored using NBR and PTFE binders, respectively. Solvent-free processing may offer advantages in terms of sustainability, safety, and cost, but it is technically and scientifically immature for SSBs. Slurry cast and solvent-free SE sheets were hot calendered to a density of approximately 84 % and with an average pore diameter generally < 1 μm. This allowed for relatively high ionic conductivities of 1.45 mS/cm for the dry processed separator and 1.19 mS/cm for the slurry cast reference at 60 °C. The slightly higher conductivity of the dry processed separator was attributed to the elongated 1D morphology of PTFE fibrils binder distribution in contrast to the globular NBR distribution. Using 600 μm separators in pellet format, dry processed separators had a CCD of 1 mA/cm^2 compared with 2 mA/cm^2 for slurry cast separators. XCT measurements showed dry processed separators had more microcracks, which increased their susceptibility to Li dendrite

propagation. The chemical compatibility of SE dry processing with ZrO_2 fibres as a potential toughening approach was demonstrated, but mechanical effects were not pursued. Although hot calendering provided additional shearing to the initial sheer mixing step and further fibrillated the PTFE, sufficient densities of > 99 % were not achievable by this route alone, with the equipment available that could impose transient loads > 500 MPa. While calendering is likely essential to ensure bonding/adhesion with the current collector, thickness control, and surface smoothness, an additional process, such as warm isostatic pressing (WIP) is likely essential. Critically, WIP can be applied both to electrodes and full cells, and may promote contact at the various interfaces and healing of any SE cracks induced during handling.

Spray printing was used to fabricate a ~ 13 μm thick Ag/CB interlayer for anode-free cells with an increased Ag nanoparticle concentration toward the current collector. Using three-electrode cells, this "structured" Ag arrangement showed a reduced Li nucleation overpotential during the first charge cycle and delivered an initial discharge capacity of > 190 mAh/g at 1 mA/cm^2, and slower subsequent capacity degradation than unstructured Ag/CB interlayers, at a high CE of $> 98\%$ after 100 cycles. The structured arrangement facilitated a generally more uniform Li layer formation on the current collector interface, which was identified by combining SEM, P-FIB-SIMS, EDS, and XPS to charged and disassembled cells. SIMS was applied for the first time to confirm Li plating in anode-free cells. A new laser cutting approach was developed that allowed higher quality and more consistent Ag/C interlayers to be deployed. The work demonstrated the opportunity for design optimization of Ag/CB interlayers to deliver improvements in SSB cell performance through the microstructural control provided by spray printing.

To facilitate other types of Ag/C interlayers and to assess if they might provide benefits, the chemical precipitation of Ag nanoparticles from an Ag-stained CB/CMC composite layer and Ag sputter deposition onto a particulate layer were explored. CMC binder was used to form a layer of a few nanometre thickness on C particles and the slurry applied to a stainless steel current collector, and Ag^+ ions then selectively bound to the CMC when exposed to an aqueous solution of $AgNO_3$. Ag

nanoparticles were precipitated during drying and/or on application of citric acid (CA). By varying the CMC and CA content, it was possible to regulate the size of Ag particles (10 - 150 nm) following annealing at 120 °C. However, CMC-based Ag/CB interlayers exhibited high polarisation in SSB cells, which was attributed principally to the coverage of CB particles with electrically insulating CMC.

An Ag/C interlayer was prepared by scalable sputtering a $\sim$ 100 nm thick Ag layer on a pre-coated C-Cu current collector foil, which again facilitated the formation of metallic Li on the first charge cycle at a reduced overpotential. The relative uniformity of both Li plating and stripping on charge/discharge was revealed by cross-sectional microscopy. Full cells delivered a high initial discharge capacity $>$ 200 mAh/g and an initial CE of 86 % at a current density of 1 mA/cm^2, and cycling for 100 cycles without cell failure or excessive Li-consuming side reactions at the Cu current collector, even though the Ag/C interlayer was only $\sim$ 1 μm thick.

Figure 7.1 compares the long-term cycling stability and nucleation overpotential of cells with structured Ag/CB and Ag C-Cu (100 nm) interlayers. Figures 7.1(a) and (b) show the cathode charge and discharge capacities respectively of full cells cycled between 2.5 and 4.3 V at a charge/discharge current of 1 mA/cm^2. While Ag C-Cu reached a higher initial CE (87 % vs. 83 %), the subsequent profiles are practically identical, with no catastrophic failure at a CE $>$ 98 % after 100 cycles. Figure 7.1(c) shows a comparison of the voltage versus Li^+/Li counter electrode of three-electrode cells as a function of time for the first charge cycle. Both interlayer arrangements significantly reduced the Li plating onset overpotential compared with uncoated current collectors, despite their very different spatial arrangements of Ag and C, and length-scale differences. Post-nucleation, the sputtered Ag Ag-Cu interlayer displayed a flatter, more stable charging profile, again despite the relatively high current density and thickness of only $\sim$ 1 μm. The qualitative advantages and disadvantages of different Ag/C interlayer manufacturing routes explored in this thesis are given in Table 7.1. Overall, the results in this thesis suggest that a broad range of interlayer compositions and formats can be effective in anode-free designs and can be realised by a variety of processing routes.

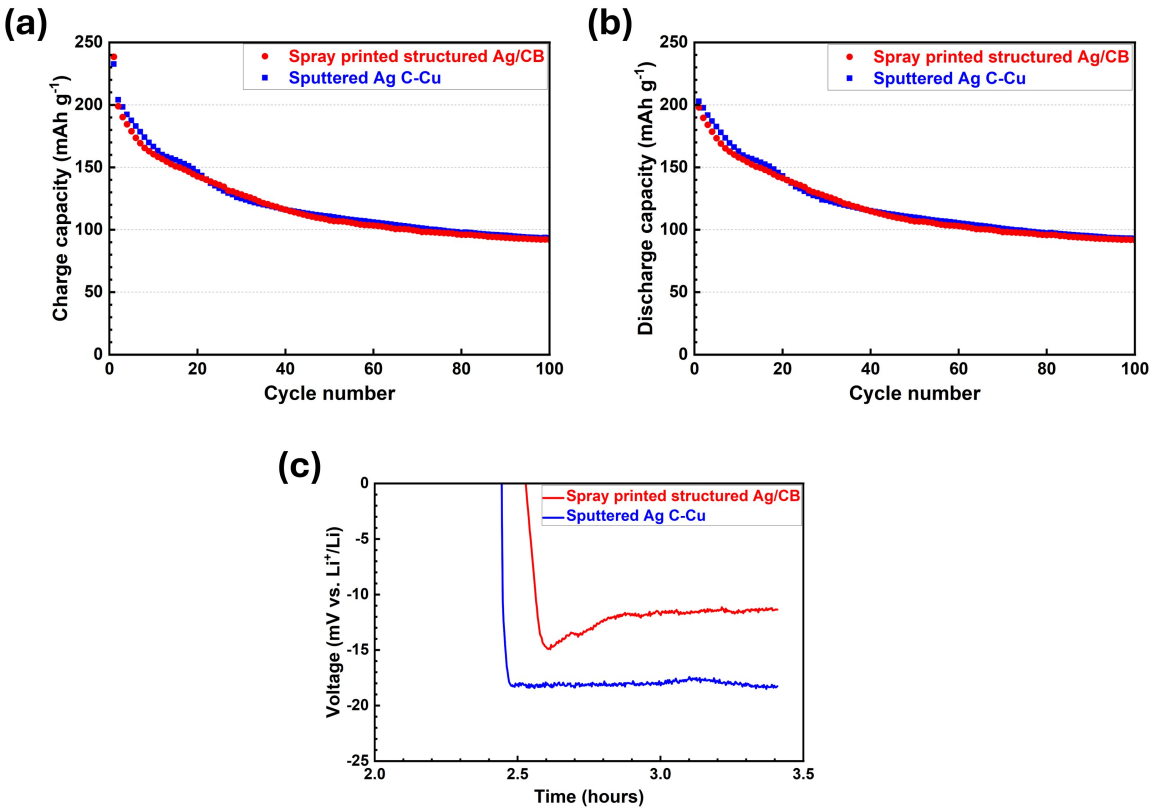

Figure 7.1: Cycling of SSB cells with structured Ag/CB and Ag C-Cu (100 nm) interlayers at 60 °C and 4 MPa stack pressure. Long-term (a) charge and (b) discharge capacity of full-cells with structured Ag/CB and Ag C-Cu (100 nm) interlayers at 1 mA/cm^2 charge/discharge current; (c) voltage/time during single-charge tests of three-electrode cells with structured Ag/C and Ag C-Cu (100 nm) interlayers at 1 mA/cm^2.

Building on the results, insights, and ideas here, some suggestions for further work are:

- Hybrid electrolytes could combine two or more types of SEs with complementary advantages, e.g. an SE with "soft" mechanical properties to ensure electrode wettability and interfacial contact, and "hard" SEs with mechanical toughness to suppress Li dendrite propagation [411]. Alternatively, SEs with stability at high electrochemical potentials on the cathode side could be coupled with SEs with high stability with Li on the anode side.

Manufacturing route	**Advantages**	**Disadvantages**
Slurry casting	Scalability; speed; maturity	Limited microstructural control; difficult to produce layers $<$ 10 μm
Spray printing	Microstructural control (e.g. layers); thickness control; scalability	Setup complexity; reproducibility yet to be demonstrated at scale
In-situ precipitation	Scalability; potential versatile applicability; safety	Relies on insulating polymeric binders; proof of concept at best
Sputtering	Maturity; thickness control; adhesion	Limited process flexibility

Table 7.1: Comparison of the advantages and disadvantages of different Ag/C interlayer manufacturing routes for anode-less SSBs.

- Hot-pressed three-electrode cells were consolidated in a hardened steel die set and subsequently retrieved and sealed in pouch cells for cycling tests. The retrieval of consolidated material from the electrically conducting die was necessary for the electrochemical testing to be meaningful, but the retrieval process was suspected of introducing microcracks into the SE and/or hybrid cathode. SSB assembly and disassembly could be improved by using a novel, modular die set of the type shown schematically in Figure 7.2. In this proposed design, the material is filled into an electrically insulating PEEK mould, which is placed inside a metallic die to provide structural support. The metallic die provides heat transfer but can be disassembled after the various compression steps and the PEEK mould containing the as fabricated pellet cell then transferred for cycling tests, without any need to retrieve or handle the cell before electrochemical testing. This setup, combined with binders with high thermal stability, may enable full cell assembly at high temperatures to promote the much-needed additional consolidation, and resulting improved

cycling performance. Hot pressing of the different material combinations, including dry processed SEs and Ag/C interlayers, would combine the different manufacturing techniques presented in this thesis to an integrated process.

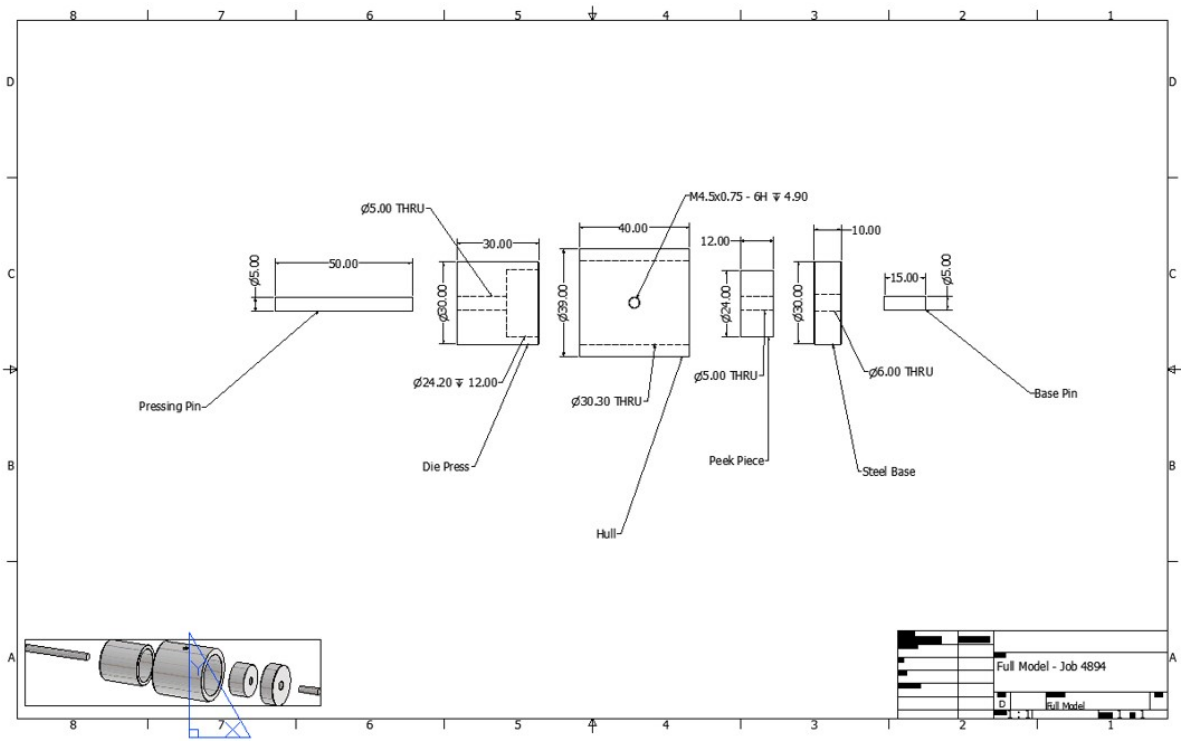

Figure 7.2: Technical drawing by Benjamin Morley of a modular hot-press die set.

- Spray printing as a flexible processing platform might be further applied to explore the effect of different processing parameters, such as Ag/C interlayer thickness, C morphologies, Ag load, or Ag particle sizes. Moreover, spray printing in an inert atmosphere would allow the combined preparation of Ag/C interlayers with other SSB components using the same process. However, a densification step in between or on the assembled cell would still be required to avoid surface asperities and to heal any cracks.

- The chemical precipitation of metallic nanoparticles on functional groups beyond carboxylate, for example, amine, amide, or hydroxyl, could be coupled with other metals other than Ag, for example, Zn, Al, Ni, or Fe.

- Although anode-free SSBs enable control over the thickness and anode capacity, and eliminate the need for problematic Li foil manufacturing, complex lithiation kinetics in the Ag/C interlayer require in-situ diagnosis conducted under realistic battery operation conditions [179]. Further insights into Li transport within the Ag/C structure, the processes of Li diffusion within Ag particles, and the intermediate and metastable phases of Ag particles during Li diffusion could enable improved interlayer designs. For example, non-noble metal alternatives to Ag could become applicable or an improved current collector surface design could control Li deposition/stripping [412].

Bibliography

[1] N. Boaretto, I. Garbayo, S. Valiyaveettil-SobhanRaj, A. Quintela, C. Li, M. Casas-Cabanas, and F. Aguesse, "Lithium Solid-State Batteries: State-of-the-Art and Challenges for Materials, Interfaces and Processing," *J. Power Sources*, vol. 502, no. 229919, 2021.

[2] B. Zakeri, G. Gissey, P. Dodds, and D. Subkhankulova, "Centralized vs. distributed energy storage - Benefits for residential users," *Energy*, vol. 236, no. 121443, 2021.

[3] T. Chen, Y. Jin, H. Lv, A. Yang, M. Liu, B. Chen, Y. Xie, and Q. Chen, "Applications of Lithium-Ion Batteries in Grid-Scale Energy Storage Systems," *Trans. Tianjin Univ.*, vol. 26 (3), pp. 208–217, 2020.

[4] P. Albertus, J. Manser, and S. Litzelman, "Long-Duration Electricity Storage Applications, Economics, and Technologies," *Joule*, vol. 4 (1), pp. 21–32, 2020.

[5] D. Dornbusch, R. Viggiano, J. Connell, Y. Lin, and V. Lvovich, "Practical considerations in designing solid state li-s cells for electric aviation," *Electrochim. Acta*, vol. 403, no. 139406, 2022.

[6] C.-Y. Wang, T. Liu, X.-G. Yang, S. Ge, N.V. Stanley, E.S. Rountree, Y. Leng, and B.D. McCarthy, "Fast charging of energy-dense lithium-ion batteries," *Nat.*, vol. 611, pp. 485—490, 2022.

[7] J. Sung, J. Heo, D.-H. Kim, S. Jo, Y.-C. Ha, D. Kim, S. Ahn, and J.-W. Park, "Recent advances in all-solid-state batteries for commercialization," *Mater. Chem. Front.*, vol. 8, pp. 1861–1887, 2024.

[8] J. Janek and W. Zeier, "A Solid Future for Battery Development," *Nat. Energy*, vol. 1 (9), no. 16141, 2016.

[9] J. Betz, G. Bieker, P. Meister, T. Placke, M. Winter, and R. Schmuch, "Theoretical versus Practical Energy: A Plea for More Transparency in the Energy Calculation of Different Rechargeable Battery Systems," *Adv. Energy Mater.*, vol. 9 (6), no. 1803170, 2019.

[10] K. Schönherr, B. Schumm, F. Hippauf, R. Lissy, H. Althues, C. Leyens, and S. Kaskel, "Liquid Lithium Metal Processing into Ultrathin Metal Anodes for Solid State Batteries," *Chem. Eng. J. Adv.*, vol. 9, no. 100218, 2022.

[11] K. Wood, M. Noked, and N. Dasgupta, "Lithium Metal Anodes: Toward an Improved Understanding of Coupled Morphological, Electrochemical, and Mechanical Behavior," *ACS Energy Lett.*, vol. 2 (3), pp. 664–672, 2017.

[12] H. Niu, N. Zhang, Y. Lu, Z. Zhang, M. Li, J. Liu, N. Zhang, W. Song, Y. Zhao, and Z. Miao, "Strategies toward the development of high-energy-density lithium batteries," *J. Energy Storage*, vol. 88, no. 111666, 2024.

[13] Y.-K. Sun, "Promising All-Solid-State Batteries for Future Electric Vehicles," *ACS Energy Lett.*, vol. 5 (10), pp. 3221–3223, 2020.

[14] P. Albertus, V. Anandan, C. Ban, N. Balsara, I. Belhaourak, J. Buettner-Garrett, Z. Chen, C. Daniel, M. Doeff, N.J. Dudney, et al., "Challenges for and Pathways toward Li-Metal-Based All-Solid-State Batteries," *ACS Energy Lett.*, vol. 6, pp. 1399–1404, 2021.

[15] D. Tan, A. Banerjee, Z. Deng, E. Wu, H. Nguyen, J.-M. Doux, X. Wang, J. Cheng, S. Ong, Y. Meng, and Z. Chen, "Enabling Thin and Flexible Solid-State Composite Electrolytes by the Scalable Solution Process," *ACS Appl. Energy Mater.*, vol. 2 (9), pp. 6542–6550, 2019.

[16] M. Singh, J. Kaiser, and H. Hahn, "Effect of Porosity on the Thick Electrodes for High Energy Density Lithium Ion Batteries for Stationary Applications," *Batteries*, vol. 2 (4), no. 35, 2016.

[17] Z. Jiang, Q. Han, S. Wang, and H. Wang, "Reducing the Interfacial Resistance in All-Solid-State Lithium Batteries Based on Oxide Ceramic Electrolytes," *ChemElectroChem*, vol. 6 (12), pp. 2970–2983, 2019.

[18] Y. Lu, C.-Z. Zhao, H. Yuan, J.-K. Hu, J.-Q. Huang, and Q. Zhang, "Dry electrode technology, the rising star in solid-state battery industrialization," *Matter*, vol. 5 (3), pp. 876–898, 2022.

[19] S.H. Lee, C. Huang, and P.S. Grant, "High energy lithium ion capacitors using hybrid cathodes comprising electrical double layer and intercalation host multi-layers," *Energy Storage Mater.*, vol. 33, pp. 408–415, 2020.

[20] C. Cheng, R. Drummond, S. Duncan, and P.S. Grant, "Micro-scale graded electrodes for improved dynamic and cycling performance of li-ion batteries," *J. Power Sources*, vol. 413, pp. 59–67, 2019.

[21] S.H. Lee, C. Huang, and P.S. Grant, "Layer-by-layer printing of multi-layered heterostructures using $Li_4Ti_5O_{12}$ and Si for high power Li-ion storage," *Nano Energy*, vol. 61, pp. 96–103, 2019.

[22] T. Hrbek, P. Kúš, Y. Kosto, M.G. Rodrígez, and I. Matolínová, "Magnetron-sputtered thin-film catalyst with low-Ir-Ru content for water electrolysis: Long-term stability and degradation analysis," *J. Power Sources*, vol. 556, no. 232375, 2023.

[23] C. Gómez-Sacedón, A.R. González-Elipe, V. Rodríguez-Pintor, J.M. Luque-Centeno, F. Yubero, J. Gil-Rostra, and A. de Lucas-Consuegra, "Recent advances in electrocatalysts fabrication by magnetron sputtering for alkaline water electrolysis," *Curr. Opin. Electrochem.*, vol. 49, no. 101622, 2025.

[24] M. Singh, J. Kaiser, and H. Hahn, "Thick Electrodes for High Energy Lithium Ion Batteries," *J. Electrochem. Soc.*, vol. 162 (7), pp. A1196–A1201, 2015.

[25] L. Wang, J. Li, G. Lu, W. Li, Q. Tao, C. Shi, H. Jin, G. Chen, and S. Wang, "Fundamentals of Electrolytes for Solid-State Batteries: Challenges and Perspectives," *Front. Mater.*, vol. 7, no. 111, 2020.

[26] M. Ma, M. Zhang, B. Jiang, Y. Du, B. Hu, and C. Sun, "A review of all-solid-state electrolytes for lithium batteries: high-voltage cathode materials, solid-state electrolytes and electrode–electrolyte interfaces," *Mater. Chem. Front.*, vol. 7, pp. 1268–1297, 2023.

[27] A. Joshi, D.K. Mishra, R. Singh, J. Zhang, and Y. Ding, "A comprehensive review of solid-state batteries," *Appl. Energy*, vol. 386, no. 125546, 2025.

[28] J. Fergus, "Recent developments in cathode materials for lithium ion batteries," *J. Power Sources*, vol. 195 (4), pp. 939–954, 2010.

[29] S.-B. Hong, Y.-J. Lee, U.-H. Kim, C. Bak, Y. Lee, W. Cho, H. Hah, Y.-K. Sun, and D.-W. Kim, "All-Solid-State Lithium Batteries: Li^+-Conducting Ionomer Binder for Dry-Processed Composite Cathodes," *ACS Energy Lett.*, vol. 7 (3), pp. 1092–1100, 2022.

[30] K. Yoon, J.-J. Kim, W. Seong, M. Lee, and K. Kang, "Investigation on the interface between $Li_{10}GeP_2S_{12}$ electrolyte and carbon conductive agents in all-solid-state lithium battery," *Sci. Rep.*, vol. 8 (1), no. 8066, 2018.

[31] M. Li, T. Liu, Z. Shi, W. Xue, Y.-S. Hu, H. Li, X. Huang, J. Li, L. Suo, and L. Chen, "Dense All-Electrochem-Active Electrodes for All-Solid-State Lithium Batteries," *Adv. Mater.*, vol. 33 (26), no. e2008723, 2021.

[32] Z. Moradi, A. Lanjan, R. Tyagi, and S. Srinivasan, "Review on current state, challenges, and potential solutions in solid-state batteries research," *J. Energy Storage*, vol. 73, Part C, no. 109048, 2023.

[33] J. Huang, C. Li, D. Jiang, J. Gao, L. Cheng, G. Li, H. Luo, Z.-L. Xu, D.-M. Shin, Y. Wang, Y. Lu, and Y. Kim, "Solid-State Electrolytes for Lithium Metal Batteries: State-of-the-Art and Perspectives," *Adv. Funct. Mater.*, vol. 35 (1), no. 2411171, 2025.

[34] J. Yang, Z. Cao, Y. Chen, X. Liu, Y. Xiang, Y. Yuan, C. Xin, Y. Xia, S. Huang, Z. Qiang, K. Fu, and J. Zhang, "Dry-Processable Polymer Electrolytes for Solid Manufactured Batteries," *ACS Nano*, vol. 17 (20), pp. 19903–19913, 2023.

[35] M. Armand, "Polymers with Ionic Conductivity," *Adv. Mater.*, vol. 2 (6-7), pp. 278–286, 1990.

[36] S.S. Park, S.A. Han, R. Chaudhary, J.H. Suh, J. Moon, M.-S. Park, and J.H. Kim, "Solid Electrolyte: Strategies to Address the Safety of All Solid-State Batteries," *Adv. Energ. Sust. Res.*, vol. 4 (11), no. 2300074, 2023.

[37] J. Li, X. Chen, S. Muhammad, S. Roy, H. Huang, C. Yu, Z. Ullah, Z. Wang, Y. Zhang, K. Wang, and B. Guo, "Development of solid polymer electrolytes for solid-state lithium battery applications," *Mater. Today Energy*, vol. 43, no. 101574, 2024.

[38] G.-R. Zhu, Q. Zhang, Q.-S. Liu, Q.-Y. Bai, Y.-Z. Quan, Y. Gao, G. Wu, and Y.-Z. Wang, "Non-flammable solvent-free liquid polymer electrolyte for lithium metal batteries," *Nat. Commun.*, vol. 14, no. 4617, 2023.

[39] P. Baudry, S. Lascaud, H. Majastre, and D. Bloch, "Lithium polymer battery development for electric vehicle application," *J. Power Sources*, vol. 68 (2), pp. 432–435, 1997.

[40] A. Blake, R. Kohlmeyer, J. Hardin, E. Carmona, B. Maruyama, J. Berrigan, H. Huang, and M. Durstock, "3D Printable Ceramic-Polymer Electrolytes for Flexible High-Performance Li-Ion Batteries with Enhanced Thermal Stability," *Adv. Energy Mater.*, vol. 7 (14), no. 1602920, 2017.

[41] W. Zaman and K. Hatzell, "Processing and manufacturing of next generation lithium-based all solid-state batteries," *Curr. Opin. Solid State Mater. Sci.*, vol. 26 (4), no. 101003, 2022.

[42] Z. Song, F. Chen, M. Martinez-Ibanez, W. Feng, M. Forsyth, Z. Zhou, M. Armand, and H. Zhang, "A reflection on polymer electrolytes for solid-state lithium metal batteries," *Nat. Commun.*, vol. 14, no. 4884, 2023.

[43] H.S. Kim, T. Kwon, C.B. Park, and B.J. Sung, "Temperature Dependence of Conformational Relaxation of Poly(ethylene oxide) Melts," *Polym.*, vol. 13 (22), no. 4049, 2021.

[44] X. Su, X.-P. Xu, Z.-Q. Ji, J. Wu, F. Ma, and L.-Z. Fan, "Polyethylene Oxide-Based Composite Solid Electrolytes for Lithium Batteries: Current Progress, Low-Temperature and High-Voltage Limitations, and Prospects," *Electrochem. Energy Rev.*, vol. 7, no. 2, 2024.

[45] H. Zhang, L. Zheng, F. Xu, W. Feng, H. Li, X. Huang, M. Armand, J. Nie, and Z. Zhou, "Lithium bis(fluorosulfonyl)imide/poly(ethylene oxide) polymer electrolyte," *Electrochim. Acta*, vol. 133, pp. 529–538, 2014.

[46] F. Croce, G.B. Appetecchi, L. and Persi, and B. Scrosati, "Nanocomposite polymer electrolytes for lithium batteries," *Nat.*, vol. 394 (6692), pp. 456–458, 1998.

[47] J. Mu, S. Liao, L. Shi, B. Su, F. Xu, Z. Guo, H. Li, and F. Wei, "Solid-state polymer electrolytes in lithium batteries: latest progress and perspective," *Polym. Chem.*, vol. 15 (6), pp. 473–499, 2024.

[48] R. Khurana, J. Schaefer, L. Archer, and G. Coates, "Suppression of lithium dendrite growth using cross-linked polyethylene/poly(ethylene oxide) electrolytes: a new approach for practical lithium-metal polymer batteries," *J. Am. Chem. Soc.*, vol. 136 (20), pp. 7395–7402, 2014.

[49] J. Li, Y. Lin, H. Yao, C. Yuan, and J. Liu, "Tuning thin-film electrolyte for lithium battery by grafting cyclic carbonate and combed poly(ethylene oxide) on polysiloxane," *ChemSusChem*, vol. 7 (7), pp. 1901–1908, 2014.

[50] R. Rohan, K. Pareek, Z. Chen, W. Cai, Y. Zhang, G. Xu, Z. Gao, and H. Cheng, "A high performance polysiloxane-based single ion conducting polymeric electrolyte membrane for application in lithium ion batteries," *J. Mater. Chem. A*, vol. 3 (40), pp. 20267–20276, 2015.

[51] J. Daigle, A. Vijh, P. Hovington, C. Gagnon, J. Hamel-Pâquet, S. Verreault, N. Turcotte, D. Clément, A. Guerfi, and K. Zaghib, "Lithium battery with solid polymer electrolyte based on comb-like copolymers," *J. Power Sources*, vol. 279, pp. 372–383, 2015.

[52] N. Boaretto, C. Joost, M. Seyfried, K. Vezzù, and V. Di Noto, "Conductivity and properties of polysiloxane-polyether cluster-LiTFSI networks as hybrid polymer electrolytes," *J. Power Sources*, vol. 325, pp. 427–437, 2016.

[53] I. Aldalur, M. Martinez-Ibañez, A. Krztoń-Maziopa, M. Piszcz, M. Armand, and H. Zhang, "Flowable polymer electrolytes for lithium metal batteries," *J. Power Sources*, vol. 423, pp. 218–226, 2019.

[54] S. Schmohl, X. He, and H. Wiemhöfer, "Boron Trifluoride Anionic Side Groups in Polyphosphazene Based Polymer Electrolyte with Enhanced Interfacial Stability in Lithium Batteries," *Polymers*, vol. 10 (12), no. 1350, 2018.

[55] W. Wei, Z. Xu, L. Xu, X. Zhang, H. Xiong, and J. Yang, "Flexible Ionic Conducting Elastomers for All-Solid-State Room-Temperature Lithium Batteries," *ACS Appl. Energy Mater.*, vol. 1 (12), pp. 6769–6773, 2018.

[56] M. Echeverri, N. Kim, and T. Kyu, "Ionic Conductivity in Relation to Ternary Phase Diagram of Poly(ethylene oxide), Succinonitrile, and Lithium Bis(trifluoromethane)sulfonimide Blends," *Macromol.*, vol. 45 (15), pp. 6068–6077, 2012.

[57] H. Zhao, F. Asfour, Y. Fu, Z. Jia, W. Yuan, Y. Bai, M. Ling, H. Hu, G. Baker, and G. Liu, "Plasticized Polymer Composite Single-Ion Conductors for Lithium Batteries," *ACS Appl. Mater. Interfaces*, vol. 7 (34), pp. 19494–19499, 2015.

[58] M. Balaish, J. Gonzalez-Rosillo, K. Kim, Y. Zhu, Z. Hood, and J. Rupp, "Processing thin but robust electrolytes for solid-state batteries," *Nat. Energy*, vol. 6 (3), pp. 227–239, 2021.

[59] M. Umair, S. Zhou, W. Li, H. Rana, J. Yang, L. Cheng, M. Li, S. Yu, and J. Wei, "Oxide Solid Electrolytes in Solid-State Batteries," *Batter. Supercaps*, no. e202400667, 2024.

[60] A. Machín, C. Morant, and F. Márquez, "Advancements and Challenges in Solid-State Battery Technology: An In-Depth Review of Solid Electrolytes and Anode Innovations," *Batteries*, vol. 10 (1), no. 29, 2024.

[61] J. Wolfenstine, J. Allen, J. Sakamoto, D. Siegel, and H. Choe, "Mechanical behavior of li-ion-conducting crystalline oxide-based solid electrolytes: a brief review," *Ionics*, vol. 24 (5), pp. 1271–1276, 2018.

[62] E. Cussen, "Structure and ionic conductivity in lithium garnets," *J. Mater. Chem.*, vol. 20 (25), pp. 5167–5173, 2010.

[63] Y. Ren, T. Danner, A. Moy, M. Finsterbusch, T. Hamann, J. Dippell, T. Fuchs, M. Müller, R. Hoft, A. Weber, et al., "Oxide-Based Solid-State Batteries: A Perspective on Composite Cathode Architecture," *Adv. Energy Mater.*, vol. 13 (1), no. 2201939, 2023.

[64] A. Schreiber, M. Rosen, K. Waetzig, K. Nikolowski, N. Schiffmann, H. Wiggers, M. Küpers, D. Fatthakova-Rohlfing, W. Kuckshinrichs, O. Guillon, and M. Finsterbusch, "Oxide ceramic electrolytes for all-solid-state lithium batteries – cost-cutting cell design and environmental impact," *Green Chem.*, vol. 25, pp. 399–414, 2023.

[65] Y.-H. Cho, E. Wolfenstine, S. Rangasamy, H. Kim, H. Choe, and J. Sakamoto, "Mechanical properties of the solid Li-ion conducting electrolyte: $Li_{0.33}La_{0.57}TiO_3$," *J. Mater. Sci.*, vol. 47 (16), pp. 5970–5977, 2012.

[66] R. Wei, S. Chen, T. Gao, and W. Liu, "Challenges, fabrications and horizons of oxide solid electrolytes for solid-state lithium batteries," *Nano Sel.*, vol. 2 (12), pp. 2256–2274, 2021.

[67] K. Kravchyk, D. Karabay, and M. Kovalenko, "On the feasibility of all-solid-state batteries with LLZO as a single electrolyte," *Sci. Rep.*, vol. 12 (1), no. 1177, 2022.

[68] J. Minkievicz, G.M. Jones, S. Ghanizadeh, S. Bostanchi, T.J. Wasely, S.A. Yamini, and V. Nekouie, "Large-scale manufacturing of solid-state electrolytes: Challenges, progress, and prospects," *Open Ceram.*, vol. 16, no. 100497, 2023.

[69] R. Mercier, J.-P. Malugani, B. Fahys, and G. Robert, "Superionic conduction in Li_2S-P_2S_5-LiI-glasses," *Solid State Ion.*, vol. 5, pp. 663–666, 1981.

[70] S. Kondo, K. Takada, and Y. Yamamura, "New lithium ion conductors based on Li_2S-SiS_2 system," *Solid State Ion.*, vol. 53-56, Part 2, pp. 1183–1186, 1992.

[71] M. Tatsumisago, M. Nagao, and A. Hayashi, "Recent development of sulfide solid electrolytes and interfacial modification for all-solid-state rechargeable lithium batteries," *J. Asian Ceram. Soc.*, vol. 1 (1), pp. 17–25, 2013.

[72] A. Kato, M. Nose, M. Yamamoto, A. Sakuda, A. Hayashi, and M. Tatsumisago, "Mechanical properties of sulfide glasses in all-solid-state batteries," *J. Ceram. Soc. Jpn.*, vol. 126 (9), pp. 719–727, 2018.

[73] A. Sakuda, A. Hayashi, and M. Tatsumisago, "Recent progress on interface formation in all-solid-state batteries," *Curr. Opin. Electrochem.*, vol. 6 (1), pp. 108–114, 2017.

[74] R. Kanno, T. Hata, Y. Kawamoto, and M. Irie, "Synthesis of a new lithium ionic conductor, thio-LISICON-lithium germanium sulfide system," *Solid State Ion.*, vol. 130 (1-2), pp. 97–104, 2000.

[75] M. Murayama, R. Kanno, M. Irie, S. Ito, T. Hata, N. Sonoyama, and Y. Kawamoto, "Synthesis of New Lithium Ionic Conductor Thio-LISICON-Lithium Silicon Sulfides System," *J. Solid State Chem.*, vol. 168 (1), pp. 140–148, 2002.

[76] R. Kanno and M. Murayama, "Lithium Ionic Conductor Thio-LISICON: The Li_2S-GeS_2-P_2S_5 System," *J. Electrochem. Soc.*, vol. 148 (7), no. A742, 2001.

[77] G. Sahu, Z. Lin, J. Li, Z. Liu, N. Dudney, and C. Liang, "Air-stable, high-conduction solid electrolytes of arsenic-substituted Li_4SnS_4," *Energy Environ. Sci.*, vol. 7 (3), pp. 1053–1058, 2014.

[78] D. Lin, Y. Liu, and Y. Cui, "Reviving the lithium metal anode for high-energy batteries," *Nat. Nanotechnol.*, vol. 12 (3), pp. 194–206, 2017.

[79] Y. Kato, S. Hori, T. Saito, K. Suzuki, M. Hirayama, A. Mitsui, M. Yonemura, H. Iba, and R. Kanno, "High-power all-solid-state batteries using sulfide superionic conductors," *Nat. Energy*, vol. 1 (4), no. 16030, 2016.

[80] Z. Wang, M. Wu, G. Liu, X. Lei, B. Xu, and C. Ouyang, "Elastic Properties of New Solid State Electrolyte Material $Li_{10}GeP_2S_{12}$: A Study from First-Principles Calculations," *Int. J. Electrochem. Sci.*, vol. 9 (2), pp. 562–568, 2014.

[81] H.-J. Deiseroth, S.-T. Kong, H. Eckert, J. Vannahme, C. Reiner, T. Zaiss, and M. Schlosser, "Li_6P_S5X: a class of crystalline Li-rich solids with an unusually high Li^+ mobility," *Angew. Chem., Int. Ed. Engl.*, vol. 47 (4), pp. 755–758, 2008.

[82] L. Zhou, K.-H. Park, X. Sun, F. Lalère, T. Adermann, P. Hartmann, and L. Nazar, "Solvent-Engineered Design of Argyrodite Li_6PS_5X (X = Cl, Br, I) Solid Electrolytes with High Ionic Conductivity," *ACS Energy Lett.*, vol. 4 (1), pp. 265–270, 2019.

[83] Z. Zhang, Y. Shao, B. Lotsch, Y.-S. Hu, H. Li, J. Janek, L. Nazar, C.-W. Nan, J. Maier, M. Armand, and L. Chen, "New horizons for inorganic solid state ion conductors," *Energy Environ. Sci.*, vol. 11, pp. 1945–1976, 2018.

[84] Y. Lee, S. Fujiki, C. Jung, N. Suzuki, N. Yashiro, R. Omoda, D. Ko, T. Shiratsuchi, T. Sugimoto, S. Ryu, and et al., "High-Energy Long-Cycling All-Solid-State Lithium Metal Batteries Enabled by Silver-Carbon Composite Anodes," *Nat. Energy*, vol. 5 (4), pp. 299–308, 2020.

[85] S. Li, Z. Yang, S.-B. Wang, M. Ye, H. He, X. Zhang, C.-W. Nan, and S. Wang, "Sulfide-based composite solid electrolyte films for all-solid-state batteries," *Commun. Mater.*, vol. 5, no. 44, 2024.

[86] J. Hu, S. Yang, Y. Pei, X. Wang, Y. Liao, S. Li, A. Yue, J.-Q. Huang, and H. Yuan, "Perspective on powder technology for all-solid-state batteries: How to pair sulfide electrolyte with high-voltage cathode," *Particuology*, vol. 86, pp. 55–66, 2024.

[87] Z. Wu, X. Li, C. Zheng, Z. Fan, W. Zhang, H. Huang, Y. Gan, Y. Xia, X. He, X. Tao, and J. Zhang, "Interfaces in Sulfide Solid Electrolyte-Based All-Solid-State Lithium Batteries: Characterization, Mechanism and Strategy," *Electrochem. Energy Rev.*, vol. 6, no. 10, 2023.

[88] T. Ohtomo, A. Hayashi, M. Tatsumisago, and K. Kawamoto, "Suppression of H_2S gas generation from the $75Li_2S{\cdot}25P_2S_5$ glass electrolyte by additives," *J. Mater. Sci.*, vol. 48 (11), pp. 4137–4142, 2013.

[89] J. Liang, X. Li, C. Wang, J.T. Kim, R. Yang, J. Wang, and X. Sun, "Current Status and Future Directions in Environmental Stability of Sulfide Solid-State Electrolytes for All-Solid-State Batteries," *Energy Mater. Adv.*, vol. 4, no. 0021, 2023.

[90] M. Liu, J.J. Hong, E. Sebti, K. Zhou, S. Wang, S. Feng, T. Pennebaker, Z. Hui, Q. Miao, E. Lu, et al., "Surface molecular engineering to enable processing of sulfide solid electrolytes in humid ambient air," *Nat. Commun.*, vol. 16, no. 213, 2025.

[91] X. Randrema, I.L. Mfiban, M. Soler, I. Profalitova, M. Berthault, R. Ramos, J. Lavie, E. De Vito, L. Blanc, S. Diry, et al., "Towards a Practical Use of Sulfide Solid Electrolytes in Solid-State

Batteries: Impact of Dry Room Exposure on H_2S Release and Material Properties," *Batter. Supercaps*, vol. 7 (1), no. e202300380, 2024.

[92] J.Y. Jung, S.A. Han, H.-S. Kim, J.H. Suh, J.-S. Yu, W. Cho, M.-S. Park, and J.H. Kim, "Dry-Electrode All-Solid-State Batteries Fortified with a Moisture Absorbent," *ACS Nano*, vol. 17 (16), pp. 15931—-15941, 2023.

[93] B. Man, Y. Zeng, Q. Liu, Y. Chen, X. Li, W. Luo, Z. Zhang, C. He, M. Jie, and S. Liu, "A Comprehensive Review of Sulfide Solid-State Electrolytes: Properties, Synthesis, Applications, and Challenges," *Crystals*, vol. 15 (6), no. 492, 2025.

[94] S. Wenzel, S. Sedlmaier, C. Dietrich, W. Zeier, and J. Janek, "Interfacial reactivity and interphase growth of argyrodite solid electrolytes at lithium metal electrodes," *Solid State Ion.*, vol. 318, pp. 102–112, 2018.

[95] B. Chen, C. Xu, H. Wang, and J. Zhou, "Insights into interfacial stability of Li_6PS_5Cl solid electrolytes with buffer layers," *Curr. Appl. Phys.*, vol. 19 (2), pp. 149–154, 2019.

[96] A. Manthiram, X. Yu, and S. Wang, "Lithium battery chemistries enabled by solid-state electrolytes," *Nat. Rev. Mater.*, vol. 2, no. 16103, 2017.

[97] S. Sun, C.-Z. Zhao, H. Yuan, Y. Lu, J.-K. Hu, J.-Q. Huang, and Q. Zhang, "Multiscale understanding of high-energy cathodes in solid-state batteries: from atomic scale to macroscopic scale," *Mater. Futures*, vol. 1, no. 012101, 2022.

[98] A.M. Kanno, L. Rabenberg, and A. Manthiram, "High Capacity Surface-Modified $LiCoO_2$ Cathodes for Lithium-Ion Batteries," *Electrochem. Solid-State Lett.*, vol. 6 (1), pp. A16–A18, 2002.

[99] J. Qiu, X. Liu, R. Chen, Q. Li, Y. Wang, P. Chen, L. Gan, S.-J. Lee, D. Nordlund, Y. Liu, X. Yu, X. Bai, H. Li, and L. Chen, "Enabling Stable Cycling of 4.2 V High-Voltage All-Solid-State Batteries with PEO-Based Solid Electrolyte," *Adv. Funct. Mater.*, vol. 30 (22), no. 1909392, 2020.

[100] M. Mikami, J. Saito, T. Ochiai, M. Takahashi, T. Takahashi, Y. Momma, K. Kuriki, R. Wada, K. Yokomizo, G. Kobayashi, S. Komaba, and S. Yamazaki, "Controlling lithium cobalt oxide phase transition using molten fluoride salt for improved lithium-ion batteries," *Commun. Mater.*, vol. 5, no. 108, 2024.

[101] G. Wang, Z. Bi, A. Zhang, P. Das, H. Lin, and Z.-S. Wu, "High-Voltage and Fast-Charging Lithium Cobalt Oxide Cathodes: From Key Challenges and Strategies to Future Perspectives," *Eng.*, vol. 37, pp. 105–127, 2024.

[102] K. Ito, K. Tamura, K. Shimizu, N.L. Yamada, K. Watanabe, K. Suzuki, R. Kanno, and M. Hirayama, "Degradation of a lithium cobalt oxide cathode under high voltage operation at an interface with an oxide solid electrolyte," *RSC Appl. Interfaces*, vol. 1, pp. 790–799, 2024.

[103] L. Wang, B. Chen, J. Ma, G. Cui, and L. Chen, "Reviving lithium cobalt oxide-based lithium secondary batteries-toward a higher energy density," *Chem. Soc. Rev.*, vol. 47 (17), pp. 6505–6602, 2018.

[104] F. Strauss, L. de Biasi, A.-Y. Kim, J. Hertle, S. Schweidler, J. Janek, P. Hartmann, and T. Brezesinski, "Rational Design of Quasi-Zero-Strain NCM Cathode Materials for Minimizing Volume Change Effects in All-Solid-State Batteries," *ACS Materials Lett.*, vol. 2 (1), pp. 84–88, 2019.

[105] Y. Yao, Z. Xue, C. Li, J. Li, J. He, X. Zhang, and Y. Xiang, "Progress and perspective of doping strategies for lithium cobalt oxide materials in lithium-ion batteries," *Energy Storage Mater.*, vol. 71, no. 103666, 2024.

[106] K. Hikima, K. Suzuki, S. Taminato, M. Hirayama, S. Yasuno, and R. Kanno, "Thin Film All-solid-state Battery Using Li_2MnO_3 Epitaxial Film Electrode," *Chem. Lett.*, vol. 48 (3), pp. 192–195, 2019.

[107] K. Hikima, Y. Hinuma, K. Shimizu, K. Suzuki, S. Taminato, M. Hirayama, T. Masuda, K. Tamura, and R. Kanno, "Reactions of the Li_2MnO_3 Cathode in an All-Solid-State Thin-Film Battery during Cycling," *ACS Appl. Mater. Interfaces*, vol. 13 (6), pp. 7650—7663, 2021.

[108] H.-Y. Jang, D. Eum, J. Cho, J. Lim, Y. Lee, J.-Y. Song, H. Park, B. Kim, D.-H. Kim, S.-P. Cho, S. Jo, J. Heo, S. Lee, J. Lim, and K. Kang, "Structurally robust lithium-rich layered oxides for high-energy and long-lasting cathodes," *Nat. Commun.*, vol. 15, no. 1288, 2024.

[109] L. De Biasi, B. Schwarz, T. Brezesinski, P. Hartmann, J. Janek, and H. Ehrenberg, "Chemical, Structural, and Electronic Aspects of Formation and Degradation Behavior on Different Length Scales of Ni-Rich NCM and Li-Rich HE-NCM Cathode Materials in Li-Ion Batteries," *Adv. Mater.*, vol. 31 (26), no. 1900985, 2019.

[110] Q. She, J. Xu, A. Huang, R. Zhou, Q. Shao, J. Wang, Y. Wang, Y. Sun, and X. Zhu, "Limiting cobalt fraction in lithium rich cathode materials for stable and fast activation," *Chem. Eng. Sci.*, vol. 284, no. 119526, 2024.

[111] G. Zhang, X. Wen, Y. Gao, R. Zhang, and Y. Huang, "Inhibiting Voltage Decay in Li-Rich Layered Oxide Cathode: From O3-Type to O2-Type Structural Design," *Nanomicro Lett.*, vol. 16, no. 260, 2024.

[112] S. Burke, M. Zhang, J.R. Croy, and Y.S. Meng, "Entropic stabilization in lithium-rich transition metal layered oxides – a perspective," *Next Mater.*, vol. 7, no. 100332, 2025.

[113] J. Liu, J. Wang, Y. Ni, K. Zhang, F. Cheng, and J. Chen, "Recent breakthroughs and perspectives of high-energy layered oxide cathode materials for lithium ion batteries," *Mater. Today*, vol. 43, pp. 132–165, 2021.

[114] A.W. Xiao, H.J. Lee, I. Capone, A. Robertson, T.-U. Wi, J. Fawdon, S. Wheeler, H.-W. Lee, N. Grobert, and M. Pasta, "Understanding the conversion mechanism and performance of monodisperse FeF_2 nanocrystal cathodes," *Nat. Mater.*, vol. 19, pp. 644—654, 2020.

[115] W. Lee, S. Muhammad, C. Sergey, H. Lee, J. Yoon, Y.-M. Kang, and W.-S. Yoon, "Advances in the Cathode Materials for Lithium Rechargeable Batteries," *Angew. Chem. Int. Ed.*, vol. 59 (7), pp. 2578–2605, 2020.

[116] X. Hua, A.S. Eggeman, E. Castillo-Martínez, R. Robert, H.S. Geddes, Z. Lu, C.J. Pickard, W. Meng, K.M. Wiaderek, N. Pereira, et al., "Revisiting metal fluorides as lithium-ion battery cathodes," *Nat. Mater.*, vol. 20, pp. 841—-850, 2021.

[117] A. Liu, H. Yuan, Y. Wang, Y. Liu, J. Luo, J. Nai, and X. Tao, "Reviewing metal fluorides as the cathode materials for high performance Li batteries," *Inf. Funct. Mater.*, vol. 1 (1), pp. 26–67, 2024.

[118] Y. Gao, J. Li, Y. Hua, Q. Yang, R. Holze, E. Mijowska, P.K. Chu, and X. Chen, "Recent advances of metal fluoride compounds cathode materials for lithium ion batteries: a review," *Mater. Futures*, vol. 3 (3), no. 032101, 2024.

[119] V. Riesgo-González, C.A. O'Keefe, C.P. Grey, and D.S. Wright, "Improving long-term capacity retention of nmc811 via lithium aluminate coatings using mixed-metal alkoxides," *J. Mater. Chem. A*, vol. 12 (33), pp. 22248–22261, 2024.

[120] W. Li, E.M. Erickson, and A. Manthiram, "High-nickel layered oxide cathodes for lithium-based automotive batteries," *Nat. Energy*, vol. 5, pp. 26–34, 2020.

[121] W. Zhang, F.H. Richter, S.P. Culver, T. Leichtweiss, J.G. Lozano, C. Dietrich, P.G. Bruce, W.G. Zeier, and J. Janek, "Degradation Mechanisms at the $Li_{10}GeP_2S_{12}/LiCoO_2$ Cathode Interface in an All-Solid-State Lithium-Ion Battery," *ACS Appl. Mater. Interfaces*, vol. 10 (26), pp. 22226––22236, 2018.

[122] S. Lou, Q. Liu, F. Zhang, Q. Liu, Z. Yu, T. Mu, Y. Zhao, J. Borovilas, Y. Chen, M. Ge, X. Xiao, W.-K. Lee, G. Yin, Y. Yang, X. Sun, and J. Wang, "Insights into interfacial effect and

local lithium-ion transport in polycrystalline cathodes of solid-state batteries," *Nat. Commun.*, vol. 11, no. 5700, 2020.

[123] R.C. McNulty, E. Hampson, L.N. Cutler, C.P. Grey, W.M. Dose, and L.R. Johnson, "Understanding the limits of Li-NMC811 half-cells," *J. Mater. Chem. A*, vol. 11 (34), pp. 18302–18312, 2023.

[124] C. Doerrer, I. Capone, S. Narayanan, J. Liu, C.R.M. Grovenor, M. Pasta, and P.S. Grant, "High Energy Density Single-Crystal NMC/Li_6PS_5Cl Cathodes for All-Solid-State Lithium-Metal Batteries," *ACS Appl. Mater. Interfaces*, vol. 13 (31), pp. 37809–37815, 2021.

[125] C. Doerrer, X. Gao, J. Bu, S. Wheeler, M. Pasta, P.G. Bruce, and P.S. Grant, "Fast-charging all-solid-state battery cathodes with long cycle life," *Nano Energy*, vol. 134, no. 110531, 2025.

[126] J. Liang, J. Hu, T. Zhou, Y. Li, X. Ren, S. Huang, X. Yang, Q. Zhang, and J. Liu, "Coating Ni-rich cathode with an amorphous carbon for improving the stability and electrochemical performance," *Compos. Commun.*, vol. 36, no. 101356, 2022.

[127] R. Schmuch, R. Wagner, G. Hörpel, T. Placke, and M. Winter, "Performance and Cost of Materials for Lithium-Based Rechargeable Automotive Batteries," *Nat. Energy*, vol. 3 (4), pp. 267–278, 2018.

[128] P. Panjan, A. Drnovšek, P. Gselman, M. Čekada, and M. Panjan, "Review of Growth Defects in Thin Films Prepared by PVD Techniques," *Coatings*, vol. 10 (5), no. 447, 2020.

[129] Y. Jiang and F. Ye, "Dead Lithium in Lithium Metal Batteries: Formation, Characterization and Strategies," *Chem. Eur. J.*, vol. 30 (43), no. e202400424, 2024.

[130] B.S. Vishnugopi and P.P. Mukherjee, ""Dead" lithium or back from the "dead"?," *Joule*, vol. 6 (2), pp. 291–293, 2022.

[131] M. Abdollahifar and A. Paolella, ""Dead Lithium" Formation and Mitigation Strategies in Anode-Free Li-Metal Batteries," *Batter. Supercaps*, vol. 8 (3), no. e202400505, 2025.

[132] Z. Ning, G. Li, D. Melvin, Y. Chen, J. Bu, D. Spencer-Jolly, J. Liu, B. Hu, X. Gao, J. Perera, et al., "Dendrite initiation and propagation in lithium metal solid-state batteries," *Nat.*, vol. 618 (7964), pp. 287–293, 2023.

[133] B. Zhang, B. Yuan, X. Yan, X. Han, J. Zhang, H. Tan, C. Wang, P. Yan, H. Gao, and Y. Liu, "Atomic mechanism of lithium dendrite penetration in solid electrolytes," *Nat. Commun.*, vol. 16, no. 1906, 2025.

[134] J. Zhang, A.F. Chadwick, and P.W. Voorhees, "Isolated metallic lithium formation in lithium-metal batteries," *Cell Rep. Phys. Sci.*, vol. 6 (1), no. 102360, 2025.

[135] R. Zhang, X. Shen, Y.-T. Zhang, X.-L. Zhong, H.-T. Ju, T.-X. Huang, X. Chen, J.-D. Zhang, and J.-Q. Huang, "Dead Lithium Formation in Lithium Metal Batteries: A Phase Field Model," *J. Energy Chem.*, vol. 71, pp. 29–35, 2022.

[136] F. Liu, R. Xu, Y. Wu, D. Boyle, A. Yang, J. Xu, Y. Zhu, Y. Ye, Z. Yu, Z. Zhang, X. Xiao, W. Huang, H. Wang, H. Chen, and Y. Cui, "Dynamic spatial progression of isolated lithium during battery operations," *Nat.*, vol. 600, pp. 659—663, 2021.

[137] B.R. Pant, Y. Ren, and Y. Cao, "Dendrite Growth and Dead Lithium Formation in Lithium Metal Batteries and Mitigation Using a Protective Layer: A Phase-Field Study," *ACS Appl. Mater. Interfaces*, vol. 16 (42), pp. 56947—56956, 2024.

[138] S. Liu, X. Ji, J. Yue, S. Hou, P. Wang, C. Cui, J. Chen, B. Shao, J. Li, F. Han, J. Tu, and C. Wang, "High Interfacial-Energy Interphase Promoting Safe Lithium Metal Batteries," *J. Am. Chem. Soc.*, vol. 142 (5), pp. 2438—-2447, 2020.

[139] Y. Wu, D. Lei, and C. Wang, "The formation of $LiAl_5O_8$ nanowires from bulk Li-Al alloy enables dendrite-free Li metal batteries," *Mater. Today Phys.*, vol. 18, no. 100395, 2021.

[140] Y. Huang, B. Shao, and F. Han, "Li alloy anodes for high-rate and high-areal-capacity solid-state batteries," *J. Mater. Chem. A*, vol. 10 (23), pp. 12350–12358, 2022.

[141] J. Cao, Y. Shi, A. Gao, G. Du, M. Dilxat, Y. Zhang, M. Cai, G. Qian, X. Lu, F. Xie, Y. Sun, and X. Lu, "Hierarchical Li electrochemistry using alloy-type anode for high-energy-density Li metal batteries," *Nat. Commun.*, vol. 15, no. 1354, 2024.

[142] W. Jing, K. Zou, X. Dai, J. Sun, Q. Tan, Y. Chen, and Y. Liu, "Li-Indium alloy anode for high-performance Li-metal batteries," *J. Alloys Compd.*, vol. 924, no. 166517, 2022.

[143] A. Santhosha, L. Medenbach, J. Buchheim, and P. Adelhelm, "The Indium-Lithium Electrode in Solid-State Lithium-Ion Batteries: Phase Formation, Redox Potentials, and Interface Stability," *Batter. Supercaps*, vol. 2 (6), pp. 524–529, 2019.

[144] S. Yanev, C. Heubner, K. Nikolowski, M. Partsch, H. Auer, and A. Michaelis, "Alleviating the Kinetic Limitations of the Li-In Alloy Anode in All-Solid-State Batteries," *J. Electrochem. Soc.*, vol. 171 (2), no. 020512, 2024.

[145] J. Li, J. Luo, X. Li, Y. Fu, J. Zhu, and X. Zhuang, "Li metal anode interface in sulfide-based all-solid-state Li batteries," *EcoMat*, vol. 5 (8), no. e12383, 2023.

[146] S. Luo, Z. Wang, X. Li, X. Liu, H. Wang, W. Ma, L. Zhang, L. Zhu, and X. Zhang, "Growth of lithium-indium dendrites in all-solid-state lithium-based batteries with sulfide electrolytes," *Nat. Commun.*, vol. 12, no. 6968, 2021.

[147] P. Molaiyan, B. Boz, G.S. dos Reis, R. Sliz, S. Wang, M. Borsari, U. Lassi, and A. Paolella, "Paving the path toward silicon as anode material for future solid-state batteries," *eTransportation*, vol. 23, no. 100391, 2025.

[148] M.T. McDowell, S.W. Lee, W.D. Nix, and Y. Cui, "25th Anniversary Article: Understanding the Lithiation of Silicon and Other Alloying Anodes for Lithium-Ion Batteries," *Adv. Mater.*, vol. 25 (36), pp. 4966–4985, 2013.

[149] Y. Wang, T. Liu, and J. Kumar, "Effect of Pressure on Lithium Metal Deposition and Stripping against Sulfide-Based Solid Electrolytes," *ACS Appl. Mater. Interfaces*, vol. 12 (31), pp. 34771—-34776, 2020.

[150] J.-M. Doux, H. Nguyen, D.H.S. Tan, A. Banerjee, X. Wang, E.A. Wu, C. Jo, H. Yang, and Y.S. Meng, "Stack Pressure Considerations for Room-Temperature All-Solid-State Lithium Metal Batteries," *Adv. Energy Mater.*, vol. 10 (1), no. 1903253, 2020.

[151] M.A. Hopcroft, W.D. Nix, and T.W. Kenny, "What is the Young's Modulus of Silicon?," *J. Microelectromechanical Syst.*, vol. 19 (2), pp. 229–238, 2010.

[152] J.Y. Kim, S. Jung, S.H. Kang, J. Park, M.J. Lee, D. Jin, D.O. Shin, Y.-G. Lee, and Y.M. Lee, "Graphite–Silicon Diffusion-Dependent Electrode with Short Effective Diffusion Length for High-Performance All-Solid-State Batteries," *Adv. Energy Mater.*, vol. 12 (3), no. 2103108, 2021.

[153] J. Wu, S. Liu, F. Han, X. Yao, and C. Wang, "Lithium/Sulfide All-Solid-State Batteries using Sulfide Electrolytes," *Adv. Mater.*, vol. 33 (6), no. 2000751, 2021.

[154] D. Cao, X. Sun, Y. Li, A. Anderson, W. Lu, and H. Zhu, "Long-Cycling Sulfide-Based All-Solid-State Batteries Enabled by Electrochemo-Mechanically Stable Electrodes," *Adv. Mater.*, vol. 34, no. 2200401, 2022.

[155] J. Lee, G. Oh, H.-Y. Jung, and J.-Y. Hwang, "Silicon Anode: A Perspective on Fast Charging Lithium-Ion Battery," *Inorganics*, vol. 11 (5), no. 182, 2023.

[156] J. Kim, J. Jung, J. Park, S. Lee, H. Lee, D. Lee, U. Paik, and T. Song, "Self-healing Si anodes with robust ionic and electronic conducting network by Ga-In-Sn liquid metal alloy in solid-state batteries," *Energy Storage Mater.*, vol. 76, no. 104108, 2025.

[157] D.L. Nelson, S.E. Sandoval, J. Pyo, D. Bistri, T.A. Thomas, K.A. Cavallaro, J.A. Lewis, A.S. Iyer, P. Shevchenko, C.V. Di Leo, and M.T. McDowell, "Fracture Dynamics in Silicon Anode Solid-State Batteries," *ACS Energy Lett.*, vol. 9 (12), pp. 6085—6095, 2024.

[158] P. Parikh, M. Sina, A. Banerjee, X. Wang, M.S. D'Souza, J.-M. Doux, E.A. Wu, O.Y. Trieu, Y. Gong, Q. Zhou, et al., "Role of Polyacrylic Acid (PAA) Binder on the Solid Electrolyte Interphase in Silicon Anodes," *Chem. Mater.*, vol. 31 (7), pp. 2535—-2544, 2019.

[159] Z. Sun, Q. Yin, H. Chen, M. Li, S. Zhou, S. Wen, J. Pan, Q. Zheng, B. Jiang, H. Liu, K. Kim, J. Li, X. Han, Y.-B. He, L. Zhang, M. Li, and Q. Zhang, "Building better solid-state batteries with silicon-based anodes," *Interd. Mater.*, vol. 2 (4), pp. 635–663, 2023.

[160] A. Pei, G. Zheng, F. Shi, Y. Li, and Y. Cui, "Nanoscale Nucleation and Growth of Electrodeposited Lithium Metal," *Nano Lett.*, vol. 17 (2), pp. 1132–1139, 2017.

[161] W. Huang, C. Zhao, P. Wu, H. Yuan, W. Feng, Z. Liu, Y. Lu, S. Sun, Z. Fu, J. Hu, and et al., "Anode-Free Solid-State Lithium Batteries: A Review," *Adv. Energy Mater.*, vol. 12 (26), no. 2201044, 2023.

[162] G. Feng, Y. Shi, H. Jia, S. Risal, X. Yang, P. Ruchhoeft, W.-C. Shih, Z. Fan, W. Xu, and X. Shan, "Progressive and instantaneous nature of lithium nucleation discovered by dynamic and operando imagings," *Sci. Adv.*, vol. 9 (21), no. eadg6813, 2023.

[163] C. Zor, S.J. Turrell, S.U. Uyanik, and S. Afyon, "Lithium Plating and Stripping: Toward Anode-Free Solid-State Batteries," *Adv. Energy Sustainability Res.*, vol. 5 (8), no. 2300001, 2023.

[164] X. Bai, G. Zhao, G. Yang, M. Wang, J. Zhang, and N. Zhang, "A Magnetic-Assisted Construction of Functional Gradient Interlayer for Dendrite-Free Solid-State Lithium Batteries," *Energy Storage Mater.*, vol. 63, no. 103041, 2023.

[165] D. Cao, T. Ji, Z. Wei, W. Liang, R. Bai, K.S. Burch, M. Geiwitz, and H. Zhu, "Enhancing Lithium Stripping Efficiency in Anode-Free Solid-State Batteries through Self-Regulated Internal Pressure," *Nano Lett.*, vol. 23 (20), pp. 9392—-9398, 2023.

[166] D. Liao, T. Cho, S. Sarna, M. Jangid, H. Kawakami, T. Kotaka, K. Aotani, and N. Dasgupta, "Interfacial dynamics of carbon interlayers in anode-free solid-state batteries," *J. Mater. Chem. A*, vol. 12 (10), pp. 5990–6003, 2024.

[167] J. Wang and H. Zhu, "Sulfide-Based Anode-Free Solid-State Batteries: Key Challenges and Emerging Solutions," *ACS Energy Lett.*, vol. 10, pp. 2377—2391, 2025.

[168] M.H. Futscher, T. Amelal, J. Sastre, A. Müller, J. Patidar, A. Aribia, K. Thorwarth, S. Siol, and Y.E. Romanyuk, "Influence of Amorphous Carbon Interlayers on Nucleation and Early Growth of Lithium Metal at the Current Collector-Solid Electrolyte Interface," *J. Mater. Chem. A*, vol. 10 (29), pp. 15535–15542, 2022.

[169] W. Feng, X. Dong, X. Zhang, Z. Lai, P. Li, C. Wang, Y. Wang, and Y. Xia, "Li/Garnet Interface Stabilization by Thermal-Decomposition Vapor Deposition of an Amorphous Carbon Layer," *Angew. Chem., Int. Ed. Engl.*, vol. 59 (13), pp. 5346–5349, 2020.

[170] L. Chen, J. Zhang, R.-A. Tong, J. Zhang, H. Wang, G. Shao, and C.-A. Wang, "Excellent Li/Garnet Interface Wettability Achieved by Porous Hard Carbon Layer for Solid State Li Metal Battery," *Small*, vol. 18 (8), no. 2106142, 2021.

[171] N. Suzuki, N. Yashiro, S. Fujiki, R. Omoda, T. Shiratsuchi, T. Watanabe, and Y. Aihara, "Highly Cyclable All–Solid–State Battery with Deposition–Type Lithium Metal Anode Based on Thin Carbon Black Layer," *Adv. Energy Sustainability Res.*, vol. 2 (11), no. 2100066, 2021.

[172] L. Su, H. Charalambous, Z. Cui, and A. Manthiram, "High-Efficiency, Anode-Free Lithium-Metal Batteries with a Close-Packed Homogeneous Lithium Morphology," *Energy Environ. Sci.*, vol. 15 (2), pp. 843–854, 2022.

[173] D. Jun, S.H. Park, J.E. Jung, S.G. Lee, K.S. Kim, J.Y. Kim, K.Y. Bae, S. Son, and Y.J. Lee, "Ultra-Stable Breathing Anode for Li-Free All-Solid-State Battery Based on Li Concentration Gradient in Magnesium Particles," *Adv. Funct. Mater.*, vol. 34 (8), no. 2310259, 2024.

[174] J. Wang, Z.and Xia, X. Ji, Y. Liu, J. Zhang, X. He, W. Zhang, H. Wan, and C. Wang, "Lithium Anode Interlayer Design for All-Solid-State Lithium-Metal Batteries," *Nat. Energy*, vol. 9 (3), pp. 1–12, 2024.

[175] O. Tamwattana, H. Park, J. Kim, I. Hwang, G. Yoon, T. Hwang, Y. Kang, J. Park, N. Meethong, and K. Kang, "High-Dielectric Polymer Coating for Uniform Lithium Deposition in Anode-Free Lithium Batteries," *ACS Energy Lett.*, vol. 6 (12), pp. 4416–4425, 2021.

[176] Q. Li, H. Pan, W. Li, Y. Wang, J. Wang, J. Zheng, X. Yu, H. Li, and L. Chen, "Homogeneous Interface Conductivity for Lithium Dendrite-Free Anode," *ACS Energy Lett.*, vol. 3 (9), pp. 2259–2266, 2018.

[177] R. Zhang, X.-R. Chen, X. Chen, X.-B. Cheng, X.-Q. Zhang, C. Yan, and Q. Zhang, "Lithiophilic Sites in Doped Graphene Guide Uniform Lithium Nucleation for Dendrite-Free Lithium Metal Anodes," *Angew. Chem., Int. Ed. Engl.*, vol. 56 (27), pp. 7764–7768, 2017.

[178] N. Lee, J. Oh, and J.W. Choi, "Anode-Less All-Solid-State Batteries: Recent Advances and Future Outlook," *Mater. Futures*, vol. 2 (1), no. 013502, 2023.

[179] S. Risal, C. Wu, F. Wang, F. Robles Hernandez, W. Zhu, Y. Yao, and Z. Fan, "Silver-Carbon Interlayers in Anode-Free Solid-State Lithium Metal Batteries: Current Development, Interfacial Issues, and Instability Challenges," *Carbon*, vol. 213, no. 118225, 2023.

[180] C. Yang, X. Zhang, J. Cao, D. Zhang, P. Kidkhunthod, S. Wannapaiboon, and J. Qin, "Interfacial Reconstruction for Regulating Zn^{2+} Deposition toward Ultrastable Zn Metal Anodes," *ACS Appl. Mater. Interfaces*, vol. 15 (22), pp. 26718–26727, 2023.

[181] Y. Wang, Z. Qu, S. Geng, M. Liao, L. Ye, Z. Shadike, X. Zhao, S. Wang, Q. Xu, B. Yuan, and et al., "Anode-Free Lithium Metal Batteries Based on an Ultrathin and Respirable Interphase Layer," *Angew. Chem., Int. Ed. Engl.*, vol. 62 (27), no. e202304978, 2023.

[182] L. Chen, J. Zhang, R. Tong, J. Zhang, H. Wang, G. Shao, and C. Wang, "Excellent Li/Garnet Interface Wettability Achieved by Porous Hard Carbon Layer for Solid State Li Metal Battery," *Small*, vol. 18 (8), no. 2106142, 2022.

[183] S. Park, D. Jun, J. Jung, S. Lee, G. Lee, and Y. Lee, "Clarification of Li Deposition Behavior on Anodes with a Porous Interlayer in Li-Free All-Solid-State Batteries," *J. Mater. Chem. A*, vol. 10 (41), pp. 21995–22006, 2022.

[184] H. Wan, B. Zhang, S. Liu, Z. Wang, J. Xu, and C. Wang, "Interface Design for High-Performance All-Solid-State Lithium Batteries," *Adv. Energy Mater.*, vol. 14 (19), no. 2303046, 2023.

[185] Z. Hu, J. Li, X. Zhang, and Y. Zhu, "Strategies to Improve the Performance of Li Metal Anode for Rechargeable Batteries," *Front. Chem.*, vol. 8, no. 409, 2020.

[186] G. Yoon, S. Kim, and J.-S. Kim, "Design Strategies for Anodes and Interfaces Toward Practical Solid-State Li-Metal Batteries," *Adv. Sci.*, vol. 10 (27), no. 2302263, 2023.

[187] X. Han, L. Gu, Z. Sun, M. Chen, Y. Zhang, L. Luo, M. Xu, S. Chen, H. Liu, J. Wan, et al., "Manipulating Charge-Transfer Kinetics and a Flow-Domain LiF-Rich Interphase to Enable High-Performance Microsized Silicon–Silver–Carbon Composite Anodes for Solid-State Batteries," *Energy Environ. Sci.*, vol. 16 (11), pp. 5395–5408, 2023.

[188] D. Spencer-Jolly, V. Agarwal, C. Doerrer, B. Hu, S. Zhang, D. Melvin, H. Gao, X. Gao, P. Adamson, O. Magdysyuk, et al., "Structural Changes in the Silver-Carbon Composite Anode Interlayer of Solid-State Batteries," *Joule*, vol. 7 (3), pp. 503–514, 2023.

[189] J.-S. Kim, G. Yoon, S. Kim, S. Sugata, N. Yashiro, S. Suzuki, M.-J. Lee, R. Kim, M. Badding, Z. Song, et al., "Surface Engineering of Inorganic Solid-State Electrolytes via Interlayers Strategy for Developing Long-Cycling Quasi-All-Solid-State Lithium Batteries," *Nat. Commun.*, vol. 14, no. 782, 2023.

[190] F. Xie, M.S. Diallo, H. Kim, Q.H. Tu, and G. Ceder, "The Microscopic Mechanism of Lithiation and Delithiation in the Ag/C Buffer Layer for Anode-Free Solid-State Batteries," *Adv. Energy Mater.*, vol. 14 (10), no. 2302960, 2024.

[191] K. Yan, Z. Lu, H.-W. Lee, F. Xiong, P.-C. Hsu, Y. Li, J. Zhao, S. Chu, and Y. Cui, "Selective Deposition and Stable Encapsulation of Lithium through Heterogeneous Seeded Growth," *Nat. Energy*, vol. 1 (3), no. 16010, 2016.

[192] H. Wang, Y. Li, Y. Li, Y. Liu, D. Lin, C. Zhu, G. Chen, A. Yang, K. Yan, H. Chen, and et al., "Wrinkled Graphene Cages as Hosts for High-Capacity Li Metal Anodes Shown by Cryogenic Electron Microscopy," *Nano Lett.*, vol. 19 (2), pp. 1326–1335, 2019.

[193] C. Yang, Y. Yao, S. He, H. Xie, E. Hitz, and L. Hu, "Ultrafine Silver Nanoparticles for Seeded Lithium Deposition toward Stable Lithium Metal Anode," *Adv. Mater.*, vol. 29 (38), no. 1702714, 2017.

[194] J. Yun, H. Shin, E.-S. Won, and J.-W. Lee, "Li Metal Storage in Porous Carbon Frameworks: Effect of Li–Substrate Interaction," *ECS Meet. Abstr.*, vol. MA2022-01, no. 529, 2022.

[195] S.H. Park, K.G. Naik, B.S. Vishnugopi, P.P. Mukherjee, and K.B. Hatzell, "Lithium Kinetics in Ag–C Porous Interlayer in Reservoir-Free Solid-State Batteries," *Adv. Energy Mater.*, vol. 15 (16), no. 2405129, 2025.

[196] V.V. Pavlyuk, G.S. Dmytric, I.I. Tarasiuk, I.V. Chumak, H. Pauly, and H. Ehrenberg, "Polymorphism of LiAg," *Solid State Sci.*, vol. 12 (2), pp. 274–280, 2010.

[197] Z. Liang, T. Li, H. Chi, J. Ziegelbauer, K. Sun, M. Wang, W. Zhang, T. Liu, Y.-T. Cheng, Z. Chen, X. Gayden, and C. Ban, "Solvent-Free Manufacturing of Lithium-Ion Battery Electrodes via Cold Plasma," *Energy Environ. Mater.*, vol. 7 (1), no. e12503, 2024.

[198] W. Jung, M. Jeon, S. Shin, J. Kim, H. Jung, B. Kim, J. Lee, Y. Chung, and H. Kim, "Functionalized Sulfide Solid Electrolyte with Air-Stable and Chemical-Resistant Oxysulfide Nanolayer for All-Solid-State Batteries," *ACS Omega*, vol. 5 (40), pp. 26015–26022, 2020.

[199] J. Ruhl, L. Riegger, M. Ghidiu, and W. Zeier, "Impact of Solvent Treatment of the Superionic Argyrodite Li_6PS_5Cl on Solid-State Battery Performance," *Adv. Energ. Sust. Res.*, vol. 2 (2), no. 2000077, 2021.

[200] S. Cangaz, F. Hippauf, F. Reuter, S. Doerfler, T. Abendroth, H. Althues, and S. Kaskel, "Enabling High-Energy Solid-State Batteries with Stable Anode Interphase by the Use of Columnar Silicon Anodes," *Adv. Energy Mater.*, vol. 10 (34), no. 2001320, 2020.

[201] T. Jiang, P. He, G. Wang, Y. Shen, C. Nan, and L. Fan, "Solvent-Free Synthesis of Thin, Flexible, Nonflammable Garnet-Based Composite Solid Electrolyte for All-Solid-State Lithium Batteries," *Adv. Energy Mater.*, vol. 10 (12), no. 1903376, 2020.

[202] C.D. Reynolds, H. Walker, A. Mahgoub, E. Adebayo, and E. Kendrick, "Battery electrode slurry rheology and its impact on manufacturing," *Energy Adv.*, vol. 4, pp. 84–93, 2025.

[203] C. Wang, R. Yu, H. Duan, Q. Lu, Q. Li, K. Adair, D. Bao, Y. Liu, R. Yang, J. Wang, S. Zhao, H. Huang, and X. Sun, "Solvent-Free Approach for Interweaving Freestanding and Ultrathin Inorganic Solid Electrolyte Membranes," *ACS Energy Lett.*, vol. 7 (1), pp. 410–416, 2022.

[204] B. Ludwig, Z. Zheng, W. Shou, Y. Wang, and H. Pan, "Solvent-Free Manufacturing of Electrodes for Lithium-ion Batteries," *Sci. Rep.*, vol. 6, no. 23150, 2016.

[205] J. Park, J. Kim, J. Kim, M. Kim, T. Song, and U. Paik, "Sustainable and cost-effective electrode manufacturing for advanced lithium batteries: the roll-to-roll dry coating process," *Chem. Sci.*, vol. 16, pp. 6598–6619, 2025.

[206] M. Ryu, Y.-K. Hong, S.-Y. Lee, and J. Park, "Ultrahigh loading dry-process for solvent-free lithium-ion battery electrode fabrication," *Nat. Commun.*, vol. 14, no. 1316, 2023.

[207] Y. Liu, X. Gong, C. Podder, F. Wang, Z. Li, J. Liu, J. Fu, X. Ma, P. Vanaphuti, R. Wang, A. Hitt, Y. Savsatli, Z. Yang, M. Ge, W.-K. Lee, B. Yonemoto, M. Tang, H. Pan, and Y. Wang, "Roll-to-roll solvent-free manufactured electrodes for fast-charging batteries," *Joule*, vol. 7 (5), pp. 952–970, 2023.

[208] W. Jin, G. Song, J.-K. Yoo, S.-K. Jung, T.-H. Kim, and J. Kim, "Advancements in Dry Electrode Technologies: Towards Sustainable and Efficient Battery Manufacturing," *ChemElectroChem*, vol. 11 (17), no. e202400288, 2024.

[209] H. Graebe, A. Netz, S. Baesch, V. Haerdtner, and A. Kwade, "A Solvent-Free Electrode Coating Technique for All Solid State Lithium Ion Batteries," *ECS Trans.*, vol. 77 (11), no. 393, 2017.

[210] Y. Li, Y. Wu, Z. Wang, J. Xu, T. Ma, L. Chen, H. Li, and F. Wu, "Progress in solvent-free dry-film technology for batteries and supercapacitors," *Mater. Today*, vol. 55, pp. 92–109, 2022.

[211] Y. Nam, D. Oh, S. Jung, and Y. Jung, "Toward practical all-solid-state lithium-ion batteries with high energy density and safety: Comparative study for electrodes fabricated by dry- and slurry-mixing processes," *J. Power Sources*, vol. 375, pp. 93–101, 2018.

[212] J. Wu, Z. Rao, Z. Cheng, L. Yuan, Z. Li, and Y. Huang, "Ultrathin, Flexible Polymer Electrolyte for Cost-Effective Fabrication of All-Solid-State Lithium Metal Batteries," *Adv. Energy Mater.*, vol. 9 (46), no. 1902767, 2019.

[213] D.-W. Park, N. Cañas, N. Wagner, and K. Friedrich, "Novel solvent-free direct coating process for battery electrodes and their electrochemical performance," *J. Power Sources*, vol. 306, pp. 758–763, 2016.

[214] J. Liu, B. Ludwig, Y. Liu, H. Pan, and Y. Wang, "Strengthening the Electrodes for Li-Ion Batteries with a Porous Adhesive Interlayer through Dry-Spraying Manufacturing," *ACS Appl. Mater. Interfaces*, vol. 11 (28), pp. 25081–25089, 2019.

[215] J. Liu, B. Ludwig, Y. Liu, Z. Zheng, F. Wang, M. Tang, J. Wang, J. Wang, H. Pan, and Y. Wang, "Scalable Dry Printing Manufacturing to Enable Long-Life and High Energy Lithium-Ion Batteries," *Adv. Mater. Technol.*, vol. 2 (10), no. 1700106, 2017.

[216] N. Verdier, G. Foran, D. Lepage, A. Prébé, D. Aymé-Perrot, and M. Dollé, "Challenges in Solvent-Free Methods for Manufacturing Electrodes and Electrolytes for Lithium-Based Batteries," *Polymers*, vol. 13 (3), no. 323, 2021.

[217] M. Al-Shroofy, Q. Zhang, J. Xu, T. Chen, A. Kaur, and Y.-T. Cheng, "Solvent-free dry powder coating process for low-cost manufacturing of $LiNi_{1/3}Mn_{1/3}Co_{1/3}O_2$ cathodes in lithium-ion batteries," *J. Power Sources*, vol. 352, pp. 187–193, 2017.

[218] B. Ludwig, J. Liu, I. Chen, Y. Liu, W. Shou, Y. Wang, and H. Pan, "Understanding Interfacial-Energy-Driven Dry Powder Mixing for Solvent-Free Additive Manufacturing of Li-Ion Battery Electrodes," *Adv. Mater. Interfaces*, vol. 4 (21), no. 1700570, 2017.

[219] V. Gregorio, N. García, and P. Tiemblo, "Addressing Manufacturability and Processability in Polymer Gel Electrolytes for Li/Na Batteries," *Polymers*, vol. 13 (13), no. 2093, 2021.

[220] S. El Khakani, N. Verdier, D. Lepage, A. Prébé, D. Aymé-Perrot, D. Rochefort, and M. Dollé, "Melt-processed electrode for lithium ion battery," *J. Power Sources*, vol. 454, no. 227884, 2020.

[221] Z. Li, A.M. Aboalsaud, X. Liu, R.L. Thankamony, I. Chen, Y. Li, and Z. Lai, "Scalable fabrication of solvent-free composite solid electrolyte by a continuous thermal-extrusion process," *J. Colloid Interface Sci.*, vol. 628, Part A, pp. 64–71, 2022.

[222] D. Cao, Y. Zhao, X. Sun, A. Natan, Y. Wang, P. Xiang, W. Wang, and H. Zhu, "Processing Strategies to Improve Cell-Level Energy Density of Metal Sulfide Electrolyte-Based All-Solid-State Li Metal Batteries and Beyond," *ACS Energy Lett.*, vol. 5 (11), pp. 3468–3489, 2020.

[223] O. Carneiro, A. Silva, and R. Gomes, "Fused deposition modeling with polypropylene," *Mater. Des.*, vol. 83, pp. 768–776, 2015.

[224] A. Maurel, M. Armand, S. Grugeon, B. Fleutot, C. Davoisne, H. Tortajada, M. Courty, S. Panier, and L. Dupont, "Poly(Ethylene Oxide)-LiTFSI Solid Polymer Electrolyte Filaments for Fused Deposition Modeling Three-Dimensional Printing," *J. Electrochem. Soc.*, vol. 167 (7), no. 070536, 2020.

[225] D. McOwen, S. Xu, Y. Gong, Y. Wen, G. Godbey, J. Gritton, T. Hamann, J. Dai, G. Hitz, L. Hu, and E. Wachsman, "3D-Printing Electrolytes for Solid-State Batteries," *Adv. Mater.*, vol. 30 (18), no. e1707132, 2018.

[226] Y. Wang, C. Chen, H. Xie, T. Gao, Y. Yao, G. Pastel, X. Han, Y. Li, J. Zhao, K. Fu, and L. Hu, "3D-Printed All-Fiber Li-Ion Battery toward Wearable Energy Storage," *Adv. Funct. Mater.*, vol. 27 (43), no. 1703140, 2017.

[227] A. Jandyal, I. Chaturvedi, I. Wazir, A. Raina, and M. Ul Haq, "3D printing - A review of processes, materials and applications in industry 4.0," *Sustain. Oper. Computers*, vol. 3, pp. 33–42, 2022.

[228] Y. Zhang, S. Lu, Z. Wang, V. Volkov, F. Lou, and Z. Yu, "Recent technology development in solvent-free electrode fabrication for lithium-ion batteries," *Renew. Sustain. Energy Rev.*, vol. 183, no. 113515, 2023.

[229] J. Li, Y. Li, S. Zhang, T. Liu, D. Li, and L. Ci, "Long cycle life all-solid-state batteries enabled by solvent-free approach for sulfide solid electrolyte and cathode films," *Chem. Eng. J.*, vol. 455, no. 140605, 2023.

[230] Y. Liu, H. Shao, J. Guo, H. Yu, H. Xu, X. Xu, Y. Deng, J. Wang, and H. Yan, "Toward scale-up of solid-state battery via dry electrode technology," *Next Energy*, vol. 7, no. 100221, 2025.

[231] Y. Nikodimos, M. Ihrig, B.W. Taklu, W.-N. Su, and B.J. Hwang, "Solvent-free fabrication of freestanding inorganic solid electrolyte membranes: Challenges, progress, and perspectives," *Energy Storage Mater.*, vol. 63, no. 103030, 2023.

[232] I. Hwang, "PTFE-Based Solvent-Free Electrode Manufacturing Process for Lithium-Ion Batteries and Solid-State Batteries," *ECS Meet. Abstr.*, vol. MA2024-02, no. 619, 2024.

[233] G.A.B. Matthews, S. Wheeler, J. Ramírez-Gonzalez, and P.S. Grant, "Solvent-free NMC electrodes for Li-ion batteries: unravelling the microstructure and formation of the PTFE nano-fibril network," *Front. Energy Res.*, vol. 11, no. 2302383, 2024.

[234] H. Choi, D. Moon, J. Sheem, J. Koo, S. Hong, S.-M. Oh, and Y.-J. Kim, "A Solvent-Free Process Enabled by Polytetrafluoroethlyene/Carbon Black Composites for Fabricating Electrodes for Lithium-Ion Batteries with a High Volumetric Energy," *J. Electrochem. Soc.*, vol. 170 (9), no. 090511, 2023.

[235] Y. Wang, S. Chen, K. Zhang, L. Huang, H. Shen, Z. Chen, C. Rong, G. Wang, and Z. Jiang, "A Polytetrafluoroethylene-Based Solvent-Free Procedure for the Manufacturing of Lithium-Ion Batteries," *Materials*, vol. 16 (22), no. 7232, 2023.

[236] S.A. Han, J.H. Suh, M.-S. Park, and J.H. Kim, "High-Loading Dry-Electrode for all Solid-State Batteries: Nanoarchitectonic Strategies and Emerging Applications," *Electrochem. Energy Rev.*, vol. 8, no. 5, 2025.

[237] Z. Zhang, L. Wu, D. Zhou, W. Weng, and X. Yao, "Flexible Sulfide Electrolyte Thin Membrane with Ultrahigh Ionic Conductivity for All-Solid-State Lithium Batteries," *Nano Lett.*, vol. 21 (12), pp. 5233–5239, 2021.

[238] T. Jiang, P. He, Y. Liang, and L.-Z. Fan, "All-dry synthesis of self-supporting thin $Li_{10}GeP_2S_{12}$ membrane and interface engineering for solid state lithium metal batteries," *Chem. Eng. J.*, vol. 421 (1), no. 129965, 2021.

[239] M. Ali, S. Nobukawa, and M. Yamaguchi, "Morphology development of polytetrafluoroethylene in a polypropylene melt (IUPAC Technical Report)," *Pure Appl. Chem.*, vol. 83 (10), pp. 1819–1830, 2011.

[240] T. Tomkovic and S. Hatzikiriakos, "Rheology and processing of polytetrafluoroethylene (PTFE) paste," *Can. J. Chem. Eng.*, vol. 98 (9), pp. 1852–1865, 2020.

[241] D.J. Lee, J. Jang, J.-P. Lee, J. Wu, Y.-T. Chen, J. Holoubek, K. Yu, S.-Y. Ham, Y. Jeon, T.-H. Kim, et al., "Physio-Electrochemically Durable Dry-Processed Solid-State Electrolyte Films for All-Solid-State Batteries," *Adv. Funct. Mater.*, vol. 33 (28), no. 2301341, 2023.

[242] F. Hippauf, B. Schumm, S. Doerfler, H. Althues, S. Fujiki, T. Shiratsuchi, T. Tsujimura, Y. Aihara, and S. Kaskel, "Overcoming binder limitations of sheet-type solid-state cathodes using a solvent-free dry-film approach," *Energy Storage Mater.*, vol. 21, pp. 390–398, 2019.

[243] D. Lee, Y. Shim, Y. Kim, G. Kwon, S.H. Choi, K. Kim, and D.-J. Yoo, "Shear force effect of the dry process on cathode contact coverage in all-solid-state batteries," *Nat. Commun.*, vol. 15, no. 4763, 2024.

[244] B. Emley, C. Wu, L. Zhao, Q. Ai, Q. Liang, Z. Chen, L. Guo, T. Terlier, J. Lou, Z. Fan, , and Y. Yao, "Impact of fabrication methods on binder distribution and charge transport in composite cathodes of all-solid-state batteries," *Mater. Futures*, vol. 2 (4), no. 045102, 2023.

[245] D. Lee and A. Manthiram, "Boosting the electrochemical performance with functionalized dry electrodes for practical all-solid-state batteries," *J. Mater. Chem. A*, vol. 12 (6), pp. 3323–3330, 2024.

[246] D. Chen, C. Hu, Q. Chen, G. Xue, L. Tang, Q. Dong, B. Chen, F. Zhang, M. Gao, J. Xu, Y. Shen, and L. Chen, "High ceramic content composite solid-state electrolyte films prepared via a scalable solvent-free process," *Nano Res.*, vol. 16, pp. 3847—-3854, 2023.

[247] L. Hu, Y. Ren, C. Wang, J. Li, Z. Wang, F. Sun, J. Ju, J. Ma, P. Han, S. Dong, and G. Cui, "Fusion Bonding Technique for Solvent-Free Fabrication of All-Solid-State Battery with Ultrathin Sulfide Electrolyte," *Adv. Mater.*, vol. 36, no. 2401909, 2024.

[248] S. Gong, S. Zhao, X. Chen, H. Liu, J. Deng, S. Li, X. Feng, Y. Li, X. Wu, and K. Pan, "Thermoplastic Polyamide Elastomers: Synthesis, Structures/Properties, and Applications," *Macromol. Mater. Eng.*, vol. 306, no. 2100568, 2021.

[249] L. Xu, Y. Lu, C.-Z. Zhao, H. Yuan, G.-L. Zhu, L.-P. Hou, Q. Zhang, and J.-Q. Huang, "Toward the Scale–Up of Solid–State Lithium Metal Batteries: The Gaps between Lab–Level Cells and Practical Large–Format Batteries," *Adv. Energy Mater.*, vol. 11 (4), no. 2002360, 2021.

[250] J. Bu, P. Leung, C. Huang, S. Lee, and P.S. Grant, "Co-spray printing of $LiFePO_4$ and PEO-$Li_{1.5}Al_{0.5}Ge_{1.5}(PO_4)_3$ hybrid electrodes for all-solid-state Li-ion battery applications," *J. Mater. Chem. A*, vol. 7 (32), pp. 19094–19103, 2019.

[251] S.H. Lee, C. Johnston, and P.S. Grant, "Scalable, Large-Area Printing of Pore-Array Electrodes for Ultrahigh Power Electrochemical Energy Storage," *ACS Appl. Mater. Interfaces*, vol. 11 (41), pp. 37859–37866, 2019.

[252] S.H. Lee, C. Huang, C. Johnston, and P.S. Grant, "Spray printing and optimization of anodes and cathodes for high performance Li-Ion batteries," *Electrochim. Acta*, vol. 292, pp. 546–557, 2018.

[253] S.H. Lee, C. Johnston, and P.S. Grant, "Scalable Multilayer Printing of Graphene Interfacial Layers for Ultrahigh Power Lithium-Ion Storage," *Energy Technol.*, vol. 8 (7), no. 2000253, 2020.

[254] C. Huang, A. Kim, D. Chung, E. Park, N. Young, K. Jurkschat, H. Kim, and P.S. Grant, "Multiscale Engineered Si/SiO_x Nanocomposite Electrodes for Lithium-Ion Batteries Using Layer-by-Layer Spray Deposition," *ACS Appl. Mater. Interfaces*, vol. 10 (18), pp. 15624–15633, 2018.

[255] P. Leung, J. Bu, P. Quijano Velasco, M. Roberts, N. Grobert, and and P.S. Grant, "Single-Step Spray Printing of Symmetric All-Organic Solid-State Batteries Based on Porous Textile Dye Electrodes," *Adv. Energy Mater.*, vol. 9 (39), no. 1901418, 2019.

[256] C. Doerrer, M. Metzler, G.A.B. Matthews, J. Bu, D. Spencer-Jolly, P.G. Bruce, M. Pasta, and P.S. Grant, "Spraying Li_6PS_5Cl and Silver-Carbon Multilayers to Facilitate Large-scale Fabrication of All-Solid-State Batteries," *Device*, vol. 2 (8), no. 100468, 2024.

[257] R.A. Surmenev, A.A. Ivanova, M. Epple, V.F. Pichugin, and M.A. Surmeneva, "Physical principles of radio-frequency magnetron sputter deposition of calcium-phosphate-based coating with tailored properties," *Surf. Coat. Technol.*, vol. 413, no. 127098, 2021.

[258] N.I. Cherkaschina, V.I. Pavlenko, S.V. Zaitsev, A.I. Gorodov, S.N. Domarev, R.V. Sidelnikov, and D.S. Romanyuk, "Adhesion Strength of Al, Cr, In, Mo, and W Metal Coatings Deposited on a Silicon–Carbon Film," *Coatings*, vol. 13 (8), no. 1353, 2023.

[259] R. Garg, S. Gonuguntla, S. Sk, M.S. Iqbal, A.O. Dada, U. Pal, and M. Ahmadipour, "Sputtering thin films: Materials, applications, challenges and future directions," *Adv. Colloid Interface Sci.*, vol. 330, no. 103203, 2024.

[260] C. Comparotto, A. Davydova, T. Ericson, L. Riekehr, M.V. Toro, T. Kubart, and J. Scragg, "Chalcogenide Perovskite $BaZrS_3$: Thin Film Growth by Sputtering and Rapid Thermal Processing," *ACS Appl. Energy Mater*, vol. 3 (3), pp. 2762—-2770, 2020.

[261] H. Hofsäss and K. Zhang, "Fundamentals of surfactant sputtering," *Nucl. Instr. Meth. Phys. Res. B*, vol. 267 (16), pp. 2731–2734, 2009.

[262] R. Sinha, R. Lavrijsen, M.A. Verheijen, E. Zoethout, H. Genuit, M.C.M. Van de Sanden, and A. Bieberle-Hütter, "Electrochemistry of Sputtered Hematite Photoanodes: A Comparison of Metallic DC versus Reactive RF Sputtering," *ACS Omega*, vol. 4 (5), pp. 9262—9270, 2019.

[263] S. Swann, "Magnetron sputtering," *Phys. Technol.*, vol. 19 (2), no. 67, 1988.

[264] T.D. Nguyen, V.T. Dang, N.M. Hung, V.K. Arepalli, J. Kim, M. Raj, and T.T.O. Ngyuen, "Synthesis of Ag-embedded SnS films by the RF method for photovoltaic applications," *Surf. Interf.*, vol. 25, no. 101151, 2021.

[265] S. Singh and B. Rout, "Simulation study of surface sputtering and distribution of ions in silicon due to low-energy high-fluence cobalt irradiation," *Surf. Interf.*, vol. 24, no. 101035, 2021.

[266] M. Cevro and G. Carter, "Ion beam sputtering and dual ion beam sputtering of titanium oxide films," *J. Phys. D: Appl. Phys.*, vol. 28 (9), pp. 1962–1976, 1995.

[267] S. Berg and T. Nyberg, "Fundamental understanding and modeling of reactive sputtering processes," *Thin Solid Films*, vol. 476 (2), pp. 215–230, 2005.

[268] S.L. Benz, I. Müller, A. Polity, P.J. Klar, M. Becker, and S. Chatterjee, "Decoupling inert and reactive gas supply to optimize ion beam sputter deposition apparatus for a more efficient material deposition," *Surf. Coat. Technol.*, vol. 486, no. 130831, 2024.

[269] P.J. Kelly and R.D. Arnell, "Magnetron sputtering: a review of recent developments and applications," *Vacuum*, vol. 56 (3), pp. 159–172, 2000.

[270] T. Summ, M. Ehrenwirth, C. Trinkl, W. Zörner, K. Pischow, R. Greenough, and M. Oyinlola, "Effect of argon concentration on thermal efficiency of gas-filled insulating glass flat-plate collectors," *Appl. Therm. Eng.*, vol. 230, Part A, no. 120657, 2023.

[271] G. Bräuer, "Magnetron Sputtering," *Comp. Mater. Process.*, vol. 4, pp. 57–73, 2014.

[272] N.S. Gultom, Q.-N. Ha, M.Z. Silitonga, and D.-H. Kuo, "Recent Progress of Electrocatalysts Made by Sputtering Technology for Electrocatalytic Water Splitting," *ChemCatChem*, vol. 16, no. e202301312, 2024.

[273] M.H. Futscher, L. Brinkman, A. Müller, J. Casella, A. Aribia, and Y.E. Romanyuk, "Monolithically-stacked thin-film solid-state batteries," *Commun. Chem.*, vol. 6, no. 110, 2023.

[274] H. Wei and H. Eilers, "From silver nanoparticles to thin films: Evolution of microstructure and electrical conduction on glass substrates," *J. Phys. Chem. Solids*, vol. 70 (2), pp. 459–465, 2009.

[275] A. Mohammedi, L. Monconduit, L. Stievano, and R. Younesi, "Measuring the Nucleation Overpotential in Lithium Metal Batteries: Never Forget the Counter Electrode!," *J. Electrochem. Soc.*, vol. 169 (7), no. 070509, 2022.

[276] P. Vadhva, J. Hu, M. Johnson, R. Stocker, M. Braglia, D. Brett, and A. Rettie, "Electrochemical Impedance Spectroscopy for All-Solid-State Batteries: Theory, Methods and Future Outlook," *ChemElectroChem*, vol. 8 (11), pp. 1930–1947, 2021.

[277] Z. Wang, D. Shi, J. Zhao, Z. Chu, D. Guo, C. Eze, X. Qu, Y. Lian, and A. Burke, "Battery health diagnostics: Bridging the gap between academia and industry," *eTransportation*, vol. 19, no. 100309, 2024.

[278] J. Smekens, R. Gopalakrishnan, N. Van den Steen, N. Omar, O. Hegazy, A. Hubin, and J. Van Mierlo, "Influence of Electrode Density on the Performance of Li-Ion Batteries: Experimental and Simulation Results," *Energies*, vol. 9 (2), no. 104, 2016.

[279] A.M. Boyce, X. Lu, D.J.L. Brett, and P.R. Shearing, "Exploring the influence of porosity and thickness on lithium-ion battery electrodes using an image-based model," *J. Power Sources*, vol. 542, no. 231779, 2022.

[280] T. Beuse, M. Fingerle, C. Wagner, M. Winter, and M. Börner, "Comprehensive Insights into the Porosity of Lithium-Ion Battery Electrodes: A Comparative Study on Positive Electrodes Based on $LiNi_{0.6}Mn_{0.2}Co_{0.2}O_2$ (NMC622)," *Batteries*, vol. 7 (4), no. 70, 2021.

[281] S.S. Zhang, T.R. Jow, K. Amine, and G.L. Henriksen, "$LiPF_6$–EC–EMC electrolyte for Li-ion battery," *J. Power Sources*, vol. 107 (1), pp. 18–23, 2002.

[282] K. Lee, S. Kim, J. Park, S.H. Park, A. Coskun, D.S. Jung, W. Cho, and J.W. Choi, "Selection of Binder and Solvent for Solution-Processed All-Solid-State Battery," *J. Electrochem. Soc.*, vol. 164, pp. A2075–A2081, 2017.

[283] A. Sakuda, K. Kuratani, M. Yamamoto, M. Takahashi, T. Takeuchi, and H. Kobayashi, "All-Solid-State Battery Electrode Sheets Prepared by a Slurry Coating Process," *J. Electrochem. Soc.*, vol. 164, pp. A2474–A2478, 2017.

[284] A. Tron, R. Hamid, N. Zhang, A. Paolella, P. Wulfert-Holzmann, V. Kolotygin, P. López-Aranguren, and A. Beutl, "Film processing of Li_6PS_5Cl electrolyte using different binders and their combinations," *J. Energy Storage*, vol. 66, no. 107480, 2023.

[285] C. Singer, S. Schmalzbauer, and R. Daub, "Influence of the slurry composition on thin-film components for the wet coating process of sulfide-based all-solid-state batteries," *J. Energy Storage*, vol. 68, no. 107703, 2023.

[286] T. Mori, T. Ochi, and K. Kitamura, "Characterization of slurries for lithium-ion battery cathodes by measuring their flow and change in hydrostatic pressure over time and clarification of the relationship between slurry and cathode properties," *J. Colloid Interface Sci.*, vol. 629, Part B, pp. 36–45, 2023.

[287] E. Zhen, J. Jiang, C. Lv, X. Huang, H. Xu, H. Dou, and X. Zhang, "Effects of binder content on low-cost solvent-free electrodes made by dry-spraying manufacturing for lithium-ion batteries," *J. Power Sources*, vol. 515, no. 230644, 2021.

[288] G. Schälicke, I. Landwehr, A. Dinter, K.-H. Pettinger, W. Haselrieder, and A. Kwade, "Solvent-Free Manufacturing of Electrodes for Lithium-Ion Batteries via Electrostatic Coating," *Energy Technol.*, vol. 8 (2), no. 1900309, 2019.

[289] M.E. Sotomayor, C. de la Torre-Gamarra, W. Bucheli, J.M. Amarilla, A. Varez, B. Levenfeld, and J.-Y. Sanchez, "Additive-free $Li_4Ti_5O_{12}$ thick electrodes for Li-ion batteries with high electrochemical performance," *J. Mater. Chem. A*, vol. 6, pp. 5952–5961, 2018.

[290] M.E. Sotomayor, C. de la Torre-Gamarra, B. Levenfeld, J.-Y. Sanchez, A. Varez, G.-T. Kim, A. Varzi and S. Passerini, "Ultra-thick battery electrodes for high gravimetric and volumetric energy density li-ion batteries," *J. Power Sources*, vol. 437, no. 226923, 2019.

[291] C. de la Torre-Gamarra, M. Sotomayor, J.-Y. Sanchez, B. Levenfeld, A. Varez, B. Laik, and J.-P. Pereira-Ramos, "High mass loading additive-free $LiFePO_4$ cathodes with 500 µm thickness for high areal capacity Li-ion batteries," *J. Power Sources*, vol. 458, no. 228033, 2020.

[292] H.A. Ardakani, E. Mitsoulis, and S.G. Hatzikiriakos, "Polytetrafluoroethylene (PTFE) Paste Extrusion: A Fibrillation Model and its Relation to Mechanical Properties," *Int. Polym. Process.*, vol. 28 (3), pp. 306–313, 2013.

[293] R. Shao, G. Wang, J. Chai, G. Wang, and G. Zhao, "Flexible, Reliable, and Lightweight Multiwalled Carbon Nanotube/Polytetrafluoroethylene Membranes with Dual-Nanofibrous Structure for Outstanding EMI Shielding and Multifunctional Applications," *Small*, vol. 20 (24), no. e2308992, 2024.

[294] J. Chai, G. Wang, A. Zhang, X. Li, Z. Xu, J. Zhao, and G. Zhao, "Robust polytetrafluoroethylene (PTFE) nanofibrous membrane achieved by shear-induced in-situ fibrillation for fast oil/water separation and solid removal in harsh solvents," *Chem. Eng. J.*, vol. 461, no. 141971, 2023.

[295] Y. Wang, R. Lim, K. Larson, A. Knab, D. Fontecha, S. Caverly, J. Song, C. Park, P. Albertus, G.W. Rubloff, S.B. Lee, and A.C. Kozen, "Chemical and Electrochemical Characterization of Hot-Pressed Li_6PS_5Cl Solid State Electrolyte: Operating Pressure-Invariant High Ionic Conductivity," *ChemSusChem*, vol. 17 (21), no. e202400718, 2024.

[296] A. Radionov, V. Gasiyarov, A. Shubin, and R. Khramshin, "Methods of Calculation of Load Modes of Roughing Stand Electric Drives of Wide-Strip Hot Rolling Mill," *2016 13th Int. Sci.-Tech. Conf. Actual Probl. Electron. Instrum. Eng. (APEIE)*, vol. 3, pp. 160–164, 2016.

[297] S. Mirzababaei, V.V.K. Doddapaneni, K. Lee, G.E. Paul, H. Pirgazi, K.-S. Tan, O. Ertorer, C.-H. Chang, B.K. Paul, and S. Pasebani, "Remarkable enhancement in thermal conductivity of stainless-steel leveraging metal composite via laser powder bed fusion: 316L-Cu composite," *Addit. Manuf.*, vol. 70, no. 103576, 2023.

[298] T. Böger, T. Bernges, Y. Li, P. Canepa, and W.G. Zeier, "Thermal Conductivities of Lithium-Ion-Conducting Solid Electrolytes," *ACS Appl. Energy Mater.*, vol. 6 (20), pp. 10704—10712, 2023.

[299] J. Piwowarczyk, R. Jedrzejewski, D. Moszynski, K. Kwiatkowski, A. Niemczyk, and J. Baranowska, "XPS and FTIR Studies of Polytetrafluoroethylene Thin Films Obtained by Physical Methods," *Polymers*, vol. 11, no. 1629, 2019.

[300] R. Henda, G. Wilson, J. Gray-Munro, O. Alshekhli, and A.M. McDonald, "Preparation of polytetrafluoroethylene by pulsed electron ablation: Deposition and wettability aspects," *Thin Solid Films*, vol. 520, pp. 1885–1889, 2012.

[301] G.B. Blanchet and S. Ismat Shah, "Deposition of polytetrafluoroethylene films by laser ablation," *Appl. Phys. Lett.*, vol. 62, pp. 1026—1028, 1993.

[302] R. Wang, G. Xu, and Y. He, "Structure and properties of polytetrafluoroethylene (PTFE) fibers," *e-Polymers*, vol. 17 (3), pp. 215—220, 2016.

[303] J. Zhang, J. Sun, H. Huang, C. Ji, M. Yan, and Z. Yuan, "Deformation and fracture mechanisms in the calendering process of lithium-ion battery electrodes," *Appl. Energy*, vol. 373, no. 123900, 2024.

[304] S. Zhao, Y.V. Petrov, Y. Zhang, G.A. Volkov, Z. Xu, and F. Huang, "Modeling of the thermal softening of metals under impact loads and their temperature–time correspondence," *Int. J. Eng. Sci.*, vol. 194, no. 103969, 2024.

[305] J. Hu, W. Chen, B. Zhao, and D. Yang, "Buildings with ETFE foils: A review on material properties, architectural performance and structural behavior," *Constr. Build. Mater.*, vol. 131, pp. 411–422, 2017.

[306] O. Mahmah, M.J. Adams, C.S. Omar, B. Gururajan, and A.D. Salman, "Roller compaction: Ribbon splitting and sticking," *Int. J. Pharm.*, vol. 559, pp. 156–172, 2019.

[307] K.W. Desmond and E.R. Weeks, "Influence of particle size distribution on random close packing of spheres," *Phys. Rev. E*, vol. 90, no. 022204, 2014.

[308] H.Y. Sohn and C. Moreland, "The effect of particle size distribution on packing density," *Can. J. Civ. Eng.*, vol. 46 (3), pp. 162–167, 1968.

[309] K.S. Singh, A. Henss, B. Mogwitz, A. Gautam, J. Horn, T. Krauskopf, S. Burkhardt, J. Sann, F.H. Richter, and J. Janek, "Li_6PS_5Cl microstructure and influence on dendrite growth in solid-state batteries with lithium metal anode," *Cell Rep. Phys. Sci.*, vol. 3 (9), no. 101043, 2022.

[310] S. Wang, X. Zhang, S. Liu, C. Xin, C. Xue, F. Richter, L. Li, L. Fan, Y. Lin, Y. Shen, J. Janek, and C.-W. Nan, "High-conductivity free-standing Li_6PS_5Cl/poly(vinylidene difluoride) composite solid electrolyte membranes for lithium-ion batteries," *J. Materiomics*, vol. 6 (1), pp. 70–76, 2020.

[311] S. Kim, Y.A. Chart, S. Naranayan, and M. Pasta, "Thin Solid Electrolyte Separators for Solid-State Lithium–Sulfur Batteries," *Nano Lett.*, vol. 22 (24), pp. 10176—10183, 2022.

[312] W.D. Richards, L.J. Miara, Y. Wang, J.C. Kim, and G. Ceder, "Interface stability in solid-state batteries," *Chem. Mater.*, vol. 28, pp. 266–273, 2016.

[313] K. Krauskopf, F.H. Richter, W.G. Zeier, and J. Janek, "Physicochemical Concepts of the Lithium Metal Anode in Solid-State Batteries," *Chem. Rev.*, vol. 120, pp. 7745–7794, 2020.

[314] A. Banerjee, X. Wang, C. Fang, E.A. Wu, and Y.S. Meng, "Interfaces and interphases in all-solid-state batteries with inorganic solid electrolytes," *Chem. Rev.*, vol. 120, pp. 6878—6933, 2020.

[315] B. Pang, Y. Gan, Y. Xia, H. Huang, X. He, and W. Zhang, "Regulation of the Interfaces Between Argyrodite Solid Electrolytes and Lithium Metal Anode," *Front. Chem.*, vol. 10, no. 837978, 2022.

[316] S. Naranayan, U. Ulissi, J.S. Gibson, Y.A. Chart, R.S. Weatherup, and M. Pasta, "Effect of current density on the solid electrolyte interphase formation at the lithium—Li_6PS_5Cl interface," *Nat. Commun.*, vol. 13, no. 7237, 2022.

[317] D. Tan, E. Wu, H. Nguyen, Z. Chen, M. Marple, J.-M. Doux, X. Wang, H. Yang, A. Banerjee, and Y. Meng, "Elucidating Reversible Electrochemical Redox of Li_6PS_5Cl Solid Electrolyte," *ACS Energy Lett.*, vol. 4 (10), pp. 2418—-2427, 2022.

[318] G. Nazri, "Preparation, structure and ionic conductivity of lithium phosphide," *Solid State Ion.*, vol. 34 (1-2), pp. 97–102, 1989.

[319] C. Yu, S. Ganapathy, E. van Eck, H. Wang, S. Basak, Z. Li, and M. Wagemaker, "Accessing the bottleneck in all-solid state batteries, lithium-ion transport over the solid-electrolyte-electrode interface.," *Nat. Commun.*, vol. 8, no. 1086, 2017.

[320] P. Lu, C. Li, E.W. Schneider, and S.J. Harris, "Chemistry, Impedance, and Morphology Evolution in Solid Electrolyte Interphase Films during Formation in Lithium Ion Batteries," *J. Phys. Chem. C*, vol. 118 (2), pp. 896–903, 2013.

[321] R. Schlenker, D. Stepien, P. Koch, T. Hupfer, S. Indris, B. Roling, V. Miß, A. Fuchs, M. Wilhelmi, and H. Ehrenberg, "Understanding the Lifetime of Battery Cells Based on Solid-State Li_6PS_5Cl Electrolyte Paired with Lithium Metal Electrode," *ACS Appl. Mater. Interfaces*, vol. 12 (7), pp. 20012–20025, 2020.

[322] J. Kasemchainan, S. Zekoll, D. Spencer-Jolly, Z. Ning, G.O. Hartley, J. Marrow, and P.G. Bruce, "Critical stripping current leads to dendrite formation on plating in lithium anode solid electrolyte cells," *Nat. Materials*, vol. 18, pp. 1105–1111, 2019.

[323] J. Irvine, D. Sinclair, and A. West, "Electroceramics: Characterization by Impedance Spectroscopy," *Adv. Mater.*, vol. 2 (3), pp. 132–138, 1990.

[324] J. Jamnik, J. Maier, and S. Pejovnik, "A powerful electrical network model for the impedance of mixed conductors," *Electrochim. Acta*, vol. 44 (24), pp. 4139–4145, 1999.

[325] M. Rosner, S. Cangaz, A. Dupuy, F. Hippauf, S. Dörfler, T. Abendroth, B. Schumm, H. Althues, and S. Kaskel, "Toward Higher Energy Density All-Solid-State Batteries by Production of Freestanding Thin Solid Sulfidic Electrolyte Membranes in a Roll-to-Roll Process," *Adv. Energy Mater.*, vol. 15 (19), no. 2404790, 2025.

[326] D. Tan, Y. Meng, and J. Jang, "Scaling up high-energy-density sulfidic solid-state batteries: A lab-to-pilot perspective," *Joule*, vol. 6 (8), pp. 1755–1769, 2022.

[327] J.V. Campos, I.R. Lavagnini, V. Avila, B. Yoon, S. Ghose, R. Raj, E.M.J.A. Pallone, and L.M. Jesus, "On the Arrhenius-like behavior of conductivity during flash sintering of 3 mol% yttria stabilized zirconia ceramics," *Scr. Mater.*, vol. 203, no. 114093, 2021.

[328] J. Baek, B. Yoon, H. Jeong, J. Jeong, S. Mamidi, H.-K. Seo, C.-R. Lee, and I. Seo, "Dependences of ionic conductivity and activation energy on germanium content in superionic $Li_{1.4}Al_{0.4}Ge_xTi_{(1.6-x)}(PO_4)_3$ solid electrolytes," *J. Electroanal. Chem.*, vol. 920, no. 116631, 2022.

[329] C. Yu, S. Ganapathy, J. Hageman, L. van Eijck, E. van Eck, L. Zhang, T. Schwietert, S. Basak, E.M. Kelder, and M. Wagemaker, "Facile Synthesis toward the Optimal Structure-Conductivity Characteristics of the Argyrodite Li_6PS_5Cl Solid-State Electrolyte," *ACS Appl. Mater. Interfaces*, vol. 10 (39), pp. 33296—-33306, 2018.

[330] S. Wang, Y. Zhang, X. Zhang, T. Liu, Y.-H. Lin, Y. Shen, L. Li, and C.-W. Nan, "High-Conductivity Argyrodite Li_6PS_5Cl Solid Electrolytes Prepared via Optimized Sintering Processes for All-Solid-State Lithium-Sulfur Batteries," *ACS Appl. Mater. Interfaces*, vol. 10, pp. 42279–42285, 2018.

[331] S. Choi, J. Ann, J. Do, S. Lim, C. Park, and D. Shin, "Application of Rod-Like Li^6PS^5Cl Directly Synthesized by a Liquid Phase Process to Sheet-Type Electrodes for All-Solid-State Lithium Batteries," *J. Electrochem. Soc.*, vol. 166 (3), pp. A5193–A5200, 2018.

[332] J. Lee, S. Ju, S. Hwang, J. You, J. Jung, Y. Kang, and S. Han, "Disorder-Dependent Li Diffusion in Li_6PS_5Cl Investigated by Machine-Learning Potential," *ACS Appl. Mater. Interfaces*, vol. 16, pp. 46442—46453, 2024.

[333] S. Yubuchi, H. Tsukasaki, A. Sakuda, S. Mori, A. Hayashi, and M. Tatsumisago, "Quantitative analysis of crystallinity in an argyrodite sulfide-based solid electrolyte synthesized via solution processing," *RSC Adv.*, vol. 25 (9), pp. 14465–14471, 2019.

[334] T. Fuchs, C. Haslam, F.H. Richter, J. Sakamoto, and J. Janek, "Evaluating the Use of Critical Current Density Tests of Symmetric Lithium Transference Cells with Solid Electrolytes," *Adv. Energy Mater.*, vol. 45 (13), no. 2302383, 2023.

[335] H. Schmalzried and J. Janek, "Berichte der Bunsengesellschaft für physikalische Chemie," *Nat. Energy*, vol. 102 (2), pp. 127–143, 1998.

[336] V. Raj, V. Venturi, V.R. Kankanallu, B. Kuiri, V. Viswanathan, and N.P.B. Aetukur, "Direct correlation between void formation and lithium dendrite growth in solid-state electrolytes with interlayers," *Nat Mater.*, vol. 9, pp. 1050–1056, 2022.

[337] K. Krauskopf, H. Hartmann, W.G. Zeier, and J. Janek, "Toward a Fundamental Understanding of the Lithium Metal Anode in Solid-State Batteries—An Electrochemo-Mechanical Study on

the Garnet-Type Solid Electrolyte $Li_{6.25}Al_{0.25}La_3Zr_2O_{12}$," *ACS Appl. Mater. Interfaces*, vol. 11 (15), pp. 14463–14477, 2019.

[338] Y. Lu, C.-Z. Zhao, J.-K. Hu, S. Sun, H. Yuan, Z.-H. Fu, X. Chen, J.-Q. Huang, M. Ouyang, and Q. Zang, "The void formation behaviors in working solid-state Li metal batteries," *Sci. Adv.*, vol. 8 (45), no. eadd0510, 2022.

[339] Y. Gao, X. Sang, Y. Chen, Y. Li, B. Liu, J. Sheng, Y. Feng, L. Li, H. Liu, X. Wang, C. Kuang, and Y. Zhai, "Polydopamine modification electrospun polyacrylonitrile fibrous membrane with decreased pore size and dendrite mitigation for lithium ion battery," *J. Mater. Sci.*, vol. 55, pp. 3549—3560, 2020.

[340] Y. Li, G. Zhang, B. Chen, W. Zhao, L. Sha, D. Wang, J. Yu, and S. Shi, "Understanding the separator pore size inhibition effect on lithium dendrite via phase-field simulations," *Chin. Chem. Lett.*, vol. 33, pp. 3287–3290, 2022.

[341] A. Jana, D.R. Ely, and R.E. Garcia, "Dendrite-separator interactions in lithium-based batteries," *J. Power Sources*, vol. 275, pp. 912–921, 2015.

[342] O. Crowther and A. West, "Effect of Electrolyte Composition on Lithium Dendrite Growth," *J. Electrochem. Soc.*, vol. 155 (11), pp. A806–A811, 2008.

[343] A. van der Ven, R. McMeeking, R. Clément, and K. Garikipati, "Ferroelastic toughening: Can it solve the mechanics challenges of solid electrolytes?," *Curr. Opin. Solid State Mater. Sci.*, vol. 27 (2), no. 101056, 2023.

[344] P. Albertus, S. Babinec, S. Litzelman, and A. Newman, "Status and challenges in enabling the lithium metal electrode for high-energy and low-cost rechargeable batteries," *Nat. Energy*, vol. 3, pp. 16–21, 2017.

[345] M.-Y. He and J.W. Hutchinson, "Crack deflection at an interface between dissimilar elastic materials," *Int. J. Solids Struct.*, vol. 25 (9), pp. 1053–1067, 1989.

[346] T. Yu, X. Zhu, H. Yu, P. Wu, C. Li, X. Han, and M. Chen, "Material extrusion-based additive manufacturing of zirconia toughened alumina: Machinability, mechanical properties and biocompatibility," *J. Manuf. Process.*, vol. 94, pp. 120–132, 2023.

[347] S.A. Dhar, H.T. Mumu, S. Sarker, and A.K.M. Rashi, "Influences of sintering time on the structures and mechanical properties of zirconia toughened alumina nanocomposites," *Mater. Today: Proceedings*, vol. 44, Part 1, pp. 1356–1360, 2021.

[348] Y. Zadorozhnaya, T.A. Khabas, O.V. Tiunova, and S.E. Malykhin, "Effect of grain size and amount of zirconia on the physical and mechanical properties and the wear resistance of zirconia-toughened alumina," *Ceram. Int.*, vol. 46 (7), pp. 9263–9270, 2020.

[349] Y. Wade-Zhu, J. Wade-Zhu, H. Wu, J. Binner, and B. Vaidhyanathan, "The ballistic impact performance of nanocrystalline zirconia-toughened alumina (nZTA) and alumina ceramics," *J. Eur. Ceram. Soc.*, vol. 41 (2), pp. 1427–1437, 2021.

[350] A. Opalinska, I. Malka, W. Dzwolak, T. Chudoba, A. Presz, and W. Lojkowski, "Size-dependent density of zirconia nanoparticles," *Beilstein J. Nanotech.*, vol. 6, pp. 27—35, 2015.

[351] S.D. Mouhamad, T. Shi, Y. Zhang, X. Peng, I. Shozib, Y. Wang, L.J. Miara, M.C. Scott, Q.H. Tu, and G. Ceder, "Effect of solid-electrolyte pellet density on failure of solid-state batteries," *Nat. Commun.*, vol. 15 (858), pp. 7778–7781, 2024.

[352] C.-H. Yim, M.S.E. Houache, E.A. Baranova, and Y. Abu-Lebdeh, "Understanding key limiting factors for the development of all-solid-state-batteries," *Chem. Eng. J. Adv.*, vol. 13, no. 100436, 2023.

[353] J. Wan, J. Xie, X. Kong, Z. Liu, K. Liu, F. Shi, A. Pei, H. Chen, W. Chen, J. Chen, X. Zhang, L. Zong, J. Wang, L.-Q. Chen, J. Qin, and Y. Cui, "Ultrathin, flexible, solid polymer composite electrolyte enabled with aligned nanoporous host for lithium batteries," *Nat Nanotechnol.*, vol. 14 (7), pp. 705–711, 2019.

[354] C. Zhao, M. Lyu, C. Bi, S. Huo, S. Li, and W. Xue, "Synthesis of high ionic conductivity Li_6PS_5Cl solid electrolyte by second sintering process," *Results Chem.*, vol. 4, no. 103969, 2022.

[355] J. Li, Y. Li, S. Zhang, D. Li, and L. Ci, "Two-step sintering of sulfide solid electrolyte with improved electrochemical properties for all-solid-state lithium batteries," *eTransportation*, vol. 16, no. 100236, 2023.

[356] A.N. Garcia, N. Viciano, and R. Font, "Products obtained in the fuel-rich combustion of PTFE at high temperature," *J. Anal. Appl. Pyrol.*, vol. 80 (1), pp. 85—91, 2007.

[357] B. Li, S. Li, M. Shen, Y. Xiao, J. Zhang, G. Xiong, and Z. Zhang, "Tribological behaviour of acrylonitrile-butadiene rubber under thermal oxidation ageing," *Polym. Test.*, vol. 93, no. 106954, 2021.

[358] Y. Ren and E.D. Wachsman, "All Solid-State Li/LLZO/LCO Battery Enabled by Alumina Interfacial Coating," *J. Electrochem. Soc.*, vol. 4 (169), no. 040529, 2022.

[359] Y. Zhang, X. Gao, Y. Mei, Z. Tang, D. Luo, and J. Deng, "Study of graphite interlayer modification on the interfacial stability of solid electrolyte $Li_7La_3Zr_2O_{12}$ with lithium metal anode," *J. Alloys Compd.*, vol. 933, no. 167736, 2023.

[360] Y. Huang, B. Shao, Y. Wang, and F. Han, "Solid-state silicon anode with extremely high initial coulombic efficiency," *EES*, vol. 16 (4), pp. 1569–1580, 2023.

[361] A. Masias, N. Felten, R. Garcia-Mendez, J. Wolfenstine, and J. Sakamoto, "Elastic, Plastic, and Creep Mechanical Properties of Lithium Metal," *J. Mater. Sci.*, vol. 54 (3), pp. 2585–2600, 2019.

[362] K. Kanamura, S. Shiraishi, and Z. Takehara, "Electrochemical Deposition of Very Smooth Lithium Using Nonaqueous Electrolytes Containing HF," *J. Electrochem. Soc.*, vol. 143 (7), pp. 2187–2197, 1996.

[363] B.J. Neudecker, N.J. Dudney, and J.B. Bates, ""Lithium-Free" Thin-Film Battery with In Situ Plated Li Anode," *J. Electrochem. Soc.*, vol. 147 (2), no. 517, 2000.

[364] S. Jeong, Y. Li, W. Sim, J. Mun, J. Kim, and H. Jeong, "Advances of Sulfide-Type Solid-State Batteries with Negative Electrodes: Progress and Perspectives," *EcoMat*, vol. 5 (6), no. e12338, 2023.

[365] S.J. Yoo, C.-Y. Kim, J.W. Shin, S.-G. Lee, J.-M. Jeong, Y.-J. Kim, S.-H. Lee, and J.-G. Kim, "Characterization of an Amorphous Carbon Film Covering a Mo Grid During in situ Heating TEM Study," *Mater. Charact.*, vol. 78, pp. 31–36, 2013.

[366] B. Kwiecińska, S. Pusz, and B. Valentine, "Application of Electron Microscopy TEM and SEM for Analysis of Coals, Organic-Rich Shales and Carbonaceous Matter," *Int. J. Coal Geol.*, vol. 211, no. 103203, 2019.

[367] P. Ruz, S. Banerjee, M. Pandey, V. Sudarsan, P.U. Sastry, and R.J. Kshirsagar, "Structural Evolution of Turbostratic Carbon: Implications in H_2 Storage," *Solid State Sci.*, vol. 62, pp. 105–111, 2016.

[368] P. Biswal, S. Stalin, A. Kludze, S. Choudhury, and L. Archer, "Nucleation and Early Stage Growth of Li Electrodeposits," *Nano Lett.*, vol. 19 (11), pp. 8191–8200, 2019.

[369] C. Haslam and J. Sakamoto, "Stable Lithium Plating in "Lithium Metal-Free" Solid-State Batteries Enabled by Seeded Lithium Nucleation," *J. Electrochem. Soc.*, vol. 170 (4), no. 040524, 2023.

[370] M. Tikekar, S. Choudhury, Z. Tu, and L. Archer, "Design Principles for Electrolytes and Interfaces for Stable Lithium-Metal Batteries," *Nat. Energy*, vol. 1, no. 16114, 2016.

[371] Y. Nomura, K. Yamamoto, M. Fujii, T. Hirayama, E. Igaki, and K. Saitoh, "Dynamic Imaging of Lithium in Solid-State Batteries by Operando Electron Energy-Loss Spectroscopy with Sparse Coding," *Nat. Commun.*, vol. 11, no. 2824, 2020.

[372] P. Hovington, V. Timoshevskii, S. Burgess, H. Demers, P. Statham, R. Gauvin, and K. Zaghib, "Can We Detect Li K X-Ray in Lithium Compounds Using Energy Dispersive Spectroscopy?," *Scanning*, vol. 38 (6), pp. 571–578, 2016.

[373] H. W. Wenzel, "Quantitative secondary ion mass spectrometry: A review," *Surf. Interface Anal.*, vol. 2 (2), pp. 56–74, 1980.

[374] N. Laegreid and G. Wehner, "Sputtering Yields of Metals for Ar^+ and Ne^+ Ions with Energies from 50 to 600 ev," *J. Appl. Phys.*, vol. 32 (3), pp. 365–369, 1961.

[375] K.L. Moore, M. Schröder, and C.R.M. Grovenor, "Imaging secondary ion mass spectroscopy. in *handbook of nanoscopy*; van tendeloo, g.; van dyck, d.; pennycook, s., eds.; wiley: Hoboken, new jersey, u.s," pp. 709–744, 2012.

[376] S. Otto, Y. Moryson, T. Krauskopf, K. Peppler, J. Sann, J. Janek, and A. Henss, "In-Depth Characterization of Lithium-Metal Surfaces with XPS and ToF-SIMS: Toward Better Understanding of the Passivation Layer," *Chem. Mater.*, vol. 33 (3), pp. 859–867, 2021.

[377] S. Otto, L. Riegger, T. Fuchs, S. Kayser, P. Schweitzer, S. Burkhardt, A. Henss, and J. Janek, "In Situ Investigation of Lithium Metal–Solid Electrolyte Anode Interfaces with ToF-SIMS," *Adv. Mater. Interfaces*, vol. 9 (13), no. 2102387, 2022.

[378] P.G. Bruce, B. Scrosati, and J.-M. Tarascon, "Nanomaterials for rechargeable lithium batteries," *Angew. Chem., Int. Ed. Engl.*, vol. 47 (16), pp. 2930–2946, 2008.

[379] P. Poizot, S. Laruelle, S. Grugeon, L. Dupont, and J. Tarascon, "Nano-sized transition-metal oxides as negative-electrode materials for lithium-ion batteries," *Nat.*, vol. 407, pp. 496—-499, 2000.

[380] C.K. Chan, H. Peng, G. Liu, K. McIlwrath, X.F. Zhang, R.A. Huggins, and Y. Cui, "High-performance lithium battery anodes using silicon nanowires," *Nat. Nanotechnol.*, vol. 3, pp. 31—-35, 2007.

[381] C.-M. Park, H. Jung, and H.-J. Sohn, "Electrochemical Behaviors and Reaction Mechanism of Nanosilver with Lithium," *Electrochem. Solid-State Lett.*, vol. 12 (9), no. A171, 2009.

[382] J.E. Marshall, A. Zhenova, S. Roberts, T. Petchey, P. Zhu, C.E.J. Dancer, C.R. McElroy, E. Kendrick, and V. Goodship, "On the Solubility and Stability of Polyvinylidene Fluoride," *Polym.*, vol. 13 (9), no. 1354, 2021.

[383] D.W. Xing, M.S. Lee, and S.H. Choi, "Separation of Ag(I) by Ion Exchange and Cementation from a Raffinate Containing Ag(I), Ni(II) and Zn(II) and Traces of Cu(II) and Sn(II)," *Process.*, vol. 6, no. 112, 2018.

[384] S. Lu, F. Lou, and Z. Yu, "Recent Progress in Two-Dimensional Materials for Electrocatalytic CO_2 Reduction," *Catal.*, vol. 12 (2), no. 228, 2022.

[385] G.M. Zarkadas, A. Stergiou, and G. Papanastasiou, "Influence of citric acid on the silver electrodeposition from aqueous $AgNO_3$ solutions," *Electrochim. Acta*, vol. 50 (25-26), pp. 5022–5031, 2005.

[386] S.E. Sandoval, J.A. Lewis, B.S. Vishnugopi, D.L. Nelson, M.M. Schneider, F.J.Q. Cortes, C.M. Matthews, J. Watt, M. Tian, P. Shevchenko, et al., "Structural and electrochemical evolution of alloy interfacial layers in anode-free solid-state batteries," *Joule*, vol. 7 (9), pp. 2054–2073, 2023.

[387] G. Taillades and J. Sarradin, "Silver: high performance anode for thin film lithium ion batteries," *J. Power Sources*, vol. 125 (2), pp. 199–205, 2004.

[388] S. Sun, H. Li, and Z. Xu, "Impact of Surface Area in Evaluation of Catalyst Activity," *Joule*, vol. 2 (6), pp. 1024–1027, 2018.

[389] P. Bernard, P. Stelmachowski, P. Broś, W. Makowski, and A. Kotarba, "Demonstration of the Influence of Specific Surface Area on Reaction Rate in Heterogeneous Catalysis," *J. Chem. Educ.*, vol. 98 (3), pp. 935–940, 2021.

[390] P. Afzali, E. Gibertini, and L. Magagnin, "Improved plating/stripping in anode-free lithium metal batteries through electrodeposition of lithiophilic zinc thin films," *Electrochim. Acta*, vol. 488, no. 144190, 2024.

[391] S.J. Raab, R. Guschlbauer, M.A. Lodes, and C. Koerner, "Thermal and Electrical Conductivity of 99.9% Pure Copper Processed via Selective Electron Beam Melting," *Adv. Eng. Mater.*, vol. 18 (9), pp. 1661–1666, 2016.

[392] N. Emalya, T. Tarmizi, S. Suhendrayatna, E. Munawar, Y. Yunardi, and U. Fathanah, "Enhancing Energy Production and Pollutants Removal in Landfill Leachate Using Anode-Modified Sediment Microbial Fuel Cells," *Ecol. Eng. Environ. Tech.*, vol. 25 (3), pp. 28–37, 2024.

[393] L. Fallarino, U.N. Chishti, A. Pesce, G. Accardo, A. Rafique, M. Casas-Cabanas, and P. López-Aranguren, "Towards lithium-free solid-state batteries with nanoscale Ag/Cu sputtered bilayer electrodes," *Chem. Commun.*, vol. 59, pp. 12346–12349, 2023.

[394] S. Mirbagheri, E. Gibertini, and L. Magagnin, "Inkjet-Printed Silver Lithiophilic Sites on Copper Current Collectors: Tuning the Interfacial Electrochemistry for Anode-Free Lithium Batteries," *Batteries*, vol. 10 (10), no. 369, 2024.

[395] A. Müller, L. Paravicini, J. Morzy, M. Krause, J. Casella, N. Osenciat, M.H. Futscher, and Y.E. Romanyuk, "Influence of Au, Pt, and C Seed Layers on Lithium Nucleation Dynamics for Anode-Free Solid-State Batteries," *ACS Appl. Mater. Interfaces*, vol. 16 (1), pp. 695–703, 2007.

[396] K.-Y. Cho, S.-H. Hong, J. Kwon, H. Song, S. Kim, S. Jo, and K. Eom, "Effects of a nanometrically formed lithiophilic silver@copper current collector on the electrochemical nucleation and growth behaviors of lithium metal anodes," *Appl. Surf. Sci.*, vol. 554, no. 149578, 2021.

[397] Y. Li, J.P. Tu, D.Q. Shi, X.H. Huang, H.M. Wu, Y.F. Yuan, and X.B. Zhao, "DC magnetron sputtering prepared Ag-C single bond thin film anode for thin film lithium ion microbatteries," *J. Alloys Compd.*, vol. 436 (1-2), pp. 290–293, 2007.

[398] D.-S. Ko, S. Kim, S. Lee, Y. G., D. Kim, C. Shin, D. Kim, J. Lee, S. Sul, D.-J. Yun, and C. Jung, "Mechanism of stable lithium plating and stripping in a metal-interlayer-inserted anode-less solid-state lithium metal battery," *Nat. Commun.*, vol. 16, no. 1066, 2025.

[399] B. Aktekin, L. Riegger, S.-K. Otto, T. Fuchs, A. Henss, and J. Janek, "SEI growth on Lithium metal anodes in solid-state batteries quantified with coulometric titration time analysis," *Nat. Commun.*, vol. 14, no. 6946, 2023.

[400] P. Molaiyan, M. Abdollahifar, B. Boz, A. Beutl, M. Krammer, N. Zhang, A. Tron, M. Romio, M. Ricci, R. Adelung, A. Kwade, U. Lassi, and A. Paolella, "Optimizing Current Collector Interfaces for Efficient "Anode-Free" Lithium Metal Batteries," *Adv. Funct. Mater.*, vol. 34, no. 2311301, 2024.

[401] K. Tang, L. Tian, Y. Zhang, and Z.J. Xu, "Anode-free lithium metal batteries: a promising flexible energy storage system," *J. Mater. Chem. A*, vol. 12, pp. 16268—-16292, 2024.

[402] B.C. Serban, O. Buiu, N. Dumbravescu, C. Cobianu, V. Avramescu, M. Brezeanu, M. Bumbac, and C.M. Nicolescu, "Oxidized Carbon Nanohorns as Novel Sensing Layer for Resistive Humidity Sensor," *Acta Chim. Slov.*, vol. 67 (2), pp. 469–475, 2020.

[403] A. Dychalska, P. Popielarski, W. Franków, K. Fabisiak, K. Paprocki, and M. Szybowicz, "Study of CVD diamond layers with amorphous carbon admixture by Raman scattering spectroscopy," *Mater. Sci.-Pol.*, vol. 33 (4), pp. 799–805, 2015.

[404] J.-B. Wu, M.-L. Lin, X. Cong, H.-N. Liu, and P.-H. Tan, "Raman spectroscopy of graphene-based materials and its applications in related devices," *Chem. Soc. Rev.*, vol. 47, pp. 1822–1873, 2018.

[405] M. Pena-Alvarez, E. Del Corro, F. Langa, V. Baonza, and M. Taravillo, "Morphological changes in carbon nanohorns under stress: a combined Raman spectroscopy and TEM study," *RSC Adv.*, vol. 6, no. 49543, 2016.

[406] R.J. Nemanich and S.A. Solin, "First- and second-order Raman scattering from finite-size crystals of graphite," *Phys. Rev. B*, vol. 20 (2), pp. 392–401, 1979.

[407] N. Larouche and B.L. Stansfield, "Classifying nanostructured carbons using graphitic indices derived from raman spectra," *Carbon*, vol. 48, pp. 620–629, 2010.

[408] O. Kwon, J. Kang, S. Kim, and T. Yoon, "Impact of Electrolyte Decomposition on Copper Corrosion in Li_6PS_5Cl-Based All-Solid-State Batteries," *Adv. Funct. Mater.*, vol. 35, no. 2420474, 2025.

[409] S.A. Savina and A.M. Abakumov, "Benchmarking the electrochemical parameters of the $LiNi_{0.8}Mn_{0.1}Co_{0.1}O_2$ positive electrode material for Li-ion batteries," *Heliyon*, vol. 9 (12), no. e21881, 2019.

[410] T. Fuchs, T. Ortmann, J. Becker, C.G. Haslam, M. Ziegler, V.K. Singh, M. Rohnke, B. Mogwitz, K. Peppler, L.F. Nazar, J. Sakamoto, and J. Janek, "Imaging the microstructure of lithium and sodium metal in anode-free solid-state batteries using electron backscatter diffraction," *Nat. Mater.*, vol. 23, pp. 1678—-1685, 2024.

[411] J. Liang, J. Luo, Q. Sun, X. Yang, R. Li, and X. Sun, "Recent progress on solid-state hybrid electrolytes for solid-state lithium batteries," *Energy Storage Mater.*, vol. 21, pp. 308–334, 2019.

[412] Y. Tian, Y. An, C. Wei, H. Jiang, S. Xiong, J. Feng, and Y. Qian, "Recently advances and perspectives of anode-free rechargeable batteries," *Nano Energy*, vol. 78, no. 105344, 2020.